A study of the charge structure and energy utilisation in a Stirred Media Detritor using DEM-SPH

Conrad B Ndimande

Thesis Presented for the Degree of

DOCTOR OF PHILOSOPHY

In the Department of

Chemical Engineering

(Centre for Minerals Research)

UNIVERSITY OF CAPE TOWN

February 2022

Plagiarism Declaration

1. I am aware that plagiarism, the reproduction of the work of another author is wrong
2. I have used the scientific convention for citation and referencing. Each significant contribution to, and quotation in this thesis from the work(s) of other authors has been attributed and has been cited and referenced.
3. This thesis is my own work.
4. I do not and will not allow anyone to take this work and pass it off as their own.

Signature: …………………………..

Date: 14/02/2022

Acknowledgements

In this section gratitude is expressed to several people for the contribution they have made to this thesis

Prof Aubrey Mainza for his thorough technical advice while overseeing this thesis,

Prof Paul Cleary for his in-depth and valuable technical feedback, and the opportunity to use the DEM-SPH code he developed,

Dr Matthew Sinnott for assistance with visualisation of DEM-SPH results,

Dr Max Richter for his assistance with data visualisation.

Abstract

The Stirred Media Detritor, (SMD), is a grinding device used for fine and ultra-fine grinding applications in mineral processing. The SMD has a vertically orientated shell that supports a shaft, with protruding impeller arms for agitating the charge. There is currently limited understanding of charge structure and motion in the SMD, particularly the interaction of the media and the slurry. Additionally, the number of arms and their arrangement on the shaft, are important aspects of the impeller that determine flow, energy consumption and grinding efficiency. Impeller geometry choices affect these characteristics of the process. This work focuses on studying the flow of grinding media and slurry for the industrial scale SMD 1100-E. This information is used to explore charge dynamics and energy utilisation in the SMD. To investigate the effect of impeller arm configuration on the operational behaviour of the SMD, the commercially available impeller configuration of the industrial scale SMD 335-E is used as the base case. Mill charge dynamics, transport and mixing, patterns of energy absorption on the mill surfaces are examined for the base case and compared to three different impeller arm arrangements. A two-way transient coupled Discrete Element Method (DEM) and Smoothed Particle Hydrodynamics model is used to achieve this. The ceramic grinding media is represented by the DEM component of the model, which is fully resolved, while the slurry (water and fine particles) is represented by the Smoothed Particle Hydrodynamics (SPH) model. The focus is on steady state operation therefore discharge from and feed into the mill are omitted. A nominal media size of 8 mm is used. The rotational action of the impeller forces the charge to the mill wall creating vortex centred on the mill shaft. The vortex is conical with a large diameter at the bottom, which decrease towards the bottom of the mill. Abrasion is found to be the dominant breakage mechanism in the SMD. Mixing behaviour is complex with media transfer past layers of impeller arms being influenced by the fall distance of media between impeller arm encounters.

Contents

1 Introduction and background 1

1.1 Motivation 3

1.2 Hypothesis 4

1.3 Objectives 5

2 Literature review 6

2.1 Comminution 7

2.1.1 Comminution Laws 7

2.2 Stirred media mills 8

2.2.1 Grinding action 10

2.3 Factors affecting fine grinding 11

2.3.1 Mill speed 12

2.3.2 Feed solids content 13

2.3.3 Mill feed rate 13

2.3.4 Grinding media size 14

2.3.5 Media density 14

2.3.6 Grinding media load 14

2.4 Stirred Media Detritor 15

2.5 Modelling stirred media mills 16

2.5.1 Power based models 17

2.5.2 Population balance model 20

2.6 Numerical modelling 21

2.6.1 DEM modelling 22

2.6.2 Contact laws 22

2.6.3 DEM parameter calibration and validation 27

2.6.4 DEM outputs 28

2.6.5 DEM modelling of stirred mills 31

2.6.6 Fluid modelling 39

2.6.7 SPH 43

2.6.8 DEM-SPH coupling 45

2.6.9 DEM-Mesh based CFD modelling of stirred media mills 46

2.6.10 DEM-SPH modelling of stirred media mills 47

2.7 Summary of Literature Review 50

3 Methodology 53

3.1 DEM solver 55

3.2 DEM-SPH coupling 55

3.3 Mill Configurations 56

3.4 Charge specifications 60

3.5 Speed selection for industrial scales 61

3.6 Charge dynamics and energy utilisation study 62

3.7 Impeller configuration study 62

3.8 Measuring mixing 66

4 SMD 1100-E 67

4.1 Averaged media distribution in the SMD 1100-E 67

4.2 Media and slurry flow in SMD 1100-E 69

4.3 Averaged velocity distribution in the SMD 1100-E 77

4.3.1 Radial velocity distribution 77

4.3.2 Axial velocity distribution 79

4.3.3 Tangential velocity distribution 79

4.3.4 Media velocity isosurfaces 80

4.4 Power draw and energy utilisation 83

4.5 Energy consumption in the SMD 84

4.6 Energy dissipation isosurface 86

4.7 Collision energy spectra 89

5 SMD 355-E 96

5.1 SMD 355-E equilibrium flow structure 96

5.2 Average media distribution for the base case impeller configuration 100

5.3 Velocity distribution in the SMD 355-E 104

5.4 Mixing and transport 110

5.5 Energy consumption in the SMD 355-E 114

5.6 Collision energy absorption spectra 119

5.7 Wear on mill internals SMD 355-E 122

6 Effect of impeller design on mill performance 125

6.1 Averaged media distribution for different configurations 125

6.2 Variation in power draw and energy utilisation with impeller design 133

6.3 Transport and mixing variation with impeller design 141

7 Main observations, conclusions, and recommendations 145

7.1 Main observations 145

7.2 Conclusions 150

7.3 Research novelty 153

7.4 Recommendations 154

8 References 155

9 Appendix 173

9.1 Mill speed selection 173

9.2 Power Data 181

9.3 ELS Data 182

9.4 Matlab Code for data extraction and analysis 183

List of Tables

Table 1: Some stirred media mills used in mineral processing Adapted from (Sinnott et al. 2006) 10
Table 2: Tested Mill Speeds 12
Table 3: Variables in published power models (Radziszewski & Allen 2014) 18
Table 4: DEM studies in tumbling mills 30
Table 5: DEM studies in stirred mills 32
Table 6: Coupled DEM-CFD for stirred media mills 46
Table 7: DEM contact parameters (Cleary et al. 2015b) 55
Table 8: Geometric details of the SMD scales 57
Table 9: Mill speed test matrix 62
Table 10: Grinding volume and charge specifications 62
Table 11: Comparison of energy utilization in DEM only and coupled SMD (Ndimande et al 2019). 83
Table 12: Summary of energy utilisation by collision type in the SMD (Ndimande et al. 2019) 90
Table 13: Modal peak values in terms of energy dissipation rate (W) for media-to-media and media-to-geometry collisions. (Adapted from Sinnott et al. 2006 & Ndimande et al. 2019)..93
Table 14: Energy utilisation by collision type in the SMD; 26% is dissipated in the slurry phase 115
Table 15: Total engagement area for each variant 135
Table 16: Average normalised fall height of the variants. 141
Table 17: Charge height of the variants 143

List of Figures

Figure 1: Comparison of a stirred mill and a ball mill energy consumption 1

Figure 2: Tumbling mills in a comminution circuit 6

Figure 3: Different breakage mechanisms and the resulting progeny (Adapted from Varinot et al. 1997) 11

Figure 4: General and internal view of the SMD (Ntsele & Allen, 2012) 16

Figure 5: Schematic of the linear spring and dashpot model showing the representation of the contacts (Adapted from Govender et al. 2004) 23

Figure 6: Schematic representation of the approach for Herts-Mindlin contact model (adapted from Bbosa 2013) 25

Figure 7: Experimental set up used to measure particle interaction properties (Chandramohan and Powell, 2005) 27

Figure 8: Change in energy spectra at different lifter heights of a) Total energy, b) normal energy and c) shear energy. (Taken from Cleary and Owen, 2019) 29

Figure 9: Wear evolution of holes on the isamil discs as predicted by DEM-CFD outputs a) new disc b) worn after 4 months (Jayasundra et al. 2011) 31

Figure 10: Media flow in a tower mill and a ball mill coloured by speed with red being 2 m/s and 0.2 m/s for the ball and tower mill respectively. Dark blue is 0.15 m/s and 0.2 m/s for the ball and tower mill respectively (Adapted from Morrison et al 2009). 33

Figure 11: DEM Simulation compared with experimental results of a lab scale mill (Adapted from Yang et al. 2006) 34

Figure 12: Different stirrer geometries investigated in an Isamill (Adapted from Jayasundra et al. 2012) 35

Figure 13: Effect of disc spacing on porosity and flow in the IsaMill (Jayasundra et al. 2012) 36

Figure 14: Steady state media distribution in the M10000 Isamill when gravity is not included in the model. The media is coloured by speed (Cleary et al. 2015b) 37

Figure 15: Impact and abrasion wear on the face of a disc of the Isamill at 80% media loading of 15 mm media and a tip speed of 22 m/s (Cleary et al. 2015a). 38

Figure 16: Various numerical methods for computational fluid dynamics (adapted from Hosain and Fdhila (2015). 40

Figure 17: One way coupled steady state flow in a tower mill showing a) Solids fraction b) radial c) tangential and d0axial velocities of slurry for μ = 0.1 (adapted from (Sinnott et al. 2011) 48

Figure 18: DEM+SPH model of Isamill 1000 classifier coloured by fluid speed at different times of the simulation (adapted from Cleary et al. 2015b) 49
Figure 19: General flow chart of the simulation process..53
Figure 20: A screen shot of Autodesk inventor 54
Figure 21: An illustration of the coupling scheme (Ndimande et al. 2019) 56
Figure 22: CAD models of the three SMD geometries. From top left, a) SMD 18.5-E with shaft in place, b) closer view of SMD 18.5-E shaft. c) SMD 355-E with shaft in place, d) closer view of SMD 1100-E shaft, e) SMD 1100-E with shaft in place, f) closer view of the SMD 1100-E shaft...58
Figure 23: Aspect ratio of sub-region of the charge below the bottom impellers of the SMD1100-E. 60
Figure 24: View of the geometric details of each impeller variant are shown on the left, (right) the variants shown in place in the mill..64
Figure 25: Vertical section through the SMD showing steady state distribution of average solid fraction. The blue section below the bottom set of impeller arms is the mill shell (Ndimande et al. 2019). 68
Figure 26: Time series plot of the kinetic and potential energies of both the granular flow (GF) and SPH (slurry) components of the model showing steady state. (Ndimande et al. 2019)....70
Figure 27: A top-down view of the steady state flow in a SMD with the shell made transparent. a) Coupled flow with media coloured by speed while the fluid is coloured white, b) slurry flow in the SMD with the slurry coloured by its speed with the media made transparent (Ndimande et al. 2019). 71
Figure 28: Top-down view of the coupled flow in the SMD, with the slurry coloured by its speed and the media-coloured white shown at time a) 2.7 s, b) 2.8 s, c) 2.9 s and d) 3.0 s. The different simulation times show the impeller at different phases (Ndimande et al. 2019). 73
Figure 29: A close-up, top-down view of the steady state coupled flow in the SMD shown at time a) 2.7 s, b) 2.8 s, c) 2.9 s and d) 3.0 s. The slurry is coloured by its speed and the media made transparent to show the fluid phase clearly (Ndimande et al. 2019). 74
Figure 30: A close-up, top view of the steady state coupled flow in the SMD, with media coloured by its speed, showing the impeller arms interacting with the charge. The fluid is coloured white at a) time 2.7 s, b) time 2.8 s, c) time 2.9 s and d) time 3.0 s. This view shows the small transient surface structures of the media (Ndimande et al. 2019). 75

Figure 31: a) Vortex structure in a 4L lab scale SMD, b) vortex structure in a pilot-scale SMD (Ntsele and Allen, 2013). Both are like that predicted by the DEM-SPH model for the SMD 1100-E (Ndimande et al. 2019). 76

Figure 32: Vertical section through the mill showing time averaged, a) media radial velocity, b) slurry radial velocity, c) media axial velocity, d) slurry axial velocity, e) media tangential velocity, and f) slurry tangential velocity (Ndimande et al. 2019). 78

Figure 33: Isosurface of the averaged media velocity distribution in a frame that is co-moving with the SMD impeller. The mill shell is transparent; a) radial velocity, with red indicating flow towards the wall and blue, flow towards the centre, b) axial velocity, with red indicating flow upwards and blue, flow downwards (Ndimande et al. 2019). 81

Figure 34: (Continued), Media coloured by c) tangential (swirl) velocity with red indicating high velocities up to 3 m/s, and blue low velocities. The green shows media moving at 2 m/s. 82

Figure 35: A vertical section through the mill showing time averaged a) normal power dissipation per unit volume, b) shear power dissipation per unit volume. The power is averaged on a frame. The red indicates areas of high-power dissipation and blue the low power dissipation areas (Ndimande et al. 2019). 85

Figure 36: An isosurface of the steady state distribution of power dissipation in the mill calculated on a grid co-moving with the impeller showing a) shear power per unit volume, b) normal power per unit volume. The mill shell is omitted. Red shows High power dissipation areas at the tip of the impeller arms and blue the low power dissipation areas further from the tips of the arms (Ndimande et al. 2019). 88

Figure 37: Collision energy spectra for the SMD (dissipation rate) vs collision energy, for a) all collisions, b) media-to-media collisions, and c) media-to-liner collisions (mill shell or impeller). The spectra are shown for normal shear and total energy components. The vertical line shows the modal peak for the total energy distribution (Ndimande et al. 2019). 92

Figure 38: Collision energy spectra showing the distribution of energy absorbed by, a) the mill shell, and b) the impeller. The spectra are shown for normal, shear and total components, with the vertical line indicating the position of the modal peak for the total energy (Ndimande et al. 2019). 95

Figure 39: A top-down view of the flow in a SMD 355-E at steady state with the shell made transparent showing a) Coupled flow with media coloured by speed while the fluid is coloured white, b) slurry flow in the SMD 355-E with the slurry coloured by its speed and the media

made transparent. The arrows show the location of the cavities produced by the rotating arms. 97
Figure 40: A narrow horizontal slice through the mill showing the steady state distribution of the charge on each of the impeller arms. With a) media coloured by speed and slurry made transparent for the top row of arms and b) the slurry coloured by speed and media made white for the top row of arms, c) media coloured by speed and the slurry made transparent for the bottom row of arms and d) the slurry coloured by speed and media made white for the bottom row of arms. 99
Figure 41: A vertical section through the SMD 355-E showing the steady state distribution of average solid fraction. The magenta lines show the vertical height (h) at which the solid fraction was assessed. 101
Figure 42: Media and slurry volume fraction profile at different heights in the mill. 102
Figure 43: Volume fraction as a function of angle around the mill at different radii for, a) the level of the top set of arms, b) the level of the bottom set of arms. The magenta lines show the angular position of the arms. 104
Figure 44: Averaged radial velocity distributions of the media and slurry at sampled heights in the mill. Negative velocities indicated motion towards the centre of the mill. 106
Figure 45: Averaged axial velocity distributions of the media and slurry at the sampled heights in the mill. Negative velocities indicate downward movement. 108
Figure 46: Averaged tangential velocity distributions of the media and slurry at the sampled heights in the mill..109
Figure 47: A horizontal section through just above the bottom set of arms showing the two sections of the charge for which the velocity vectors are presented. The position of the top row of arms is shown by the red dotted lines. 111
Figure 48: A vertical slice through the mill showing the radial- axial flow field of the charge for a section A of the SMD 355-E 112
Figure 49: A vertical slice through the mill showing the radial- axial flow field of the charge shown for a section B...113
Figure 50: Axial mixing per revolution for the SMD 355-E. 114
Figure 51: A vertical section through the SMD showing shear and normal power dissipation. a) Shear power dissipation per unit volume and b) normal power dissipation per unit volume. The power is averaged in a frame rotating with the impeller. Red, yellow, and green indicate high power dissipation areas while blue shows negligible energy dissipation. 117

Figure 52: Isosurfaces of the steady state distribution of both the shear and normal power. a) shear power per unit volume and b) normal power per unit volume calculated on a grid that is co-moving with the impeller. The mill shell is omitted in the image for clarity. The high-power dissipation areas (red) occur near the tip of the impeller arms. Intermediate power dissipation areas (blue) occur in advance of the impeller arm tips. 118

Figure 53: Collision energy spectra for the SMD (dissipation rate) for a) media-to-media collisions, and b) media-to-liner collisions (mill shell or impeller). The spectra are shown for normal shear and total energy components. The vertical line shows the modal average for the total energy dissipated........ 120

Figure 54: Collision energy spectra showing the distribution of energy absorbed by, a) the mill shell, and b) the impeller. The spectra are shown for normal, shear and total components, with the vertical line indicating the position of the modal peak for the total energy........ 122

Figure 55: Abrasion wear on the surfaces plotted as rate of shear energy absorption per square metre of a) the impeller and b) the mill shell viewed obliquely from the top down. Highest wear (red) on the impeller occurs at the tip of the arms. Dark blue shows areas where there is little wear......... 124

Figure 56: A vertical section through the SMD for a) base case, b) variant 1, c) variant 2 and d) variant 3, showing steady state distribution of average solid fraction........ 126

Figure 57: Media volume fraction against mill radius at sampled heights for all variants.... 128

Figure 58: Media distribution around the bottom impeller arms (lower arms) and the top impeller arms (upper arms) for a) the base case, b) variant 1, c) Variant 2 and d) Variant 3. The mill is made transparent and media close to the shell corners is not shown......... 130

Figure 59: Illustration of the direction of the charge when interacting with the arms for the base case. The orange arrows show the trajectory of the charge. 131

Figure 60: Illustration of the direction of the charge when interacting with the arms for variant 1. The orange arrows show the trajectory of the charge......... 131

Figure 61: Illustration of the trajectory of the charge when interacting with the arms of variant 2. The red orange arrows show the trajectory of the charge......... 132

Figure 62: Locating the volume fraction data that will assist in determining the engagement area of each arm. Three levels of the cylindrical grid are sufficient for determining the fraction of each arm covered by the charge. Only the volume fraction of the media for the base case is shown here. 134

Figure 63: Media volume fraction plots for three heights in the mill. Each row shows data for one of the three layers from solid fraction data is read. The first column is a horizontal slice at just above the top set of arms. 136

Figure 64: Power draw against engagement area for all variants. 137

Figure 65: Shear media-to-media collision peak energy and associated dissipation rate against total engagement area. 138

Figure 66: Shear media-to-liner (both shell and impeller) collision peak energy and associated dissipation rate against total engagement area. 139

Figure 67: Shear media-to-shell collision peak energy and associated dissipation rate against total engagement area. 139

Figure 68: Shear media-to-impeller collision peak energy and associated dissipation rate against total engagement area. 140

Figure 69: Average fall height against average % mixed per revolution. 142

Figure 70: Total engagement area against average % mixed per revolution 143

Figure 71: A horizontal section through the mill for all configurations showing the charge. 144

Figure 75: Horizontal section through the SMD 18.5-E. Each row shows a different phase of the impeller. Media is coloured by velocity in the first column, and axial velocity in the second column 174

Figure 76: Horizontal section through the SMD 355-E. Each row shows a different phase of the impeller like that of the SMD18.5-E. Media is coloured by velocity. 175

Figure 77: Horizontal section through the SMD 355-E. Each row shows a different phase of the impeller like that of the SMD18.5-E. Media is coloured by velocity. 176

Figure 78: Horizontal section through the SMD 355-E. Each row shows a different phase of the impeller like that of the SMD18.5-E. Media is coloured by velocity. 177

Figure 79: Horizontal section through the SMD 355-E. Each row shows a different phase of the impeller like that of the SMD18.5-E. Media is coloured by axial velocity. 178

Figure 80 Horizontal section through the SMD 1100-E. Each row shows a different phase of the impeller like that of the SMD18.5-E. Media is coloured by velocity. 179

Figure 81: Horizontal section through the SMD 1100-E. Each row shows a different phase of the impeller like that of the SMD18.5-E. Media is coloured by axial velocity. 180

1 Introduction and background

In the mineral processing context, the comminution process has a twofold purpose, to liberate the valuable minerals in an ore from the gangue and to prepare the product particles for subsequent downstream separation processes. There is an exponential relationship between grinding energy requirements and product size as shown in Figure 1 (Jankovic, 2003). The finer the product the higher the energy input requirements (Gao and Weller 1993; Jankovic, 2003; Napier-Munn et al. 1996). When tumbling mills are used, only a small fraction of the input energy goes into useful breakage and size reduction. Stirred mills however, when applied in regrind applications that require grinding the particles to P80s in the region of 45 µm and sub 45 µm, have been shown to be about 30% to 40% more efficient than tumbling mills (Jankovic, 2003; Mazzinghy et al. 2012; Nesset et al., 2006).

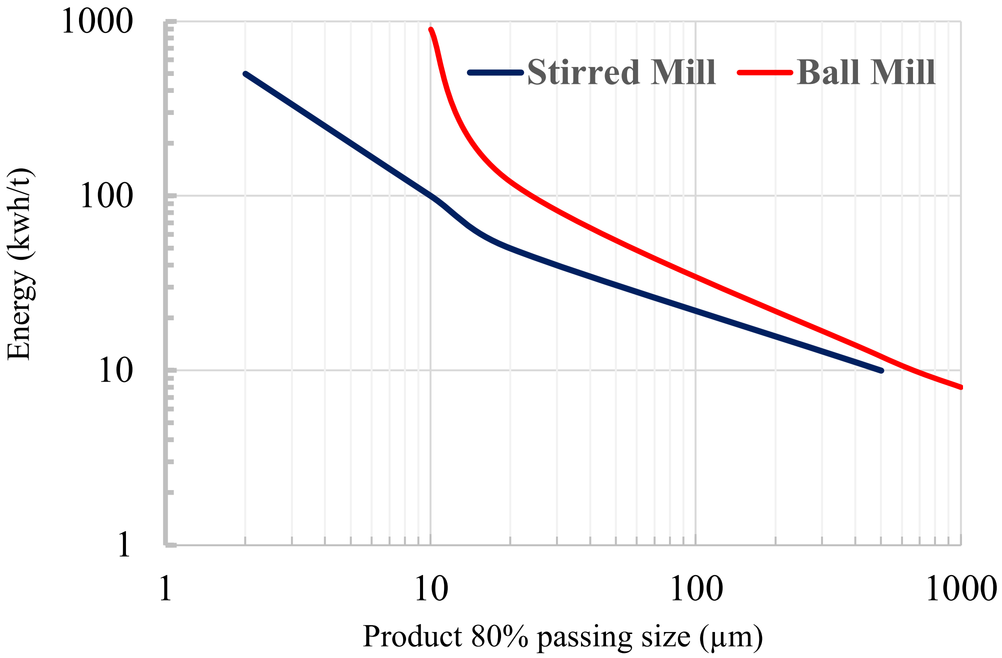

Figure 1: Comparison of a stirred mill and a ball mill energy consumption

The motivation for introducing stirred media mills in the mineral processing industry stems from the increasing need to grind ever finer in an energy efficient environment (Jankovic, 2003; Radziszewski, 2013). Since their introduction in the mining industry in 1953 (Shibayama and Mori, 1999), more than 400 units have been installed (Jankovic, 2003). As of 2011, 40 stirred media mills were installed and operating in the South Africa platinum group metal (PGM) industry (Rule 2011). Of the 40, 27 were in main-stream inert grinding (MIG), and the rest in the ultra-fine grinding (UFG) application.

Stirred mills unlike tumbling mills, have a smaller footprint. This is one advantage stirred mills have over tumbling mills. The use of inert grinding media which does not induce unwanted galvanic interactions on the particle surfaces is a desirable feature of stirred mills. While tumbling mills have the ability to use inert grinding media (ceramic media), the energy input decreases due to the low density of most inert media.

Despite the advantages stirred mills have over tumbling mills in fine and ultra-fine grinding applications, tumbling mills are still used in these applications, primarily because the industry is conservative and has preferred these mills, which have been used for a long time (Radziszewski 2014). Therefore, all new or modern technologies are subjected to stringent vetting before they are considered for application. To increase the understanding of the operation of stirred mills, models for power consumption and energy usage have been developed by a number of authors (Novosad ,1964; Jenczewski, 1972; Herbst and Sepulveda, 1978; Weit and Schwedes , 1987; Tuzun, 1993; Duffy, 1994; Gao et al. 1996; Jankovic, 1998). Unfortunately, the models do not capture the contact and flow environment in the mill, because the particle fluid interactions and their effect on mill performance are unknown. The lack of knowledge of the contact environment is detrimental to the predictive capability of the models, making optimisation and control of these devices difficult. Therefore, there is scope to study the system, particularly the particle fluid interactions that are not yet fully understood.

The purpose of this thesis is to use a two-way coupled Discrete Element Method and Smoothed Particle Hydrodynamics (DEM–SPH) model to understand the following in an SMD:

1. The particle to fluid interactions, charge flow and structure.
2. Mixing transport and flow behaviour with different impeller configurations.
3. Energy utilization and how this change with impeller configurations.

These are important aspects of the device which drive the outputs such as product size distribution, power draw and liner wear. The particle-to-particle contacts and their effects cannot be easily studied using the available experimental techniques. The DEM constituent of the model is used to represent the grinding media and the SPH is used to represent the slurry containing the fine particles.

SPH being a meshless particle method is well suited to predicting slurry flow in devices such as the SMD, that have moving equipment producing complex slurry free surfaces (e.g., splashing and fragmentation). An evaluation of the performance of a commercially available impeller design of an industrial scale SMD 355E is carried out. This is done by studying the charge dynamics, transport and mixing, patterns of energy absorption and wear on the mill surfaces in the SMD. This is then extended to investigating how the charge behaviour is affected by the number and arrangement of arms on the shaft. This will provide the information that will aid in the selection of the appropriate impeller arm configuration for such mills.

1.1 Motivation

There are experimental techniques available for studying the complex operational behaviour of comminution devices such as stirred mills. These include but are not limited to:

1. Transparent shells to visualise the grinding environments. (Cleary and Hoyer, 2000, Venugopal and Rajamani, 2001, Cleary et al. 2003, Maleki-Moghaddam et al. 2013, and Mulenga and Moys, 2014)
2. Positron Emission Particle tracking PEPT (Govender et al. 2013; van de Westhuizen et al. 2011; De Klerk et al. 2019; Tamblyn, 2009)

The use of transparent shells makes only the outer layers of the flow visible and not the interaction of the layers. Information on the motion of the charge and its structure is critical as these drive mill operational outputs such as power draw and product size distribution (Powell and Nurick, 1996; Kulya, 2008; Cleary and Owen, 2016). While PEPT offers information on the charge structure and kinematics, it does not give the effects of particle to particle and particle to geometry interactions.

The inability to obtain both particle interaction and flow information in a mill, limits the rate of improvement of comminution devices, and the development of models to control their operation. Tracking the motion of the particles and determining the effect of their collisions with each other and with geometry will enhance the understanding of the operational behaviour of these devices. The Discrete Element Method (DEM) has the capability to track individual particles and the effect of their collisions (Cundall and Strack, 1979) using a computational framework. For systems that are operated wet, the fluid phase of the charge will influence mill outputs depending on the extent of packing of the solid media.

To account for the effect of the solid particles on the fluid and the other way round, the motion of the solid particles must be coupled with a suitable solution method for the fluid (Cleary et al. 2015b).

Available options for the fluid solution method are the Eulerian based mesh methods such as computation Finite Volume method and the Lagrangian meshless particle-based techniques such as smoothed particle hydrodynamics (SPH). A meshless Lagrangian based method like SPH has advantages over Eulerian based ones. This is because the fully Lagrangian methods have been proven to inherently capture the interfaces in multiphase flow around complex geometries (Aubram et al. 2010). Therefore, in this work the Lagrangian SPH is used to model the fluid phase of the mill charge.

Coupled discrete element modelling (DEM) and smoothed particle hydrodynamics (SPH) modelling techniques are powerful tools for aiding the understanding of the particle-particle and particle-fluid interactions and how these affect power draw and energy utilization in the system. The model based on coupled DEM-SPH will be used to perform studies to assess the charge behaviour and the influence of various design variables, on power draw, transport and mixing, energy utilization and liner wear in the SMD.

1.2 Hypothesis

The following hypotheses will be tested in this work

1. Two-way coupled DEM-SPH can simulate the flow of media and fluid in a vertical stirred mill, giving the energy spectra which characterises the grinding environment. This is because the motions of both the media particles and the fluid are tracked.
2. DEM-SPH simulation outputs can be used to understand energy utilisation in the SMD and identify areas of high energy dissipation in the mill, known as the grinding zone, and determine how efficiently the feed is transported into and out of this area. This is because the motions of both the fluid and the particles and the effects of their interaction can be tracked using the model.
3. DEM-SPH outputs can be used to assess the effect different arm configurations have on charge structure, power draw, mixing and energy utilisation. This is because the collisions of the media particles to the geometry and their effects are measured by the model.

Two-way coupled DEM-SPH simulation is used to understand the particle to particle and particle to fluid interactions in a Stirred Media Detritor at three different scales. The study will provide insights on the charge structure in the SMD, how the energy drawn is used to agitate the charge, mixing and transport. The effect of different design and operating variables on the afore mentioned aspects will be determined.

1.3 Objectives

The main aims are as follows:

1. Perform DEM only simulations for three SMD scales which will then be extended to include DEM-SPH two-way coupling. This is done to study both the particle to particle and particle to fluid interactions and evaluate the effect the fluid phase has on them. This is important because these devices are operated wet in mineral processing applications, therefore, excluding the fluid phase does not adequately describe the grinding environment.
2. Use the averaged motions of the DEM and SPH particles for the three scales, to study the structure of the charge and the distribution of both media and slurry. The energy spectra will be used to evaluate energy consumption in the SMD.
3. Perform parametric studies to evaluate the influence of stirrer arm positioning on the particle to particle and particle to fluid interactions, power draw, mixing and transport in the SMD.

2 Literature review

The purpose of the literature review chapter is to provide a background firstly to comminution in general, then to stirred mills and their application in the mineral processing industry. Papers dealing with the effect of key operational and design parameters on the behaviour of the mill are reviewed. A review of papers reporting on modelling stirred media mills computationally is also presented here. The papers reviewed provide the background for the selection of operating and design parameters that were investigated in this thesis, and a general review of what is considered important in stirred milling studies.

Valuable minerals are liberated from the undesirable gangue and prepared for subsequent processing through comminution process. This process involves crushing and grinding the ore using a few devices such as crushers, tumbling mills and stirred media mills. This process has been shown to consume the largest quantity of energy in a mineral processing circuit (Napier-Mun et al., 1999). Tumbling mills are the most used devices for grinding in mineral processing despite consuming 50% of the total concentrator energy (Mainza, 2006).

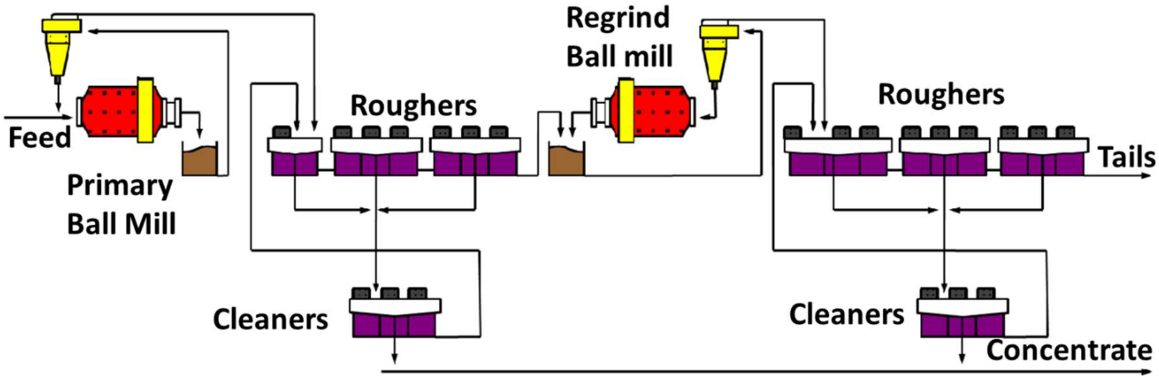

Figure 2: Tumbling mills in a comminution circuit

A typical flow sheet for platinum group metal (PGM) recovery is shown in figure 2, with the tumbling mills employed for grinding. These mills are known to be notoriously energy inefficient, especially in cases where they are used for treating ores that have fine particle intergrowth and require finer grinding to achieve good liberation (Fuerstenau and Abuzeid, 2002). To ensure the concentrators profitability, grinding in tumbling mills must be controlled and optimised to prevent over grinding (Wills, 1992). Tumbling mills have been shown to be capable of grinding finer than is conventionally acknowledged by using small media (Napier-Mun et al., 1999). Stirred mills however, have been found to be more efficient than tumbling mills for regrind applications requiring P80s in the region of 45 µm and sub 45 µm (Jankovic, 2003; Mazzinghy et al. 2012; Nesset et al., 2006). Consequently, the mineral processing industry is adopting stirred media mills for regrind duty in comminution circuits.

The superior efficiency of stirred mills in regrind applications may be attributed to more efficient transfer of energy to the charge and the ability to use very small media ~ 2mm. Additionally, comparison of the energy spectra of a stirred mill (Vertimill) and a tumbling mill of the same power show that more energy is dissipated in shear events in the stirred mill than in the ball mill (Radziszewski and Allan, 2014). Furthermore, stirred media mills are being used for grinding requirements of F80s of 150 µm, though there is a need to select the correct type of stirred media mill to provide the benefits of these devices.

Several stirred milling technologies have been developed in recent years (Kalra, 1999; Jankovic, 2003). These differ mainly in the orientation of the shell and stirrer design. To develop a good understanding of their capabilities, studies that consider the flow of particles and fluid, such as computational studies are required (Jankovic, 1998 & 2003; Jayasundra, 2011; Sinnot et al., 2006, 2011; Clear et al., 2006). Since computational studies require intricate details, only one technology will be considered in this study.

2.1 Comminution

2.1.1 Comminution Laws

In comminution it is important to be able to predict the energy required to reduce a given mass of feed to a device. Empirical laws developed by Von Rittinger (1867), Kick (1885) and Bond (1952), known as “The three laws of comminution” address this challenge. The laws generally relate energy consumption of a comminution device to the particle size of the product produced. The laws are represented mathematically as follows:

$$E = K\left(\frac{1}{x_2} - \frac{1}{x_1}\right) \tag{1}$$

$$E = K_k\left(\frac{x_f}{x_p}\right) \tag{2}$$

$$W = \frac{10W_i}{\sqrt{P}} - \frac{10W_i}{\sqrt{F}} \tag{3}$$

Equation 1 is Rittingers law, where E is the energy required to produce a product of size x_2 from a feed of size x_1 while K is a constant of proportionality. Equation 2 is Kick's law which relates the energy E, to the ratio of the feed x_f and product x_p size indices (Kick, 1885). Equation 3 is Bond's law relating W to the particle size of the feed F and the product P, at which 80% of the material passes (Bond, 1952). W_i is the work index, defined as the specific energy required to grind material from infinite grain size to 80% passing 100 µm.

Several researchers have attempted to show that these "three laws of comminution" are variations of a single general equation (Fuestenau and Abouzeid, 2002; Morrel, 2007). After a review of a wide range of comminution devices, Hukki (1961) reported that none of these relationships were adequate when taken alone. Bond's law predicted well, the energy vs size behaviour for rod and ball mills; Kick's law worked for crushing sizes greater than 1 cm while that of Von Rittinger better predicted the energy vs size behaviour at finer sizes (10 – 1000 µm). This means that the size energy relationship is best described by an equation that is a composite of the three laws. It has been shown that larger particles have more flaws or cracks than the smaller particles. Generally, particle strength increases with decreasing particle size. This means that higher energy is required to break smaller particles than larger ones as suggested by the laws of Rittinger and Bond (Tavares and King, 1998; Banini, 2000; Shi and Kojovic, 2007). Therefore, studies that focus on the grinding/collision environment in stirred mills are important because they provide information on the mechanisms in these devices which result in their energy efficiency.

2.2 Stirred media mills

The principles of stirred milling, according to Stehr and Schwedes (1983) can be traced back over 70 years. The early versions of these mills were called attritors and were used for surface cleaning of the charge. Over the years, they have been applied successfully for deagglomeration, dispersion and grinding processes in different industries, and can be seen particularly where high product fineness is required (Kwade 2013). Stirred media technology is applied but not limited to the following industries (Kwade 2013):

- Paint and lacquer - used for size reduction of pigment particles and dispersing them in the mixture of resin and pigment
- Chemical and pharmaceutical – used for size reduction of materials such as vitamins
- Ceramics – used mostly for size reduction of raw materials such as clay

- Mineral Processing – used for milling the ore particles and at times for polishing particle surfaces.

In this computational study, the focus is on stirred mills with the context of applications in the mineral processing industry. Stirred mills consist of a static grinding chamber whose axis can be oriented vertically or horizontally (Napier-Munn et al. 1996). Suspended in the grinding shell is a shaft with an agitator. A motor drives and rotates the agitator attached to a central shaft, to set the charge in motion (Sinnott et al. 2006). The agitator can come in the form of pins or discs in different configurations. Stirred media mills are usually operated in wet mode; this is done for ease of transport of the product from the mill to the next processing stage. The cement industry is one of the exceptions, with air introduced into the mill for transport of material out of the mill (Altun et al. 2013). Stirred mills with a horizontal grinding chamber are sealed and pressurized unlike the vertical grinding chambers which have a much simpler design that has no pressure seal. The power intensity in vertical mills is an order of magnitude lower than in horizontal mills. This is owing to the fact that vertical mills have an upper limit on the speed of the agitator to prevent slurry overflow (Sinnott et al., 2006). Table 1 lists some of the commercially available stirred media mills used in the mineral processing industry.
Generally, stirred mills can be classified according to the flow type produced in the mill. There are two major categories; fluidized and gravity- induced charge mill types (Ntsele and Allen, 2012). The tower mill/VERTIMILL is an example of a commercially available gravity induced mill. These have a low speed double helical screw type agitator. This lifts the charge up through the central region of the mill to near the free surface from where it then flows downward through an annular outer region before returning to the screw (Ntsele and Allen, 2012; Sinnott et al. 2006). Fluidized mill types on the other hand, use discs or impeller arms at high speeds to fluidize the charge to suspend almost homogeneously the media and ore particles. Examples of such mill types are the Higmill, the VXPmill, the Maxxmill, the Isamill^{TM}and the stirred media detritor (SMD). Stirred media mills can be used in a variety of circuit designs. The most common arrangement for gravity induced stirred mills is in a pre-classified closed circuit with hydrocyclones. Fluidised mills are most used in pre-classified open circuits (Ntsele and Allen, 2012; Knorr and Allen, 2010).

The media size used in stirred mills is smaller compared to that used in conventional ball mills. Gravity induced mills typically use high density steel media in the size range of 12-40 mm (Ntsele and Allen, 2012). Fluidised mills typically use inert media such as ceramic or competent silica sand media size ranging between 8-2 mm. To keep the grinding media from escaping the mill, stirred media mills employ a sieve or a hydrodynamic classifier, which is placed on the discharge outlet of the mill (Napier-Munn et al. 1996). In this work, the focus will be on a stirred media mill with pins as the mechanism for agitating the charge, specifically the Stirred media detritor.

Table 1: Some stirred media mills used in mineral processing Adapted from (Sinnott et al. 2006)

Mill Type	Manufacturer	Orientation	Agitator type	Category
Vertimill	Metso	Vertical	Helical screw	Gravity induced
SMD	Metso	Vertical	Impellers	Fluidized
VXPmill	FLSmidth	Vertical	Rotor discs	Fluidized
Tower mill	Kubota	Vertical	Helical screw	Gravity induced
Isamill^{TM}	Xstrata	Horizontal	Rotor discs	Fluidized
Higmill	Outotec	Vertical	Rotor discs	Fluidized

2.2.1 Grinding action

The particle size distribution of a material after comminution depends on the size reduction mechanism. It has been shown that three main breakage mechanisms occur in stirred mills, such as impact, abrasion/attrition, and compression/cleavage (Kwade 1999; Varinot et al. 1997; Hennart et al. 2009; Kapur et al. 1997; Napier-Munn et al. 1996). Figure 3 shows the different breakage mechanisms. Impact or fracture breakage occurs when rapid intense stresses are applied (impact). The progeny produced is smaller than the parent particle with a wide size distribution.

Cleavage occurs when relatively low stresses are slowly applied (compression), resulting in progeny whose size distribution is 50 – 80% smaller than the parent particle. Abrasion or attrition is the dominant mechanism in stirred mills. Abrasion/attrition occurs when local low intensity stresses are applied. The progeny thereof has a bimodal size distribution as shown in Figure 3. In practise, these mechanisms do not occur in isolation. Computational modelling has the capability of quantifying the energy dissipation of each of these breakage mechanisms. This is a more quantitative approach to determining the dominant mechanism in the stirred mill which is abrasion or attrition.

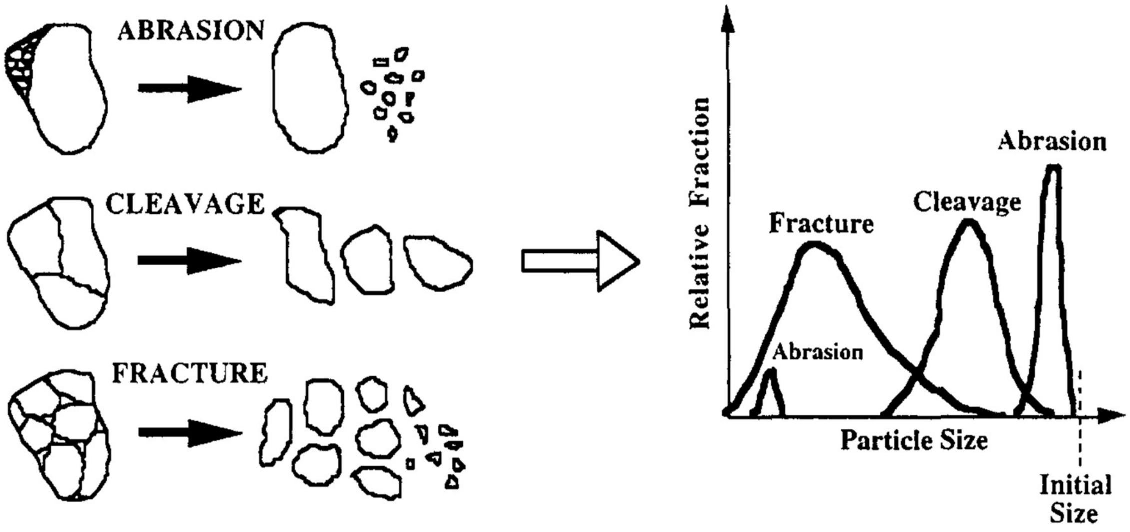

Figure 3: Different breakage mechanisms and the resulting progeny (Adapted from Varinot et al. 1997)

2.3 Factors affecting fine grinding

According to Jankovic (2003), numerous factors affect the grinding performance in a stirred mill. Molls and Hornle (1972) identified 44 of these factors that included both operational and design variables. While they are many, not all of them have a significant effect on the comminution process in a stirred mill. The study of Hornle (1972) did not endeavour to determine which of the 44 are significant and which are not. There is a large body of work investigating the effects of most of the operating factors that affect fine grinding (Lisso 2013; Chaponda 2011; He et al. 2006; Jayasundara et al. 2010; He and Forsberg, 2007; Jayasundara et al. 2012; Gao & Forssberg 1993; Gao & Forssberg 1996: Jankovic 2013; Toraman & Katircioglu 2011). Toraman and Katircioglu (2011) determined that grinding time, Stirrer speed, slurry density and ball loading (expressed usually as a percentage of the grinding volume) had a significant effect at the 95% confidence level, on product particle size and particle distribution. Moreover, they noted that the variables had statistically significant interactions which agrees with the observation made by Jankovic (2013). In this section the variables that have been shown to be significant are discussed.

2.3.1 Mill speed

The agitator/mill speed is known to influence grinding efficiency in stirred mills. The agitator transfers energy to the charge causing motion. A variety of speeds have been tested in both horizontal and vertical stirred mills. .

Table 2 shows some researchers that have tested a wide range of the speeds on both horizontal and vertical mills. Higher agitator speeds have been shown to increase product fineness and the mill power draw. This comes with a decrease in the energy efficiency of the mill (Weller and Gao, 1999; Jankovic, 2003; Zheng et al. 1996). Jankovic (2003) used a high speed Netzch mill and a pilot scale tower mill. He reported an increase in grinding efficiency with increasing mill speed for the Netzch mill and the opposite for the pilot scale tower mill. Chaponda (2011) reported a decrease in energy efficiency with increasing mill speed in the Isamill. This finding agrees with that of Zheng et al. (1996) who used a vertical stirred mill. The contradictory findings of the effect of speed on grinding efficiency suggest the existence of an optimum stirrer speed which is consistent with the findings of He and Forsberg (2007). These findings show that for a mill that has a variable speed drive, it is important to determine the speed optimum efficiency. In this work the mill speed is not varied because the mill used (SMD) has a fixed speed.

Table 2: Tested Mill Speeds

Author	Mill type	Speed (RPM)
Toraman and Katircioglu (2011)	Vertical	300 - 500
Jankovic (2003)	Vertical	50 - 150
Zheng et al. (1996)	Vertical	260 - 1000
Lisso (2013)	Vertical	235 - 586
Jayasundra et al. (2010)	Horizontal	400 - 1000
He and Forrsberg (2006)	Horizontal	1204 - 2255
Chaponda (2011)	Horizontal	1500 - 2100
Fadhel and Francis (2001)	Horizontal	2130 - 4370
Gao et al. (1996)	Horizontal	805 - 2253

2.3.2 Feed solids content

Solids concentration is the mass fraction of solids in the slurry. This has a direct influence on the fineness of the product and the mill specific energy consumption (Gao et al. 2007; He et al. 2006; Jankovic, 2003; Zheng et al. 1996). Solids concentration also affects slurry viscosity. Slurry viscosity is defined as the resistance of particles to flow (Nappier - Munn et al. 1999). Solids concentration has been shown to have a non-linear relationship to viscosity. High slurry viscosities result in an increase in mill power draw and a decrease in grind efficiency.

High solids concentration (> 40%) results in increased grinding efficiency, since the probability of an ore particle being trapped and sufficiently stressed by the media is lower at low solids concentration (Kwade, 1999). Product fineness has also been reported to increase with increasing solids concentration to a limit beyond which it decreases (He et al. 2006; Jankovic, 2003; Zheng et al. 1996). For a constant slurry volume, a few researchers have reported a critical solids concentration, above which viscosity becomes detrimental to grind efficiency, due to low mobility of the charge (He and Forsberg 2007; Ding et al. 2007; Bernhardt et al. 1999; Jankovic 2003; Zheng et al. 1996). It is therefore, crucial to ensure that the solids concentration is kept at an optimum point to maximise milling efficiency. In this work a solids concentration of 40% w/w is used for all simulations.

2.3.3 Mill feed rate

Feed rate of the slurry to the mill is an important factor that affects key aspects of the process such as throughput and residence time. Feed rate has been reported to affect the energy consumption in horizontal mills differently compared to vertical mills. Chaponda (2011) reported a decrease in specific energy as feed rate increased when milling UG2 ore in an Isamill. The same observation has also been made by Weller and Gao (1999) when milling Dolomite in a horizontal stirred mill. This is largely because, high feed rates interrupt the flow dynamics of media in horizontal stirred mills, which results in uneven distribution of media along the mill length (Jankovic 2008). Feed rate is reported to have little effect on specific energy in a vertical stirred mill (Jankovic 2008). In this work, batch studies are carried out in the stirred media detritor (SMD), so the effect of feed rate is not considered.

2.3.4 Grinding media size

Grinding media size has been identified as an important variable in fine grinding (Jayasundra 2008; Kwade and Schwedes 2002). Generally, media size is usually chosen based on the feed top size. The probability of particle breakage from shear stress is a function of grinding media size (He and Forsberg 2007). Mostly, product fineness increases with decreasing media size to a point beyond which the media becomes too small to cause breakage (Jankovic, 2003; Zheng et al, 1996). If the media size is too small the result is a decrease in grinding efficiency and a wide product distribution containing material that is unbroken (Gao et al. 2007). According to Jankovic (2003), for a specific stirrer speed, there is a decrease in the transfer of momentum between the agitator and the media with decreasing media size. Therefore, it is important to select the optimum media size for a given mill speed and feed size to ensure energy efficiency and optimal mill performance (Wang and Forssberg, 2000; Gao et al. 2007). In this work the grinding media size used is 8 mm, the design limit for the SMD, which minimizes computational cost.

2.3.5 Media density

Media density is known to have a significant effect on product fineness from a comminution device. It has been reported that product fineness increases with increasing media density (He and Forsberg 2007; Zheng et al. 1996). Generally, the higher the density of the grinding media, the higher the power draw of the mill which may result in low energy efficiency (Zheng et al. 1996). Mankosa et al. (1986) compared steel balls to glass beads and observed that for the same residence time, media that is less dense requires low torque compared to high density media. As such, it is imperative to select the correct media density to ensure energy efficient comminution. In this work the media density used is 2700 kg/m^3.

2.3.6 Grinding media load

Grinding media load commonly refers to the volume fraction occupied by the media in the mill. In horizontal stirred mills according to Yang et al. (2006), compressive forces on particles and flow velocities increase with increasing media loading. This means that energy efficiency and product fineness are better at high media loading, for horizontal mills at the same specific energy (Yang et al. 2006; Weller and Gao, 1999). Weller and Gao (1999) also demonstrated that high media loads in horizontal mills increases the capacity of the device. Low media loading tends to reduce the stirrer to media interaction resulting in decreased grinding efficiency (Yang et al. 2006; Weller and Gao, 1999). The increase in efficiency with increasing media loading has an optimum point (Gao et al. 2007; Van der westhuizen et al. 2011). This optimum point is a function of media properties as well (Gao et al. 2007; Van der westhuizen et al. 2011). Locating this optimum media loading is important for efficient comminution.

In vertical mills Weller and Gao (1999) proposed that the media must cover a minimum number of pins, above which increasing media load does not increase grinding efficiency. The upper limit of the media loading in a vertical mill is determined by the position of the topmost stirrer relative to the product discharge area (Weller and Gao, 1999). It has been observed that the mill loading has a significant effect on the power draw of the device (He et al. 2006). The relationship between mill loading and power draw has been observed to be linear; this has been used industrially to maintain power set points in the mill (Gao et al. 2007; Wills and Napier-Munn, 2006).

2.4 Stirred Media Detritor

The SMD is the stirred media mill of interest in this thesis and three models are used in the study. The SMD has a vertical, octagonal shell that supports a shaft equipped with arms. A motor drives the shaft which is centred in the grinding chamber (Allen, 2013). Figure 4 shows the external and internal features of the SMD. Energy is imparted to the grinding media/slurry mixture by the rotating arms, resulting in shear and compressive forces that cause size reduction (Ntsele and Allen, 2012). Due to its vertical orientation, the SMD does not require slurry seals or inlet feed pressure.

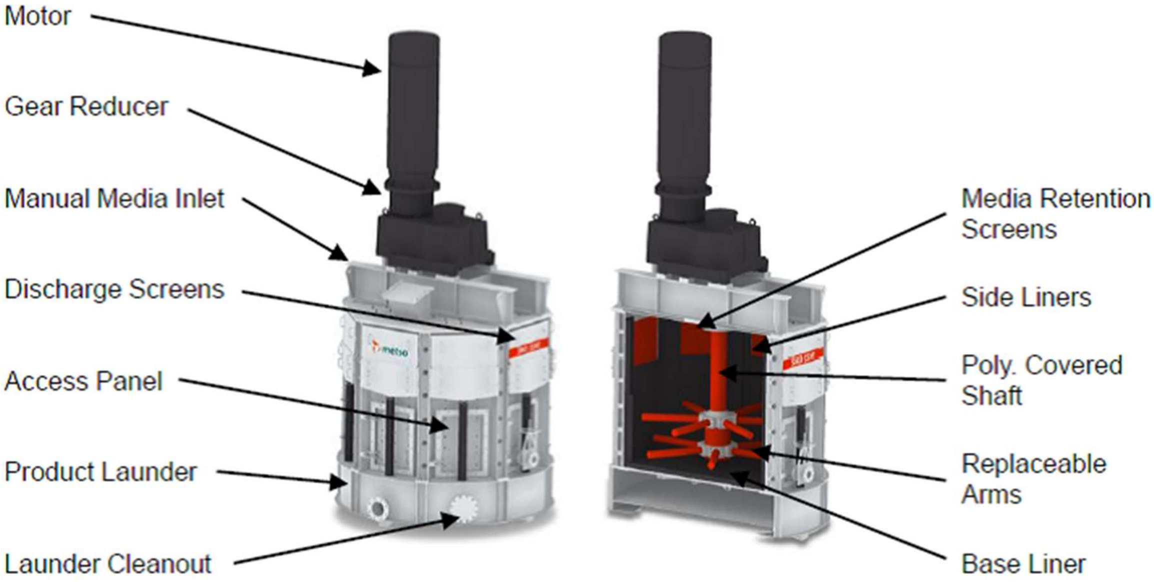

Figure 4: General and internal view of the SMD (Ntsele & Allen, 2012)

Presently, the SMD is available with a maximum installed power of 18.5 KW for the 18.5-E, 355 KW for the 355-E and 1100 KW for the 1100-E. Polyurethane rubber is used to line all the mill internals, shaft, and impellers. The slurry feed is charged through the inlet at the top of the mill and directed into the grinding zone. The Mill also has an inlet for the grinding media situated at the top of the mill. On each of the eight sides of the mill shell is a screen whose purpose is to allow ground ore particles to discharge while retaining the grinding media.

The mill is designed to process a slurry solids content ranging between 30 – 60% by weight and can grind down to P_{80} of 5-35 µm. The SMD uses ceramic media with a size range of 1 - 8 mm (Allen, 2013). The size of the media used is usually chosen based on the feed top size.

2.5 Modelling stirred media mills

This section details research done in modelling stirred media mills, both horizontal and vertical that is pertinent to this work. Given here is a summary of the approach that has been taken to predict the power consumption of stirred media mills. This is followed by approaches taken to extend the prediction from just power draw to product size distribution. A discussion on the research work done on the application of DEM and SPH numerical methods of stirred media mills is presented.

Since grinding is a very energy intensive process, detailed understanding of the operational behaviour of stirred media mills is vital to optimise operations. The operational behaviour of these devices is highly complex. Modelling this equipment mechanistically is not an easy task as the physics behind the operational behaviour is not entirely understood (King 2001). This is mainly because the comminution devices have a highly abrasive environment and an opaque shell. The solid opaque shell makes it impossible to observe particle interactions and flow patterns in the mill. In addition, placing any measuring instrument in the mill is not possible because of the harsh damaging environment.

Due to the difficulties associated with obtaining measurements in stirred mills, the dominant approach to understanding the milling process has been to use the measurable inputs and outputs of the process. These are commonly used in a population balance framework with breakage tests of ore used to develop calibrated empirical models of the process.

2.5.1 Power based models

The ability to predict the behaviour of a comminution device begins with successfully predicting the power drawn by the device in operation (Radziszewski & Allen 2014). These calibrated empirical models are known as power models, and they relate the factors affecting grinding in stirred mills and the power consumption. The common approach to develop the models has been to use measurable inputs and outputs of the process in a population balance framework, with breakage tests of the ore. Table 3 summarises some of the variables used to develop power models reported in literature. A brief review of the power models developed for stirred media mills is given here.

The authors listed in Table 3 developed power models using experimental data from different types of stirred mills. The variables studied (also listed in Table 3) are correlated to the power consumption of the mill either by multiple linear regression or dimensional analysis. These models are principally fitted averages over collections of ostensibly similar data sets. The power model structure developed using linear regression is of the following form:

$$Y = \alpha + \beta_1 X_1 + \beta_2 X_2 + \beta_3 X_3 + \beta_4 X_4 \tag{4}$$

Where Y is the power drawn by the mill in KW, α being the constant, β the regression coefficient for each factor (variable), and the factor (variable) considered.

Table 3: Variables in published power models (Radziszewski & Allen 2014)

	Novosad (1964, 1965)	Jenczewski (1972)	Herbst, Sepulveda (1978)	Weit, Schwedes (1987)	Tuzun (1993)	Duffy (1994)	Gao (1996)	Jankovic (1999)
Impellor speed	X	X	X	X	X	X	X	X
Mill Diameter	X	X	X	X	X			X
Slurry density	X			X	X		X	X
Media depth	X		X		X	X		X
Impellor diameter	X	X				X		X
Charge density	X				X	X		X
Media density			X				X	X
Media top size			X			X		X
Shaft diameter	X			X				X
Number of screw Helixes						X		X
Friction								X
Media Mass		X						X
Screw pitch								X
Length of impellor				X				
Screw thickness								X
Thickness of pins	X							
Viscosity				X				
Disperant							X	

Duffy (1994) carried out experiments on a tower mill at both pilot and industrial scale. Data from those experiments was used to develop a power model. Some of that data was used to validate the model. The No load Power was related to the mass of the screw W_s, the diameter of the stirrer D_s and speed of the stirrer N_s. It was postulated that the net power was related also to the charge height H_b. media size D_b, media density ρ_c and stirrer geometry T (number of turns on the screw stirrer). The no load and the net power equation took the following form

$$\text{No Load Power (KW)} = 0.000134\ N_s W_s D_s^{0.57} \tag{5}$$

$$\text{Net Power} = K H_b N_s \rho_c D_b^{0.111} D_s^{a} T^{b} \tag{6}$$

Gao et al (1996) studied the dependence of power on slurry density ρ_s, stirrer speed N_s, media density ρ_b and the amount of dispersant added to the feed, d (% w/w of ground solids). Gao et al (1996) then concluded that stirrer speed was the dominant factor having a significantly non-linear effect on power whereas slurry density was also found to be significantly non-linear. A simple power law equation was developed by Gao et al (1996).

$$P = 10^{9.29}(N_s)^{1.429}(\rho_s)^{2.9}(\rho_b)^{0.180}(d)^{-0.096}\ \text{KW} \tag{7}$$

More recently, Martins & Radziszewski (2015) proposed a generalized analytical shear based power model. This model expresses power as a function of angular rotational speed ω, viscosity μ and the shear volume V_{τ}.

$$P \cong \mu\omega^2 V_{\tau} \tag{8}$$

These models have been used to aid the design and optimization process of stirred mills; however, they have key limitations. Firstly, they capture very little of the physics of the comminution process. The nature of the collision environment and how this change with conditions is not considered. This limits their predictive capability and accuracy when used particularly outside the range of conditions for which they were developed.

Kwade (1999) introduced a model that seeks to characterize the collision environment. He suggested that the comminution process is governed by two factors. The frequency with which feed particles, and their progeny are stressed (number of stress events) and the magnitude of the stress of each stress event, known as the stress intensity. For a batch grinding process, the number of stress events for each particle (SN) is a function of the number of media contacts, the probability that a particle is caught and sufficiently stressed and the number of product particles in the mill. Kwade (1999) expressed the stress number as a function of the media filling ration of the φ_{GM}, the grinding time t, the number of revolutions of the stirrer n, the volume concentration c_v, the grinding media diameter d_{GM} and the porosity of the bulk grinding media ε.

$$SN \propto \frac{\varphi_{GM}(1-\varepsilon)nt}{\left(1-\varphi_{GM}(1-\varepsilon)\right)C_v d_{GM}^2} \tag{9}$$

Some assumptions were made to develop a mathematical representation of the stress intensity (SI). These assumptions are that only single particles are stressed between the grinding media, the tangential velocity of grinding media is proportional to the circumferential speed of the disks and the elasticity of the feed material is much smaller than that of the grinding media (Kwade 1999a; Kwade 1999b). The stress intensity can then be derived as a function of the grinding media density ρ_{GM}, slurry density ρ_{sl}, and the speed of the stirrer *v*.

$$SI = d_{GM}^3(\rho_{GM} - \rho_{sl})v^2 \tag{10}$$

Stress intensity has the units of Nm, multiplying by ω gives units of power.

$$\text{Power} = f_c SI\omega \text{ (W)} \tag{11}$$

A knowledge of the number of contacts and the intensity of these contacts is important for understanding the grinding process. To have an accurate measure of this, particles and their contacts must be tracked.

2.5.2 Population balance model

The power models reviewed so far do not have the capability to predict the product size distribution from a comminution device. The population balance model is used to account for the appearance and disappearance of certain size classes in the mill. This model, first introduced by Epstein (1948), is used in conjunction with the power models to predict the product size distribution of the comminution device. It has since been developed further for mineral processing applications by several researchers (Whiten, 1974; Herbst and Fuerstenau, 1968, 1973; Austin and Shah, 1983). The population balance essentially reduces what is happening in the mill to three relationships (Powell & Morrison 2007):

- The first is the selection function S_i, which is the fraction of a specified particle type selected for breakage.
- The second is the breakage or appearance function b_{ij}, which is the degree to which the selected particle type undergoes breakage.
- Finally, the discharge function d_i, the fraction of material selected to exit the milling process.

The assumption made is that first order breakage occurs. This is based on the proposition that the product of ground material from a given size class per unit time is a function only of the mass of that size fraction in the mill (Austin, 1990). For batch grinding kinetics the population balance model is as follows:

$$\frac{dm_i}{dt} = -S_i m_i(t) + \sum_{j=1}^{i-1} S_j b_{ij} m_j(t) \qquad (12)$$

Where m_i is the mass fraction of particles in size class i. The population balance model has been used extensively to scale up tumbling mills (Datta and Rajamani, 2001; Herbst and Fuestenau, 1968, 1973; Austin and Shah, 1983). To determine the selection and breakage function, laboratory scale experiments are performed using the same as the industrial scale mill.

Researchers such as Kwade (1999), Yue and Klein (2004) carried out studies in stirred media mills that showed the assumption of first order breakage holds in these mills. Other researchers investigated the applicability of the population balance for stirred milling (Gao and Forssberg, 1994; Tuzun et al. 1993). Yue and Klein (2004) reported that the Rosin-Rammler equation fitted first order breakage in stirred mills better than the Gaudin-Shuhmann equation. Their results showed that the fit becomes poor at particles sizes below 5 μm. This showed non first order breakage in the ultra-fine size range. Hogg (1999) and Gao and Forssberg (1994) used theoretical models which confirmed that when attrition is the dominant breakage mechanism first order breakage does not exist, meaning the population balance cannot be applied. The challenge with the population balance model for ultra-fine grinding is that the experimental method for obtaining the selection and breakage functions become increasingly difficult as the product size becomes smaller.

The models reviewed have been used to assist with design and optimization of stirred mills. The power models are essentially fitted averages over collections of similar data sets. They do not consider the nature of the collision environment and how it changes with conditions, and they capture very little of the comminution physics of the process. This limits their predictive capability and accuracy when used particularly outside the range of conditions for which they were developed.

An understanding of particle flow and breakage in a stirred mill is imperative for developing robust models that predict the behaviour of these devices at different conditions. The motion of the charge and the media-to-media interactions govern process outputs such as power draw, product size distribution and discharge rate. To gain understanding of these aspects of the process requires the motion of the particles to be tracked. In addition to that, the effect of the collisions of the media with both the mill geometry and other media particles must be determined. There are numerical modelling techniques which can predict the flow of particulates in a comminution device. The Discrete Element Method (DEM) is the main method available with such capability. A description of DEM is given in the next section.

2.6 Numerical modelling

In this section a description of the Discrete Element Method is given and how it can be implemented to predict the flow of particles. The outputs of this method and how they can be used to gain understanding of charge motion and particle interactions in a stirred mill are also discussed.

2.6.1 DEM modelling

DEM is a computational method that simulates the rotations, displacements, and contacts of discrete bodies/particles. This method can be used to study the motion of the charge (media and ore particles) in any comminution device. The method tracks the motion of each particle and models all particle-to-particle and particle-to-geometry collisions. The particles are allowed to overlap when they come into contact hence, it is called a 'soft contact' method. This technique was pioneered by Cundall and Strack (1979) when they used it to model the behaviour of soil particles under dynamic loading conditions. The method essentially has three stages:

1. A search grid is set up and employed to intermittently keep track of possible particle-to-particle and particle-to-geometry collisions.
2. The normal and tangential forces from particle-to-particle and particle-to-geometry collisions are determined using a suitable contact force law.
3. The forces acting on each particle are summed to determine the translational and rotational motion using Newton's second law. The equations of motion are then integrated to obtain the position, velocity, and acceleration of each particle.

Each cycle of calculations involves the above-mentioned steps, and the cycle moves the system from time t to $t+\Delta t$. The time step used for the calculations (Δt) is less than the critical time step ($\Delta t_{critical}$), which is calculated from the Rayleigh wave speed of the particles. There are a variety of contact force laws that can be used to solve the force-displacement of the discrete particles. A review of the search grid that keeps track of probable particle-to-particle and particle-to-geometry collisions and the most frequently used contact laws is given in the next chapter.

2.6.2 Contact laws

There are many contact laws/models that can be used to describe the particle-particle and particle-geometry interactions. These models describe contacts between elastic particles of different kinds of shapes, with friction and adhesion considered (Mishra and Rajamani, 1992; Thornton et al. 2013). Majority of the contact models are variations of three main models (Zhou et al. 1999; Bbosa, 2013). These are the linear spring and dashpot model (Cundall and Strack, 1979), the Hertz-Mindlin (Langston et al. 1994 & 1995; Zhou et al. 1999; Zhu and Yu, 2002) and the Walton and Braun model (Braun, 1986; Walton, 1993). The review of the contact force laws in this work will be limited to these three.

2.6.2.1 Linear spring and dashpot model

The linear spring and dashpot model, introduced by Cundall and Strack (1979), is the most used contact law for both normal and tangential interaction (Thornton et al. 2013; Agrawala et al. 1997; Cleary and Morrison, 2011; Mishra and Rajamani, 1992; van Nierop et al. 2001). Figure **5** shows a schematic of the spring and dashpot contact law. The assumption made in this model is that the interactions between the particles is linear and elastic. The spring and the dashpot define the normal force F_n, and is expressed as follows:

$$F_n = C_n v_n - K_n \Delta x_n. \tag{13}$$

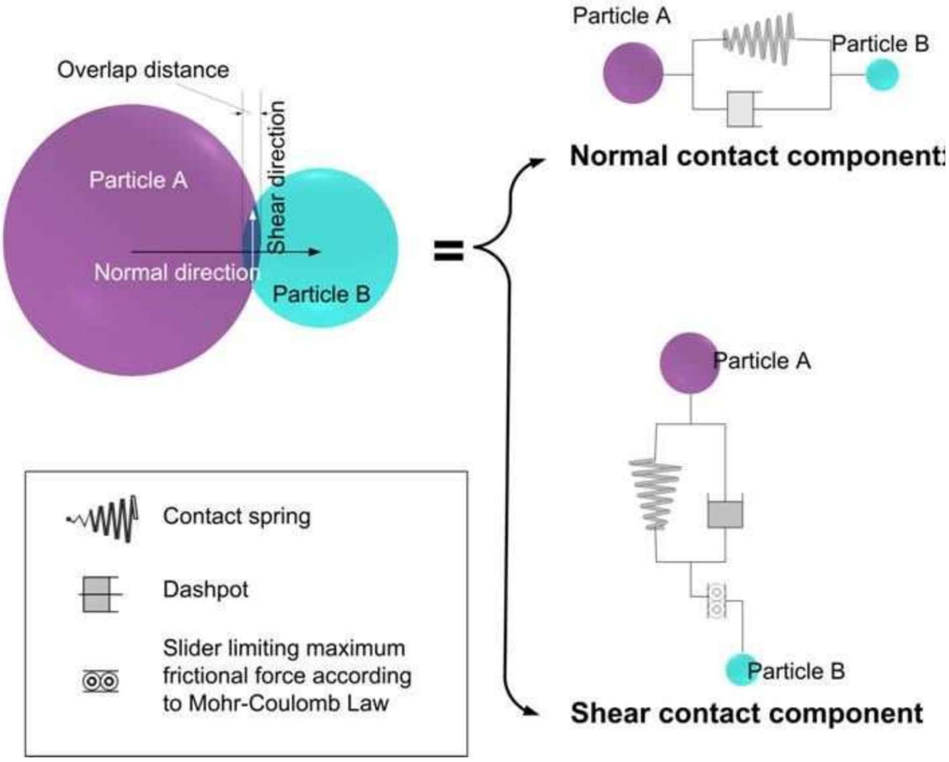

Figure 5: Schematic of the linear spring and dashpot model showing the representation of the contacts (Adapted from Govender et al. 2004)

The linear spring provides the repulsive force while the dashpot provides an inelastic component to the collision and consists of the normal damping coefficient C_n and v_n which is the normal component of the relative velocity at the point of contact. The damping coefficient is selected to give the required coefficient of friction ε. K_n, is the normal spring constant and

Δx_n, is the particle overlap and μ, the coefficient of friction (Campbell, 1990; Govender et al. 2004). The tangential force F_t, is represented as follows (Cleary et al. 2006):

$$F_t = \min\{\mu F_n, \sum K_t v_t \Delta t + C_t v_t\}. \tag{14}$$

Similarly, it has a dashpot for inelastic dissipation and an incremental spring constant based on incremental tangential displacement (Shown by the summation term). Here, K_t, C_t, and v_t, are the tangential components of the spring constant, the damping coefficient, and the velocity respectively. The tangential force is limited by the coulomb frictional limit $\mu F_{n,}$.

The advantage of this model is that it is simple to implement and has been successfully used by many researchers to predict charge behaviour and power draw in comminution devices (Mishra and Rajamani, 1992; Cleary et al. 2006; Delaney et al. 2013; Fernandez et al. 2011; Sinnott et al. 2011; Govender et al. 2013). However, Johnson (1985) presented that the force-displacement between colliding bodies is non-linear. This means the assumption of a linear increase in the contact and damping forces with displacement may be oversimplified. The model also assumes that the viscous damping is minimum when the overlap between the particles is small. This is indicative of the how unphysical the model is, as damping should be at a minimum when the particles come into contact, and when they move apart (Kulya, 2008).

2.6.2.2 Hertz – Midlin model

Unlike the linear spring and dashpot model, the Hertz-Mindlin uses Hertzian theories of elastic contact to define forces between colliding particles. Several researchers have used this model such as Misra and Cheung (1999), Yang et al. (2003) and Khanal and Morrison (2009). Figure **6** shows a schematic of the Hertz-Mindlin particle contact theory.

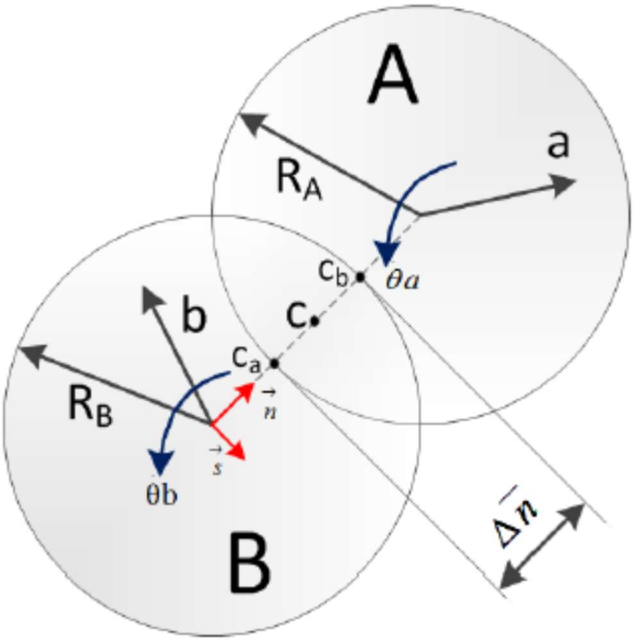

Figure 6: Schematic representation of the approach for Herts-Mindlin contact model (adapted from Bbosa 2013)

The Hertz-Mindlin model basically, assumes that the relationship between displacement and force F_n is non-linear (Hertz, 1882; Johnson, 1985). The collisional forces are characterised by measurable material properties such as Youngs modulus E^* as shown by equation (15)

$$F_n = -{}^{4}\!/_{3}\, E^*\sqrt{R^*}\Delta\bar{n}^{\frac{3}{2}}, \tag{15}$$

Where R^* the effective radius of the two bodies in contact, and the effective Youngs modulus is E^* is, $\bar{n}$ is the normal displacement between the particles,

$$\frac{1}{E^*} = \frac{1-\gamma_A^2}{E_A} + \frac{1-\gamma_B^2}{E_B}, \tag{16}$$

Where γ_A , γ_B , E_A and E_B are the poisson's ratio and Youngs Moduli for particles A and B. The effective radius is

$$\frac{1}{R^*} = \frac{1}{R_A} + \frac{1}{R_B}, \tag{17}$$

The tangential force is given by the product of the displacement and the shear contact stiffness K_s where:

$$K_s = \frac{E^*.\sqrt{2R^*}}{(1+\gamma)(2-\gamma)}.\sqrt{\Delta\bar{n}}, \tag{18}$$

based on the theory by Mindlin and Deresiewiscz (1953).

2.6.2.3 Walton and Braun model

Walton and Braun modified the Hertz-Mindlin approach (Walton and Braun, 1986). It is well suited in cases where the contacts between particles include results in plastic deformation. In this model a partially latched spring is used to determine the relationship between force and displacement. This results in different spring stiffness values for loading and unloading. The normal force is then represented as

$$F_n = \begin{cases} K_1 \alpha \ (loading), \\ k_2(\alpha - \alpha_0) \ (unloading), \end{cases} \tag{19}$$

Where α_0 is the overlap when the spring is completely unloaded; K_1 and K_2 are the stiffness during loading and unloading. A simplified form of the Mindlin-Deresiewicz model is applied for the tangential direction of the force. The tangential stiffness is then given by,

$$k_t = \begin{cases} k_0 . \left(1 - \dfrac{F_t - {F_t}^*}{\mu F_n - {F_t}^*}\right)^{\gamma}, (for\ increasing\ F_t), \\ k_0 . \left(1 - \dfrac{{F_t}^* - F_t}{\mu F_n - {F_t}^*}\right)^{\gamma} \ (for\ decreasing\ F_t), \end{cases} \tag{20}$$

Where F_t is the tangential force, ${F_t}^*$ is the tangential force at an existing path, γ is a fixed parameter, and k_0 is the initial gradient of the force displacement curve. The non-linear models based on Hertzian and Mindlin- Deresiewicz theories are more complex than the linear spring and dashpot model. Theoretically, these models should yield more accurate results than the linear spring and dashpot model. Di Renzo and Di Maio (2004) compared, on a macroscopic scale, the prediction of the linear spring and dashpot model with that of the models based on Hertzian and Mindlin- Deresiewicz theories, for an elastic collision of a sphere with a flat wall. They reported that the linear model gives better results for post collision velocities. This kind of agreement with experimental results can only be achieved if the parameters of the contact model are precise. For this reason, and the fact that it is simpler to implement numerically, the linear spring and dashpot model will be used in DEM simulations of this work. In mineral processing applications DEM is used to model the contacts and motions of the media particles. In cases where it is not computationally expensive to resolve the ore particles DEM is also used to model the ore particles. In this work DEM will be used to model the media particles only.

2.6.3 DEM parameter calibration and validation

The selection of the parameters required to use the contact laws has implications on the predictive capability of the contact law. The calibration of these parameters for milling applications typically involves comparing the velocity and positions of particles in a simplified experiment with DEM predictions of the same system. The simplified tests involve a single particle dropped on a flat bed or fired onto a wall (Mishra and Rajamani, 1992; Kharaz et al. 2001; Chandramohan and Powell, 2005). An example of such a simplified experiment is that used by Chandramohan and Powell (2005) shown in Figure **7**.

In their work two 8.51 mm steel balls are subjected to free fall and their collision (mid-air) is captured by a digital SLR camera. An image analysis software is then used to determine the position and velocities of the particles before and after they collide. This then gives the input required to solve for the parameters required in the DEM (Chandramohan and Powell, 2005). The slope and intercept of the incident and rebound angles of the particles are used to determine normal and tangential restitution and friction. In this work the contact parameters used by Cleary et al. (2015b) for wet modelling in an industrial scale Isamill$^{\text{TM}}$ are used. These have been validated and used extensively for milling applications at pilot and industrial scale (Cleary et al. 2015b).

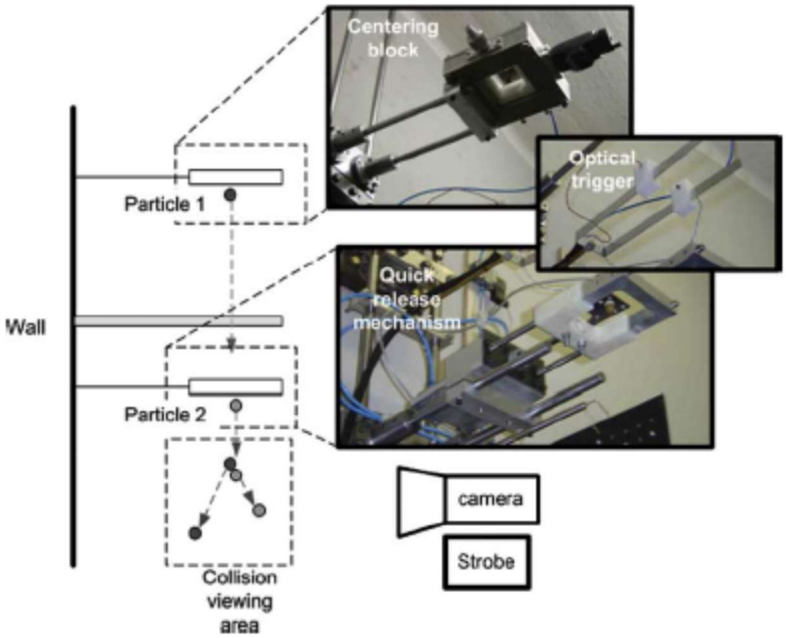

Figure 7: Experimental set up used to measure particle interaction properties (Chandramohan and Powell, 2005)

2.6.4 DEM outputs

The DEM modelling technique tracks all particle-to-particle, and particle-to-geometry collisions. The energy dissipated in these collisions is also available to researchers. This is very useful information as it can give insights on how a device uses the energy it draws. Moreover, provided by the DEM modelling approach, are the particle position history and velocities. This allows the detailed study of charge motion in a device (Mishra and Rajamani, 1994; Malahe, 2011; Bbosa, 2013; de Carnalho and Tavares, 2013; Mayank et al. 2015; Cleary and Owen, 2019). DEM modelling of tumbling mills was first carried out by Mishra and Rajamani, (1992, 1994), where they studied the ball charge motion in a tumbling mill in two dimensions. This was extended to three dimensions for charge motion studies in tumbling mills (Herbst and Nordell, 2001; Cleary 2001; Morrison and Cleary, 2008).

One of the frequently examined outputs of DEM simulations in mills is the collision energy distribution (Yang et al. 2008; Powell et al. 2008; Khan and Morrison, 2019; Weerasekera et al. 2010; Cleary and Owen, 2019; Bbosa 2013). This can be used to characterise the grinding environment as was done by Cleary and Owen (2019). In their work, the collision energy distribution was represented as dissipation rate against energy. The peak dissipation rate, shown in Figure 8 for different lifter heights, was used to show how the grinding environment changes with liner heights. For decreasing lifter height, ball to rock ratio and increasing filling, a decrease in impact breakage and increase in grinding action was reported (Cleary and Owen, 2019). A summary of a select few DEM studies on tumbling mills is shown in Table 4.

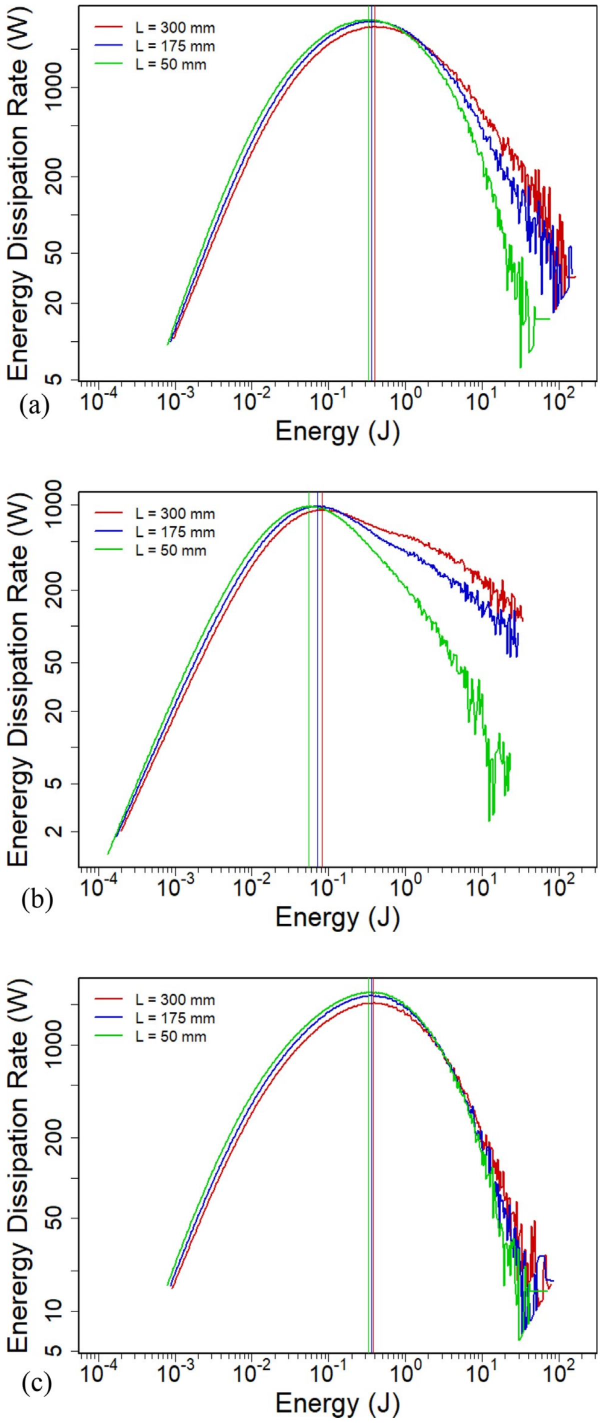

Figure 8: Change in energy spectra at different lifter heights of a) Total energy, b) normal energy and c) shear energy. (Taken from Cleary and Owen, 2019)

Table 4: DEM studies in tumbling mills

Authors	Study
Inoue and Okaya, (1996)	Grinding mechanisms.
Mishra and Rajamani (1994)	Simulation of charge motion in ball mills
Cleary, (1998a)	Power draw, charge motion, segregation.
Djordjevic, (2003 & 2005)	Influence of lifters and charge size distribution on power draw.
McBride and Powell, (2006)	Liner evolution
Kalala et al. (2008)	Effect of liner wear on load behaviour.
Kulya, (2008)	Study of the grinding environment
Weerasekera et al. (2010)	Modelling breakage environment
Powell et al. (2011)	Effect of liner evolution on grinding rates.
Carvalho and Tavares, (2011)	Mechanistic model framework.
Wang et al. (2012)	Modelling particle breakage in tumbling ball mills
Govender et al. (2013)	DEM and PEPT comparison.
Bbosa (2013)	Probability based models for power draw and energy spectra.
Franke et al. (2015)	Accounting for variability in operating conditions when determining liner operating life.
Cleary and Owen, (2019)	Effect of particle shape on charge structure and energy utilisation.
De klerk et al (2019)	Geometric features in tumbling mill flows

The availability of the energy dissipated by particle collisions with the mill geometry makes it possible to determine wear patterns on liners. The wear is proportional to the energy absorbed by the mill surfaces. Jayasundra et al. (2011) used outputs from DEM and CFD to study wear patterns and evolution of the holes in the Isamill discs as shown in Figure 9. They reported that impact energy increases with increasing wear on the holes of the discs.

In this work, all these DEM outputs will be used to understand the operational behaviour of the SMD.

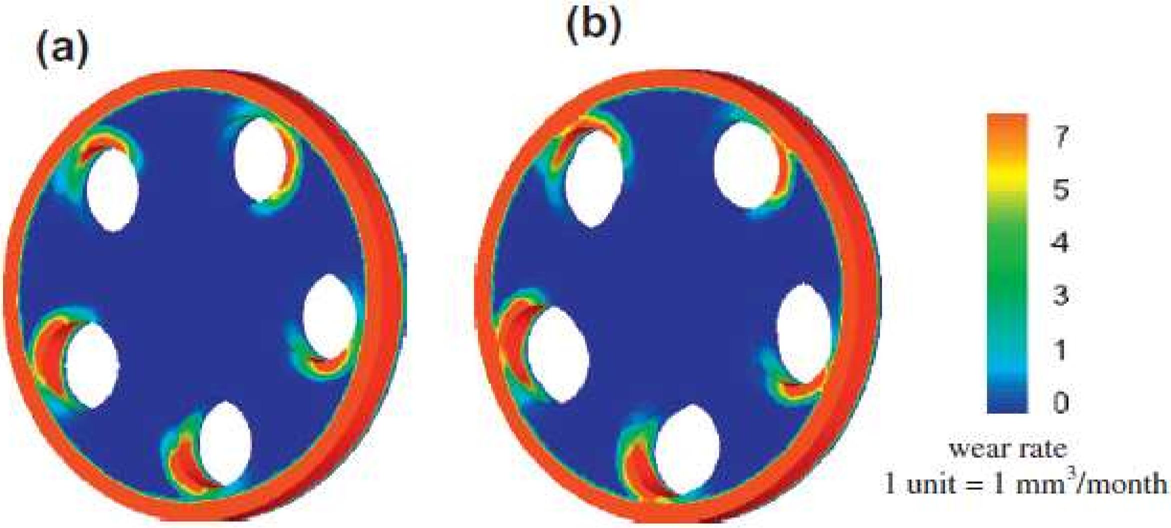

Figure 9: Wear evolution of holes on the isamil discs as predicted by DEM-CFD outputs a) new disc b) worn after 4 months (Jayasundra et al. 2011)

2.6.5 DEM modelling of stirred mills

The study of stirred media mills in the mineral processing context using DEM is recent. A summary of selected work that has been published is given in Table 5. Sinnott et al. (2006) used outputs from DEM to investigate the collision environment, media motion and energy consumption in pilot tower and pin mills. These mills have a similar grinding chamber, but they differ in the mechanism for agitating the charge. The Tower mill has a double helical steel screw agitator which stirs the charge and simultaneously lifts it. The Pin mill is equipped with a central shaft that has rows of pins that are offset to each other. The rotational speed of the pin mill (250 rpm) is typically faster than that of the tower mill (100 rpm). Using the linear spring and dashpot contact model, they modelled in the tower and pin mill 29 000 (particle size -14+9mm) and 61 625 (particle size of 8mm) media particles respectively. For both mills attrition was found to be the dominant breakage mechanism, as the average rate of shear energy absorption was found to be approximately three times higher than the normal energies.

Flow in the tower mill was reported to be strongly swirling around the screw with axial recirculation. Media in the vicinity of the screw was found to move in the direction of the screw, then flows down in a thin outer region close to the mill wall. The mill was found to have a high media participation rate as most of the media contributed to comminution. The pin mill media flow was reported to be circular with minimal vertical variation, with the rotating pins generating high pressure zones around them and on themselves. A sharp decrease in media energy absorption with increasing mill height was reported for the pin mill, including poor media participation rates.

Table 5: DEM studies in stirred mills

Authors	Study
Cleary et al. (2006)	Flow structures, liner wear, mixing and transport
Sinnott et al. (2006)	Flow structures, liner wear, mixing and transport
Yang et al. (2006)	Modelling media flow in an Isamill
Gudin et al. (2007)	Media friction coefficient of friction
Jayasundra et al. (2008)	Effect of grinding media properties
Kim and Choi (2008)	Modelling media motion
Morrison et al. (2009)	Energy efficiency comparison between tower and tumbling mill
Kim et al. (2009)	Analysis of grinding rate constant in a stirred mill
Jayasundra et al. (2010)	Effect of disc speed on media motion
Jayasundra et al. (2011)	Prediction of wear on the discs in an Isamill
McElroy et al (2012)	A soft sensor approach to impact energy prediction
Sanatham and Dreizin (2012)	Predicting conditions for scaled-up manufacturing of materials prepared by ball milling
Santhanam et al. (2013)	Modelling charge motion in a pin mill
Yamamoto et al (2014)	Modelling media motion in a horizontal mill
Keikkala et al (2018)	Energy efficient rotor desing in Higmills

This was then followed by the work of Cleary et al. (2006), who studied flow structures, liner stress, mixing and transport in the tower and pin mill. This study showed that the tower mill has good mixing characteristics due to strong effective axial transport of the media in the mill. Wear in the tower mill was predicted to be caused by the abrasion to the grinding chamber and the surface of the agitator. Energy absorption isosurfaces were used to show that this (energy absorption) is high over a broad volume of the charge. The DEM predicted power draw for the tower mill was found to be favourably comparable with the current best semi-empirical models. The tower mill was found to perform better on all measures whereas the pin mill suffered from extensive localisation of high energy impacts near the pins (Cleary et al. 2006). Morrison et al. (2009) compared the energy efficiency of pilot scale tower and ball mills. They showed through a comparison of the collision environment of both mills that the tower mill is potentially more energy efficient than the ball mill. Ball mills were reported to be more tolerant in variations of feed size distribution and hardness than the tower mill. Figure 10 shows the media distribution in the tower and ball mill modelled in their work.

Sinnott et al. (2011a) looked at the influence of media shape on the grinding performance of a lab scale tower mill. This mill was used as a generic representation of all stirred mills. Super-quadrics were used to describe non-spherical media particles. They reported that using media that is reasonably non spherical would result in poor transport of the media and the interstitial slurry which would result in poor grinding performance. Increased dilation in the grinding was observes as media becomes non-spherical, which reduces grinding rates. Another consequence of using non-spherical media is the loss of much of the grinding volume and increased wear rates on the helical screw.

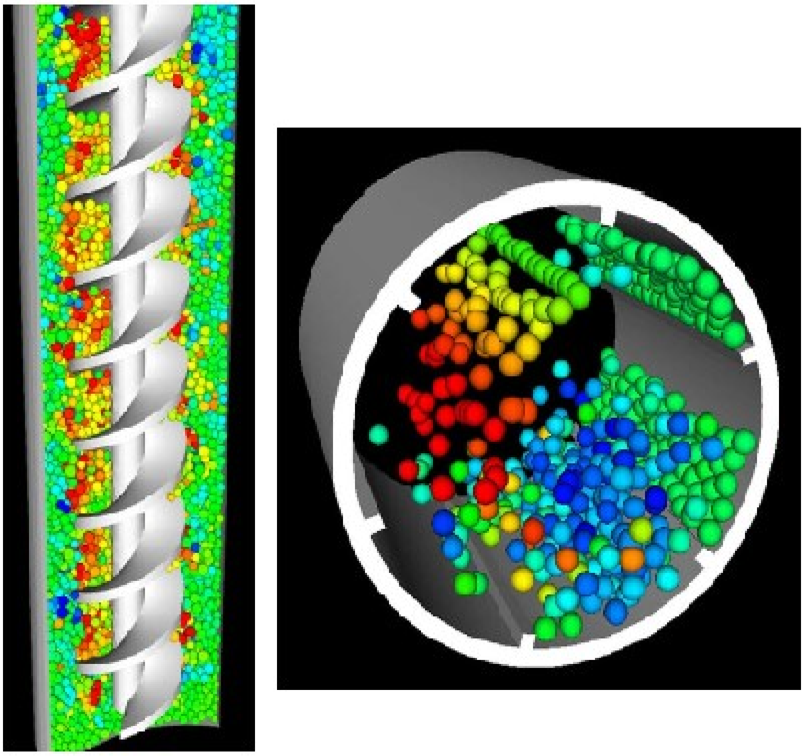

Figure 10: Media flow in a tower mill and a ball mill coloured by speed with red being 2 m/s and 0.2 m/s for the ball and tower mill respectively. Dark blue is 0.15 m/s and 0.2 m/s for the ball and tower mill respectively (Adapted from Morrison et al 2009).

DEM has been used to study the Isamill$^{\text{TM}}$ by Yang et al. (2006), who considered the flow of grinding media. The DEM model was first validated by comparing its predictions with the flow and mixing pattern and power draw of a similar experimental setup. Figure 11 shows the flow pattern from their DEM simulations and adjacent to it the experimental set up of the same system. Once the validation was done, the effects of sliding friction (0.01 – 1), damping coefficient ($5x10^{-6}$ – $2x10^{-5}$ s^{-1}), mill speed (500 – 200 rpm) and media loading (40 – 80%) were investigated. The damping coefficient was reported to have negligible effect on power draw, flow patter, velocity, and force field. Sliding friction on the other hand had a significant effect. Increasing sliding friction decreases velocity to a minimum then increases, while increasing the power draw. Media loading and mill speed was also shown to increase flow velocity and power draw.

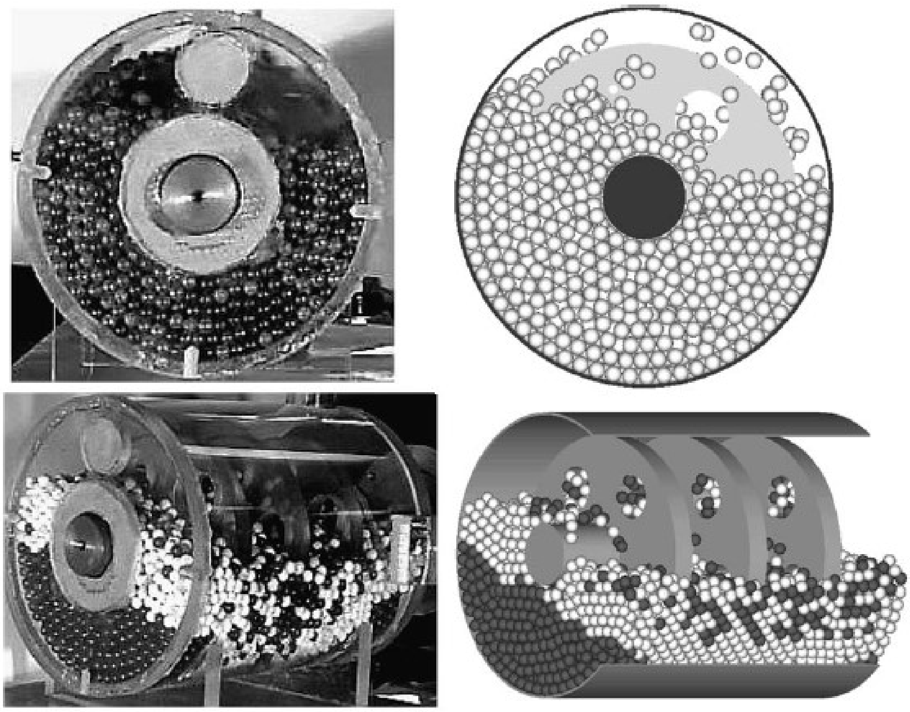

Figure 11: DEM Simulation compared with experimental results of a lab scale mill (Adapted from Yang et al. 2006)

Cleary et al. (2008) studied segregation of coarse feed from within a charge of significantly larger grinding media for the IsaMill^{TM}. Jayasundra et al. (2008, 2009, 2012) studied the effect of grinding media and mill design on the performance of the Isamill^{TM}. They investigated in a lab scale mill, the effect of different stirrer geometries namely a pin stirrer, disc stirrer with no holes, a disc stirrer and a disc stirrer with holes, these are shown in Figure 12. They also investigated the effect of the spacing of the discs/pins on mill performance.

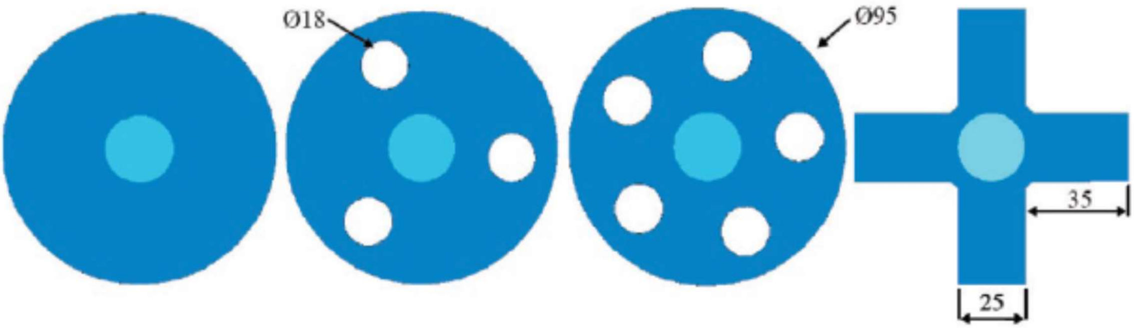

Figure 12: Different stirrer geometries investigated in an Isamill (Adapted from Jayasundra et al. 2012)

Of the geometries studied, the pin stirrer was shown to produce higher media kinetic energy and centrifugal velocity. This is because the normal impact between the media and the stirrer is greater for the pin stirrer than the disc stirrer (Jayasundra et al. 2012**)**. The pin stirrer also produced better mixed flow with higher impact energy intensity and power draw compared to the disc stirrers. In terms of grinding efficiency, they reported that the 5-disc stirrer would produce higher grinding efficiency than the pin stirrer, with the pin stirrer configuration having higher throughput. For the disc stirrers investigated, it was observed that energy transfer is more efficient when there are holes on the disc. Larger holes result in high particle velocities, particle collision frequency and energy.

It is also reported by Jayasundra et al (2012) that the disc spacing in the Isamill influences the circulation of grinding media between the discs. Figure 13 shows the media distribution and velocity vectors at different disc spacing. More media particles stay close to the mill shaft because energy propagation is less efficient with increasing disc space.

Particle collision frequency was observed to decrease whereas collision energy increased with increasing disc space. The largest disc spacing used in the study of Jayasundra et al. (2012) is 30 mm. The DEM simulations were validated with data collected using the positron emission particle tracking technique (PEPT).

Bao et al. (2012) used a 1.4 litre lab scale Isamill^{TM} to predict media impact intensity that can be used to develop a soft sensor approach to predicting impact intensity in the mill. A soft sensor is a partial model of a unit or a process which can be programmed to provide variables which cannot be directly measured (also known as soft sensor variables) online. This can only be done if a correlation exists between measurable input variables and the soft sensor variable.

DEM was used to determine the media impact energy required for the development of the model.

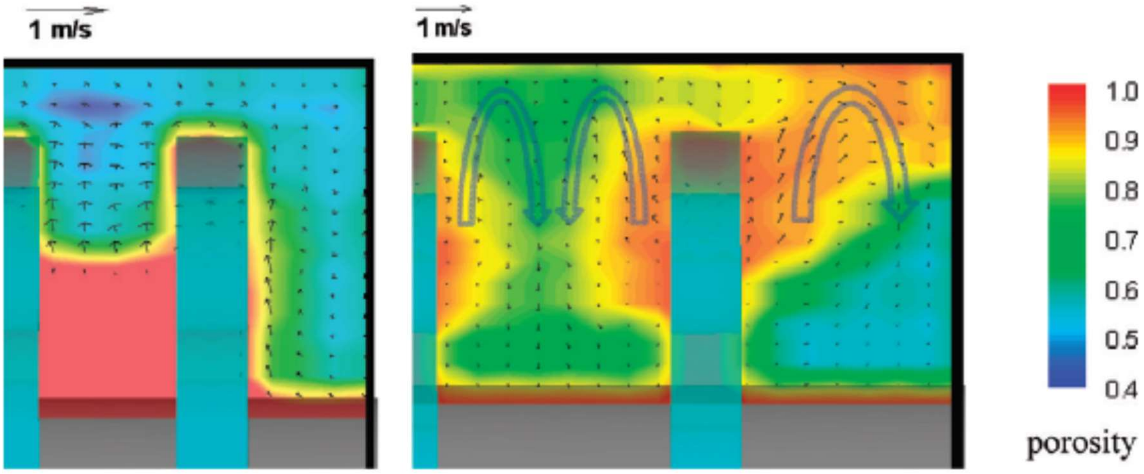

Figure 13: Effect of disc spacing on porosity and flow in the IsaMill (Jayasundra et al. 2012)

More recently, Cleary et al. (2015a) studied the media flow structure and energy usage in an industrial scale M10000 Isamill^{TM}. They reported that one of the key factors controlling the dynamics of the media in this mill is the force balance on the media adjacent to the discs. Gravity is shown to provide a restoring force that pushes the media downwards and to the sides adjacent to the rotating discs. This pressure keeps the bed of media in contact with (pressed to) the discs ensuring energy transfer from the discs to the adjacent media. Figure 14 shows steady state distribution of media in the industrial scale M10000 Isamill^{TM} when gravity is not included in the DEM model. The media centrifuged to the mill shell, and has low velocities on average of about 1.2 m/s.

This shows that the centrifugal acceleration generated by the high rotation of the agitator is not the only factor controlling the performance of the mill, but gravity also plays a very critical role. Cleary et al. (2015a) also reported normal and shear power absorption on the agitator, which are a good indicator of impact and abrasion wear respectively on the geometry, shown in Figure 15. The impact was described to be more than an order of magnitude lower than the abrasion wear, with the impact wear mainly concentrated on the surface of the holes of the discs. This further shows that the dominant comminution mechanism is abrasion.

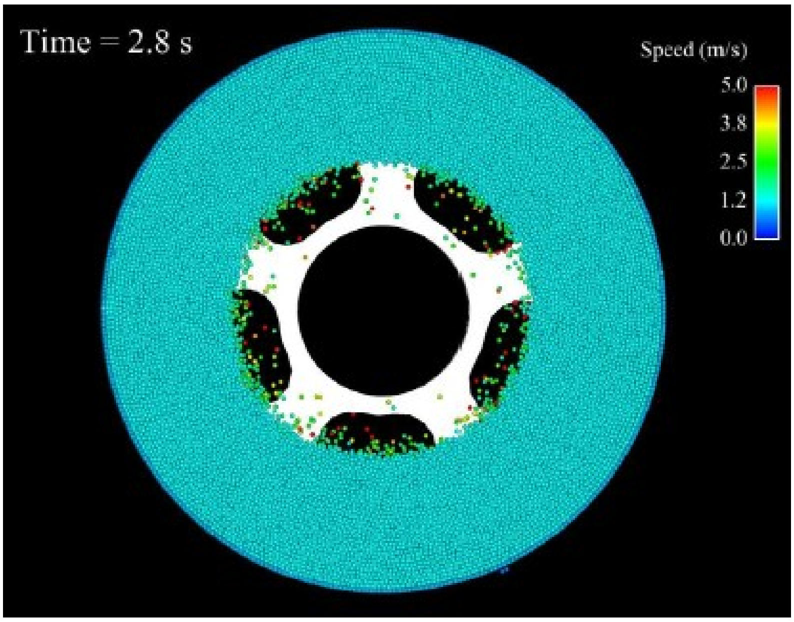

Figure 14: Steady state media distribution in the M10000 Isamill when gravity is not included in the model. The media is coloured by speed (Cleary et al. 2015b)

This body of work on stirred mills shows the details DEM can provide for the study of the behaviour of these devices. The charge motion in the mill can be better characterised when the individual particles are tracked. The ability to determine the energy dissipated in particle-to-particle and particle-to-geometry collisions aids in determining energy utilisation, the dominant breakage mechanism, and the prediction of liner wear. Most stirred mills are operated wet, excluding the fluid will not give an accurate description of the grinding environment. The slurry/fluid part of the charge must be accounted for, and this was not done in the studies presented so far.

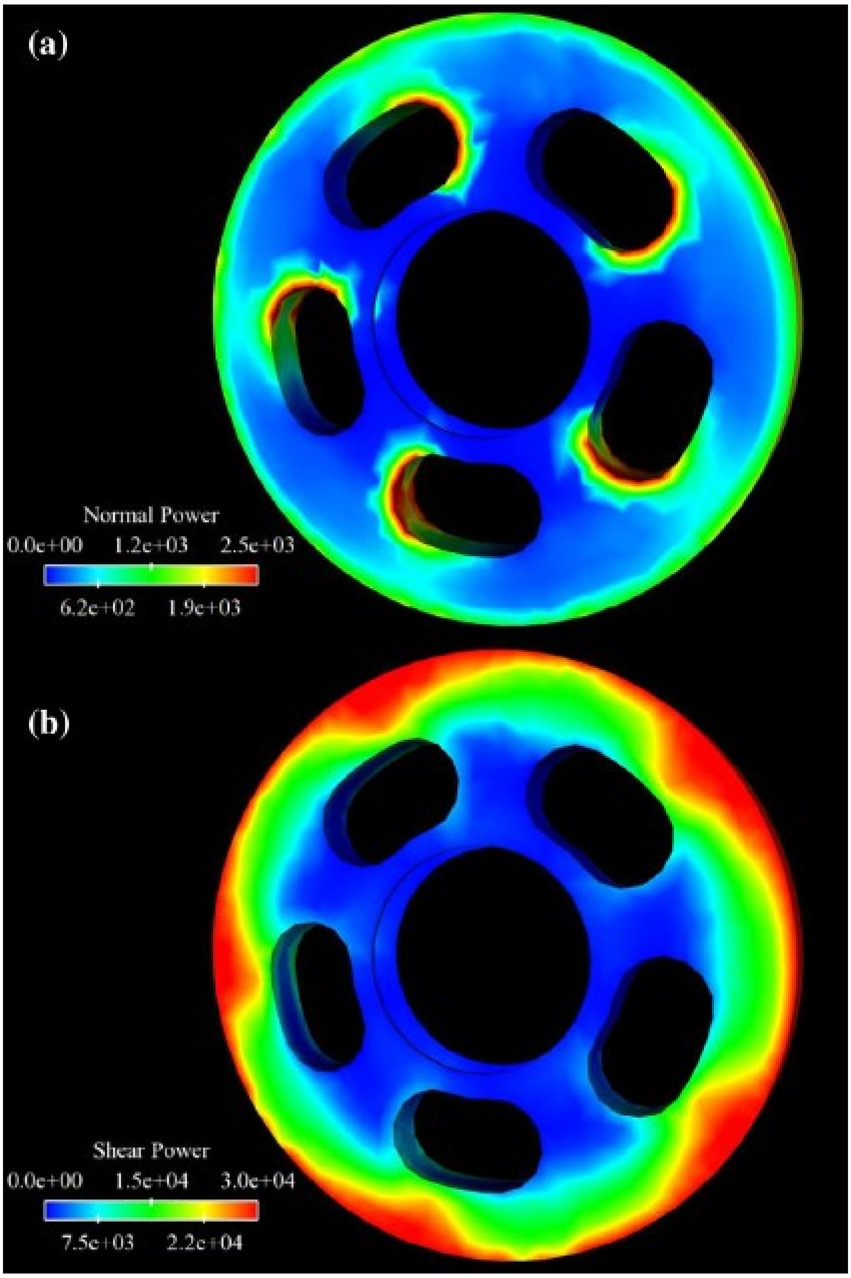

Figure 15: Impact and abrasion wear on the face of a disc of the Isamill at 80% media loading of 15 mm media and a tip speed of 22 m/s (Cleary et al. 2015a).

2.6.6 Fluid modelling

Since Stirred media mills in the mineral processing context are operated wet, modelling only the particle interactions will not give a true picture of the collision environment. To model such systems and account for the effect of the fluid phase, the motion of the solid particles must be coupled with an appropriate solution method for the fluid (Cleary et al. 2015b).

Several numerical methods have been developed to describe the behaviour of a fluid. The most widely used methods solve the Navier-Stokes equations; apart from that, some solve the Boltzmann equations (Hosain and Fdhila, 2015). The focus of the review will be on the methods that solve the Navier-Stokes equations.

The Navier-Stokes and the continuity equations are governing laws for multiphase flow of incompressible fluids.

$$\frac{\partial \varepsilon_f \rho_f u_f}{\partial t} + \nabla \varepsilon_f \rho_f u_f = -\nabla p + \nabla \tau_f + \varepsilon_f \rho_f u_f + F_{fp}, \tag{21}$$

$$\frac{\partial \varepsilon_f \rho_f}{\partial t} + \nabla \varepsilon_f \rho_f u_f = 0, \tag{22}$$

Where ε_f, ρ_f, u_f and τ_f are the volume fraction, density, velocity and viscous stress of the fluid respectively. The fluid pressure is denoted by p, for a Newtonian fluid $\nabla \tau_f = \mu \nabla u_f$. These equations are used in computational fluid dynamics to simulate fluid flow. Typically, the approach to the simulation is either the Eulerian or Lagrangian. The Eulerian approach uses a stationery mesh which does not deform to describe the fluid properties between the mesh cells. In the Lagrangian approach, the fluid is represented as particles which are tracked as time goes on. These particles carry the fluid properties such as velocity and temperature. There are some methods that are based on both the Eulerian (mesh) and Lagrangian (meshless) frames of reference. A summary of the numerical methods is shown in Figure 16.

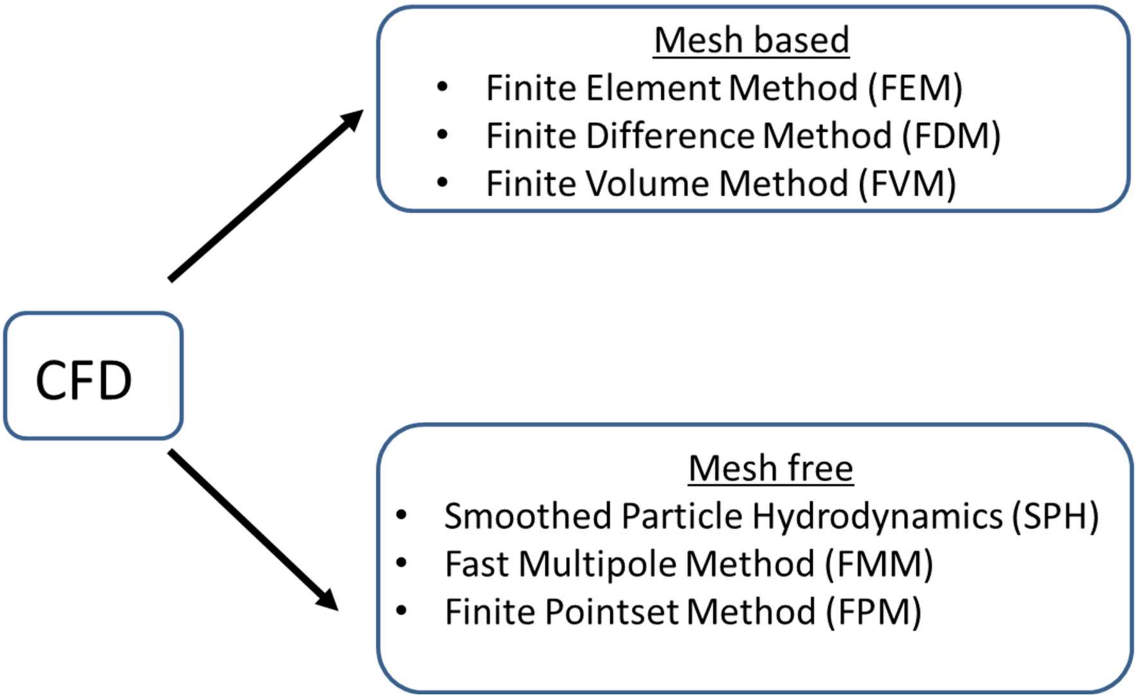

Figure 16: Various numerical methods for computational fluid dynamics (adapted from Hosain and Fdhila (2015).

2.6.6.1 Mesh based Methods

To solve the governing equations for fluid flow, the geometry or domain of interest is discretised into a grid (forming the computational domain). This process is known as meshing and it produces a set of non-overlapping cells that cover the computational domain. The partial differential equations (PDEs) are discretised or transformed into a set of equivalent algebraic equations, which are defined over each cell or element (Moukalled et al. 2016). An iterative solver is then used to compute the solution field. There are several methods available for discretisation. In this section a brief review of the most common ones is presented.

Finite difference method: In this method the PDEs are approximated at the point of intersection of the grid lines. The PDEs are expressed as a series expansion, usually a Taylor series. The accuracy of the solution increases with increasing number of terms in the Taylor series. This method has numerical complexities for domains/geometries with irregular shapes (Moukalled et al. 2016).

Finite element method: In this approach, the non-overlapping cells that make up the computational domain are called elements. The PDEs are expressed in an integral form (weak form). Using a method such as Galerkins method of weighted residuals, the integrals are evaluated over an element. The disadvantage of FEM is the difficulty in putting physical meaning to the algebraic equations developed from the weak form of the PDEs (Moukalled et al. 2016).

Finite Volume method: In this method the grid cells are called volume elements. The PDEs are represented in conservative form and the integral conservation law is then applied for each control volume. This means that fluxes are balanced across the boundaries of each volume element. For irregular meshes, difficulties in ensuring that fluxes have been calculated correctly may arise. The advantage of this method is the inherent conservative discretisation.

Eulerian mesh-based methods such as FVM are commonly used for predicting the behaviour of the fluids in a wide range of industrial problems. However, these methods are incapable of capturing the movement of the free surface of the fluid. Free surface flows are generally common in several industrial processes. Stirred media mills in operation have complex free surfaces. To overcome the inability to capture the free surface, the Marker and Cell method was developed (Souto-Iglesias et al. 2008). This method uses particle markers to indicate fluid containing cells and the movement of the free surface is tracked by interpolation (Hosain and Fdhila, 2015). The limitation of this method is that the markers do not track the free surface in regions of converging/diverging flow (Nickols and Hirt, 1975). Other methods have been introduced such as the Volume of Fluid method (VOF). In this method a function is used to describe the fraction of a cell occupied by a fluid. VOF is widely used in many software packages utilised academically to solve free surface flows (Garg et al. 2018). The advantage of this method is that mass is conserved. The disadvantage is that it does not accurately capture the free surface (Garg et al. 2018).

Alternatively, fully Lagrangian and meshless methods can be used in systems that have complicated geometry performing non-trivial motion, and where there are complex free surfaces to predict. A meshless lagrangian based method has advantages over Eulerian based methods because the fully lagrangian methods have been proven to inherently capture the interfaces in multiphase flow (Aubram et al. 2010). Stirred media mills in operation have complex free surfaces therefore a brief review of the meshless methods is given in the next section.

2.6.6.2 Mesh free methods

In the Lagrangian approach of modelling fluid dynamics, the fluid is treated as particles. The particles hold the properties of the fluid such as density and velocity. The motion of the fluid (Which is discretised into particles) can then be modelled using the Lagrangian equations of motion (Abouzied, 2016). In this approach, the derivative of the velocity incorporates the convective terms of the governing equations (Abouzied, 2016). This makes it possible to model free surfaces, discontinuous fluids, multi-phase flows and flows around complex geometries (Cleary, 2015; Abouzied, 2016).

Smoothed Particle hydrodynamics (SPH): SPH is a particle method that does not need a grid to calculate spatial derivatives (Monaghan 1992). They are instead converted into systems of ordinary differential equations, which can be solved using an appropriate integration method. SPH was originally developed for compressible astrophysics problems in the 1970s. It has since undergone great development and has become one of the standard methods used to model astrophysical fluid flow. SPH, being a particle method, uses discrete particles to model a fluid (this is done by solving Navier-Stokes equations). These particles carry at their centre the fluid properties. A kernel is used to produce a smooth pressure or density field from the discrete values held by each SPH particle (Cleary 2015). SPH has been used to simulate slurry and particle flows in comminution devices such as screens and tumbling mills (Cleary 2015).

Fast Multipole Method: This is a particle method developed by Greengard and Rokhlin (1987) to evaluate pairwise interactions between N electrical charges, given a pairwise interaction Kernel. It was later adapted by Cheng et al. (1999) to evaluate potential fields in three dimensions. Greengard and Kropinski (1998) used the Fast Multipole Method to solve the incompressible Navier-Stokes equation in two dimensions. In FMM, the equations are expressed as nonlinear fourth-order partial differential equations based on a stream function. The integral equations are then solved using O(M) or O(MlogM) operations, where M is the number of points in the discretisation of the domain (Greengard and Kropinski, 1998).

Finite Pointset Method: This is another particle method used to simulate complex flows, free surfaces, and heat transfer (Hosain and Fdhila, 2015). In this method a list of neighbour particles around a point/particle is determined for each time step. An appropriate interpolation function is then constructed to smooth the discrete values of the function. This is done by fitting a polynomial function to the discrete values using a moving least squares method (Traneçon et al. 2006). This method has been used to simulate incompressible Navier-Stokes equations for composite material by Traneçon et al. 2006.

A major drawback of the particle-based methods is that they become computationally expensive. This problem can be addressed by paralleled computing using graphical processing units (GPU). In this work SPH is the method used to model the fluid in the SMD for the many advantages this particle-based mesh free method has over the mesh-based methods. The coupling can be done in two ways, those are:

- One-way coupling – the particles (DEM) influence the fluid only.
- Two-way coupling – The particles (DEM) and fluid influence each other

In this work two-way coupling is used.

2.6.7 SPH

In this section a summary of the SPH method used here is provided. The value of a function A can be interpolated at any position r using the expression:

$$A(r) = \sum_b m_b \frac{A_b}{\rho_b} W(r - r_b, h), \tag{23}$$

Where b, the summation index is the particle label. The mass, density and position of the particle b are denoted as m_b, ρ_b, and r_a respectively. The summation is done over all the SPH particles with A_b denoting the value of quantity$A$ at r. In principle, a differentiable interpolant of any function at the SPH particle can be constructed. This is done by use of a differentiable smoothing kernel, $W(r - r_b, h)$ of radius 2 h. The Kernel approximates a Gaussian function. Ordinary differentiation can then be used to determine the derivative of A:

$$\nabla A(r) = \sum_b m_b \frac{A_b}{\rho_b} W(r - r_b, h), \tag{24}$$

Essentially partial differential equations can be converted, using this interpolation technique, into ordinary differential equations for the motion of the SPH particles. The same goes for the rates of change of the properties of the SPH particles. The SPH form of the continuity equation taken from Monaghan (1992, 1994) is:

$$\frac{d\rho_a}{dt} = \sum_b m_b (v_a - v_b). \nabla W(r_{ab}, h), \tag{25}$$

Where ρ_a denotes the density of an SPH particle that has a velocity v_a. Here the position vector from particle b to particle a is represented by $r_{ab} = r_a - r_b$. $W(r_{ab}, h)$ is the interpolation kernel evaluated for the distance $|r_{ab}|$ with a length of h. Since the positions and velocities are expressed as differences; this makes the continuity equation Galilean invariant. Such a form is unaffected by density discontinuities or free surfaces and has good numerical conservation properties (Cleary et al. 2007). The continuity equation in this form is useful for predicting free surface flows. As two SPH particles approach each other, they have a negative relative velocity from equation (25). The gradient of the smoothing kernel is also negative. The result is an increase in $\frac{d\rho_a}{dt}$, which produces a positive pressure which pushes the particles apart. If the said particles move apart, the rate of change of density decreases, creating a negative pressure that pulls the particles towards each other. This ensures that the particles are relatively equally spaced. The SPH form of the momentum equation then becomes the acceleration of a particle a.

$$\frac{dv_a}{dt} = -\varepsilon_a \sum_b m_b \left[\left(\frac{P_b}{\rho_b} + \frac{P_a}{\rho_a} \right) - \frac{\xi}{\rho_a \rho_b} \frac{\mu_a \mu_b}{(\mu_a + \mu_b)} \frac{v_{ab} r_{ab}}{r_{ab}^2 + \eta^2} \right] \nabla_a W_{ab} - \frac{\mu_a \varepsilon_a^2}{\rho_a K_a} + g, \qquad (26)$$

An equation of state that gives the relationship between the fluid pressure and the particle density is:

$$P = P_0 \left[\left(\frac{\rho}{\rho_0} \right)^{\gamma} - 1 \right], \qquad (27)$$

Where ρ_0 and P_0 are the reference density and pressure. γ is a factor whose value is equal to 7 for water and molten liquids. This is used because this SPH method is quasi-compressible. The pressure P is then used in equation (26). A pressure scale factor P_0 is:

$$\frac{\gamma P_0}{\rho_0} = 100V^2 = C_s^2, \qquad (28)$$

where V and C_s are the maximum fluid velocity and the speed of sound. From equation (27), the speed of sound is ten times the maximum fluid speed. This ensures that the density variations are less than 1%, rendering the flow close to incompressible (Monaghan, 1994; Cleary et al. 2007).

2.6.8 DEM-SPH coupling

The coupling force on the media by the fluid is determined using the Darcy drag law, which is represented as:

$$F_{darcy} = \varepsilon_{DEM}^2 \mu_a \frac{v_a - v_{DEM}}{\rho_a K_{DEM}}, \tag{29}$$

Where μ_a and ε_{DEM} are the viscosity of SPH particle a and the void fraction (porosity). The v_{DEM} term is the average media velocity at the SPH particle. v_a, and ρ_a are the fluid pore velocity and the bulk density of the fluid. These are the SPH state variables which are solved for. This is an appropriate empirical relation for fluid flow in porous media. The force from the Darcy drag law (F_{darcy}) is subtracted from the standard SPH momentum equation (26) to yield equation (30).

$$\frac{dv_a}{dt} = -\varepsilon_a \sum_b m_b \left[\left(\frac{P_b}{\rho_b} + \frac{P_a}{\rho_a} \right) - \frac{\xi}{\rho_a \rho_b} \frac{\mu_a \mu_b}{(\mu_a + \mu_b)} \frac{v_{ab} r_{ab}}{r_{ab}^2 + \eta^2} \right] \nabla_a W_{ab} - \frac{\mu_a \varepsilon_a^2}{\rho_a K_a} + g, \tag{30}$$

The Kozeny-Carmen equation is used to determine the permeability K, of the porous media at any point of the charge:

$$K = \frac{\varepsilon_{DEM}^3}{CT(1-\varepsilon)^2} S^2, \tag{31}$$

Where C and T are the shape factor and the tortuosity of the fluid and S, is the surface area to volume ratio. The drag force of the fluid on the solid particles is calculated for each individual solid particle. This force is dependent on the solid and fluid relative velocity and the presence of surrounding particles (Liang et al. 1996). An empirical correlation is suitable for determining the force $\boldsymbol{F_0}$, exerted by the fluid on the DEM solid particles (Xu and Yu, 1997; Kafui et al. 2002; Hilton et al. 2010; Cleary et al. 2017).

$$\boldsymbol{F_0} = \frac{1}{2} C_d A \rho_f U^2 \widetilde{\boldsymbol{V}}, \tag{32}$$

Where ρ_f and C_d are the fluid density and the fluid drag coefficient respectively. U denotes the speed of the fluid flow relative to the particle, A is the particle cross-sectional area perpendicular to the fluid flow. $\widetilde{\boldsymbol{V}}$ is the unit vector in the direction of the fluid velocity relative to the media particle. In cases that have multiple particle systems, the particle crowding effect must be accounted for. To do this a correction factor taken from Di Felice (1994) is used to determine the drag force on each DEM particle:

$$F_d = F_0 \epsilon^{-\chi}, \tag{33}$$

where:

$$\chi = 3.7 - 0.65 \exp\left(-\frac{1}{2}\left(1.5 - \log Re_p\right)^2\right). \tag{34}$$

When the coupling is two-way, conservation of momentum must be ensured. The drag laws used for coupling are dependent on different entities, the magnitudes of the forces are certain to be different. To ensure momentum is conserved, the two calculated coupling forces are stored independently. The ratio of the total coupling forces is determined and the coupling force on the fluid is scaled globally by this ratio to ensure that it matches the force on the particles (Cleary, 2015).

2.6.9 DEM-Mesh based CFD modelling of stirred media mills

DEM coupled with mesh based CFD has been carried out for tumbling mills by several researchers (Alkac, 2005; Malahe, 2011; Rajamani et al. 2011; Mayank et al. 2015). The method used for simulating the fluid by all these authors is the Finite Volume Method. Here the focus will be on the application in stirred media mills. The works that couple DEM with the mesh based CFD methods in stirred mill are presented in Table 6.

Table 6: Coupled DEM-CFD for stirred media mills

Authors	Study
Gudin et al. (2006)	Motion of grinding media in the presence of slurry
Jayasundra et al. (2009)	Effect of slurry on particle motion in an Isamill
Jayasundra et al. (2011)	Particle flow in an Isamill, comparison with PEPT experiments
Jayasundra et al. (2012)	Effect of media size on grinding performance in an Isamill
Beinert et al. (2015)	Analysis of media contacts
Beinert et al. (2018)	Multiscale simulation of fine grinding and dispersing processes

Jayasundra et al (2011) used one way coupled DEM-CFD to model fluid and particle flows in an Isamill, with the FVM used for fluid modelling. The objective was to compare the predicted to experimental results (PEPT). Glass beads and ceramic grinding media were used with water as the fluid in the simulations. The highest number of particles simulated was 224 800 for both media types. A comparison of the DEM-CFD simulations and PEPT measurements of velocity profiles in the radial plane showed reasonable agreement, demonstrating the consistency of the DEM and CFD techniques (Jayasundara et al. 2011). These simulations of the Isamill did not include one part of the internal geometry of the mill, which is the expeller. These results therefore, do not fully represent the actual system. Beinert et al (2015) used one way coupled DEM with CFD to model and compare grinding media contacts in wet operated stirred media mills and planetary ball mills. The number of particles modelled was 112 000 with a size ranging from 0.8mm to 1.2mm. An extended contact analysis was developed which enabled the description of contact types induced by rotational and translational velocities (Beinert et al. 2015). This extended analysis makes it possible to characterize the energy spectrum for different mill types and operating conditions (Beinert et al. 2015). This shows that DEM-CFD modelling can be used to generate micro dynamic information on flow in stirred media mills (Jayasundara et al. 2011).

2.6.10 DEM-SPH modelling of stirred media mills

DEM coupled with SPH has been used for several industrial problems. Presented here are the applications of DEM and SPH coupling in the mineral processing context, particularly stirred mills.

Sinnott et al. (2011) used it to predict slurry flow in a tower mill. An SPH resolution of 5.9 mm, with a slurry volume consisting of about 74 000 SPH particles was used. The slurry viscosities investigated are 0.01 Pa s and 0.1 Pa s. In their work they demonstrated the strong influence viscosity has on slurry transport rate in a tower mill. Figure 17 shows the predicted behaviour of the slurry in the tower mill at a viscosity of 0.1 Pa s. Their work did not focus on the effect of the slurry on media-to-media contacts, which is important for efficient comminution.

Cleary et al. (2015b) used the same DEM-SPH framework to study slurry flow in an industrial scale Isamil M10000 with an installed power of 3 MW. In this work the effect of the classifier in the mill was investigated, including the effect slurry viscosity (0.1 Pas, 1 Pa s and 10 Pa s) has on the flow. The number of SPH particles required for this work was about 30 000. Figure

18 shows the simulation from time 0 to 1 s coloured by fluid speed. Viscosity was shown to have no effect on the basic flow in the mill, the strength of the flow though, decreased with increasing viscosity. The classifier was shown to have a significant effect on the flow in the Isamill and was found to control slurry transport and discharge. In this work the effect of the slurry on the media-to-media and media-to-geometry collisions was not reported. The media-to-geometry collision energies can be used to predict liner wear in a comminution device.

Recently Cleary (2015) proposed a two-way coupling of the fluid and solid phase using DEM for the solids and SPH for the fluid phase. Transient one-way coupling is sufficient in cases where the solids have a greater effect on the fluid. When this is not the case, the one-way coupling may not predict the behaviour of the charge and slurry correctly. For two-way transient coupling, the coupling forces are exchanged between the phases at every time step. The continuum representations of the phases are also updated unceasingly (Cleary 2015).

Cleary (2015) also acknowledged the importance of carrying out experimental measurements to quantify the extent of phase coupling.

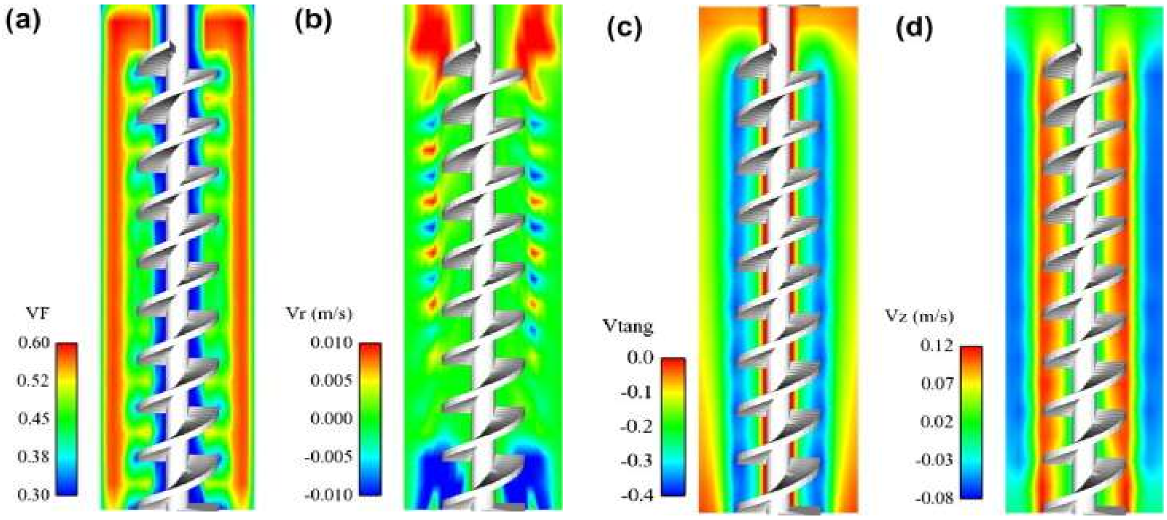

Figure 17: One way coupled steady state flow in a tower mill showing a) Solids fraction b) radial c) tangential and d0axial velocities of slurry for $\mu = 0.1$ (adapted from (Sinnott et al. 2011)

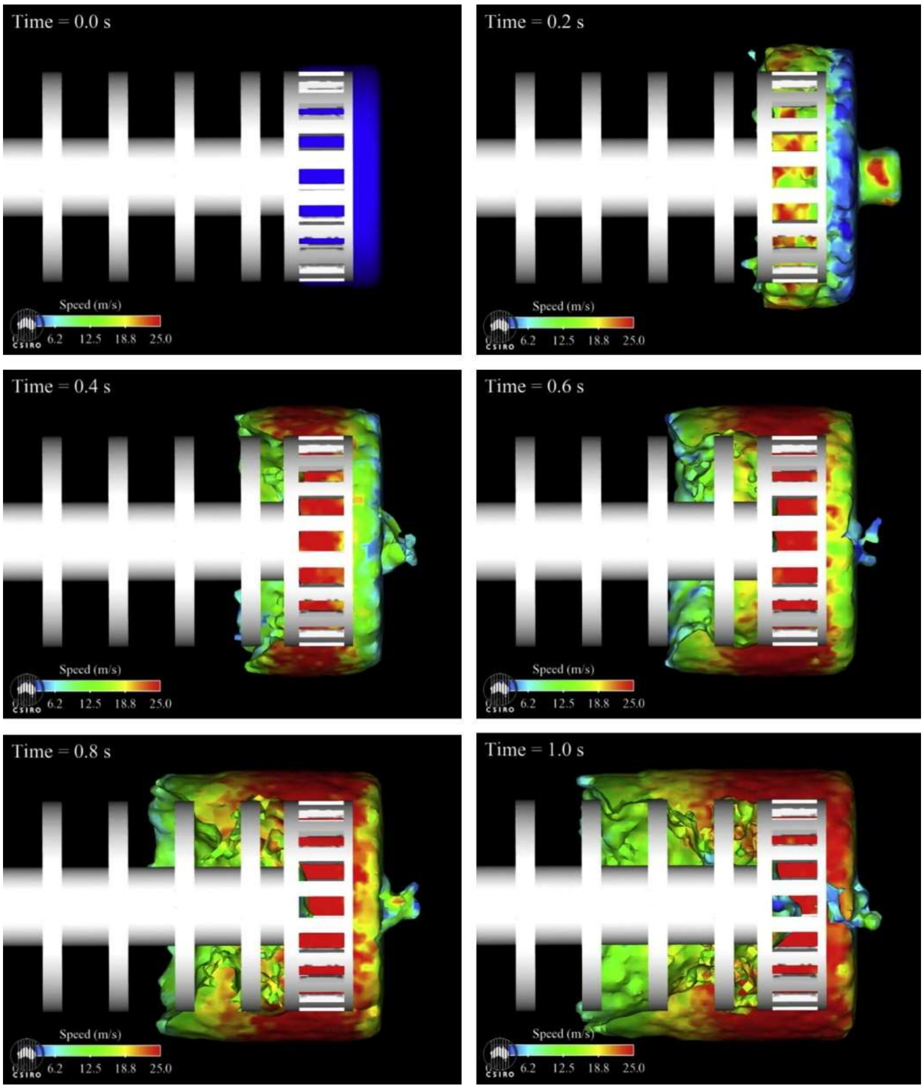

Figure 18: DEM+SPH model of Isamill 1000 classifier coloured by fluid speed at different times of the simulation (adapted from Cleary et al. 2015b)

2.7 Summary of Literature Review

From the broad spectrum of work considered in this review, the following observations are made. These observations define the basis of this thesis.

Stirred mills have become the technology of choice for fine and ultra-fine grinding in the minerals industry. This is due to their demonstrable efficiency compared to tumbling mills when deployed in this duty. Grinding is an energy intensive process even if stirred mills are used. It is, therefore, important to have a detailed understanding of the operational behaviour of stirred media mills to optimise operations. The operational behaviour of these devices is highly complex; and modelling it mechanistically is not a trivial task since the physics behind the operational behaviour is not entirely understood. This is because the comminution has a highly abrasive environment and an opaque shell. The abrasive environment makes placing any measuring instrument in the mill impossible. In addition, the opaque shell makes it impossible to observe particle interactions and flow patterns in the mill.

Owing to the difficulty of getting direct measurements from within the grinding environments in stirred mills, most of the bodies of work have focused on using the measurable inputs and outputs of the process to develop power models. These are commonly used in a population balance framework with breakage tests of ore used to develop calibrated empirical models of the process. These empirical models, which are essentially fitted averages over collections of similar data sets, have been used to assist with design and optimization of stirred mills. The power models are essentially fitted averages over collections of similar data sets. Unfortunately, they do not consider the nature of the collision environment and how it changes with operating conditions. Additionally, they capture very little of the comminution physics of the process. These shortcomings limit their predictive capability and accuracy when used especially outside the range of conditions for which they were developed.

The inability to obtain both particle interaction and flow information in a stirred mill, limits the rate of improvement of comminution devices, and the development of models to control their operation too. Tracking the motion of the particles and determining the effect of their collisions with each other and with the mill geometry will enhance the understanding of the operational behaviour of these devices and improve predictive capabilities of models. The review of literature shows that the Discrete Element Method (DEM) has the capability to track individual particles and the effect of their collisions in a computational framework. There are numerous works published on DEM application for tumbling mills and more recently stirred mills. For stirred milling systems that are operated wet, the fluid phase of the charge must be accounted for, as it will influence mill outputs. The magnitude of this influence is a function of the extent of the solid media packing.

The available numerical methods for describing the behaviour of the fluid part of the charge are, the Eulerian based mesh methods such as the Finite Volume method and, the Lagrangian meshless particle-based techniques such as smoothed particle hydrodynamics (SPH). These can be coupled with DEM to model the grinding environment in comminution devices. In cases where the effect of the fluid phase is significant, two-way coupling can be implemented. The reviewed literature shows that a lot of progress has been made in computational modelling to the extent where it can be used to describe flow in complex systems including stirred grinding mills. A large body of work shows the implementation of these numerical modelling techniques to tumbling mills and more recently to stirred mills at industrial scale. The literature review shows that numerical modelling can be used to quantify the energy dissipated by the grinding media in a comminution device. Numerical modelling makes it possible to characterize the energy spectrum for different mill types and operating conditions (Beinert et al. 2015). This shows that DEM-CFD modelling can be used to generate micro dynamic information on flow in stirred media mills (Jayasundara et al. 2011).

The reviewed research for this thesis has found that the interaction of the particles (grinding media) and the fluid (slurry phase) are not well understood in the SMD. The current experimental techniques used to study these devices do not give detailed information on:

1. Particle-to-particle, particle-to-geometry, and particle-to-fluid interactions, including the energy they dissipate.
2. Physical structure of the charge in stirred mills.

These two factors affect the process outputs such as the power the SMD draws and the product quality. Consequently, the available models for these devices do not incorporate the physics of the comminution process. Models which do not consider these factors will have limited predictive capabilities. In this work Transient two-way coupled DEM-SPH simulation is used to understand the particle-to-particle and particle-to-fluid interactions in a SMD at two different industrial scales. The model based on coupled DEM-SPH will be used to assess the charge behaviour and the influence of impeller configuration on power draw, transport and mixing, energy utilization and liner wear in the SMD.

Smoothed Particle Hydrodynamics is the method of choice for describing the fluid part of the charge because it is inherently capable of modelling free surface flows and flows around complex geometry. Coupling DEM with the fluid will give a better representation of the grinding environment in the SMD as they are usually operated wet. DEM coupled with an appropriate solution method for the fluid can provide detailed information on particle position history and velocities. This allows for detailed study of charge motion and dynamics. Since all interactions are tracked, their energy dissipation is also available to study. This information gives insight on how the device uses the energy that it draws.

3 Methodology

A description of the approach taken to address the objectives of this work mentioned in the introduction are detailed in this chapter. The computational work done in this thesis involved simulating the batch operation of an SMD at two scales. DEM was used to model the media particles and SPH was used to model the slurry.

The work in this thesis is focused on developing a computational model for the Stirred Media Detritor. It involves developing computational models using DEM only and then extending these to two-way coupled DEM-SPH simulations. A workflow of the process of is shown in Figure 19.

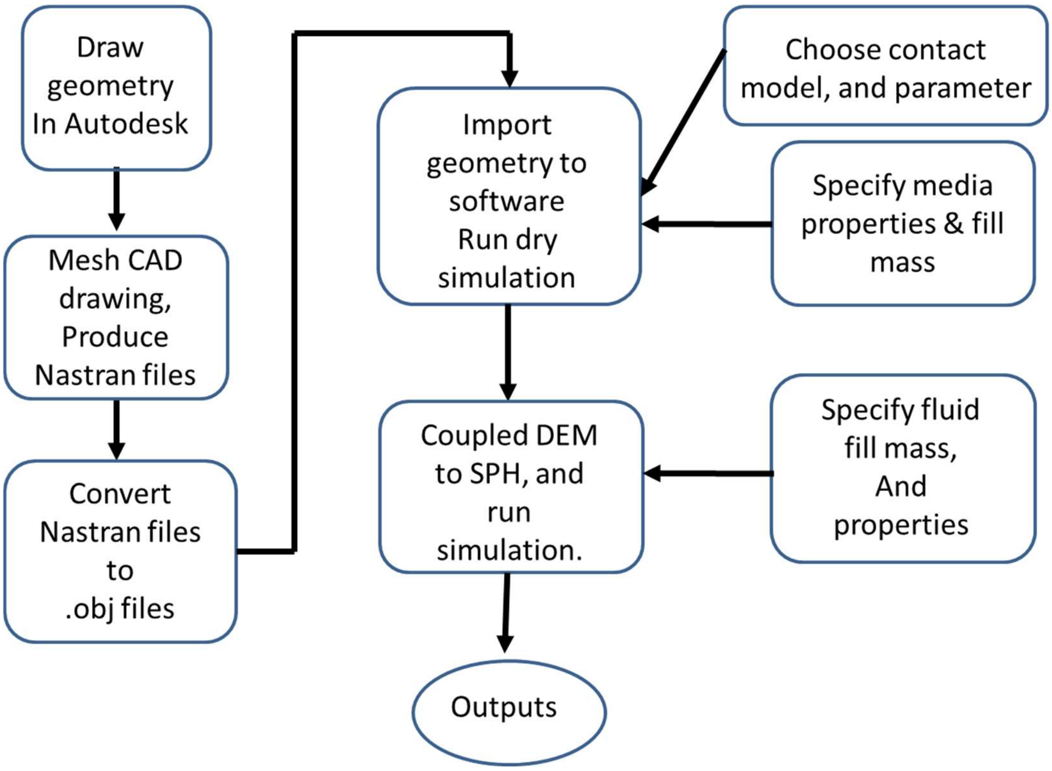

Figure 19: General flow chart of the simulation process

The CAD drawings of the SMD models studied in this work are created using Autodesk inventor. This is a computer aided design application in which 3D models of the mill can be rendered. Details of the mills' geometries are given in the mill geometry section. Figure 20 shows a cutaway view of an SMD CAD model with the shaft in place. These 3D CAD drawings are converted to IGES format that can be read by the meshing software. The IGES format from Autodesk is imported into a finite element pre-processing software called Hypermesh.

Hypermesh (https://altairhyperworks.com/About-Hyperworks#) can generate both 2 and 3 dimensional meshes quickly

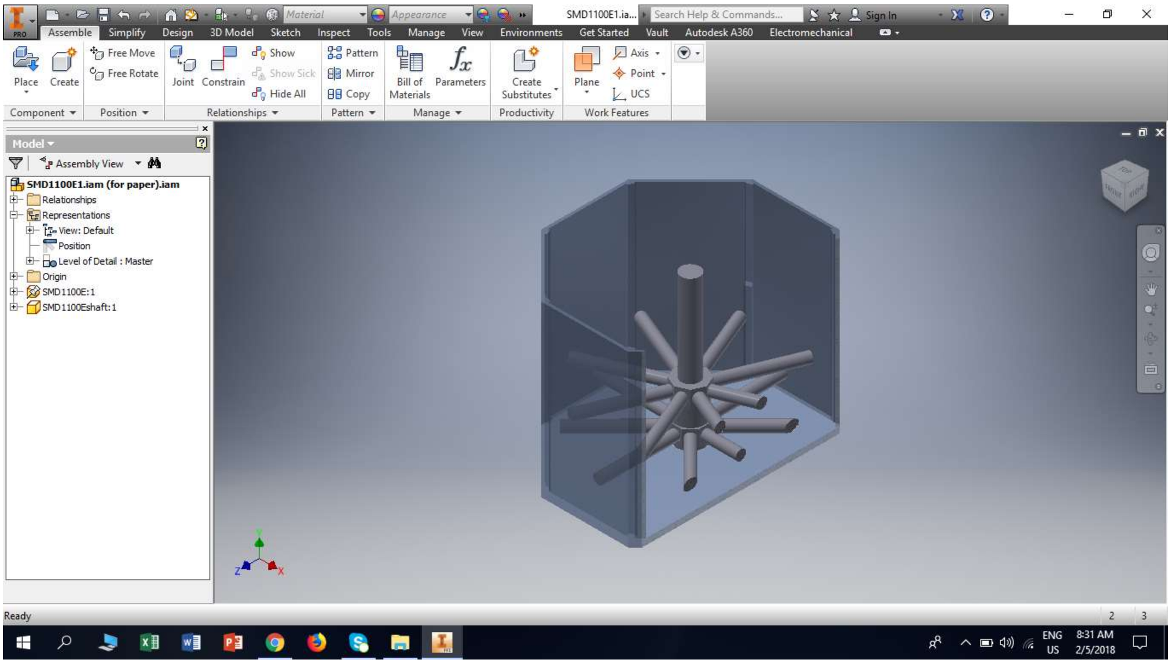

Figure 20: A screen shot of Autodesk inventor

For the grinding chambers only a surface mesh was generated. For the shaft and impeller arms, a surface and volume mesh are generated. A 50mm mesh is used in this work for surface and volume meshes. The Meshed geometries are converted to Nastran format and exported to a software called workspace. Workspace is a proprietary software of the Commonwealth Scientific and Industrial Research Organisation (CSIRO) https://research.csiro.au/workspace/ . A Nastran reader in workspace is used to specify the speed and axis of rotation of the shaft. The software converts the Nastran file to an OBJ format which can then be exported to the solvers for the DEM and SPH simulations. The solvers used here are proprietary to the CSIRO which contain the fully two-way coupled and transient DEM and SPH method used by Cleary (2015). The code used for the DEM component of the solution has been used and validated for various milling applications, (Cleary, 2004; 2009a; Cleary and Hoyer, 2000; Govender et al. 2013).

3.1 DEM solver

The DEM part of the code uses the linear spring and dashpot contact law, with a spring stiffness K_n , of 100,000 kN/m. The mathematical formulation of this model is detailed in the literature review section. The spring stiffness controls the amount of overlap between particles. Cleary et al. (2015b and 2016) has shown that a spring stiffness that produces average particle overlaps in the range 0.1- 0.5% generally result in accurate outcomes that are independent of the spring stiffness. For the SPH solution, the speed of sound used is dependent on the peripheral speed of the impeller arms of the SMD. The media contact and physical parameters and filling must be specified. The same contact parameters used by Cleary et al. (2015b) for modelling an industrial scale Isamill$^{\text{TM}}$ were used in this study. The media-media coefficient of friction and restitution used are 0.4 and 0.6 respectively. The media-mill coefficient of friction and restitution used are 0.3 and 0.5 respectively. These contact parameters have been shown to be adequate for studying flow in both industrial and pilot scale stirred mills. A Summary of the physical contact parameters used here are given in Table 7. Media physical properties and charge filling must be specified in the DEM solvers. Details of the quantities of these parameters is outlined in the charge specification section.

Table 7: DEM contact parameters (Cleary et al. 2015b)

Friction coefficient (Media-Media)	0.4
Friction coefficient (Media-Mill)	0.3
Coefficient of restitution (Media-Media)	0.6
Coefficient of friction (Media-Mill)	0.5

Once the charge specifications and filling are made, the simulation of the media in the SMD is started. The simulation is performed until the media charge is steady. The kinetic energy of the media and the power draw is used to determine steady state.

3.2 DEM-SPH coupling

SPH is used to model the slurry which is composed of water and ore particles. The mathematical formulation is presented in the literature review section. We do not attempt to resolve the fine ore particles in the slurry as this would greatly increase the computational time. For the SPH solver, the physical properties and filling of the slurry are specified; details of which are given in the charge specification section. The steady media charge is the starting configuration for the coupled simulations. This is to ensure that the coupled simulation is started at a state as near to steady as possible. The SPH particles are added automatically to the simulation, in the regions covered by the media charge. This is done on the basis that the slurry is largely driven by the media motion, with minimal perturbing effect on the overall structure of the charge. A schematic of the coupling scheme is shown in Figure 21.

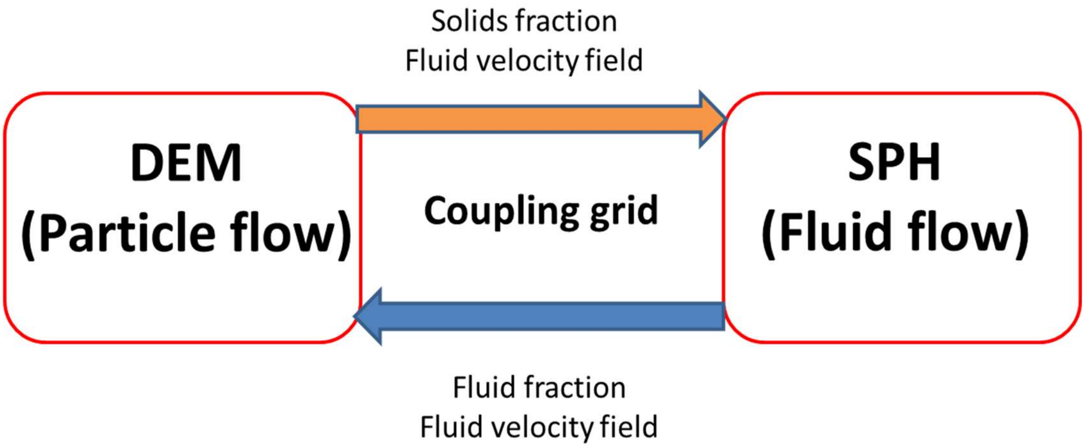

Figure 21: An illustration of the coupling scheme (Ndimande et al. 2019)

The SPH component of the code has been used in mill modelling to predict slurry flow, (Cleary et al. 2006; Sinnott et al. 2011; Fernandez et al. 2011; Cleary and Morrison, 2011, 2012; Cleary et al. 2015b; Cleary, 2015; Sinnott et al. 2015; Sinnott and Cleary, 2017). Cleary (2015) demonstrated robust and stable performance of this two-way coupling of these methods for predicting multiphase flow in a chute, in a central slice of a 36’ SAG mill and in a 1.8 m diameter Hardinge pilot mill.

3.3 Mill Configurations

In this section descriptions of the three SMD models used in this study are given. The models are of different scales, the SMD 18.5-E is a pilot scale mill while the SMD 355-E and the SMD 1100-E are both industrial scale mills. Geometric details of the mill shell and the impeller are outlined for each mill.

The SMD 18.5-E is a pilot scale model and the other two are industrial scale models. Figure 22 shows annotated CAD drawings of the three mills considered while Table 8 shows a summary of the geometric details of the SMD mills considered in this work. The three scales differ in aspect ratio of the grinding shell, which is the ratio of the diameter of the mill to its height. The mill shell becomes squatter as the physical size of the mill increases. The aspect ratios are 0.72 for the 18.5-E, 1.05 for the 355-E and 1.26 for the 1100-E. The height of the grinding chamber at each scale varies, however no studies have provided a charge dynamics reason for these differences.

Table 8: Geometric details of the SMD scales

	SMD-185-E	SMD-355-E	SMD-1100-E
Mill Height (mm)	1010	2127	2687
Mill Diameter (mm)	728	2228	3575
Mill Volume (m^3)	0.46	9.65	28.45
Shaft Diameter (mm)	138	220	324
Impeller Diameter (mm)	85	100	180
Impeller Speed (rpm)	200	129	83.75
Impeller Set Distance (center-center) (mm)	125	400	600
No. arms per set	2	6	8
Installed Power (kW)	18.5	355	1100

The 18.5-E mill has three sets of two arms on the shaft placed one above the other, whilst the 355-E shaft has two sets of six arms each (that is six arms per set) with one set positioned above the other. As shown in Figure 22, the shaft of the 1100-E has two sets of eight arms each (that is eight arms per set). The arrangement of the impeller arm sets in all the geometries is such that when viewed from the top/bottom, all the impeller arms are visible. This means that none of the arms occupy the same azimuthal position as any arm in any of the other sets.

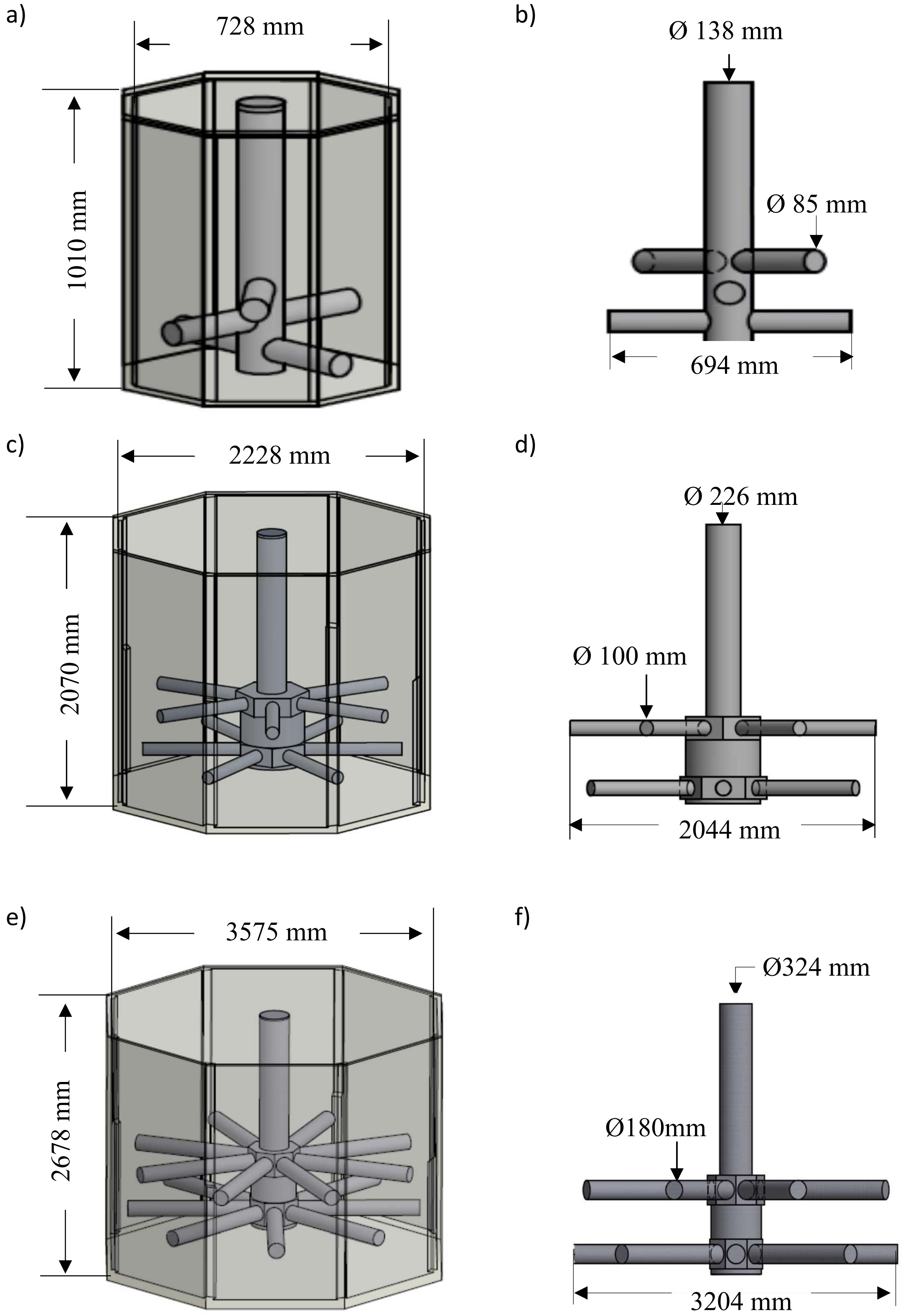

Figure 22: CAD models of the three SMD geometries. From top left, a) SMD 18.5-E with shaft in place, b) closer view of SMD 18.5-E shaft. c) SMD 355-E with shaft in place, d) closer view of SMD 1100-E shaft, e) SMD 1100-E with shaft in place, f) closer view of the SMD 1100-E shaft.

Besides the aspect ratio of the shell, the SMDs at the three scales differ also in:

1. Number of sets of arms on the impeller,
2. Number of arms in each set,
3. Spacing of the sets of arms,
4. Impeller arm diameter and length all vary between the impeller designs at the different scales.

The impeller of the SMD18.5-E has three sets of arms while the other two scales have two sets. The SMD18.5-E has only two arms in each of the three sets whilst the SMD355-E and the SMD1100-E have six and eight arms per set respectively. The vertical spacing (centre to centre distance) for the SMD18.5-E is 125 mm, 400 mm for the SMD355-E and 600mm for the SMD1100-E.

The vertical location of the impeller in the SMD affects the dynamics of the charge at the bottom of the mill (Ndimande et al. 2019). This position is defined by the distance from the bottom of the mill to the bottom of the impeller. The value used by the manufacturer for each scale is not published and is therefore, unknown. It is also unclear whether the general practice used in the selection produces geometric scale-up. Consequently, a method to set the vertical location of the impellor so that the charge structure can be maximally similar for each of the scales is chosen. The vertical location of the impeller in the SMD18.5-E (which is known) is used as the basis for setting the vertical location of the impellers at the larger scales. This was done by defining Ψ, as the ratio of the mill diameter to the distance from the bottom of the impeller arm (bottom set) to the bottom of the grinding chamber as shown in Figure 23.

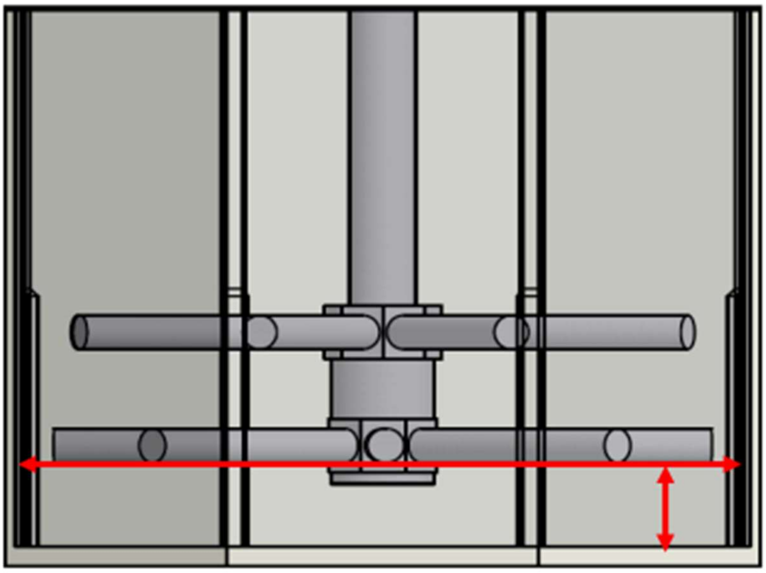

Figure 23: Aspect ratio of sub-region of the charge below the bottom impellers of the SMD1100-E.

This ratio, Ψ, defines the aspect ratio of an elongated more inactive horizontal sub-region that is located at the bottom of the mill which lies below the bottom arms of the impeller. This aspect ratio is kept constant as the mill size increases to ensure similarity of flow in this sub-region. The ratio Ψ, from the SMD18.5-E is 7.28 with a clearance from the bottom of the impeller to the mill floor of 23 mm. This is used to set the impeller clearance for the SMD 355-E and the SMD 1100-E. The clearance from the impeller bottom to the mill flow used is 67.4 mm for the SMD 355-E and 115.3 mm for the SMD 1100-E. The objective is to simulate steady state conditions, therefore, discharge from, and feed into the mill will be omitted, as will water addition and slurry discharge for all simulations. This is reasonable because the amount of flow through and discharge from the mills which occurs during the simulation duration is negligible.

3.4 Charge specifications

The SMD at any scale is designed to use media sizes that range from 1 to 8 mm (Allen, 2011). In practise the media size is selected based on the feed top size. In this study for all scales, the media size used has a mean diameter of 8 mm with a small variation of ±10 %, since real media is intrinsically slightly variable in size. This size is preferred because it is computationally amenable. The media specific gravity considered in this work is 2.7. Here breakage is decoupled and the fine ore particles in the slurry are not resolved. Instead, they are modelled as a homogeneous slurry phase, together with water. This is done on the basis that interaction with the water phase controls the major dynamics of the ore particles.

In this study, a slurry solid loading (w/w) of 40% is used. This is within the recommended slurry solids loading for the SMD reported by Ntsele and Allen (2012). The ore whose properties are used here is Merensky ore with an SG of 3.2. A solids loading of 40% (w/w) gives a slurry solids loading by volume which is less than 20%, its rheology can be assumed to be Newtonian (Mueller et al 2010). As such, the slurry which is composed of water and the ore is modelled using SPH with a Newtonian rheology. The viscosity of the slurry is then a function of the slurry solids loading, which for all cases in this work is 2.2 mPa s. In all wet simulations, each mill is charged with equal volumes of the media and slurry, this is standard practise for the SMD at lab scale (Moore at al. 2016).

3.5 Speed selection for industrial scales

The rotational speed of the SMD 355-E and the SMD 1100-E are not available in the public domain, while that of the SMD 18.5-E is known to be 200 rpm. Therefore, the speed of the SMD 18.5-E is used as the base case for determining that of the larger scales. Similarity in the motion and structure of the charge (media only), is chosen as the basis for establishing similarity of operation for the larger scales. Specifically, the flow pattern of the different mill geometries is compared and used to determine the speed of the larger scales that gives equivalent flow behaviour. This method has been used by Cleary and Owen, (2016), for their scale up study of the HICOM mill. This method is preferred because the physical structure and motion of the charge drive the operational outputs of the comminution device such as power draw and product size distribution (Cleary and Owen, 2016). The mills are charged with the same volumetric fill of media for this method. Assuming a solids fraction of 0.6 for spheres at rest, the media loading used is 23% of the available grinding volume. This translates to a media mass of 180 kg, 4100 kg, and 12000 kg for the SMD 18.5-E, the SMD 355-E and the SMD 1100-E respectively. For the speed selection, the slurry is omitted because it is not expected to significantly affect the charge structure. The speeds tested are summarised in Table 9. A speed of 115 rpm for the SMD 355-E, 78 rpm for the SMD1100-E were found to give a similar flow pattern to that of the SMD 18.5-E. These are therefore, implemented in this study.

Table 9: Mill speed test matrix

Speed number	SMD 355E	SMD 110E
1	100 rpm	75 rpm
2	110 rpm	78 rpm
3	115 rpm	83.75 rpm
4	120 rpm	-
5	129 rpm	-
6	135 rpm	-

3.6 Charge dynamics and energy utilisation study

Once the speed of the mill is selected, a study of the motion of grinding media and slurry in the industrial scale SMDs is then carried out. This is achieved by use of a two-way coupled DEM-SPH numerical model. The objective is to understand charge dynamics and energy utilization in the SMD, which cannot be studied using most of the experimental methods available. The importance of including the slurry phase in simulations is quantified by comparing the modal peaks for the energy spectra of DEM only and DEM+SPH simulations of the industrial scale SMD mills. A summary of the charge specifics for each mill are presented in Table 10. The SMD 1100E is used to study charge dynamics and energy utilization while the SMD 355E is used to study the effect of impeller configuration on the grinding environment.

Table 10: Grinding volume and charge specifications

Mill	Grinding Volume (m^3)	Volume of slurry (m^3)	Volume of the Media (m^3)	Media mass (kg)
SMD1100-E	27.57	4.44	4.44	12000
SMD355-E	8.51	1.28	1.28	3447

3.7 Impeller configuration study

The two-way coupled DEM-SPH numerical model is also used to investigate how the number of arms and their physical arrangement on the impeller, affect the collision environment and mill performance. Varying the design of the impeller is expected to affect the charge motion and consequently, the collision environment and thereby, the resulting comminution. The effect the impeller configuration has on mixing and transport are also explored, as these have major impact on the efficiency of comminution. This will provide the information that is needed to assist in the selection of impeller arm configuration for such mills. The industrial scale SMD355-E model with a 355 KW motor is used as the base case for this study. This is because it is computationally amenable compared to the larger SMD1100-E, while providing representative flow behaviour of a full-size mill. The critical geometric attributes of impeller arm arrangement investigated are:

1. Number of arms in each set in the shaft,
2. Vertical spacing of the impeller arm sets on the shaft,
3. Number of sets of impeller arms.

These were considered in selecting the impeller variants studied here. Six impeller variants are considered in this study to understand how different realistic impeller arm configurations affect key aspects of the comminution process. Figure 24 shows annotated CAD drawings of each the impeller variants considered, as well as their position within the mill. Specifically, these variants are:

- **Variant 1**. This impeller has two sets of arms, with the upper set having four arms and the lower set having 6 arms. The vertical separation along the shaft, of the two sets of impeller arms is 400 mm as shown in Figure 24.
- **Variant 2**. This variant has two sets of four arms on the impeller. The vertical separation of the arm layers is 400 mm.
- **Variant 3.** This impeller has two sets of arms. The upper set has six arms while the lower set has four arms. The sets have a vertical separation of 400 mm along the shaft.

The media charge mass used in this study is slightly less than the mass used to determine impeller speed.

Variant 1

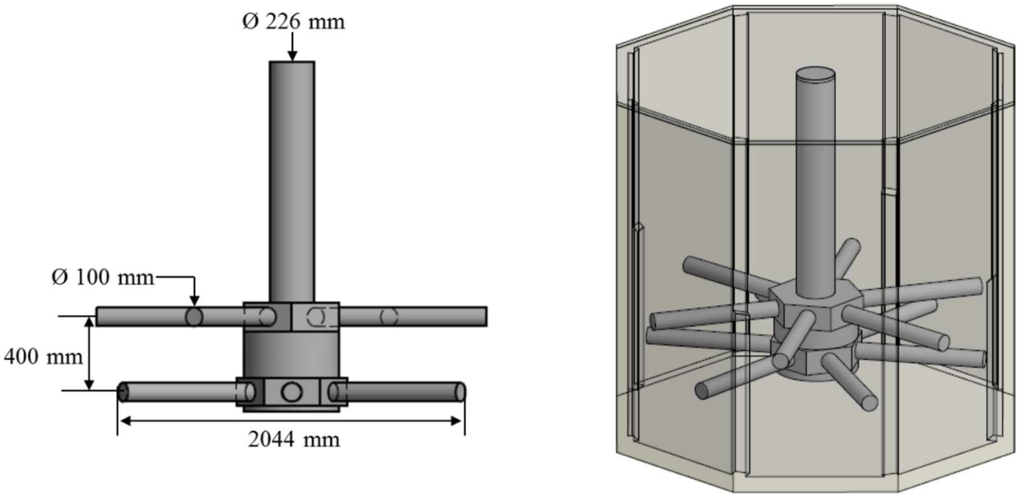

Variant 2

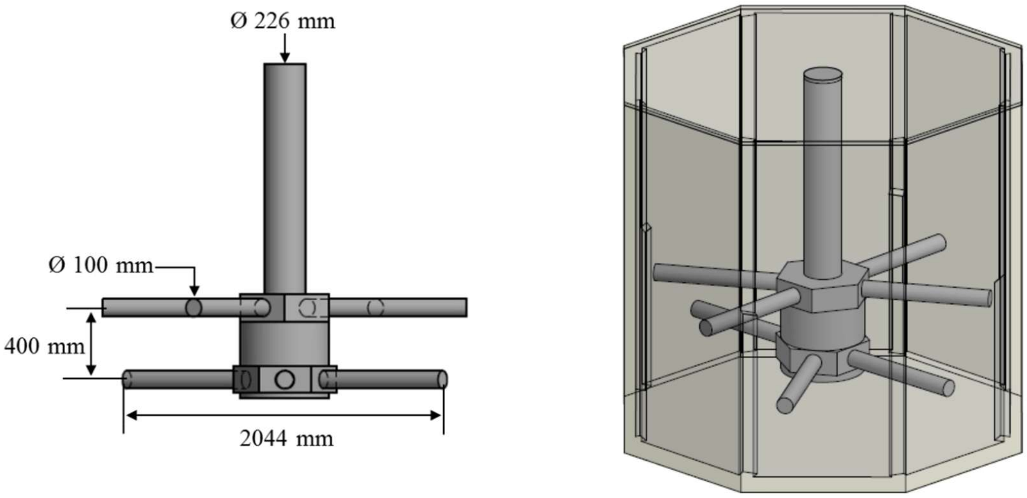

Variant 3

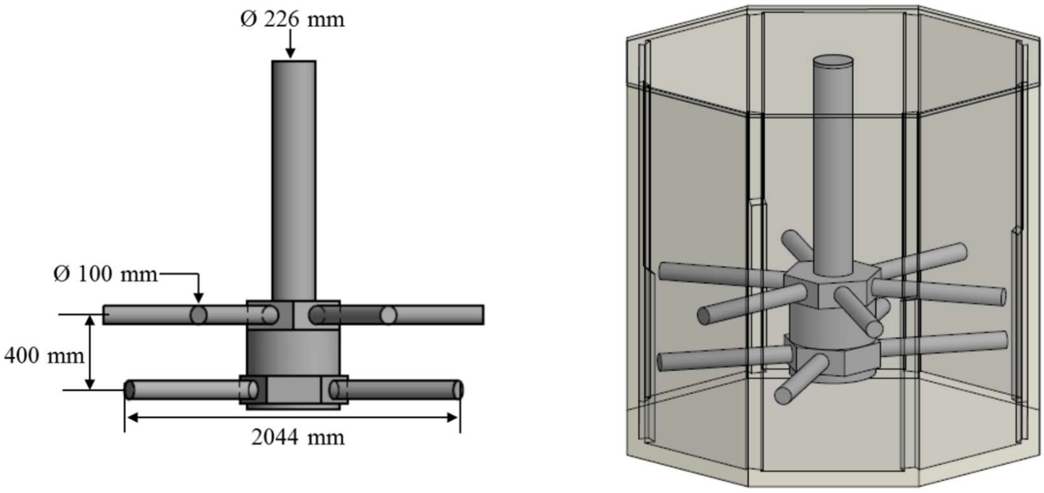

Figure 24: View of the geometric details of each impeller variant are shown on the left, (right) the variants shown in place in the mill

One of the common methods for describing solids distribution in a stirred vessel is the cloud/charge height. This is the distinct height to which most of the solids are lifted in the vessel along with the fluid by the motion of the impeller. The distance from the bottom of the vessel to this level is called the "charge height" (Paul et al. 2004). Knowledge of the charge height is often important for selecting the vessel outlet. In this work charge height is used as one of the measures for comparing the charge structure produced by different impeller configurations. The velocities of the media and the slurry (SPH particles) are averaged on a grid co-rotating with the impeller to capture the steady state structure of the charge. A vertical section through the centre of the mill, showing the average occupancy of each grid cell is used to determine charge height. To identify the free surface, areas with a volume fraction less than 0.16 are considered outside the charge. The highest vertical point of the free surface near the wall, which is the charge height, can then be determined

A row of impeller arms represents a substantial dynamic obstacle (Ndimande et al. 2019) which restricts axial flow through these locations and which sub-divides the charge into different flow compartments. Within each compartment the particles are free to circulate but there is restricted ability of particles to flow between them. The angular spacing of the arms is expected to influence transport and mixing in the mill because of their impact on the ability of particles to migrate between compartments. This inter-arm angle determines the time available for the particle to fall downwards between successive impeller arms. Large angular spacing gives particles longer to travel downward and hence, they fall further. This means particles have a higher chance of falling through the plane of the impeller arms and into the next compartment. This can be expected to affect the ease with which particles move axially down (and upwards) across a row. Low angular spacing gives the particles a shorter travel time, which means they fall a shorter distance and are less likely to be able to change flow compartments. Consequently, such particles are less likely to fall below the centre-plane of the impeller arm row which could be expected to impede mixing and transport in the mill.

Thus, the fall height is a significant measure for analysing the mixing performance of a particular impeller design. We define a "particle fall height" as the vertical distance that a media particle falls, in the time it takes an impeller arm to travel the angular distance to the position of the preceding arm. The degree to which the particle fall height influences mixing will be investigated later. The fall height is calculated for all particles at the top impeller row and not the bottom row (since the media is densely packed below and there is no fall component to the flow). The time t taken for an arm to travel one angular spacing is given by:

$$t = \frac{\theta_s}{\omega}, \tag{35}$$

Where ω is the angular speed of the shaft and θ_s is the angular spacing of the arms. The motions of all the DEM and SPH particles are averaged (both locally in space and temporally) on a cylindrical grid. Therefore, the time t is used with the average velocity of particles at the row level to calculate the fall height τ as shown below.

$$\tau = tv_{av} + \frac{at^2}{2}, \tag{36}$$

Where v_{av} is the average velocity at the row level and a the acceleration due to gravity. The fall height (τ) is expressed as a fraction of the diameter of the impeller arm. In cases where a row of arms has multiple angular spacings then the fall height is averaged across the row.

3.8 Measuring mixing

The effect of different impeller configurations on mixing and transport in the SMD355E is investigated. The focus will be on the transport and mixing of the media. This is because the slurry transport in the bulk of the charge in such a batch mill is predominantly controlled by the packed media and its flow behaviour. The mixing measure used here is determined by analysis of the probability distribution of local averages of an attribute of the particles. The attribute used in this work is colour which is assigned according to initial vertical position and which allows the progress of mixing to be predicted. Horizontal strata are used since these provide the best mixing information for investigating vertical (axial) transport. This is a flexible method that measures the degree of local homogeneity of the charge.

This method has been used and described by Cleary et al. (1998) and Cleary and Sinnott (2008). A cubic cell grid is superimposed over the media bed and local averages of the colours are calculated, using all particles in the region with the centre at each grid point. The averages are then used to determine a mixing state by normalisation relative to the maximal range between fully segregated and fully mixed states. The mixing rate is then given by the gradient of the mixing state with respect to time.

4 SMD 1100-E

This chapter presents the DEM-SPH simulation results for the SMD1100-E to study the charge motion and structure and energy utilisation. The DEM-SPH model is better suited for studying the particle-particle and particle-fluid interactions which drive important outputs such as power draw and product size distribution. The energy spectra obtained from the DEM outputs is used to characterise the grinding environment in the SMD. To quantify the importance of including the slurry phase, the modal peaks for the energy spectra of DEM only and coupled DEM-SPH simulations of the SMD are presented. The two-way coupled DEM-SPH has not been used to study in detail these important aspects of the SMD. It has also been demonstrated that conventional laboratory techniques are incapable of giving detailed information of the grinding environment. To obtain meaningful results, all simulations were run until both the media and the slurry reached steady state. The results presented are obtained from simulations after reaching steady state.

4.1 Averaged media distribution in the SMD 1100-E

It is useful to separate the transient motions (which are mostly restricted to the free surface regions of the charge) from the underlying steady charge structure and flow. The motion of the DEM and SPH particles are, therefore, averaged on a cylindrical grid that is co-rotating with the impeller. Using a co-rotating grid allows the capture of the steady state structures around the impeller as seen in its frame of reference while the fixed grid allows resolution of structures closer to the shell. Figure 25 shows the resulting average media distribution as indicated by the solid fraction in a vertical section through the centre of the mill. The red/orange sections show the locations where the media is densely packed. The solid fraction in these regions is 0.55. Light blue represents a region at the boundary with the vortex and the solid fraction ranges from 0.10 to 0.16.

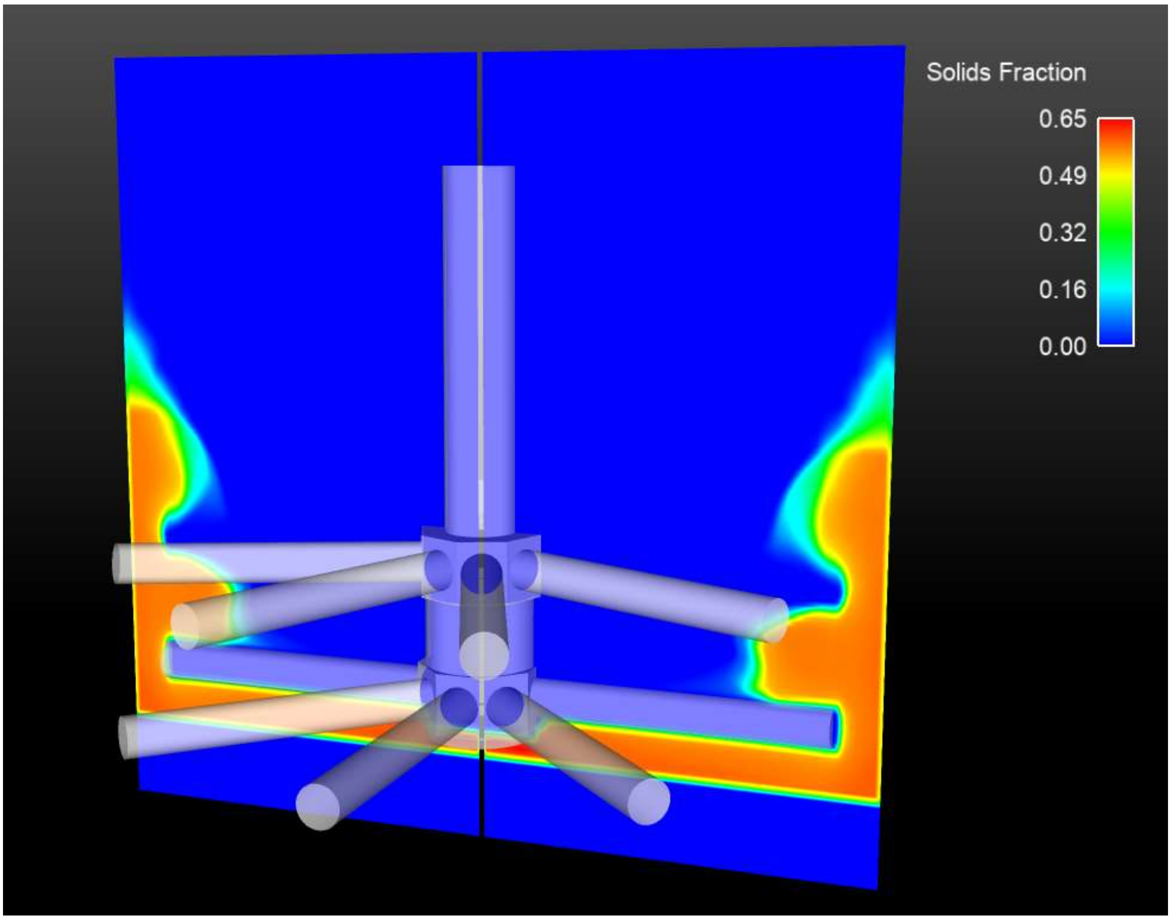

Figure 25: Vertical section through the SMD showing steady state distribution of average solid fraction. The blue section below the bottom set of impeller arms is the mill shell (Ndimande et al. 2019).

The red coloured region below the bottom row of impeller arms represents an area where the media is densely packed. This high particle concentration below an impeller was reported by Derksen (2003) for solids suspension in a stirred tank. The impeller arms cut through the charge which is centrifuged against the side walls of the mill creating two large persistent indentations. In the region above the top row of impeller arms, the moderate downward slope of the charge terminates at the level of the top row of arms. The packed region between the two rows of impeller arms extends radially inwards further than does the charge above the top row of arms.

The average solid fraction in the dense areas of the charge (>0.5), is close to the solids fraction expected in a packed bed of spheres at rest which is around 0.64. This means the distance between the media is fairly small, and that dilation of grinding media is comparatively small in terms of mean free path or distance between the surfaces of the media particles. Slurry fills these void spaces between the media particles. Since this phase is incompressible, it acts as a constraint on the dilation of the charge which contributes to the uniformity of the packed media distribution. The interstitial slurry plays a critical dynamic role by strongly influencing the degree of separation of the media particles in the bulk of the charge. The degree of charge dilation is, therefore, indirectly controlled by the slurry fill level which then strongly influences the selection and breakage of the fine rock particles in the slurry. In contrast, for a dry SMD (which can be modelled using DEM by itself) the average solid in the densely packed areas of the charge (i.e. average of areas with volume fraction > 0.5) is higher at 0.58. The reduction in the solid fraction from this level to the 0.55 level found for the coupled slurry and media charge is a direct consequence of the presence of the slurry and its dynamic effect on the charge. It means that there are less direct media-media contacts when interstitial slurry is present which has important impacts for a range of mill performance characteristics such as the power draw and energy utilisation (which will be discussed in detail below).

4.2 Media and slurry flow in SMD 1100-E

The SMD 1100-E is used to study the charge dynamics and energy utilisation of these devices at industrial scale. The mill is charged with 12 t of media and run until steady state is reached. When the kinetic and potential energies of both the media and slurry equilibrate, that indicates the system is at steady state. Analysis of the results is performed at steady state. Figure 26 shows a time series plot of the media (GF) and slurry (SPH) kinetic energies. From the start of the simulation to 2.0 s, the flow shows an oscillatory behaviour. After 2.0s effective steady state for the SMD1100-E simulated under the conditions chosen was reached as the potential and kinetic energy components of both phases equilibrate. After the 2.0 s mark there is a gradual rise in the GF kinetic energy. The SPH kinetic energy oscillates with a very low amplitude, while the potential energy components are constant. The flow in the mill is fully equilibrated though in the strictest sense the energies are not constant. The start-up transients have dissipated, and the variations have a small amplitude, this is adequate for calculating long term “steady state” averages to represent the overall flow behaviour.

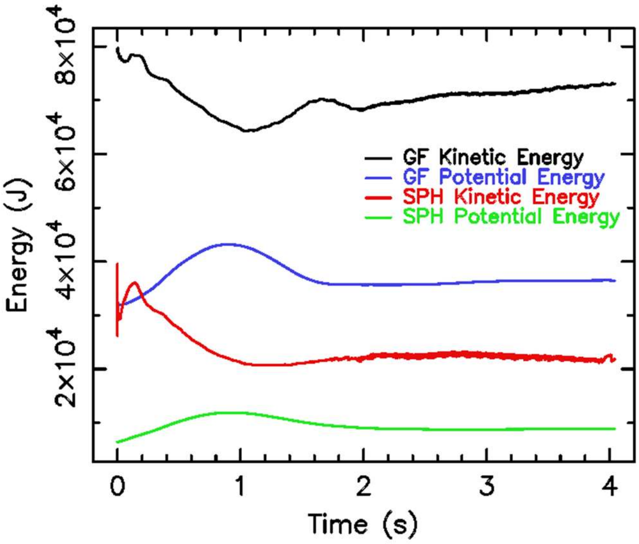

Figure 26: Time series plot of the kinetic and potential energies of both the granular flow (GF) and SPH (slurry) components of the model showing steady state. (Ndimande et al. 2019)

A top-down view of the steady state charge structure in the SMD at time 2.7 s is shown in Figure 27, with the mill viewed at an angle from the top and the shell made transparent. Media flow coloured by speed and the slurry made white is shown in Figure 27a. Figure 27b shows the slurry flow coloured by speed and the media made transparent. Red (hot colour) shows the highest velocities and blue (cool colour) the lowest. The rotational action of the impeller fluidises the media. The resultant centrifugal force pushes both the media and the slurry toward the mill wall, creating a vortex in the region around the shaft located at the centre of the mill.

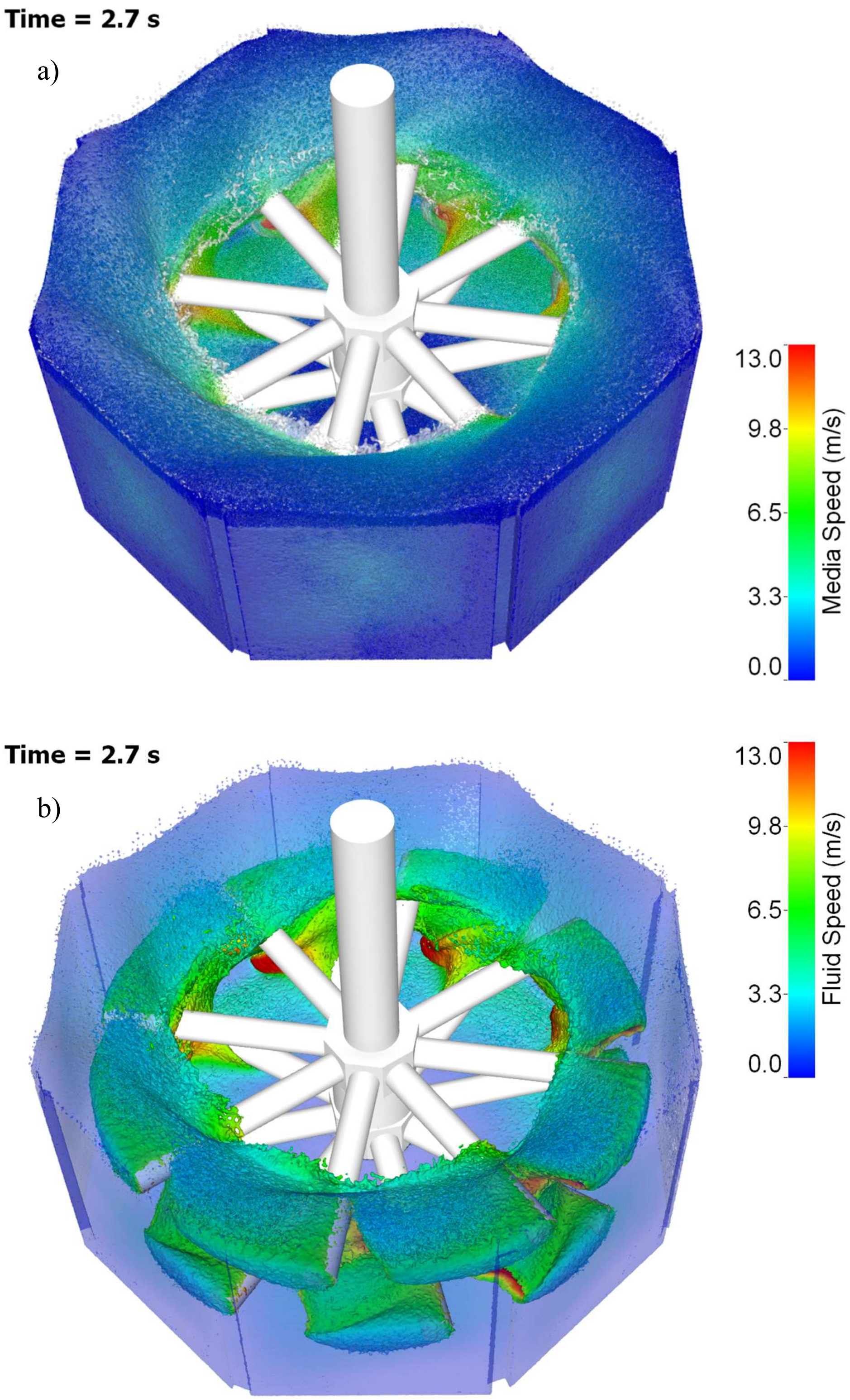

Figure 27: A top-down view of the steady state flow in a SMD with the shell made transparent. a) Coupled flow with media coloured by speed while the fluid is coloured white, b) slurry flow in the SMD with the slurry coloured by its speed with the media made transparent (Ndimande et al. 2019).

The vortex is conical in shape with a large diameter at the top that decreases with depth into the mill. The charge swirls in the rotational direction of the impeller, with speeds of up to 13 m/s. The highest velocities for both the media and the slurry are mostly at the tip of the impeller arms. As the impeller arms move through the charge, they create elongated cavities on the inside of the vortex which can be seen in Figure 27a. Figure 27a shows that at the upper free surface are undulations starting at each of the corners of the octagonal shell. From Figure 27b the cavities generated by the high rotational speed of the impeller arms are more visible in the structure in the fluid surface presented. The cavities extend radially from the inner free surface of the vortex to the tip of the impeller arms. They narrow with distance behind each arm (azimuthally) and extend a distance towards the trailing arm. The impeller speed and the azimuthal spacing of the arms governs the fraction of the space between the arms that the cavities extend over (Ndiamdne et al. 2019).

Shown in Figure 28 is the steady state coupled flow in the SMD at different times of the simulation from 2.7 seconds to 3 seconds. The media is made white while the fluid is coloured by its speed. This figure shows that a stable vortex is formed with small transient structure located near the tips of the arms at the point of interaction with the charge. To show the behaviour of the slurry, a close, top-down view of the coupled flow in the SMD is shown in Figure 29. The media is made transparent, and the slurry coloured by its speed. Figure 30 shows the same close, top-down view of the coupled flow, this time coloured by media speed. The slurry is coloured white and is obscured at the top of the vortex by media which is above it. The close-up views of the charge motion are shown at the same times as Figure 28 to analyse the complex multi-component flow. The solid media dominates the flow in the mill. The rotating arms compress the media towards the wall and introduces a shear profile. This forms tortuous paths between the media particles in which the fluid flows. This network of channels not only defines the motion of the fluid, but also the rate at which it moves. When the channels are filled with fluid, the excess flows on or near the surface of the vortex.

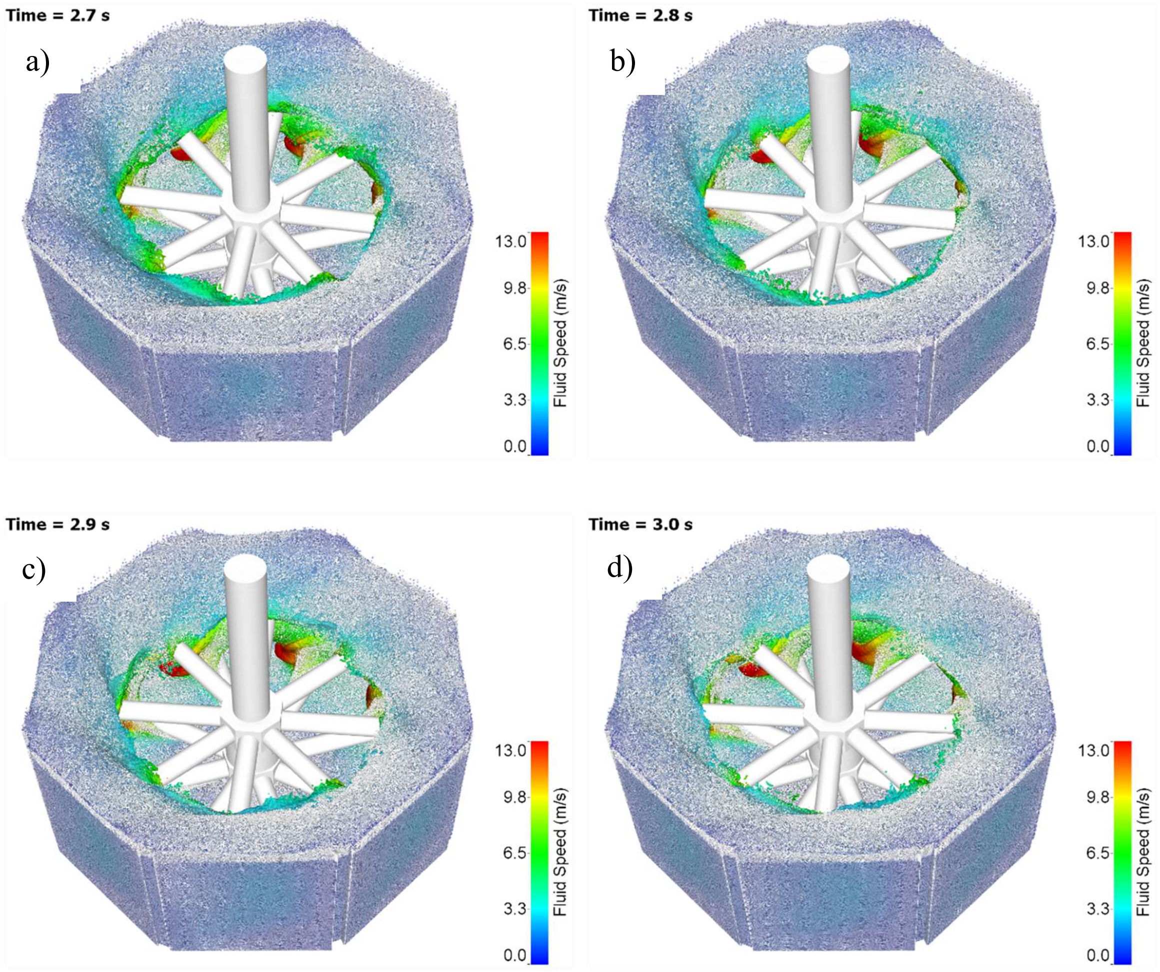

Figure 28: Top-down view of the coupled flow in the SMD, with the slurry coloured by its speed and the media-coloured white shown at time a) 2.7 s, b) 2.8 s, c) 2.9 s and d) 3.0 s. The different simulation times show the impeller at different phases (Ndimande et al. 2019).

The free surface of the slurry phase is visible at the surface and bottom of the vortex just above the base of the mill (Figure 29). The mobility of the slurry is highest at the surface layer where the media solid fraction is low. Low media solid fraction means less resistance to motion of the slurry, resulting in the slurry moving more independently. This is also because the resistance to motion of the slurry by the air at the vortex is less compared to the media. Movement of the top impeller arms through the charge generates standing wave structures at the free surface. These structures move with the rotating impeller.

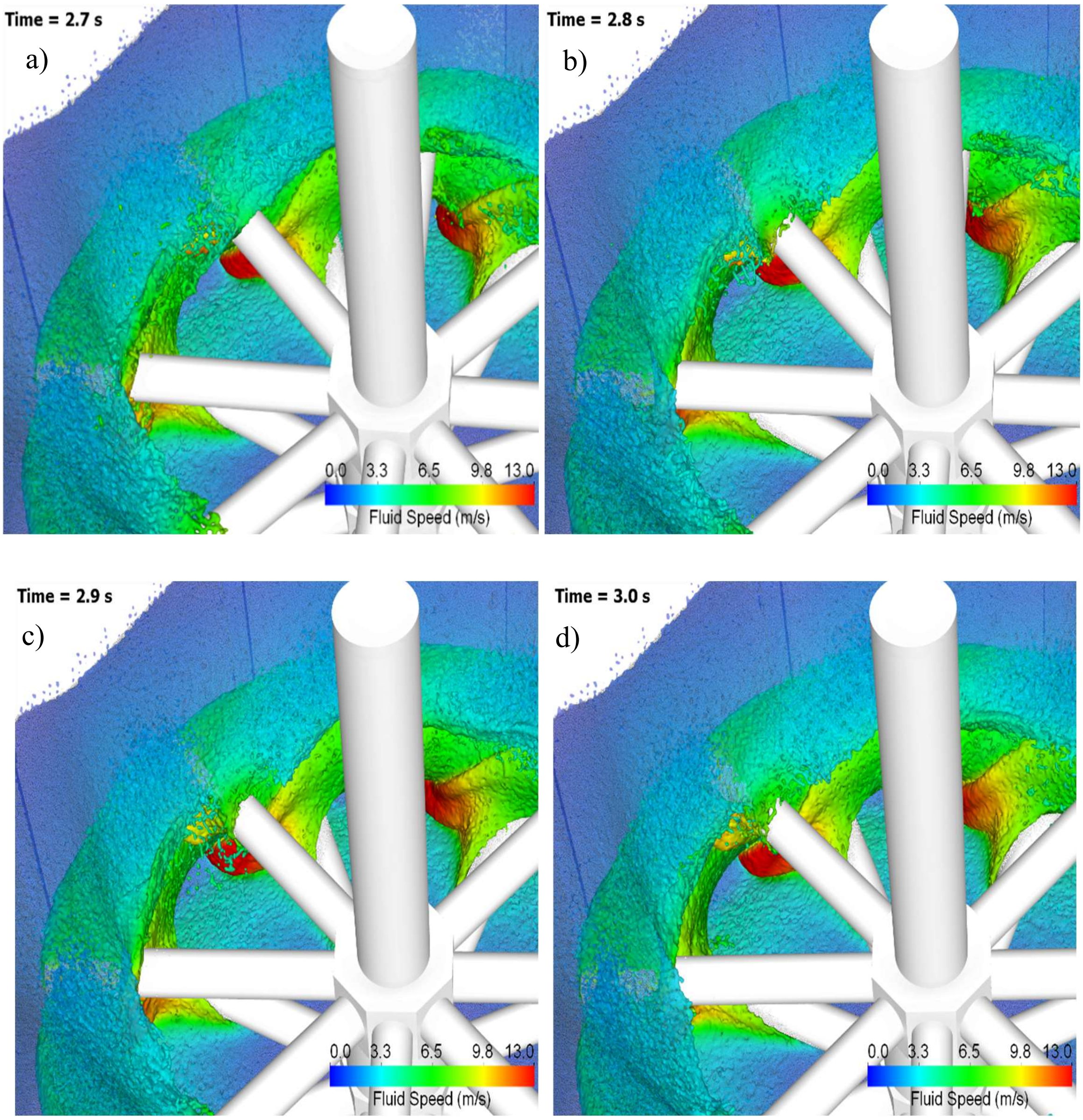

Figure 29: A close-up, top-down view of the steady state coupled flow in the SMD shown at time a) 2.7 s, b) 2.8 s, c) 2.9 s and d) 3.0 s. The slurry is coloured by its speed and the media made transparent to show the fluid phase clearly (Ndimande et al. 2019).

As the top impeller arms rotate, they cause a splash of the charge at the free surface. The position of the charge normal to the leading surface of the arms is pushed azimuthally in their direction of rotation. Some of the charge flows above the arms while some is pushed downwards toward the lower set of arms.

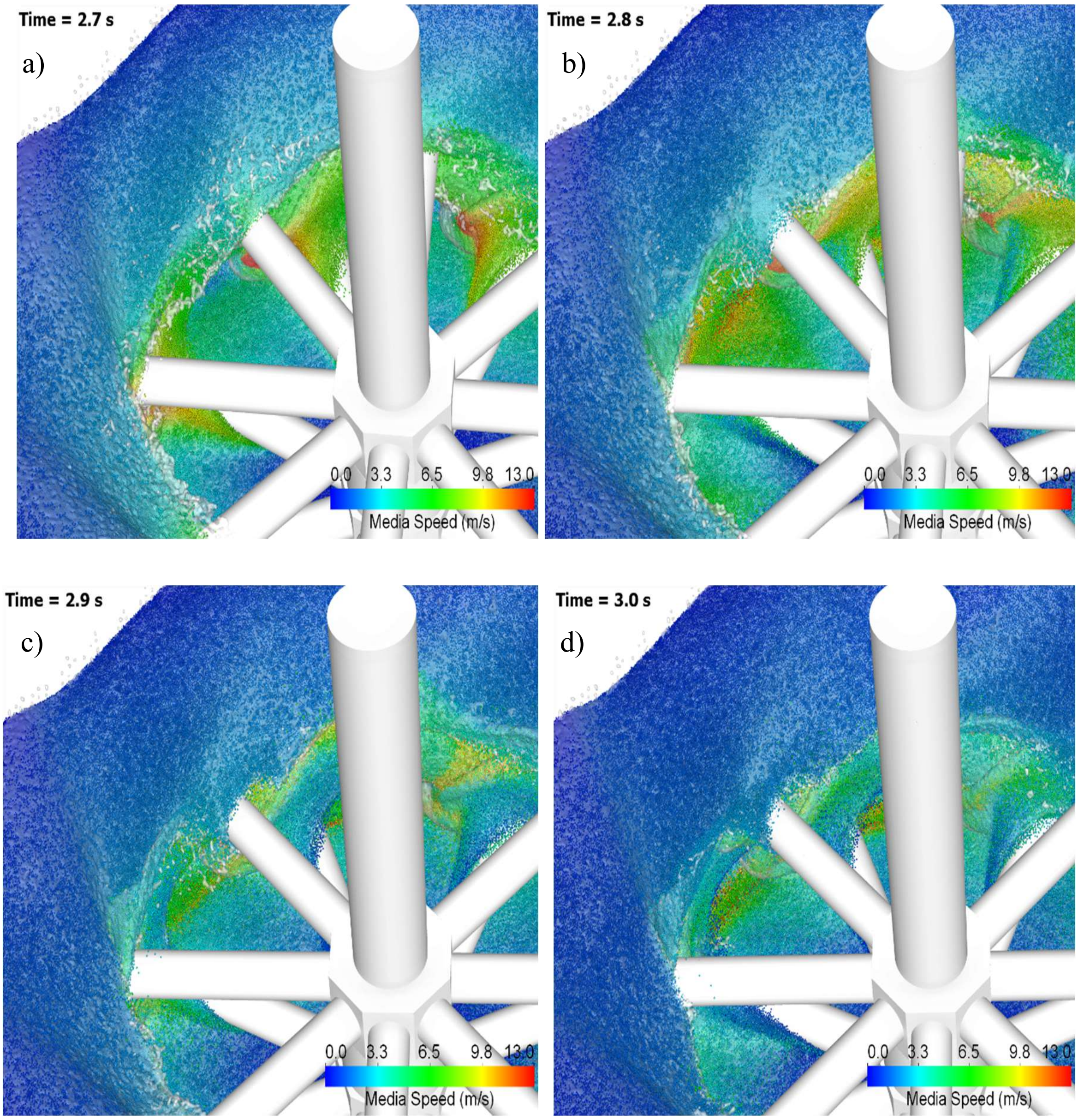

Figure 30: A close-up, top view of the steady state coupled flow in the SMD, with media coloured by its speed, showing the impeller arms interacting with the charge. The fluid is coloured white at a) time 2.7 s, b) time 2.8 s, c) time 2.9 s and d) time 3.0 s. This view shows the small transient surface structures of the media (Ndimande et al. 2019).

The arm in the lower set also drags some of the charge along with it in the direction of rotation, along its length towards the shaft. Some of the charge is pushed up towards the upper set of arms. The structure of the vortex observed here agrees with experimental reports of Bailey et al. (2016) and Norejko et al. (2018) in their study of vortex stability in the SMD. The vortex structure in a 4L laboratory scale SMD from Grinding Solutions Ltd and a pilot scale one is shown in Figure 31. The lab scale mill is operating in continuous mode while the pilot scale is operated in batch mode. The finite exposure time of the images in Figure 31 make it impossible to see details of the fine structure. The vortex structure in both these mills at different scales is similar to that predicted by the two-way coupled DEM-SPH model used in this work (as shown in Figures 27-29). The cavities predicted by the model in the SMD1100-E (Figure 27b) can be seen also in the lab and pilot scales shown in Figure 31.

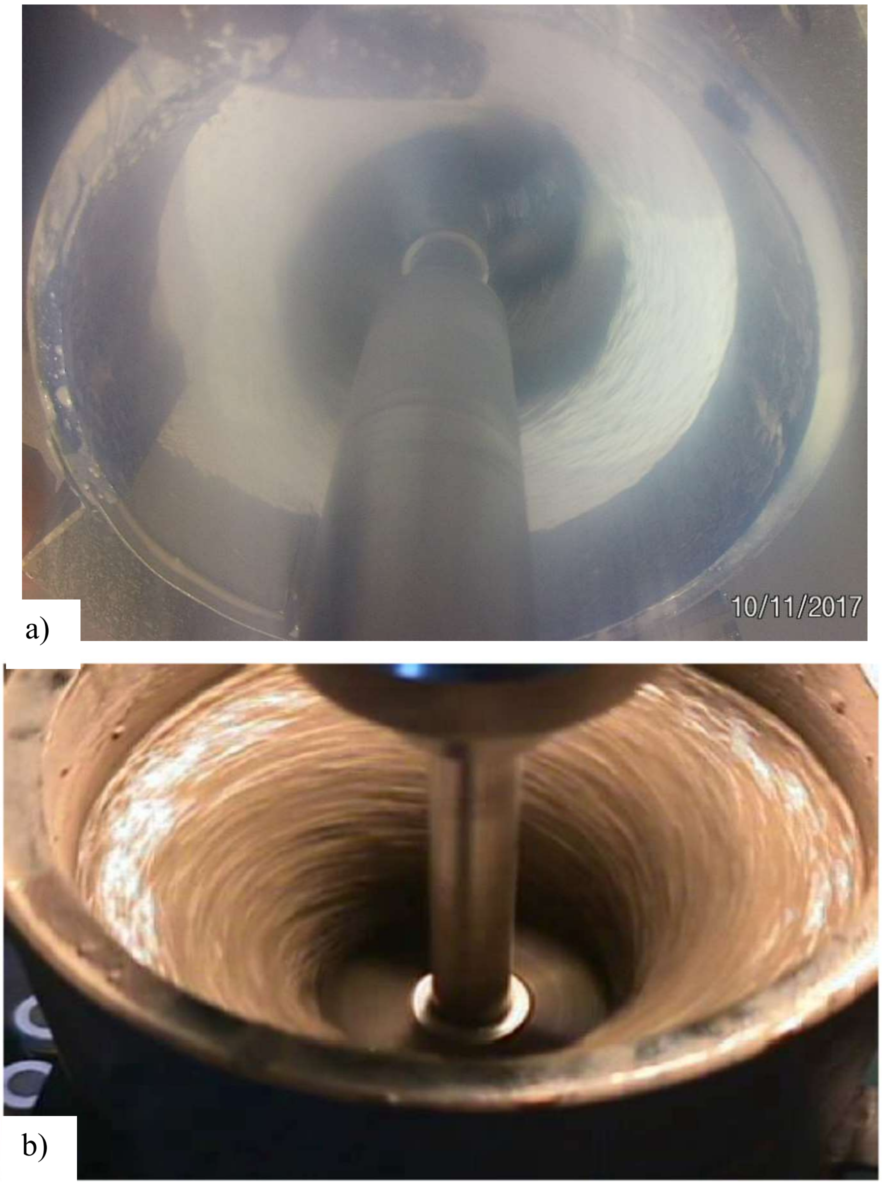

Figure 31: a) Vortex structure in a 4L lab scale SMD, b) vortex structure in a pilot-scale SMD (Ntsele and Allen, 2013). Both are like that predicted by the DEM-SPH model for the SMD 1100-E (Ndimande et al. 2019).

4.3 Averaged velocity distribution in the SMD 1100-E

4.3.1 Radial velocity distribution

The different velocity components (radial, axial, and tangential) of the media and the fluid are shown in Figure 32. Figure 32a shows the radial velocity distribution of the media. The negative radial velocities indicate the direction towards the centre of the mill. In all three regions of the charge the radial velocity is restricted to a thin active surface layer, with no movement in the bulk of the charge. This is due to the centrifugal force generated by the rotating impeller limiting the radial movement in the bulk of the charge. Above the bottom set of impeller arms, the flow of the active surface layer is towards the wall of the mill with a radial velocity of about 1.5 m/s (shown in red). This is due to the rotating action of the bottom impeller arms, which pushes some of the media towards the wall. In the region above the top impeller arms, there is motion towards the mill centre (Blue) and motion towards the mill wall (red). The top impeller arms drive some of the charge towards the mill wall and upwards. Gravity brings that material back to the mill seen here as motion towards the centre of the mill. Figure 32b shows the radial velocity distribution of the slurry. The radial behaviour of the slurry is generally like that of the media in Figure 32a. The only difference is that the magnitude of the slurry movement is higher than that of the media at the free surface of the vortex. In the bulk of the charge the slurry is trapped by the media and shows little independence because of the resistance to its motion by the solid phase. At the free surface layers where there is less resistance due to the media, the slurry moves more independently. The resistance on the motion of the slurry by the air is less than that of the media.

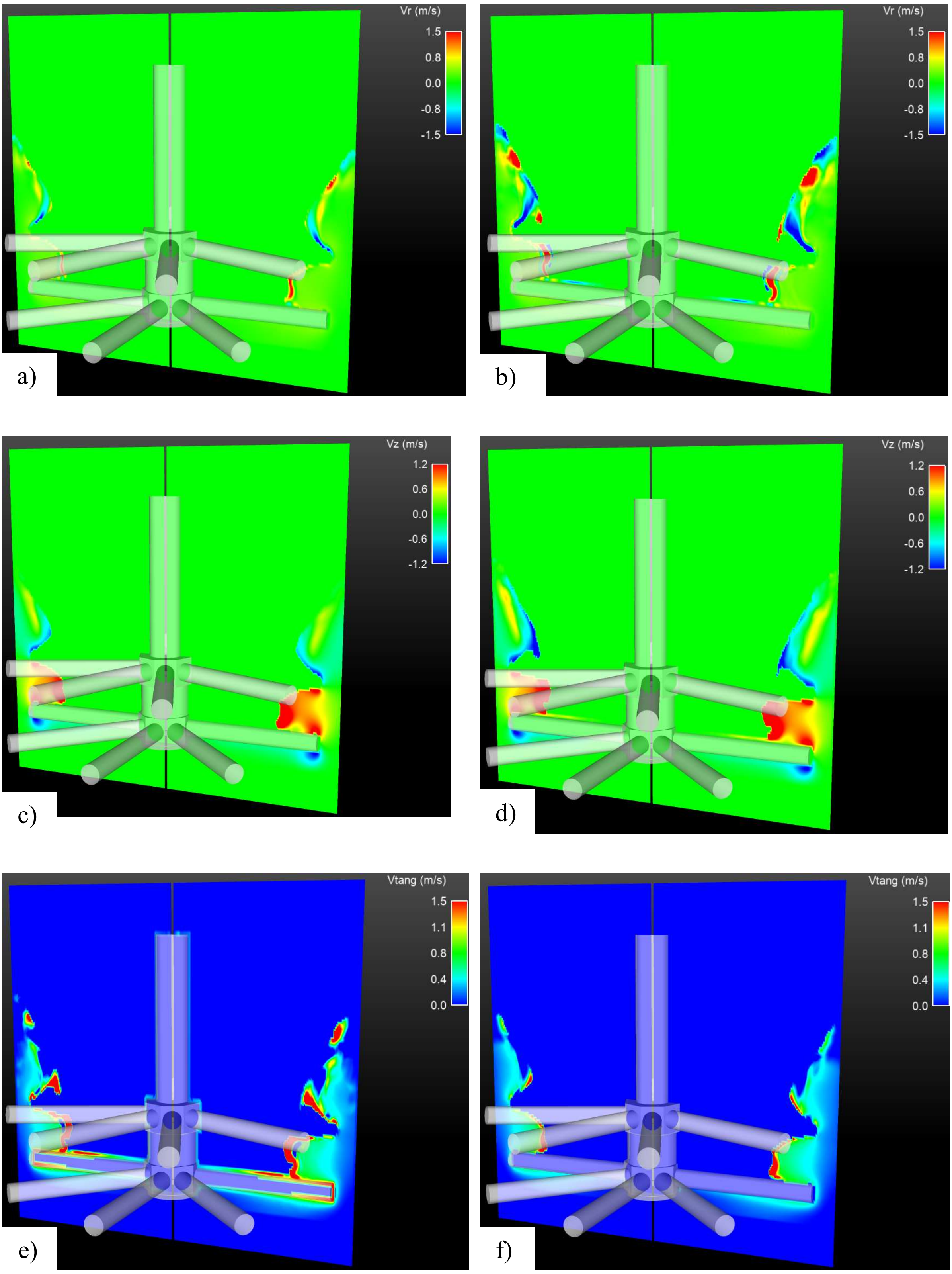

Figure 32: Vertical section through the mill showing time averaged, a) media radial velocity, b) slurry radial velocity, c) media axial velocity, d) slurry axial velocity, e) media tangential velocity, and f) slurry tangential velocity (Ndimande et al. 2019).

4.3.2 Axial velocity distribution

The axial velocity distribution of the media is shown in Figure 32c. The negative velocities (coloured in blue) indicate flow downward. There is a highly active agitated zone in the region between the impeller arm sets. This shows that the bottom impeller arms are pushing the media upward in this region. The axial velocity at the free surface in this region is about 1.2 m/s, moving towards the mill wall, the axial velocity decreases to 0.0 m/s. The media in contact with the bottom of the lower impeller arms has an axial velocity of 1.2 m/s downward because of the pressure exerted by the arms. Above the top set of impeller arms is material with upward (yellow) and downward (blue) axial velocity of 0.6 m/s and 0.8 m/s respectively. This means there is recirculation of the charge in this region above the top set of impeller arms, with the free surface moving downwards. The recirculation occurs because the material pushed upwards by the top set of impellers is forced downwards by gravity. The media at the wall has an axial velocity of 0.0 m/s.

Figure 32d shows the axial velocity distribution of the slurry. Like the media, the high slurry axial velocities are observed to be in the region between the top and bottom sets of impeller arms. The major difference being that the slurry free surface is closer to the shaft (shown in yellow along the lower impeller arm). Generally, the impeller arms are forcing most of the charge towards the wall and upwards. The material is then forced downwards by gravity back into the mill. This flow pattern has been reported by Tamblyn (2009) who used PEPT to study the flow in the grinding environment.

This axial mobility controls the transport of feed materials to regions of high energy dissipation, and of ground product out of the mill. The axial component of the flow is crucial for the performance of the mill.

4.3.3 Tangential velocity distribution

The tangential (swirl) velocity distribution of the media in the mill is shown in Figure 32e which shows that the tangential velocity is zero at the mill wall. This means there is a layer of media in contact with the mill shell that is not sliding along the shell. This is an advantage because there will be less abrasion wear on the mill walls. For the two regions above and between the impeller arm sets, the tangential velocity increases with distance from the mill wall to a velocity of 1.5 m/s at the free surface. There is a thin layer below the bottom set of impellers that is active tangentially with a velocity of 0.8 m/s. Generally, media at the tip of the impeller arms has a high tangential velocity of 1.5 m/s which decrease with distance from the tip towards the wall. This is because resistance to flow at the wall is highest. The tangential velocity distribution of the slurry is shown in Figure 32f. The behaviour of the slurry again is like that of the media. For the region between the two sets of impeller arms the tangential velocity at the free surface is about 1.5 m/s. From the free surface moving toward the mill wall this decreases to 0.0 m/s. There is a layer of media with low tangential speeds in the range 0.2-0.3 m/s (as shown by light blue near the wall) that extends out from the wall for most of the charge depth. The mill corners provide some circumferential resistance to flow along the wall, which may reduce the mobility of particles sliding along the wall (in the direction of impeller motion). This is an advantage from the perspective of minimising abrasion wear on the mill walls (Mayfield, 2018). The tangential and axial charge motion is responsible for most of the transport of slurry within the charge because these components are higher in magnitude than the radial component.

4.3.4 Media velocity isosurfaces

The media velocity components are presented as isosurfaces in Figure 33. These show the three-dimensional nature of the velocity field which was examined in a vertical slice in Figure 32. The radial velocity shown in Figure 33a is structured as bands of closed concentric surfaces. The region below the impeller arms is a band of media moving towards the mill wall at a velocity of 0.2 m/s. Directly above this region are alternating bands of media moving towards the mill wall (shown in red moving at 0.2 m/s) and media moving towards the mill centre (shown in blue moving at 0.2 m/s). The axial component shows that the media in contact with the leading surface of the arms has upward motion (shown in red in Figure 33b), and the media forced to travel below the arms shown in blue. The red isosurface extends azimuthally from the leading surface of the arms and forms a fork like structure that is not continuous. This isosurface also extends slightly upwards from the leading surface of the arms. For the lower row of arms, this region of upward moving media also stretches along the length of the arm towards the shaft. The blue isosurface occurs directly below the tip of the arms, as well as after the red isosurface which is at the leading surface of the arm. The structure of the blue isosurface between the tips of the arms that are in the same row is also not continuous.

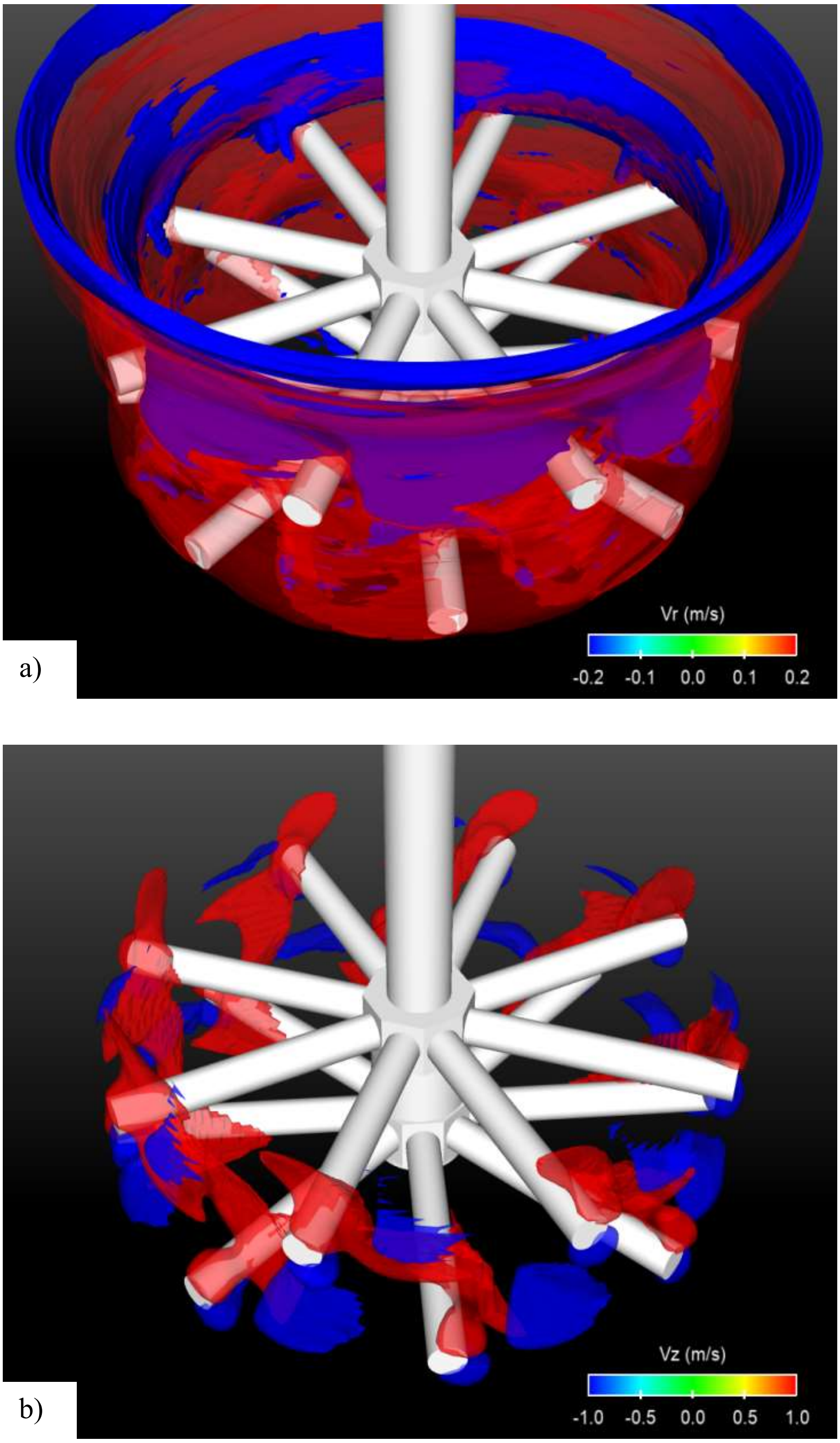
a)

b)

Figure 33: Isosurface of the averaged media velocity distribution in a frame that is co-moving with the SMD impeller. The mill shell is transparent; a) radial velocity, with red indicating flow towards the wall and blue, flow towards the centre, b) axial velocity, with red indicating flow upwards and blue, flow downwards (Ndimande et al. 2019).

The peak tangential velocity (shown in orange/red) occurs at the tip and in discrete areas between the arms (for both rows of impeller arms), extending radially towards the shaft from the tips. The orange/red isosurface represents media that is highly accelerated by the impeller arms and piles-up in front of and strikes the leading surface of the arm at 3 m/s. Intermediate velocities (shown in green) also occur around the impeller arm tips, extending above and under the arms. For the bottom row of arms, the intermediate velocity isosurface extends continuously between the arms, extending slightly along the length of each arm towards the shaft. This represents media that is mildly accelerated by the impeller arm as it flows around the arm at 2 m/s. Low velocities occur at the top of the charge in a thin circular band shown by the blue isosurface.

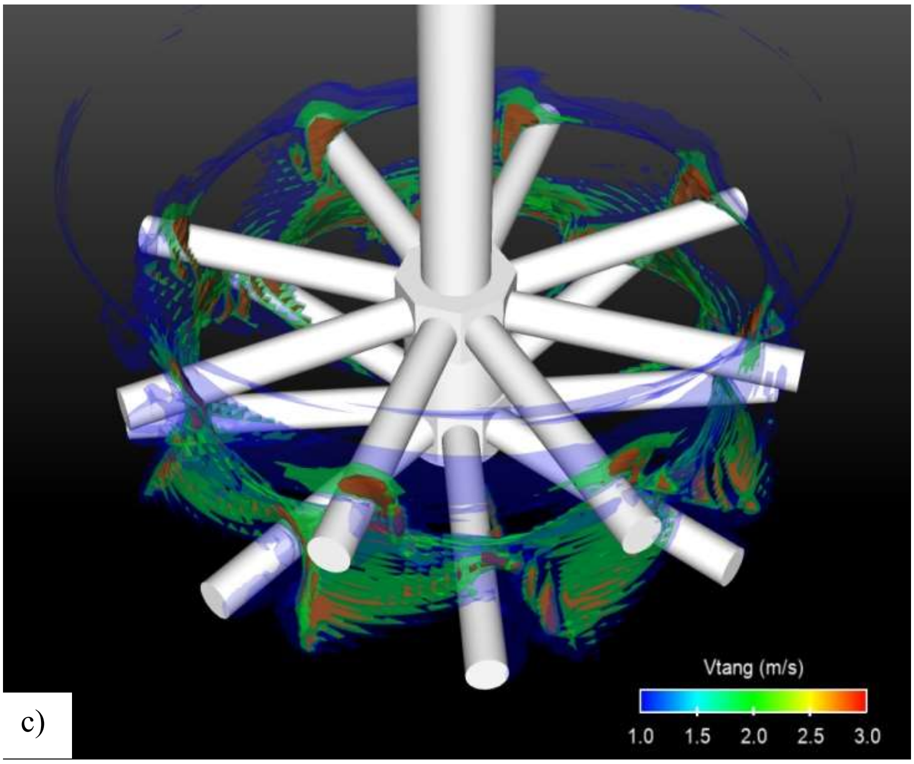

Figure 34: (Continued), Media coloured by c) tangential (swirl) velocity with red indicating high velocities up to 3 m/s, and blue low velocities. The green shows media moving at 2 m/s.

This isosurface also occurs just above the tip of the impeller arms in a circular band, showing media travelling at 1 m/s. The sharp velocity gradients indicated by the spacing between the isosurfaces give the shear which leads to size reduction in the mill (Theuerkauf et al. 1996). This happens as layers of the media and slurry moving at different speeds slide past each other.

The result of which is stress applied to the fine ore particles caught between these layers, which in turn leads to breakage of these fine particles.

4.4 Power draw and energy utilisation

The power draw of the mill at the conditions used in this work is determined by summing all the forces acting on the impeller (both media and slurry). The product of the impeller rotation rate and the torque generated by all contact forces gives the power draw (Cleary et al. 2006). The predicted power draw of the SMD 1100-E mill coupled DEM-SPH and the DEM only simulations are summarised in Table 11. For the coupled Simulation, the predicted power draw is 985.7 kW (which represents 89.6% of the installed power). The media collisions (Media-to-media and media-to-geometry) dissipate 66% (651.3 kW) of the power drawn by the mill. This is a summation of all energy dissipation components of the media collisions which are calculated by the DEM contact model. Viscous stresses in the slurry phase account for the remaining 34% (334.4 kW).

Table 11: Comparison of energy utilization in DEM only and coupled SMD (Ndimande et al 2019).

	Coupled (DEM+SPH)	DRY (DEM only)
Power draw (kW)	985.7	953
DEM dissipation (kW)	651.3	953
Slurry dissipation (kW)	334.4	-

To ascertain the effect of the slurry phase on the energy utilisation in the SMD, the power drawn by the coupled simulation is compared to DEM only. The media loading is kept constant for both simulations, this comparison is presented in Table 11. The DEM only simulation has a power draw of 953 kW, which is 3% lower than the coupled one. In the dry simulation (DEM only), all the power drawn is dissipated only through media collisions. The coupled simulation (DEM+SPH) has a higher power draw because of the increased resistance to the rotation of the impeller due the additional mass of the viscous slurry. The presence of the slurry affects the micromechanical interactions of the media by dilating the charge. This leads to reduced rates for the media collisions and dampening the contacts resulting in lower energy dissipation of the media phase as shown in Table 11 as DEM dissipation for the coupled (DEM+SPH).

4.5 Energy consumption in the SMD

Knowledge of a comminution device's usage of the energy it draws is very important for design and optimisation purposes. This section focuses on how energy drawn by the SMD is used. The discussion will focus on the energy dissipated by media collisions, which will be followed by energy dissipated by viscous stresses in the slurry. To examine energy usage in the SMD the locally averaged distributions of the shear and normal media power plots were developed. Shear is important because grinding in this device is attributed to breakage by this mode.

Figure 35 shows a vertical slice through the centre of the mill, showing the distribution of the shear and normal media power in the SMD 1100-E. This is calculated by summing all normal media energy dissipation per unit time onto a grid. The same is done for the shear media energy dissipation to determine the shear power. This is the same approach used by Sinnott et al. (2006) in their analysis of the energy utilisation in the tower and pin mill. Figure 35 shows that the normal and the shear power dissipation is mostly concentrated near the tips of the impeller arms. This is the region experiencing high velocities. The shear power increases radially with distance from the mill wall and further extends to the bottom of the mill, due to the pressure exerted by the bottom row of impeller arms on the media bed below it. Between the rows of arms are two near circular regions with very high shear power of 5 X 10^4 W/m^3 (shown in red). In the region between the rows of arms, the shear power is lowest at the free surface (light blue) with the intermediate power dissipation shown by the yellow and green colours. Directly below the shaft of the impeller the shear power is zero. This is indicative of the lack of motion of the media in this region (Figure 32) as the impeller does not agitate this region.

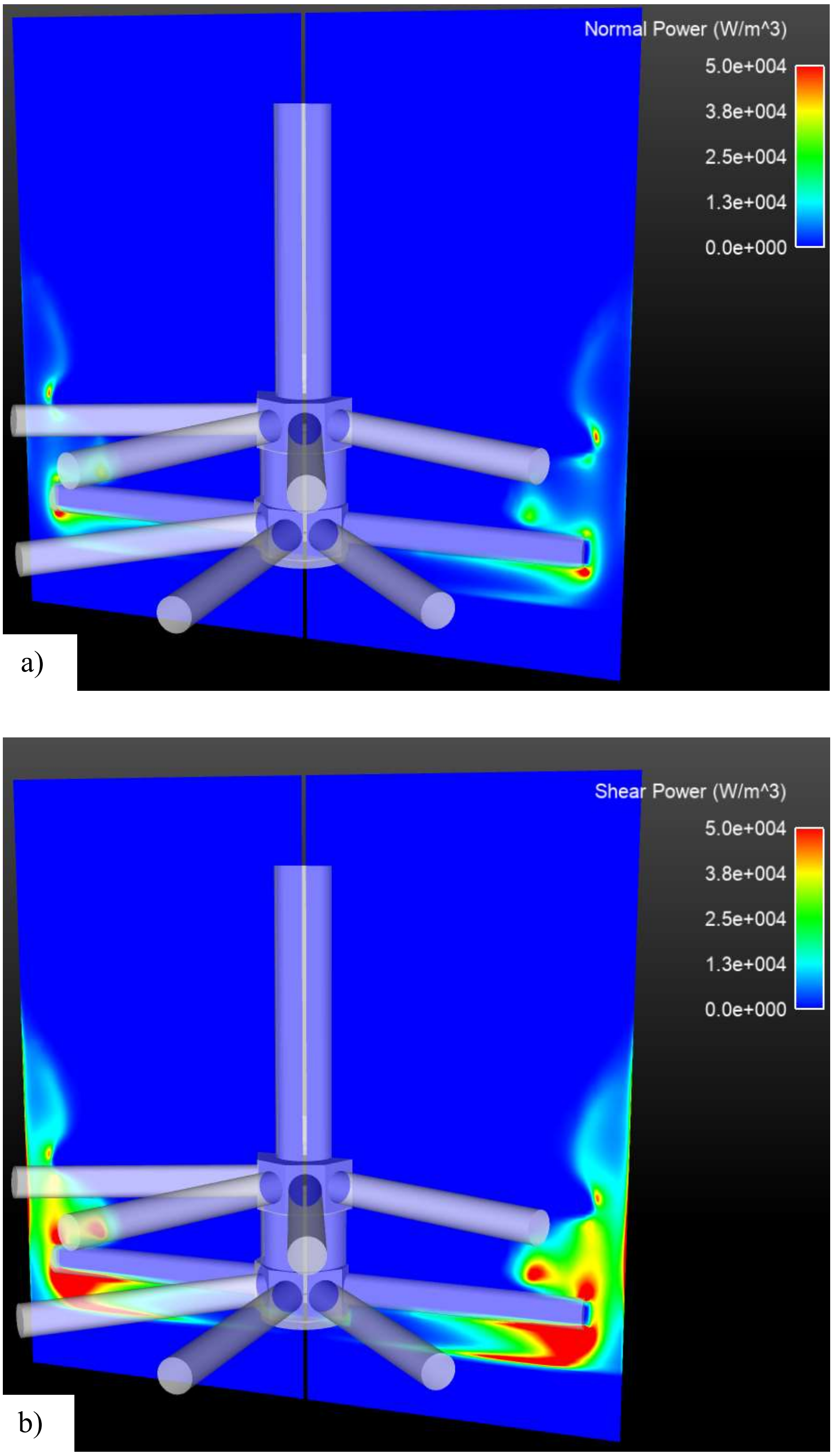

Figure 35: A vertical section through the mill showing time averaged a) normal power dissipation per unit volume, b) shear power dissipation per unit volume. The power is averaged on a frame. The red indicates areas of high-power dissipation and blue the low power dissipation areas (Ndimande et al. 2019).

Approaching the mill shell, the shear power increases reaching a maximum of 5 X 10^4 W/m^3 (shown in red) in a crescent shaped region which extends over the last 30% of the impeller arm length. This is a result of the pressure exerted by the bed and the impeller arm which decreases the mobility of the media progressively more with charge depth below the bottom impeller arm tip, resulting in high shear dissipation. This is the largest volume where the most intense comminution by abrasion takes place. The size and shape of this volume is most likely controlled by the vertical location of the shaft, the speed of the impeller, and the amount of charge in the mill. Shear power then rapidly decreases once beyond the arm tips as the mill wall is approached. In the region above the top row of impeller arms, shear power dissipation is about 1.3 X 10^4 W/m^3 (shown in light blue) at the free surface and decreases towards the mill shell.

The distribution of the normal power is spatially like that of the shear power, with the difference being in their magnitudes. Generally, the shear component of the energy dissipation is higher than the normal component. This suggests that energy dissipation occurs largely due to shear interaction, with the highest shear power being ~ 4 times the highest normal power. Since breakage is related to the amount of energy dissipated, this means that the dominant mechanism for breakage in the SMD is the shearing of feed particles caught between media particles sliding past each other. This has previously been observed in other stirred mills (Sinnott et al. 2006; Jayasundra et al. 2012; Morrison et al. 2006). The normal power dissipation in comparison, is high only in a thin area located near the free surface immediately above and between the rows of impeller arms. In these two regions (above and between the rows of arms) the normal power decreases with increasing distance from the free surface towards the mill shell. The highest normal power occurs just below the tip of the lower arms, and above the tip of the upper arms (shown in red and yellow). As the mill shell is approached from the tip of the impeller arms, the normal power dissipation decreases.

4.6 Energy dissipation isosurface

Isosurface plots can be useful in studying the distribution, in three dimensions of energy dissipation in a comminution device. Figure 36 shows isosurfaces of the shear and normal power components, calculated in a grid co-moving with the impeller. Again, the high energy dissipation for both shear and normal components is mainly situated around the tips of the impeller arms. That is media just in advance of, above and below the impeller arms. The grinding zone of the mill is, therefore, defined by these regions of high shear and normal energy dissipation. Figure 36 depicts that media above the regions of high energy dissipation (above the top set of impeller arms) contributes minimally to comminution in these devices when applied for grinding purposes. Above the top set of impeller arms, discharge of the ground product and recirculation of the charge take place in the devices applied for grinding operation. The power dissipation of both components is spatially similar. For both components this distribution has a complex shape around each impeller arm tip.

For the shear component, high energy dissipation is shown by the volume interior to the blue isosurface, surrounding the red. It extends above and below the impeller arm tips. It also extends continuously azimuthally between impeller arms in the same row. Generally, the high energy dissipation isosurface is larger for the shear than the normal component. This also confirms the dominance of shear power dissipation over the normal in the SMD as shown in Figure 35. The high energy dissipation of the normal component is restricted more to the tips of the arms. The regions of high energy dissipation correlate closely with the areas where the media moves at high speed. The three-dimensional structure of the power dissipation isosurfaces suggests that the grinding zone in the SMD can be increased by the addition of another set of impeller arms. Another set of arms can be added above the top set which may improve the grinding performance of the SMD.

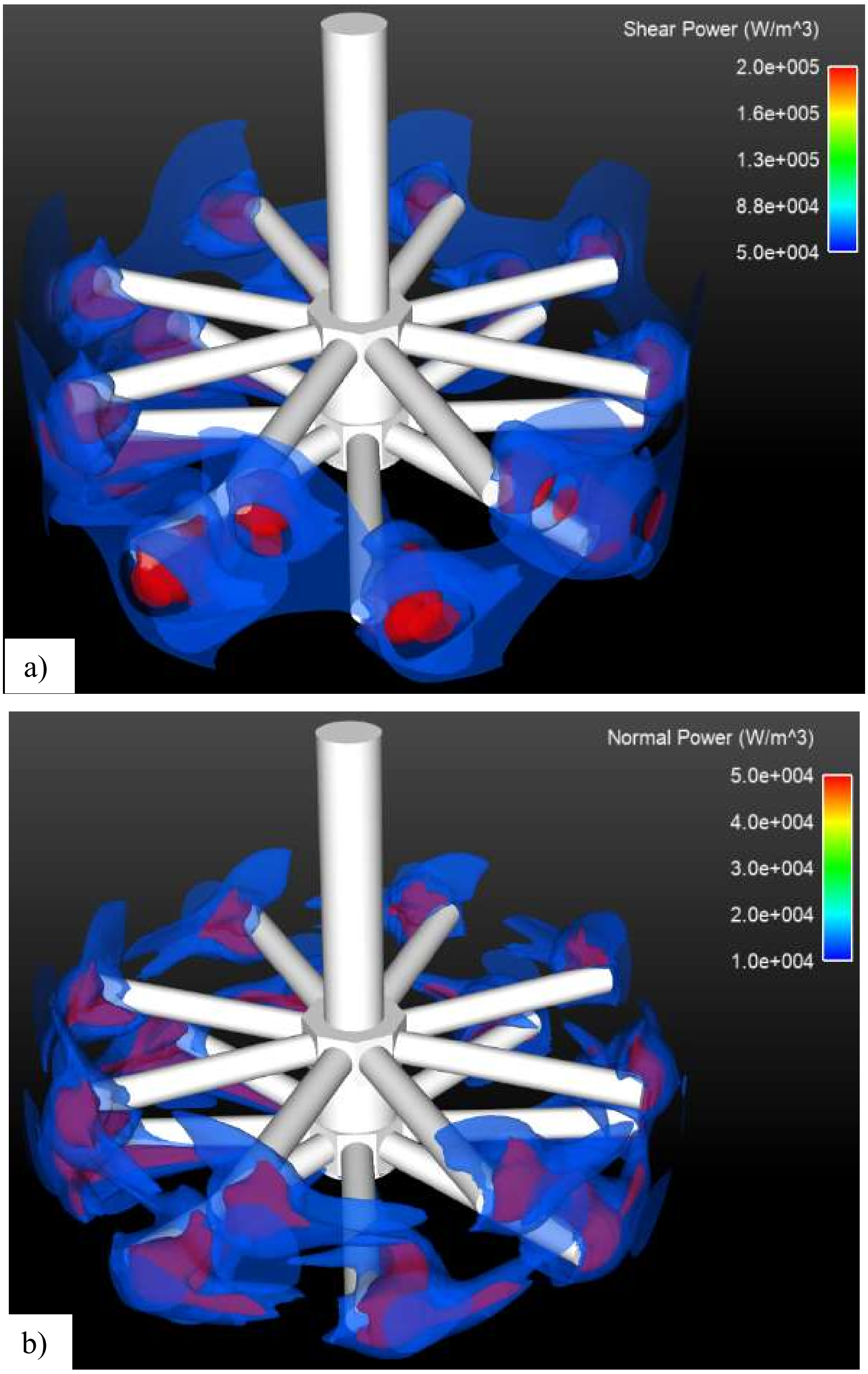

Figure 36: An isosurface of the steady state distribution of power dissipation in the mill calculated on a grid co-moving with the impeller showing a) shear power per unit volume, b) normal power per unit volume. The mill shell is omitted. Red shows High power dissipation areas at the tip of the impeller arms and blue the low power dissipation areas further from the tips of the arms (Ndimande et al. 2019).

The configuration of the impeller seems to be an important design aspect, this will be explored in section 6. It has been shown that 34% of the power drawn by the SMD 1100-E at the conditions tested, is dissipated through viscous stresses in the slurry. The contribution of this energy to the process by either breakage, or even incremental damage of the fine ore particles in the feed is unknown. What is known is that strength generally increases as the particle size decreases, meaning that high stress is required to break smaller particles than larger ones (Tavares and King, 1998; Banini, 2000; Shi and Kojovic, 2007). Fayed and Otten, (1997) have shown that energy dissipated through viscous stresses is sufficient to break weak particles or agglomerates but not the small competent ones (Palaniandy, 2017; Barrios et al. 2011). Therefore, material properties will be one of the factors that determine whether the slurry shear fields are adequate for breakage. In cases where the fine ore particles are competent the energy dissipated in viscous stresses will largely be dissipated as heat.

4.7 Collision energy spectra

It is of interest to know and understand how the energy drawn by the mill is utilized. The collision energy spectra can be of use in characterizing the collision environment. The energy spectra are essentially a probability distribution of different collision energies in the mill. The energy spectra can be used to ascertain which contact component is dominant, either normal or shear as these represent body and surface breakage mechanisms respectively. The different contact components affect the product quality. The shape of the spectra is often a characteristic of the machine and controls the fraction of energy that is wasted (for being below the elastic threshold for breakage) and the resulting progeny size distribution. The energy spectra can be represented as a histogram of either collision frequency (collisions/second) energy dissipation rate (W) against the collision energy levels. This has been done by several researchers such as Morrison et al. (2006) for the pin and tower mill, Sinnott et al. (2011) for the tower mill and Jayasundra et al. (2012) for a laboratory scale Isamill and Cleary et al. (2015a) for an industrial scale Isamill. It is important to understand how the spectra change with process conditions or design variables. This information may be useful for making decisions that will increase efficiency in these devices. An example is the impeller arm arrangement for a device like the SMD. An arrangement that results in more energy dissipated in media-to-media contacts is desirable.

A breakdown of the media collision energy for all collision types is shown in Table 12. The energy is expressed as a percentage of the total power drawn to have a better perspective of how the power drawn is used.

Table 12: Summary of energy utilisation by collision type in the SMD (Ndimande et al. 2019)

Total power utilization	% of total power draw
media to media	66.0
media to liner	4.0
Shear loss	
media to media	54.0
media to liner	3.6
Normal loss	
media to media	12.0
media to liner	0.4

The media-to-media interactions dissipate 66 % of the power drawn while 4% is dissipated by media to liner collisions. The media-to-media interactions are further classified according to collision type, with the shear dissipation being 54% and the normal being 12% of the total power drawn. For the media to liner interactions, again the shear is dominant with 3.6% while the normal dissipation is 0.4% of the total power drawn. The dissipation due to normal interaction is low because of the high media packing in the charge resulting in low relative speeds of the normal collisions as shown in Figure 32, Figure 33 and Figure 34. In addition to that, the dominant motion in the mill is swirl which generates more shear interactions.

The media to liner energy loss can be split between the media damage and the liner wear. The wear on the mill internals (the mill wall and the impeller arms) is proportional to the energy absorbed by these objects (Kalala et al. 2005; Powell et al. 2011; Boemer, 2015). This energy is again expressed as a function of the total power drawn by the mill. The mill shell absorbs 1.0%, while the impeller absorbs 0.9% of the total power draw. These figures may be comparable in magnitude; the area of the impeller arms that is in contact with the charge is significantly smaller than that of the shell. This means the wear rates on the impeller will be much higher than the shell. This finding has been shown to be consistent with observations of

SMDs in operation (Mayfield 2018). A detailed look at the media to shell and media to impeller energy spectra is presented in this section. Details of the dominant mechanism by which wear occurs in these devices is presented further in this section.

The front surfaces of the impeller arms will experience the largest wear as this is the part that is in contact with the charge. The wear is expected to flatten the arm, thus reducing its diameter. Moore et al (2016) in a case study review of an SMD deployed for grinding course feed of 160 µm using 6mm ceramic media showed worn impellers with a similar wear pattern. They reported that coarse applications will mean a rise in wear rates of the impeller arms

The collision energy spectra expressed as dissipation rate against energy is show in Figure 37. The plots show the spectra for total, media-to-media and media-to-liner interactions. Each graph has three curves with the blue and green indicating the normal and the shear component respectively, while the red indicates the total of the two. The shapes of the curves are skewed to the left like a log normal distribution. This has also been reported by other researchers who have studied the collision environment in vertical mills such as the Tower mill (Sinnott et al. 2006a; Sinnott et al. 2006b; Morrison et al. 2009; Ndimande et al. 2019) and horizontal mills such as the Isamill (Jayasundra et al. 2012; Beinert et al. 2015, Cleary et al. 2015a; Cleary et al. 2015b).

The plot of dissipation rate for all collisions (media-to-liner and media-to-media) is shown in Figure 37a. From this plot, the shear component curve is almost the same as that of the total collision curve. This is another demonstration of the dominance of the shear component in the dissipation rate.

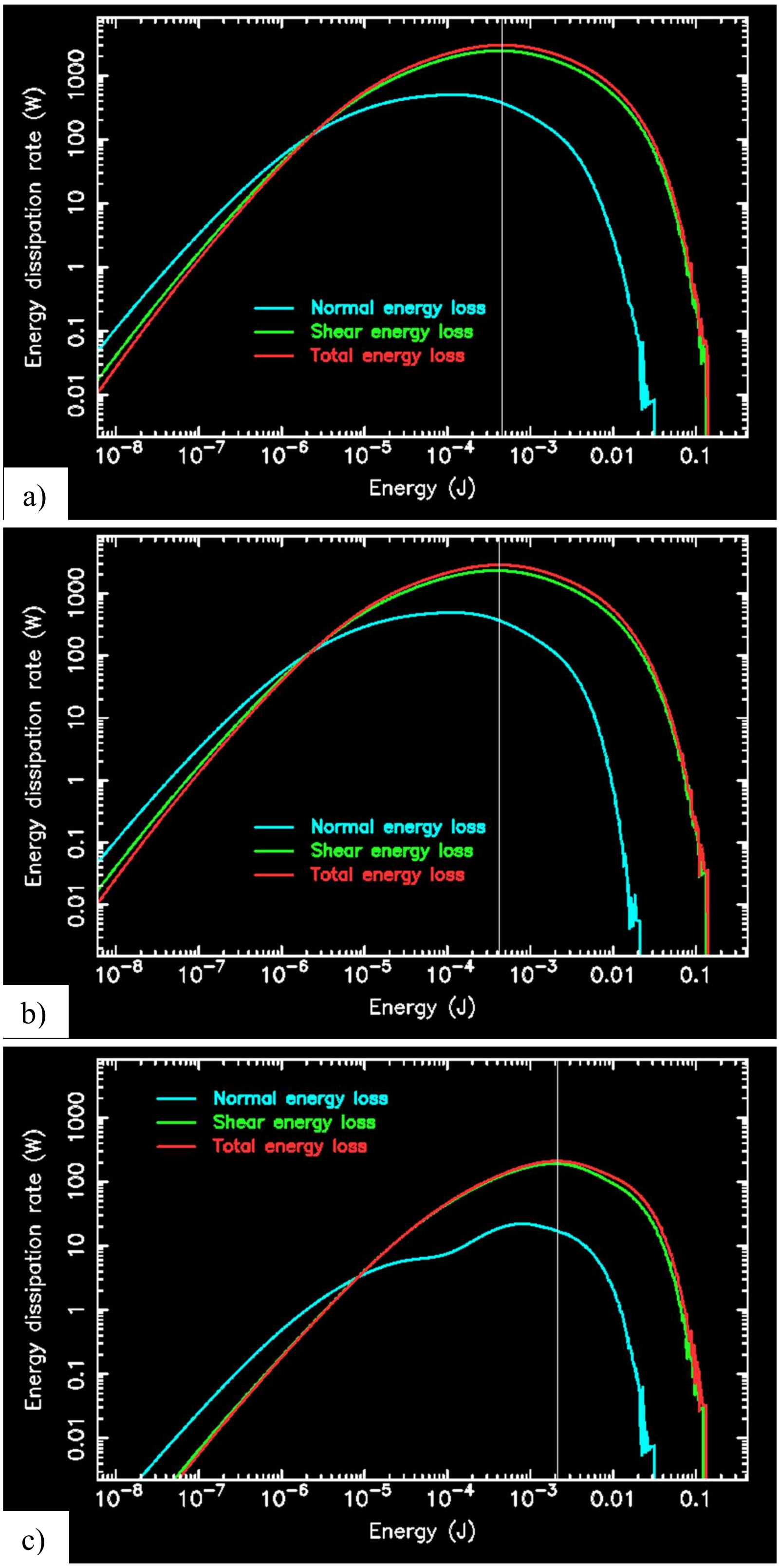

Figure 37: Collision energy spectra for the SMD (dissipation rate) vs collision energy, for a) all collisions, b) media-to-media collisions, and c) media-to-liner collisions (mill shell or impeller). The spectra are shown for normal shear and total energy components. The vertical line shows the modal peak for the total energy distribution (Ndimande et al. 2019).

The normal interactions are dominant for energies below 10^{-6} J which is the low end of the collision energies. The reason for this is that most of the motion in the mill is swirl which leaves little opportunity for significant normal interactions.

It is useful to characterise the spectra using the peak of the distribution. The modal peak of dissipation rate for all collisions occurs at 4.5 x 10^{-4} J, while that of the shear and normal components occurs at 4.1 x 10^{-4} J and 1.1 x 10^{-4} J respectively. Figure 37b and Figure 37c show, the sub spectra of the media-to-media and media-to-liner collisions respectively. Furthermore, we can observe that the media-to-media is very similar in shape to the overall spectra (Figure 37a). This shows that the grinding environment is dominated by media-to-media collisions. The shear component of the media-to-liner spectra has a form like that of the media-to-media spectra.

These only differ in the location of their modal dissipation peaks, with that of the media-to-liner spectra being higher than that of the media-to-media. The normal component of the media-to-liner collisions differ from the rest of the curves in that it has two inflection points. The peak energy dissipation rates for media-to-media and media-to-liner collisions occur at 4.2 x 10^{-4} J and 2.1 x 10^{-3} J respectively. More energy is dissipated in media-to-media collisions than media-to-liner collisions. This shows that more energy is consumed in media-to-media collisions than the media-to-liner ones (Ndimande et al. 2019). Sinnott et al. (2006a) in their study of a pilot scale tower and pin mill reported the same observation. Stirred media mills are typically designed such that the dominant grinding mechanism is the same at all scales (Cleary and Owen, 2016). On this basis the peak location for all collision types for the pilot scale tower and pin mill are compared to that of the SMD 1100-E in Table 13.

Table 13: Modal peak values in terms of energy dissipation rate (W) for media-to-media and media-to-geometry collisions. (Adapted from Sinnott et al. 2006 & Ndimande et al. 2019)

		Media to media energy μJ			Media to mill energy μJ		
	Mill scale	Normal	Shear	Total	Normal	Shear	Total
SMD	Industrial	113	380	423	793	1970	2148
Tower mill	pilot	30	150	150	40	300	300
Pin mill	pilot	60	300	300	100	600	600

It is observed that the peak locations of the shear component and the total energy occur at equal energies for the tower and pin mill, while for the SMD they are similar. This shows that in these devices, shear energy is dominant, meaning that abrasion is the dominant breakage mechanism in these devices.

The media-to-liner energy loss can be further broken down to the two components which are the shell and the impeller. A plot of the spectra for these is shown in Figure 38. It has been observed that both the shear and total energies peak at the same energies while that of the normal component occurs at significantly lower energies. This demonstrates that the shear interactions have a larger contribution to the energy absorbed by both the shell and the impeller than the normal collisions.

The normal contacts are dominant for the media to shell spectra at energies below $3 \text{ X } 10^{-6}$ J, while for the media-to-impeller spectra below $2 \text{ X } 10^{-6}$ J. This indicates that the impeller absorbs more energy from the normal contacts than does the shell. The energy absorbed by the shell and the impeller causes wear on the surfaces. The information provided by the energy spectra is important for wear prediction. The ability to predict wear on mill surfaces will help with determining how worn surfaces affect charge motion and structure and how the collision environment is affected.

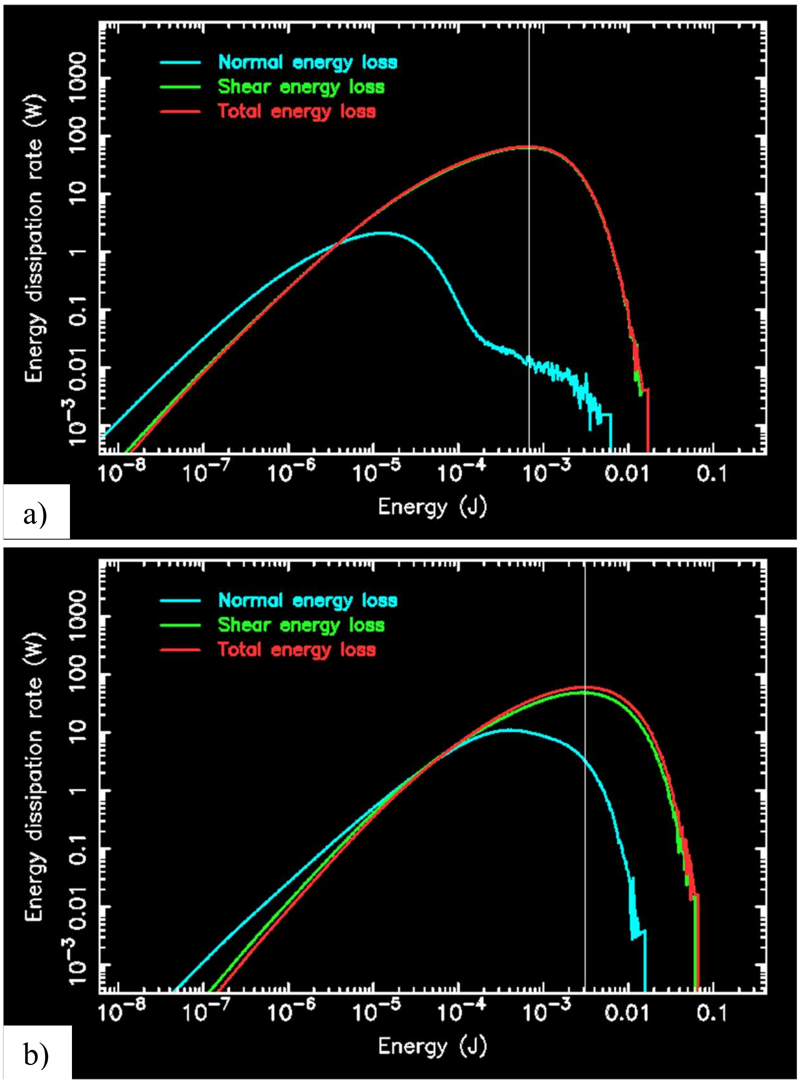

Figure 38: Collision energy spectra showing the distribution of energy absorbed by, a) the mill shell, and b) the impeller. The spectra are shown for normal, shear and total components, with the vertical line indicating the position of the modal peak for the total energy (Ndimande et al. 2019).

5 SMD 355-E

In this section, an analysis of the charge structure, media velocity profile, energy utilisation, mixing and wear in an industrial scale SMD 355-E model is presented. From this study a comparison of different impeller configurations for this SMD 355-E will be presented in the next chapter. The impeller configuration presented here will be termed the base case impeller as it will be compared to three other designs.

5.1 SMD 355-E equilibrium flow structure

The equilibrium flow structure for the SMD 355-E with the impeller configuration shown in Figure 39 (a) and (b) was studied. The simulations were performed with the impeller rotating at a tip speed of 12.31 m/s. This rotational action creates a strong radial centrifugal force field that drives the charge (both media and slurry) out towards the mill shell. This action fluidises the media and creates a vortex with the impeller at its centre. Figure 39 shows the steady state charge structure at t = 12.8 s. The mill is viewed from above looking obliquely downward, with the mill shell made transparent. The vortex is funnel-shaped with a large diameter at the top which decreases with depth towards the base of the mill. At the upper surface of the vortex are undulations originating at each corner of the mill. These occur when the charge is redirected by the corner of the shell.

The steady state charge structure with the media coloured by speed and the slurry, coloured white is shown in Figure 39a. The charge with the highest velocity of 10 m/s is located at the tip of the impeller arms. Just above the top set of arms on the inside of the vortex the media has a speed of about 2.5 m/s. At the bottom of the vortex, beneath the impeller, the charge is nearly stationary. The charge in contact with the leading surface of the bottom set of arms extends along the arms towards the shaft. The media compressed by the centrifugal action of the impeller has tortuous channels in which the fluid flows. When these channels are filled, the remaining fluid flows on the surface of the vortex.

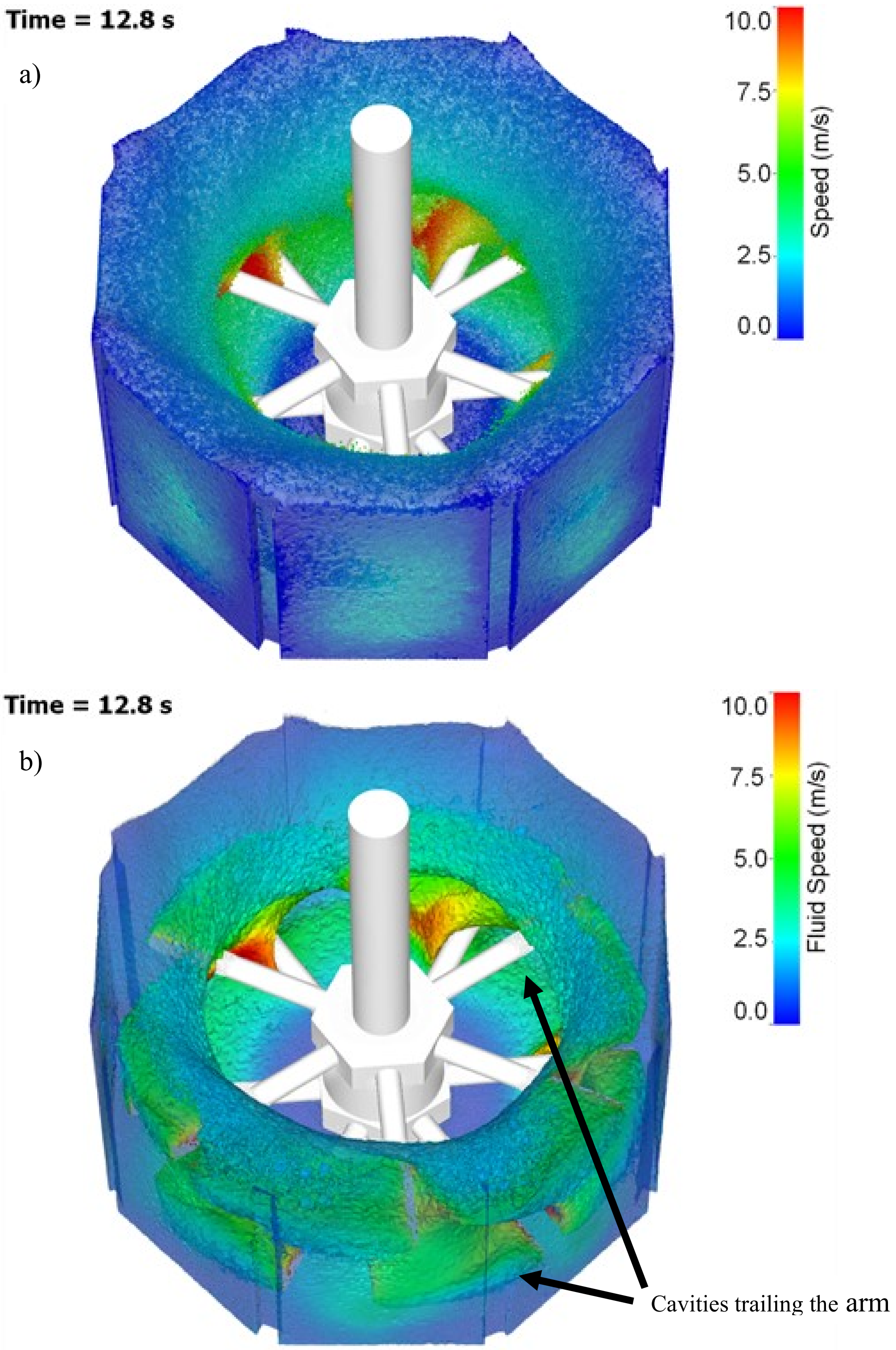

Figure 39: A top-down view of the flow in a SMD 355-E at steady state with the shell made transparent showing a) Coupled flow with media coloured by speed while the fluid is coloured white, b) slurry flow in the SMD 355-E with the slurry coloured by its speed and the media made transparent. The arrows show the location of the cavities produced by the rotating arms.

Figure 39b shows the slurry coloured by speed with the media transparent, making the internal structure of the slurry phase visible. From the inside of the vortex at the lower set of arms, the trailing surface is not in contact with the charge. In other words, there is a cavity trailing each arm. The cavities in the charge produced by the impeller arms are more visible when the media is made transparent. Looking through the side of the mill, they are seen as structure. These azimuthal cavities in the charge are generated by the rotational action of the arms as they pass through the charge. The arms displace charge and force material to flow around these obstacles generating extended trailing cavities. These are small in vertical dimension, extending radially from the inside of the vortex to the ends of the arms and narrow with distance behind each generating arm. The azimuthal length of the cavities is controlled by the rotational speed of the impeller. What this means is that for a given rotational speed, there is a limit to the number of arms that can be put in each row. Having too many arms would mean some will not be in contact with the charge, hence they will not contribute to the transfer of energy to the charge. Horizontal sections of the mill at the impeller arm levels were used to study the charge structure and velocity profile around the impeller arms. Figure 40 shows the speed of the charge (media and slurry) around the arms of each row in a horizontal plane, viewed from the top looking down.

This view shows that each arm pushes a portion of the charge as it rotates. Generally, the distribution of the charge is such that the opposite pair of arms are essentially identical. Figure 40a shows the media coloured by speed while the slurry is made transparent, and in Figure 40b the slurry is coloured by speed with the media made white, at the top row. The fast-moving media and slurry (coloured red) is in direct contact with the arms. The fragmented free surface media (Figure 40a) and slurry (Figure 40b) just in advance of the arms, is falling in the direction perpendicular to the paper. This occurs when the top arms meet upward flowing material pushed by the preceding one in the bottom row. The top arms force a part of the upward flowing charge downwards.

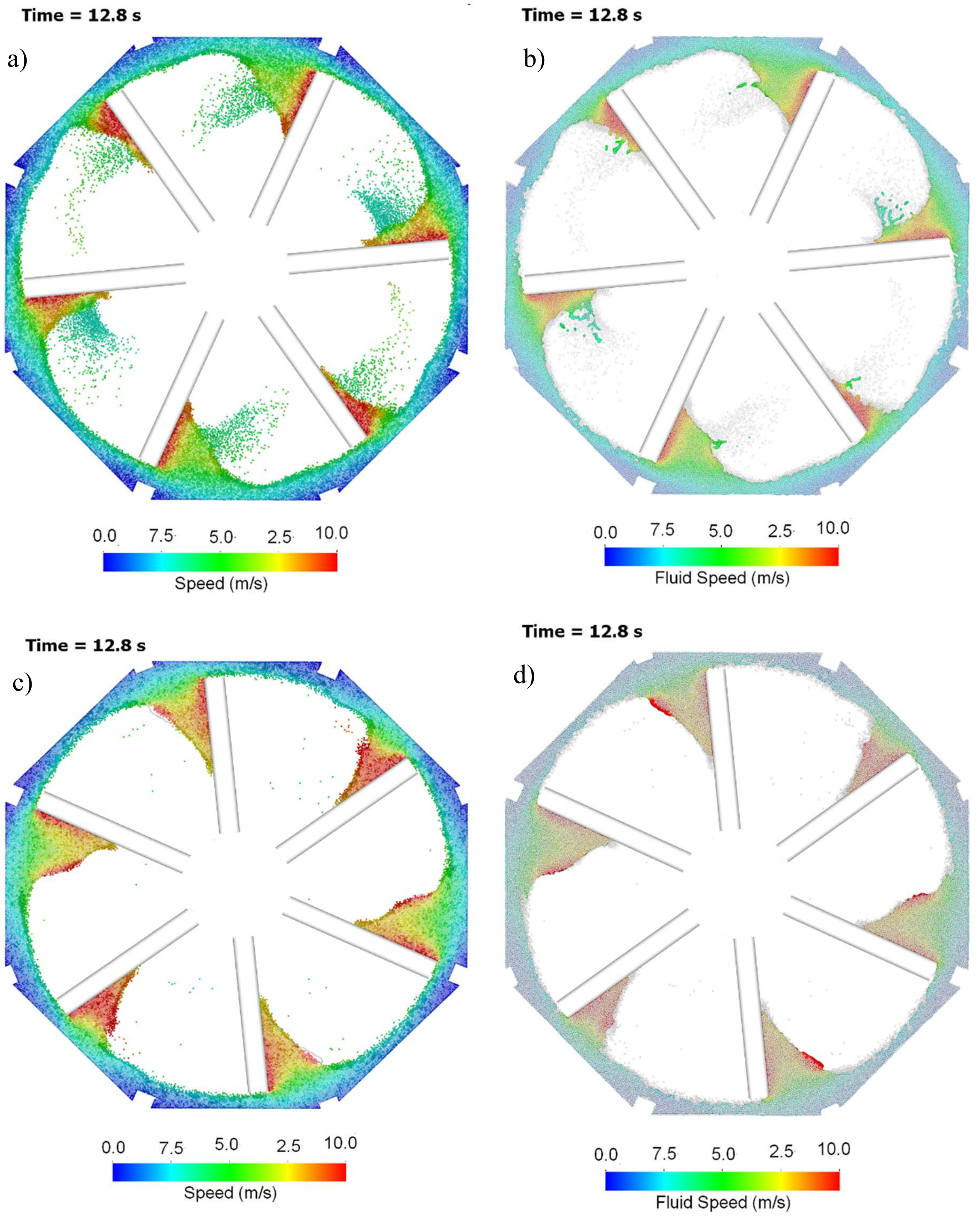

Figure 40: A narrow horizontal slice through the mill showing the steady state distribution of the charge on each of the impeller arms. With a) media coloured by speed and slurry made transparent for the top row of arms and b) the slurry coloured by speed and media made white for the top row of arms, c) media coloured by speed and the slurry made transparent for the bottom row of arms and d) the slurry coloured by speed and media made white for the bottom row of arms.

Figure 40c and Figure 40d show a similar view of the charge for the bottom row. The media (Figure 40c) and slurry (Figure 40d) with the highest speed (red) is in direct contact with the arm and at the free surface. The slurry in the interstices of the media does not move independently. The pair of arms pushing the largest amount of charge (Figure 40d), has a slurry pool like structure in advance of the media (which is coloured white). This occurs due to the compression of the media pushed by the arms. This reduces the voids between the media and forces some slurry out of the network of channels. This figure shows more clearly that the trailing section of each arm is not in contact with the charge. This again suggests a limit to the number of arms that can be put in each row. The more abundant the arms in a row, the less contribution they will have to comminution in the device.

5.2 Average media distribution for the base case impeller configuration

The motion of both the DEM and SPH particles is averaged, both locally in space and temporally on a cylindrical grid that is co-rotating with the impeller. This allows for the study of the overall charge structure produced by the base case impeller configuration. Five heights were chosen in the SMD to assess the media and slurry volume fraction and velocity profiles. The selected heights in the mill are 33mm, 250 mm, 450 mm, 650 mm and finally 850 mm. Taking the volume fraction measurements at these locations ensures that the general dimensions of the vortex are captured and that the cavities in the charge produced by the arms do not affect the characterisation.

Figure 41 shows a snapshot of the steady state average media volume fraction in the SMD 355-E. The impeller configuration of the SMD 355-E produces a similar symmetric charge structure to the SMD 1100-E shown in the preceding section. Charge structure of this nature in these devices has been reported by Daraio et al. (2019) in their work that used PEPT to validate DEM modelling of an attritor mill. The charge is funnel shaped with the diameter being greatest at the top of the charge and smallest at the bottom of the charge. As was observed for the SMD 1100-E, the impeller arms divide the charge into three zones. One zone beneath the bottom arms, one between the bottom and the top arms and another above the top set of arms. The magenta lines in Figure 41 show the heights where the volume fraction is sampled. The volume fraction of both the media and the slurry at the sampled points are shown in Figure 42.

The general trend at all heights except h = 33 mm, for both media and slurry is that the volume fraction increases with increasing distance from the centre of the mill. This is expected because of the rotation of the arms that push the charge towards the centre of the mill. This results in the charge becoming more compact.

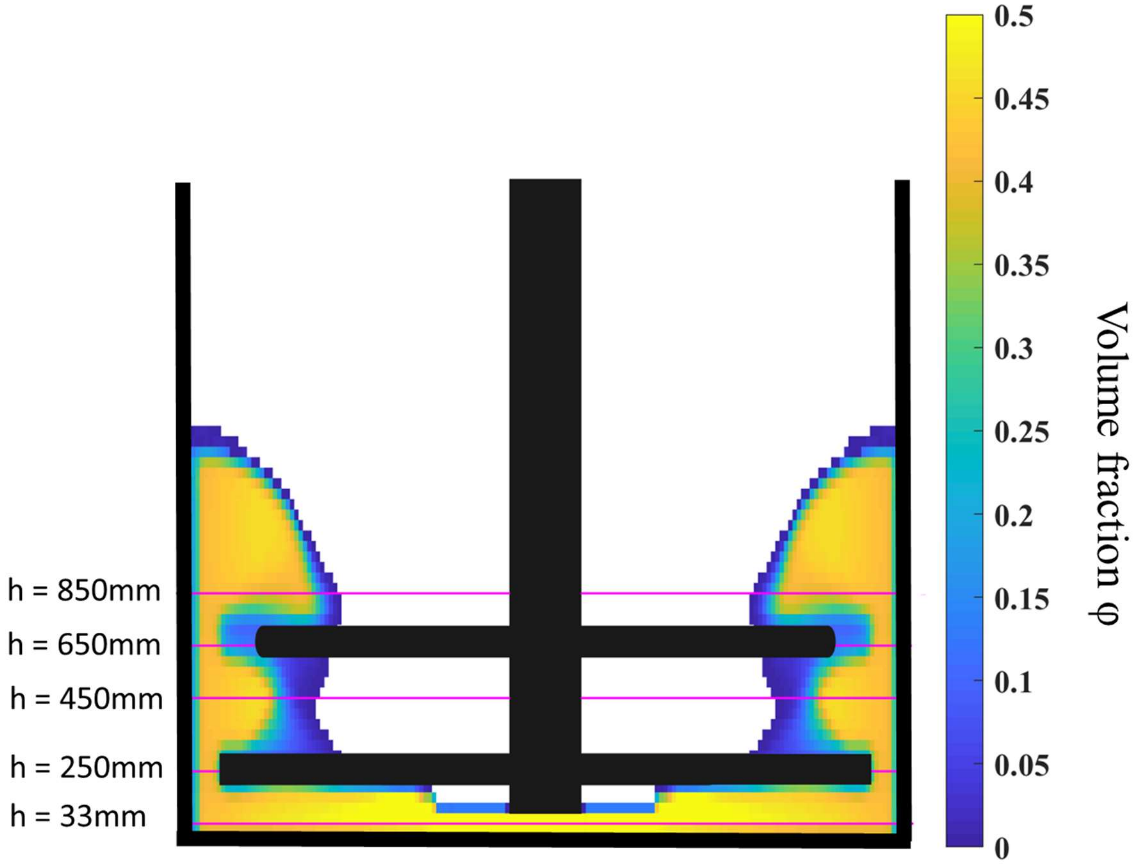

Figure 41: A vertical section through the SMD 355-E showing the steady state distribution of average solid fraction. The magenta lines show the vertical height (h) at which the solid fraction was assessed.

The region below the impeller (h = 33 mm) has a high media volume fraction, slightly below 0.6 at the mill centre which decreases radially towards the mill wall to 0.42. This is attributed to the rotating action of the lower set of arms. They drive some of the charge below the tip of the arms upwards and some flows along the arm towards the centre of the mill (See also Figure 39). From these volume fraction plots, the position of the slurry relative to the media can be inferred. For better media utilisation, the slurry volume fraction must be high in areas where the media volume fraction is also high. The plots show the slurry volume fraction is high in regions where the volume fraction of the media is high.

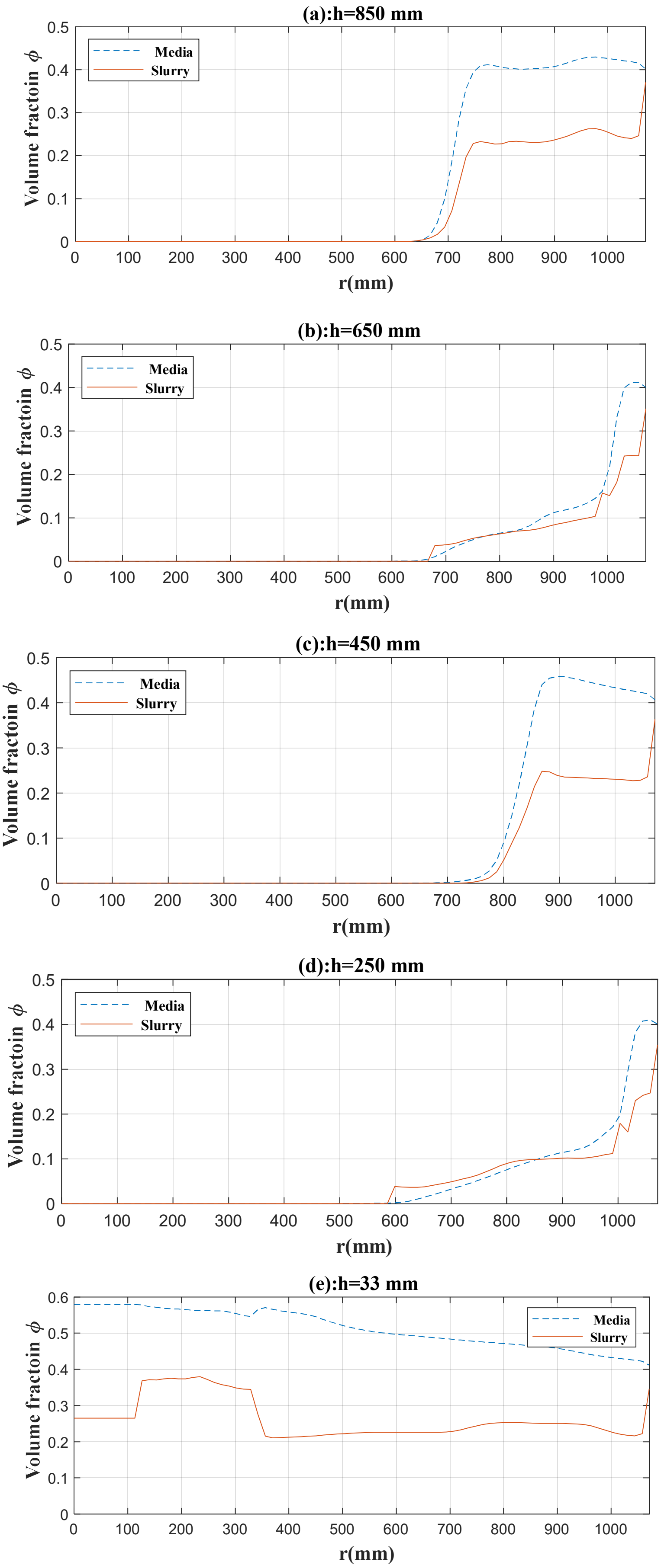

Figure 42: Media and slurry volume fraction profile at different heights in the mill.

The volume fraction profile at the level of the impeller arms is studied at three radii to observe how it changes angularly around the mill. Figure 43 shows the azimuthal change in volume fraction around the mill at the levels of the impeller arms. Figure 43a illustrates the volume fraction at the top set of impeller arms, at radii 850 mm, 936 mm and 1022 mm from the centre of the mill. Figure 43b shows the volume fraction at the bottom set of impeller arms, at radii 724 mm, 873 mm, and 1022 mm from the centre of the mill. For the lower set of arms, the radii are closer to the centre of the mill because of the funnel shape of the charge close to the bottom of the mill. For both impeller arm levels, the volume fraction has a periodic behaviour at all the sampled radii as shown in Figure 43. The peak volume fraction occurs near/at the positions of the impeller. The magenta lines mark the location of the centre of the arms. This pattern of the volume fraction arises because the arms push approximately the same amount charge. This is because of the way the arms are arranged which will be further studied in section 6 of this thesis.

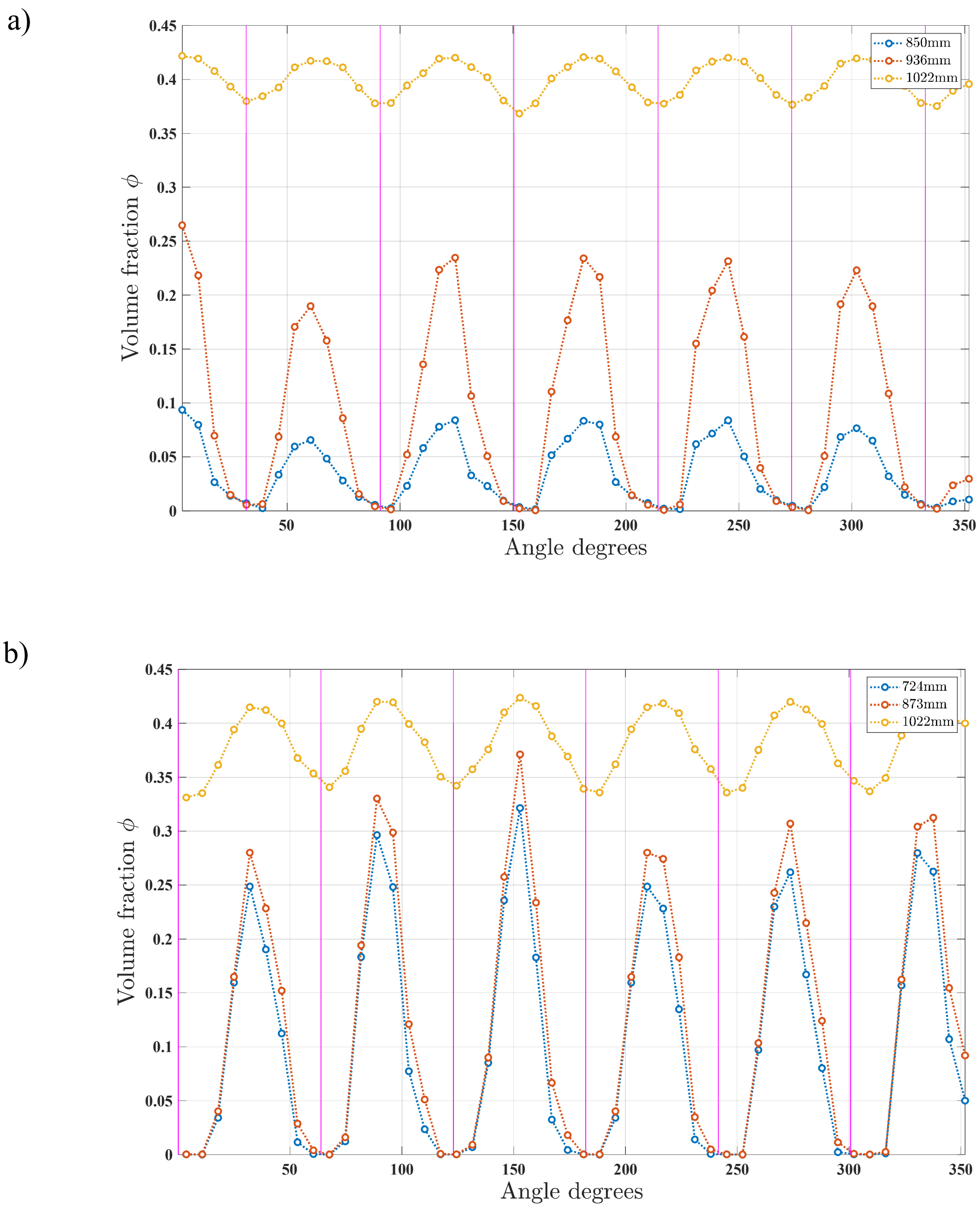

Figure 43: Volume fraction as a function of angle around the mill at different radii for, a) the level of the top set of arms, b) the level of the bottom set of arms. The magenta lines show the angular position of the arms.

5.3 Velocity distribution in the SMD 355-E

The velocity distribution of the charge in stirred mills is important because it has implications on the grinding process. The averaged distribution of the radial, axial and tangential components of the velocity are examined for both the media and the slurry. These are studied at the heights shown in Figure 41. Figure 44 depicts the radial velocity of both the media and the slurry. The blue lines represent the radial velocity distribution of the media while the orange shows that of the slurry.

Due to the rotational action of the impeller arms, Charge will have a radial velocity in the direction towards the mill shell. The negative sign signifies movement towards the mill centre. At h = 650 mm, 450 mm, and 250 mm the slurry and the media both move towards the mill shell as they have positive radial velocities. The radial velocity decreases to zero at the mill wall. At h =33 mm, which is at the bottom of the mill, the media and the slurry generally have the same radial velocity except near the centre of the mill. Close to the mill centre the media has zero radial velocity while the slurry radial velocity toward the mill centre increases to a maximum of 0.5 m/s before decreasing to zero again. Both the media and slurry then have a maximum radial velocity of 0.4 m/s toward the mill shell at r = 850 mm, before dropping to zero at the mill wall. The maximum radius towards the wall occurs in the region where the tips of the impellers are located. Above the top set of arms (h = 850 mm), at the boundary between the vortex and the fluid/solid phase, both the media and slurry move towards the mill centre. In this zone material is recirculated back into the mill.

The averaged axial component of the velocity of the media and slurry is shown in Figure 45. The negative velocities represent downward movement of the charge. Generally, at all levels except h = 33 mm the slurry moves independently of the media at the boundary between the vortex and the fluid/solid phase. This is because the volume fraction of the media decreases with distance from the mill wall. When the media volume fraction is low, its influence on the motion of the slurry decreases. Positive axial velocities occur closer to the mill wall at all sampled heights except h = 250 mm and h = 33 mm. This demonstrates that the charge is moving upwards. With distance from the mill wall negative velocities occur signifying downward motion of the charge. At h = 250 mm and h = 33 mm the axial velocities are negative near the mill and become positive with distance from the mill wall. This is due to the action of the arms in the bottom row which force the charge at their level (h = 250 mm) and in the region below them (h = 33 mm) downwards from the radial position of the tip of the arms to the mill wall.

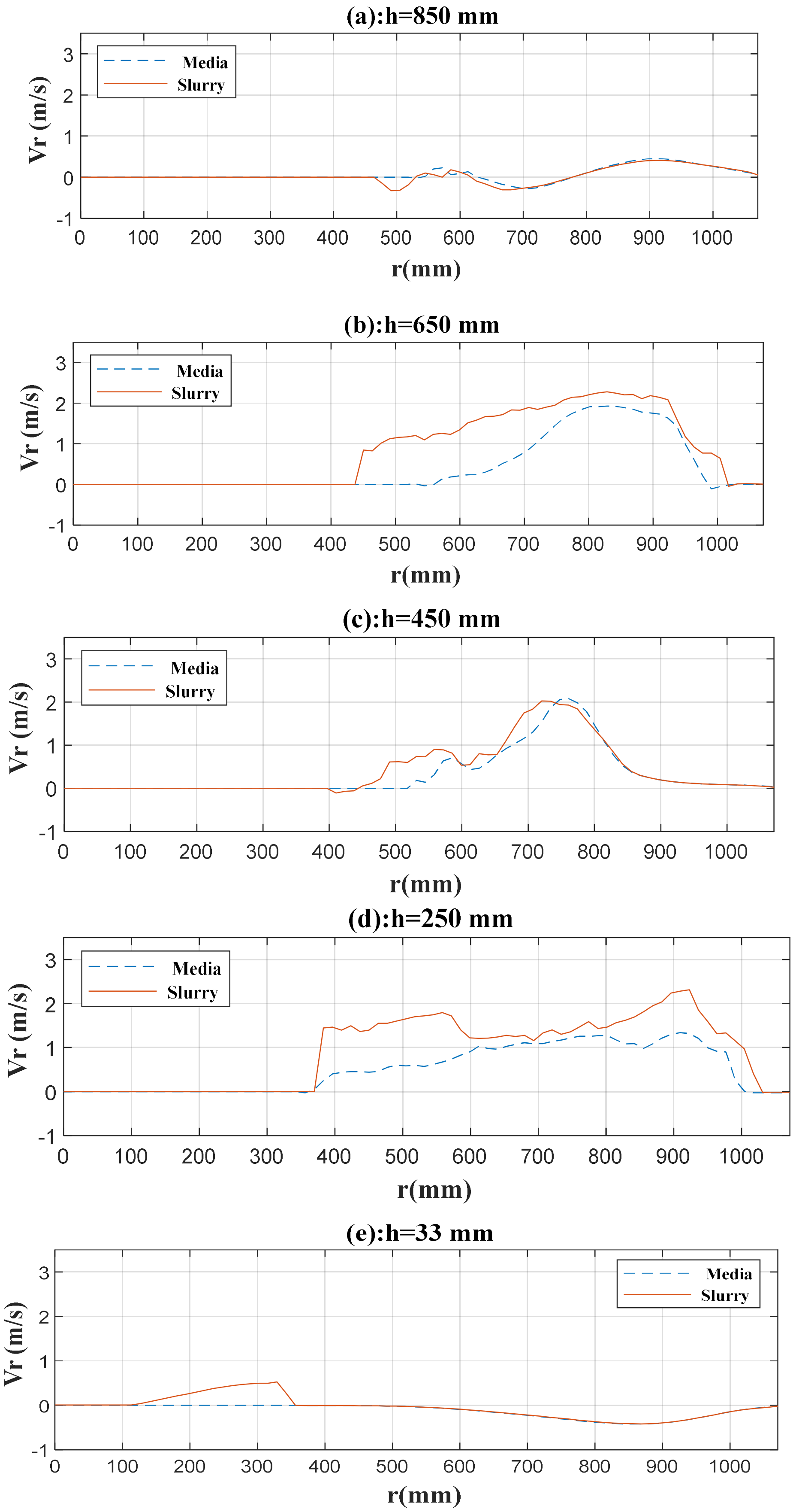

Figure 44: Averaged radial velocity distributions of the media and slurry at sampled heights in the mill. Negative velocities indicated motion towards the centre of the mill.

The tangential velocity (swirl) at different vertical locations in the mill for both media and slurry is shown in Figure 46. Generally, the peak tangential velocity is higher than the peak axial and radial velocities, meaning that most of the motion in the mill is swirl. At all sampled levels there is a general increase in the tangential velocity with distance from the centre of the mill. The tangential velocity of the media and the slurry are similar in regions where the volume fraction of the media is high. Since the volume fraction of the media increases with increasing distance from the centre of the mill, similarity of the tangential velocity of the media and the slurry increases with distance from the centre of the mill. The profiles of the different components of velocity show that there are velocity gradients in the SMD. These gradients create a shear profile which is responsible for the comminution in these devices.

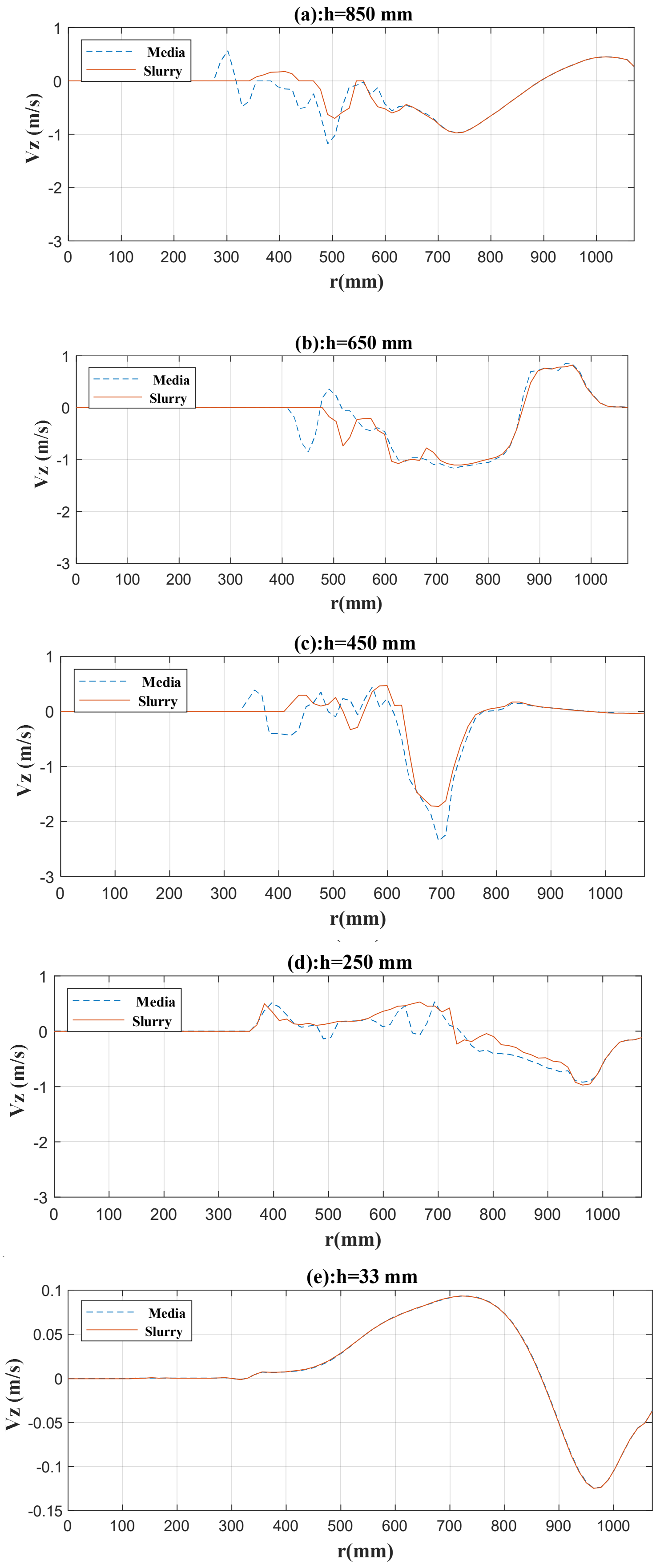

Figure 45: Averaged axial velocity distributions of the media and slurry at the sampled heights in the mill. Negative velocities indicate downward movement.

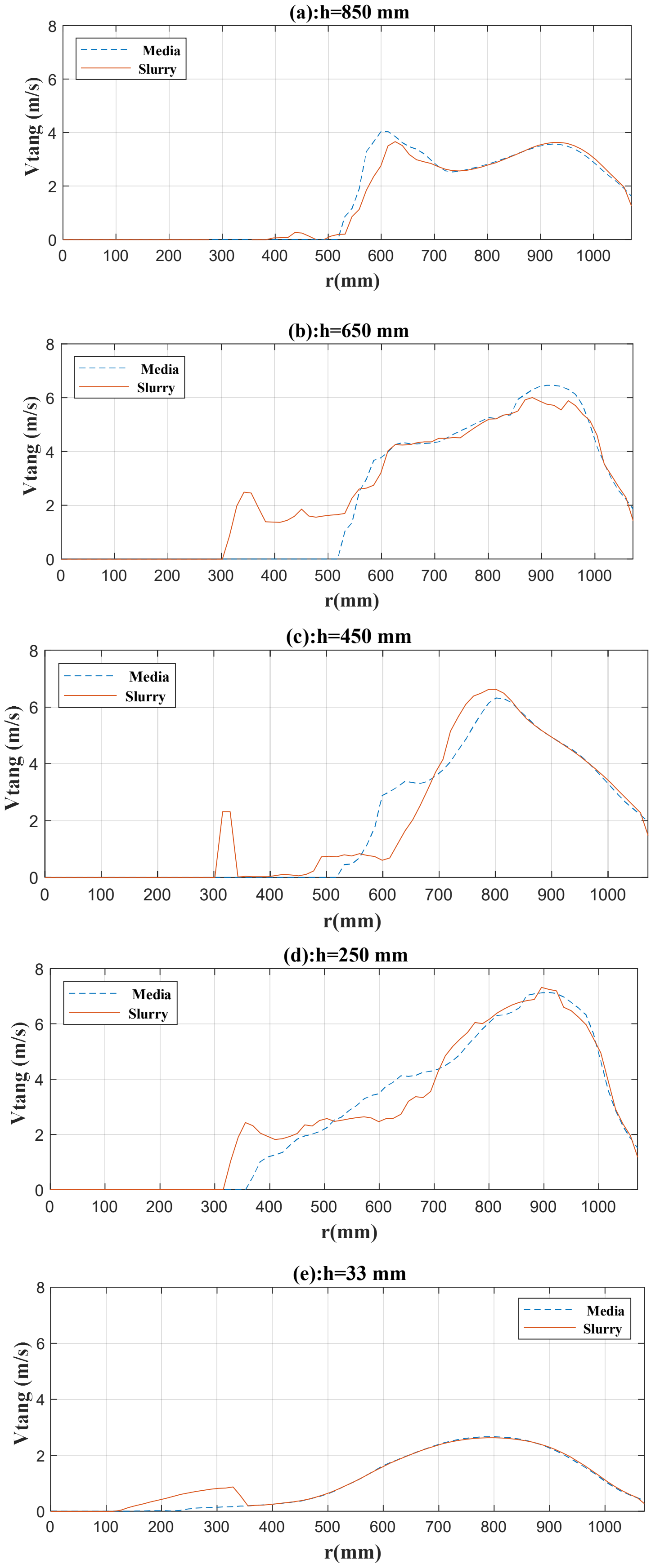

Figure 46: Averaged tangential velocity distributions of the media and slurry at the sampled heights in the mill.

5.4 Mixing and transport

Transport and mixing in the mill are critically important aspects of the comminution process. The two principal directions in which mixing occurs in the SMD are radial and vertical. Mixing in the vertical is the slowest and therefore represents a key limit on grinding performance. It controls the rate at which feed material is transported in and out of the areas of high energy dissipation where grinding occurs. The vertical direction is also critical for transport or movement of product to and from the areas of high energy dissipation and product discharge from the mill. Since the operations being modelled here are batch, focus will be on the transport and mixing of the media. The principal component of transport considered in this work is the vertical direction. The slurry transport in the bulk of the charge is predominantly controlled by the media packing and flow structure (Ndimande et al. 2019). If water addition and slurry removal is included (as in continuous operation) then there is an additional flow component for the slurry superimposed on the basic transport imposed by the media motion. Flow into and discharge from the mill is not expected to influence to a great extent the steady state charge structure of the charge. The rotational action of the impeller provides the force that is chiefly responsible for the charge structure. This has been observed on site during operation.

The rotational action of the impeller and the arms produces a pumping like effect that drives the charge (media and slurry) up from the bottom of the mill chamber. The azimuthal spacing of the arms is a factor that greatly affects the axial movement of material from the bottom of the mill through the layer of impeller arms. In this work, it will be demonstrated that a small azimuthal spacing will result in the charge not passing through the layer of impeller arms. Segregation will occur between the layers of impeller arms which may result in poor discharge of ground material. The bottom row of arms pushes the charge upwards. Some of that charge is pushed back towards the bottom of the mill by the top layer of impeller arms. It is through this up and down motion caused by the arms that gives rise to vertical mixing of the charge. What is also important is the arrangement of the bottom row of arms relative to the top. When viewed from the top down, the arms in the top row must not occupy the same azimuthal position as those in the bottom. The angular distance between arms in the bottom and top row plays a critical role in axial transport and hence mixing in the SMD. A large angle results in less vertical transport of material. This will be shown in section 6.3.

A horizontal slice of the mill just above the bottom set of arms is shown in Figure 47: The figure shows two points A and B both in areas between two bottom impeller arms and opposite each other. The volume occupied by the two areas is used to further study the charge structure.

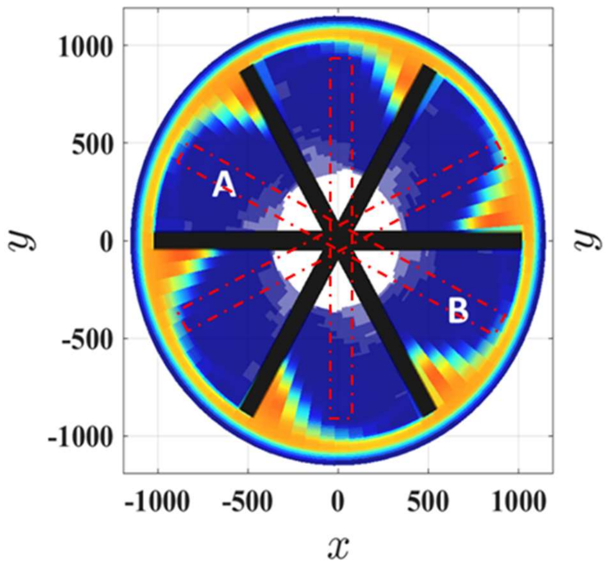

Figure 47: A horizontal section through just above the bottom set of arms showing the two sections of the charge for which the velocity vectors are presented. The position of the top row of arms is shown by the red dotted lines.

The velocity of the charge in the two volumes is averaged and represented in two dimensions. A velocity arrow plot of the media charge in the section marked A (vertical slice) of the charge is shown in Figure 48, the opposite section is depicted in Figure 49. For both figures the top impeller arm precedes the one at the bottom. Generally, the flow field is similar for both slices of the charge, again displaying the symmetry of the charge produced by the impeller configuration in the SMD 355-E.

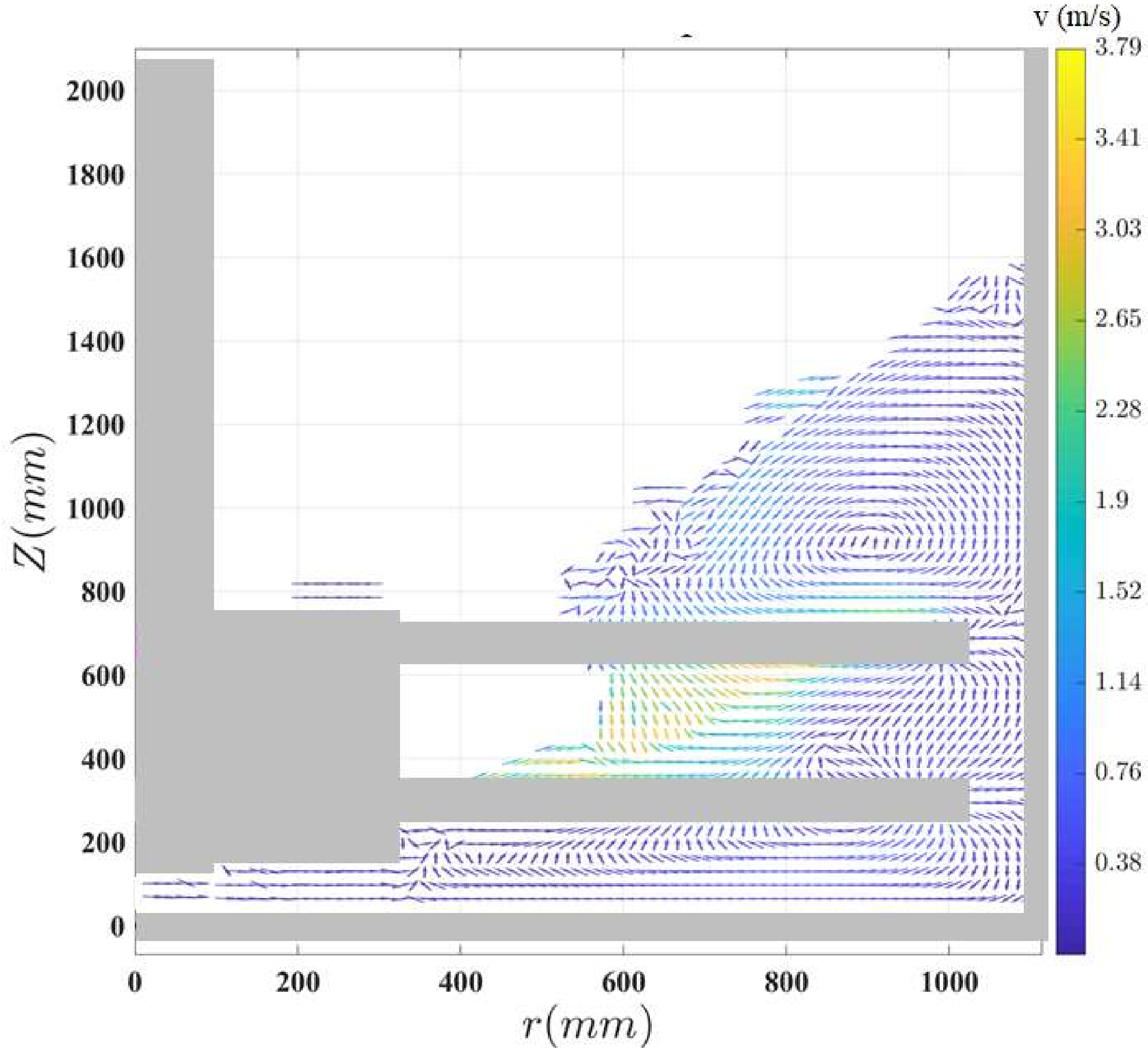

Figure 48: A vertical slice through the mill showing the radial- axial flow field of the charge for a section A of the SMD 355-E

The velocity arrows show the recirculation of the charge above the top set of arms with the centre of circulation visible above the top arms. Between the arms the plot shows that there is material near the free surface of the vortex moving downwards and radially towards the mill wall. Below the bottom set of arms, the charge is moving towards the mill centre and upwards. At the tip of the arm in the bottom row, there is a region where the charge is moving downwards, which was reflected in the axial velocity profile (Figure 45).

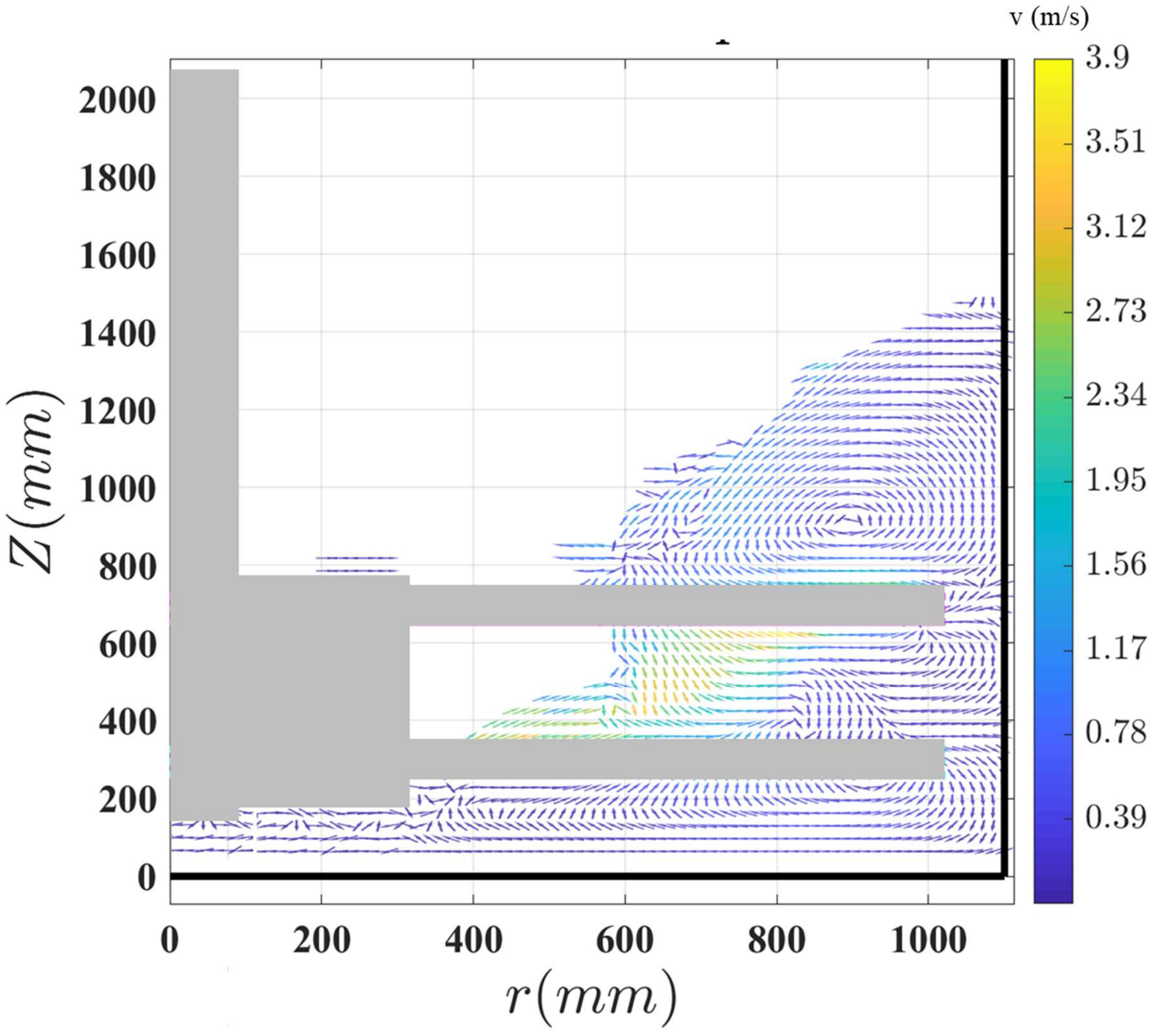

Figure 49: A vertical slice through the mill showing the radial- axial flow field of the charge shown for a section B

To quantify the measure of mixing, Horizontal strata of different colours are used. The progress of mixing can be predicted since the initial vertical position of each colour strata is known. This is a flexible method that measures the degree of local homogeneity of the charge. A cubic cell grid is superimposed over the media bed and local averages of the colours are calculated, using all particles in the region with the centre at each grid point. The averages are then used to determine a mixing state by normalisation relative to the maximal range between fully segregated and fully mixed states. Figure 50 displays the mixing state (labelled as percent mixed) plotted against the number of revolutions. The charge is 90% mixed at about 25 revolutions. From this mixing data we can infer that material can move relatively easily in and out of the grinding zone of the mill. Only material that is beneath the shaft where there is very little vertical transport will not move easy.

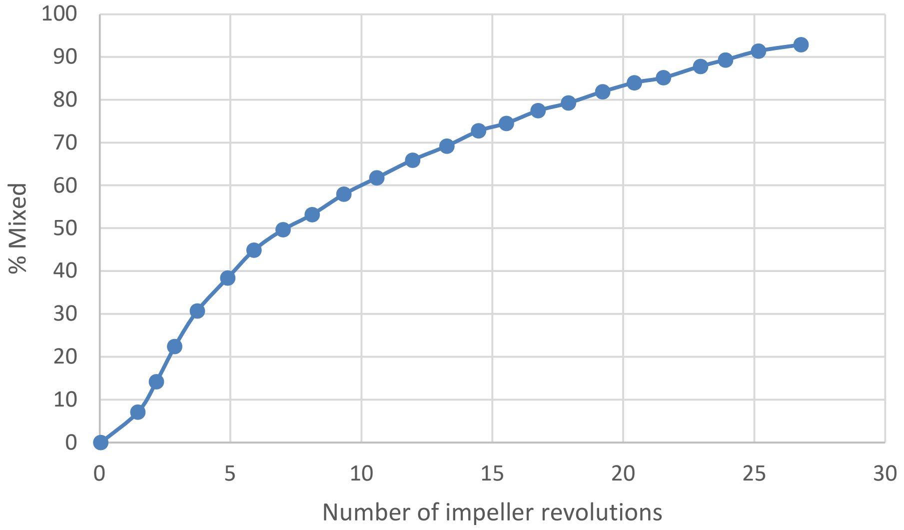

Figure 50: Axial mixing per revolution for the SMD 355-E.

5.5 Energy consumption in the SMD 355-E

The net power drawn by the SMD is given by the product of the rotational rate of the impeller and the net torque produced by the contact forces. For the conditions studied here, the predicted average net power draw for the SMD 355-E is 388.60 kW, of which 74% is dissipated in media collisions (both media-to-media and media-to-mill collisions). Dissipation through viscous stresses in the slurry phase accounts for the remaining 26%.

A summary of the quantitative break down of the DEM energy dissipation is given in Table 14. The energy dissipation of different collision types is expressed as a percentage of power drawn by the mill. Media-to-media and media-to-liner collisions dissipate 68% and 6% of the net power drawn respectively, with the rest of the power dissipated in viscous stresses in the slurry.

Table 14: Energy utilisation by collision type in the SMD; 26% is dissipated in the slurry phase

Collision type	**Total Energy loss % of power draw**	**Shear Energy loss % of power draw**	**Normal Energy loss % of power draw**
Media to media	68	53	15
Media to liner	6	5	1

For the media-to-media collisions the shear component is 3.5 times higher than the normal; so, energy dissipation (and therefore grinding) is strongly dominated by the shear component of the flow. For the media-to-liner collisions, the shear interactions dissipate 5% compared to the 1% of the normal component. This indicates that the wear on the mill surfaces is also dominated by the shear interactions and thus, wear will be predominantly due to abrasion. The ratio of shear to normal dissipation (10.6) is higher for media-to-liner collisions than media-to-media ones (3.5). This is because the motion of the charge is predominantly swirl, resulting in little normal media-to-liner collisions. However, in the swirling charge, there is higher normal media-to-media collisions. The energy absorbed by the mill shell and the impeller as a function of power draw are 2% and 1% respectively. The shell dissipation rates are much lower, but its large area relative to the impeller means it consumes more of the energy.

The spatial distribution of the time averaged shear and normal power dissipated by the media, is shown in Figure 51 . This is calculated by summing the energy dissipation from the normal and shear contacts of the media (both media-to-media and media-to-mill) and averaging this data onto a stationery grid. Both the shear and normal power are high (light blue, yellow, green, and red) bellow the tip of the bottom arms extending radially inwards, close to the wall and between the rows of arms. Shear power (coloured red) is highest below the tip of the bottom row of arms. This region has a sector like shape with a power of 7.5 X 10^4 W/m^3. The most intense comminution by abrasion occurs in this region. To ensure efficient comminution, it is important that transport of feed into and ground product out of this region is not impeded. The shape and size of this region is dependent on the amount of charge in the mill, impeller speed and its vertical location (Ndimande et al. 2019). Directly below the impeller, the shear power is negligible since the shaft is ineffective at agitating the charge in this region.

Between the two rows of arms, the shear power is highest close to the wall (coloured in green corresponding to 5 X 10^4 W/m^3). This decreases rapidly at first with radial distance from the mill wall and is then fairly constant at about 2 X 10^4 W/m^3 out to the free surface. The highest shear power is twice the highest normal power showing the dominance of the shear component. The pattern of normal power dissipation is fairly similar to that of the shear, just weaker in its contribution to energy dissipation.

Isosurfaces of the normal and shear power in the mill as shown in Figure 52 are a useful way to visualise the three-dimensional nature of the energy dissipation. Generally, for both energy components, high levels of energy dissipation occur largely below and in advance (azimuthally) of the tip of the arms. Below the arms the high energy dissipation isosurface extends two thirds of the length of the arm towards the vortex. The high energy dissipation region slightly extends above the top set of arms. The volume enclosed by the isosurfaces defines the grinding zone of the mill. Mostly recirculation of the charge and discharge of the ground material occur above the grinding zone.

The shape of the power dissipation around each arm is quite complex. For the shear component, the highest dissipation region is the volume enclosed by the red surface. This is directly in front of and below the impeller arms and stretching radially inwards towards the vortex. For the top row this region stretches along a third of the length of the arms, while for the bottom row it stretches along two thirds of the arm towards the vortex. This is due to the diameter of the vortex being smaller closer to the bottom of the mill. Surrounding the red isosurfaces is the region of high energy dissipation (volume enclosed by the blue surface). This extends azimuthally from the tip of an arm in the bottom row to the tip of a preceding arm in the top row.

The level of the highest normal dissipation is four times lower than that of the shear component, again indicating the dominance of the shear. The distributions of the isosurfaces differ mildly. The difference is that for the normal component, the high dissipation regions extend azimuthally between arms in each row, while for the shear they do not.

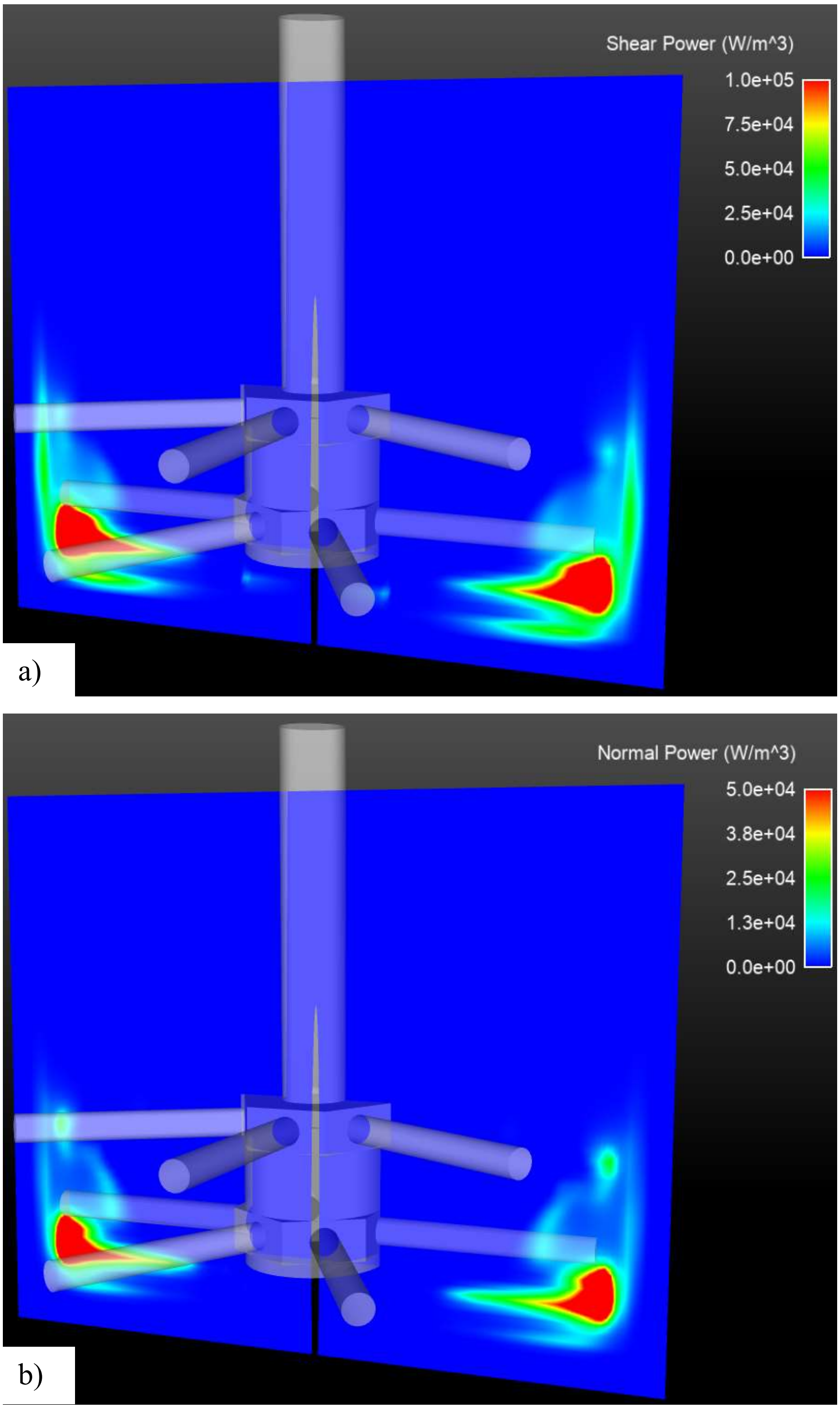

Figure 51: A vertical section through the SMD showing shear and normal power dissipation. a) Shear power dissipation per unit volume and b) normal power dissipation per unit volume. The power is averaged in a frame rotating with the impeller. Red, yellow, and green indicate high power dissipation areas while blue shows negligible energy dissipation.

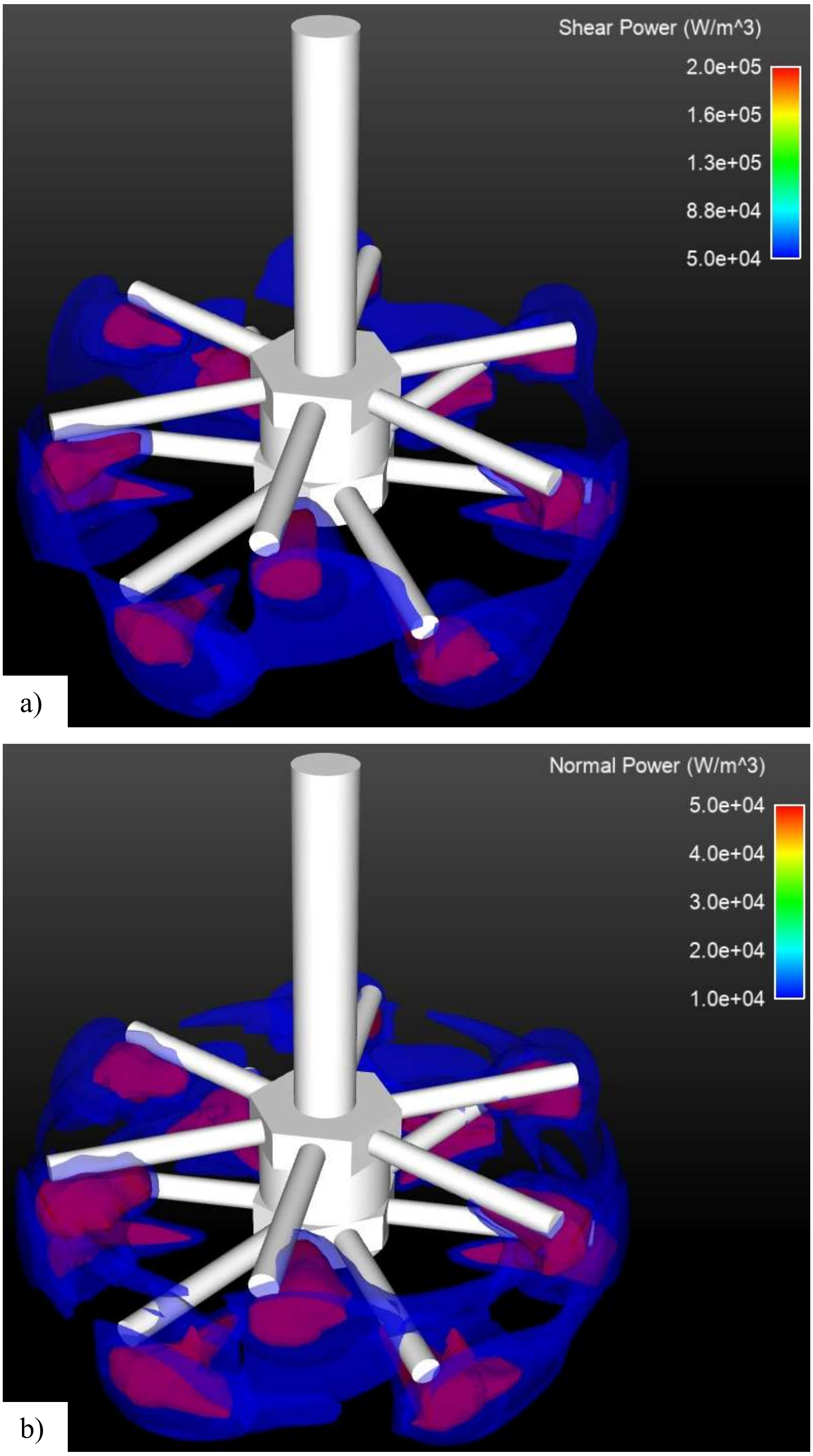

Figure 52: Isosurfaces of the steady state distribution of both the shear and normal power. a) shear power per unit volume and b) normal power per unit volume calculated on a grid that is co-moving with the impeller. The mill shell is omitted in the image for clarity. The high-power dissipation areas (red) occur near the tip of the impeller arms. Intermediate power dissipation areas (blue) occur in advance of the impeller arm tips.

5.6 Collision energy absorption spectra

Collision energy spectra of the SMD 355-E were extracted to assess the grinding environment. Figure 53a, and Figure 53b show the spectra for media-to-media and media-to-liner collisions respectively. These are plotted as dissipation rates against energies on a log-log scale. Each graph has three curves with blue representing the normal, green representing the shear component, and red representing the total energy. All these spectra have similar shapes that can be characterised by a skewed log-normal distribution. For both collision types, the total and shear energy loss curves are almost identical, which is a result of the dominance of the shear component. The peak location of the distributions is a good way of characterizing the spectra as this gives the highest dissipation rate which is the energy available for breakage. For the media-to-media collisions (Figure 53a) the shear and total energy loss curves peak at 0.6 mJ and 0.68 mJ respectively. The associated dissipation rates for the shear and Total energy loss curves are 900 W and 1000 W respectively. These values are the maximum dissipation rates due to shear collisions and the sum of all collisions respectively. This information is often used with fracture energies of the ore treated to model breakage. The normal curves are weighted to lower energy levels and dissipation rates. For the media-to-media collisions the normal component peaks at 0.14 mJ with a dissipation rate of 200 W. This shows that the shear component of the media-to-media collisions dominates, therefore, the prevalent mechanism of breakage is abrasion in the SMD. This is consistent with what has been reported by Radziszewski (2012) on the mechanism of breakage in these devices.

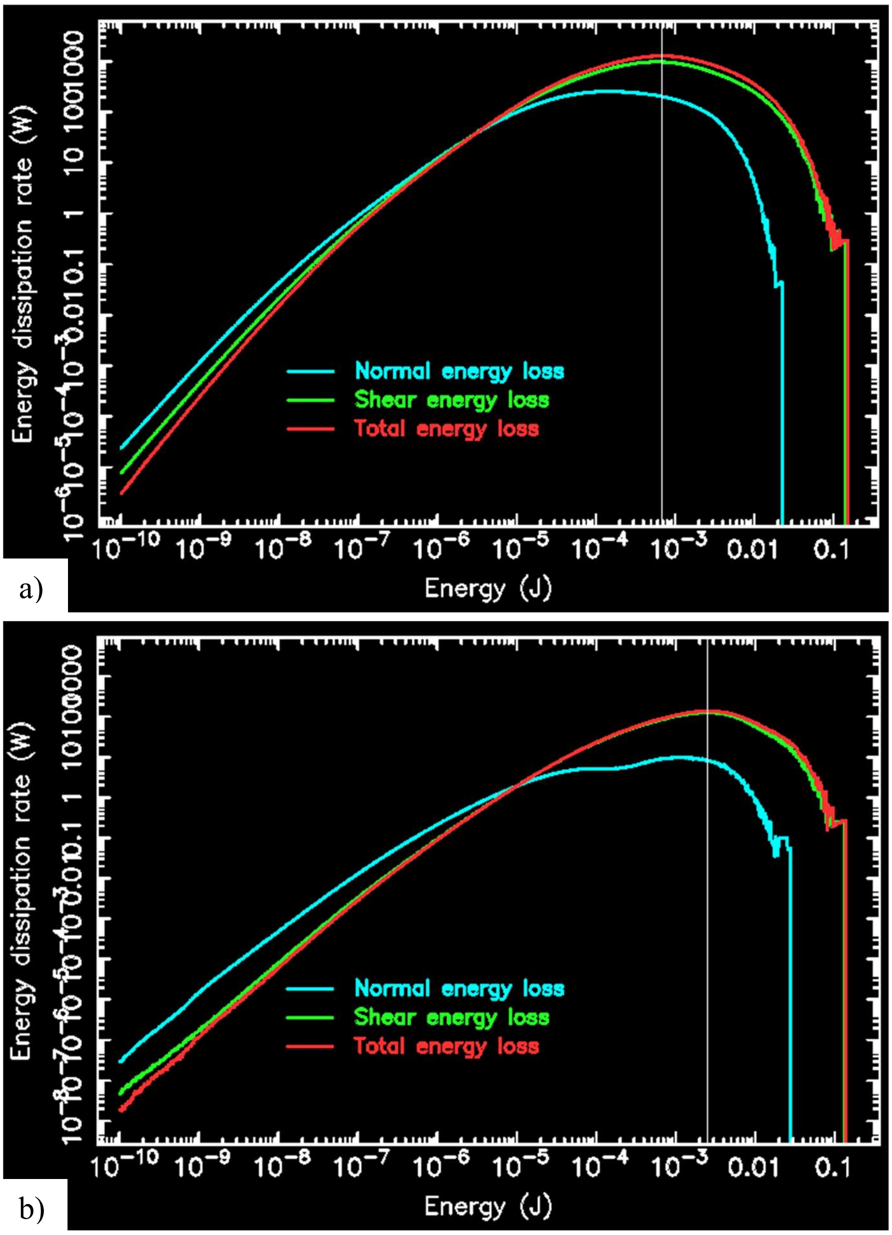

Figure 53: Collision energy spectra for the SMD (dissipation rate) for a) media-to-media collisions, and b) media-to-liner collisions (mill shell or impeller). The spectra are shown for normal shear and total energy components. The vertical line shows the modal average for the total energy dissipated.

For the media-to-liner collisions, the shear energy loss curve peaks at 2.52 mJ with a dissipation rate of 100 W. The normal energy loss curve peaks at 1.07 mJ with a dissipation rate of 5 W. The shear component of the media-to-liner collisions is dominant, therefore, wear on the mill surfaces will be due to abrasion. This is because much of the motion of the charge is swirl with little normal interaction with the mill surfaces. The normal component of the media-to-mill curve is slightly different from the others in that it has two inflection points with an intermediate step, but no dynamical significance can be identified with this. The total media-to-media dissipation rates (1000 W) are 5.3 times higher than those of the media-to-mill (190 W), which indicates that media-to-media collisions contribute more to comminution than media-to-mill ones. The total peak energy dissipation rates for media-to-liner collisions occur at 3.7 times the collision energy level of the media-to-media. This indicates that the media-to-media collisions are more efficient at dissipating energy than media-to-liner ones.

Figure 54 shows the disaggregated spectra for the mill shell and the impeller. The shear and total energy curves are again indistinguishable for both spectra. The peak energy dissipations of the shear and total energy loss curves, for the shell (Figure 16a) occur at 0.94 mJ and 0.96 mJ respectively. The associated dissipation rates for the shear and the total energy loss curves are both 15 W. For the impeller (Figure 16b), the peak dissipation occurs at 3.63 mJ and 4.13 mJ for the shear and total energy loss curves respectively. The relative dissipation rates are 12 W and 13 W for the shear and total energy loss curves. This demonstrates the dominance of the shear component of the media-to-shell interactions in energy dissipation. Wear on the mill surfaces will mostly be abrasion damage. The total energy curves for the mill shell and the impeller peak at 0.96 mJ and 4.13 mJ respectively. The associated dissipation rate for the mill shell is 15 W and that of the impeller is 13 W. The mill shell generally absorbs slightly more energy than the impeller.

The normal spectra have lower peaks at lower collision energies. For the shell the normal energy loss curve peak dissipation occurs at 0.03 mJ and for the impeller at 0.8 mJ. The peak dissipation rate for the shell is 2 W and for the impeller 5 W. These are significantly lower than the shear component showing that the normal impacts are relatively insignificant in energy dissipation and wear. At energies bellow 0.03 mJ for the media-to-mill collision and 1.0 mJ for the media-to-impeller collisions, normal dissipation is dominant.

This occurs at lower energies for the media-to-mill spectra than the media-to-impeller spectra, which indicates that the impeller absorbs more energy due to normal interactions with the media, than the mill shell.

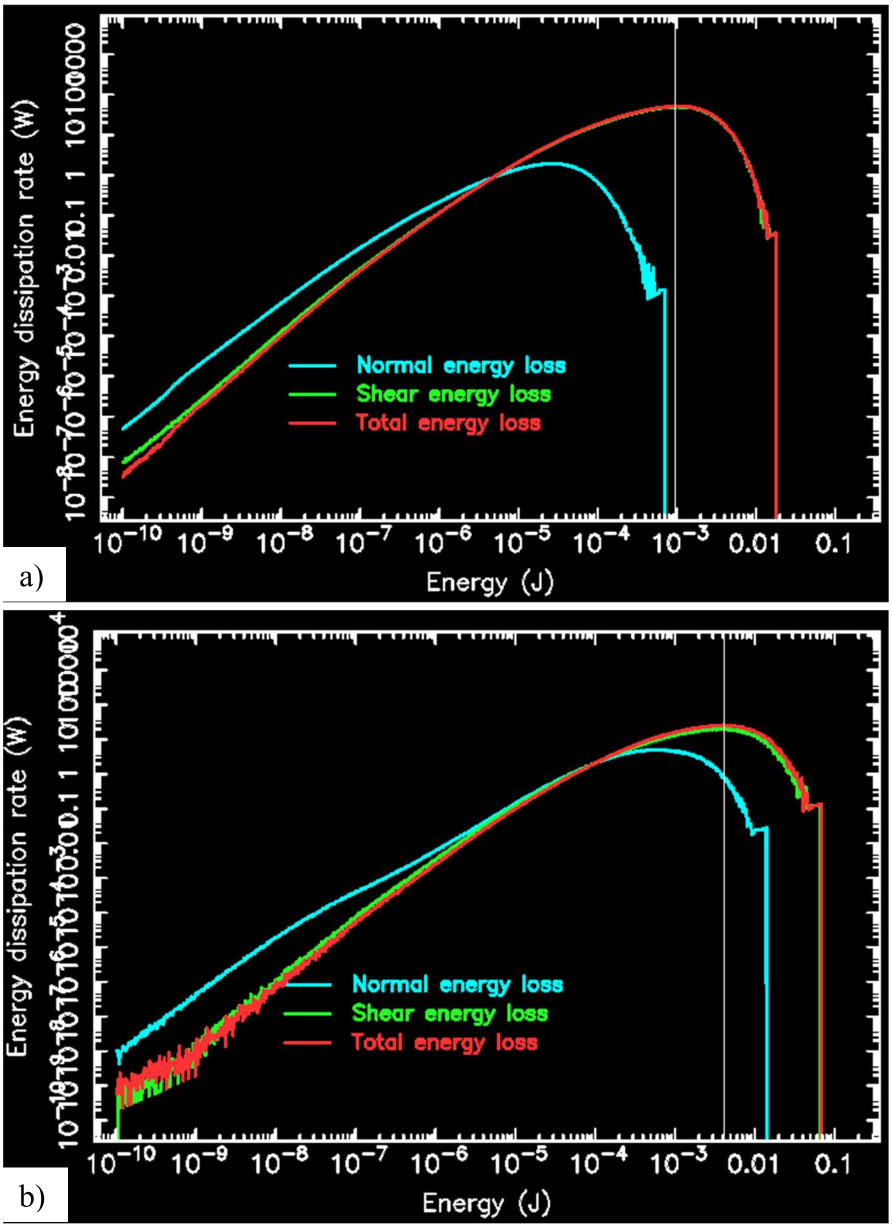

Figure 54: Collision energy spectra showing the distribution of energy absorbed by, a) the mill shell, and b) the impeller. The spectra are shown for normal, shear and total components, with the vertical line indicating the position of the modal peak for the total energy.

5.7 Wear on mill internals SMD 355-E

Wear on the working surfaces of a mill is generally considered to be proportional to the rate at which energy is absorbed by these surfaces (Kalala et al. 2005; Cleary et al. 2006; Powell et al. 2011; Boemer, 2015). Impact damage is usually considered to be controlled by the rate of energy absorption from the normal components of collisions while the abrasive wear is related to the rate of shear energy absorption (Cleary et al. 2006; Cleary et al. 2015). Figure 55 shows the abrasion power absorption distribution for the impeller and mill shell. Only the abrasion power absorption density of the surfaces is shown because energy dissipation in this mill has been shown to be dominated by the shear interactions.

Abrasion is highest (red, yellow and green) on the leading surface of the impeller arms (Figure 55a), which should be expected since this is the primary area of high-speed contact with the charge. Wear decreases with distance from the tips reflecting the radial decrease in the swirling speed of the charge and is zero once beyond the free surface of the vortex. The wear distribution is the same for all arms in each row. The relative size of the high wear area (coloured red, yellow and green) is different for the two rows. The area of high wear extends further radially inward at the bottom row than the top, a result of the vortex having a smaller core diameter lower in the mill. This wear pattern will result in the progressive flattening of the leading surface of the arms. This is consistent to the wear observed by Moore et al (2016) in their tests of the materials used to make the arms on the SMD 355-E. They tested different materials of construction and observed progressive flattening of the leading surfaces of the arms.

The mill shell (Figure 55b) experiences high abrasive wear on the floor, the lower half of the walls and the baffles. The same scale for abrasion wear used for the impeller is used for the shell. On the mill floor, peak wear (coloured light blue) forms a circular pattern with a radius of 1.0 m, which is the radial location of the tip of the arms. The wear decreases radially inwards and outwards.

This is due to the decrease in swirl speed of the charge with distance radially, from the tip of the arms toward both the wall and the vortex. There is no abrasion wear below the shaft because the charge is not mobile in this region. The vertical location of the impeller will affect the wear rate at the bottom of the SMD. Higher wear rates should be expected if the impeller is closer to the mill floor and lower if it is further away. All eight side walls have a similar wear pattern which is broadly ellipsoidal in shape (coloured light green). This is due to the very low speeds of the charge at the vertices of the walls and the baffles. The lower parts of the baffles at each corner experience stronger abrasion as these surfaces protrude into the mill and play a role in the charge changing direction at each of the octagonal wall transitions.

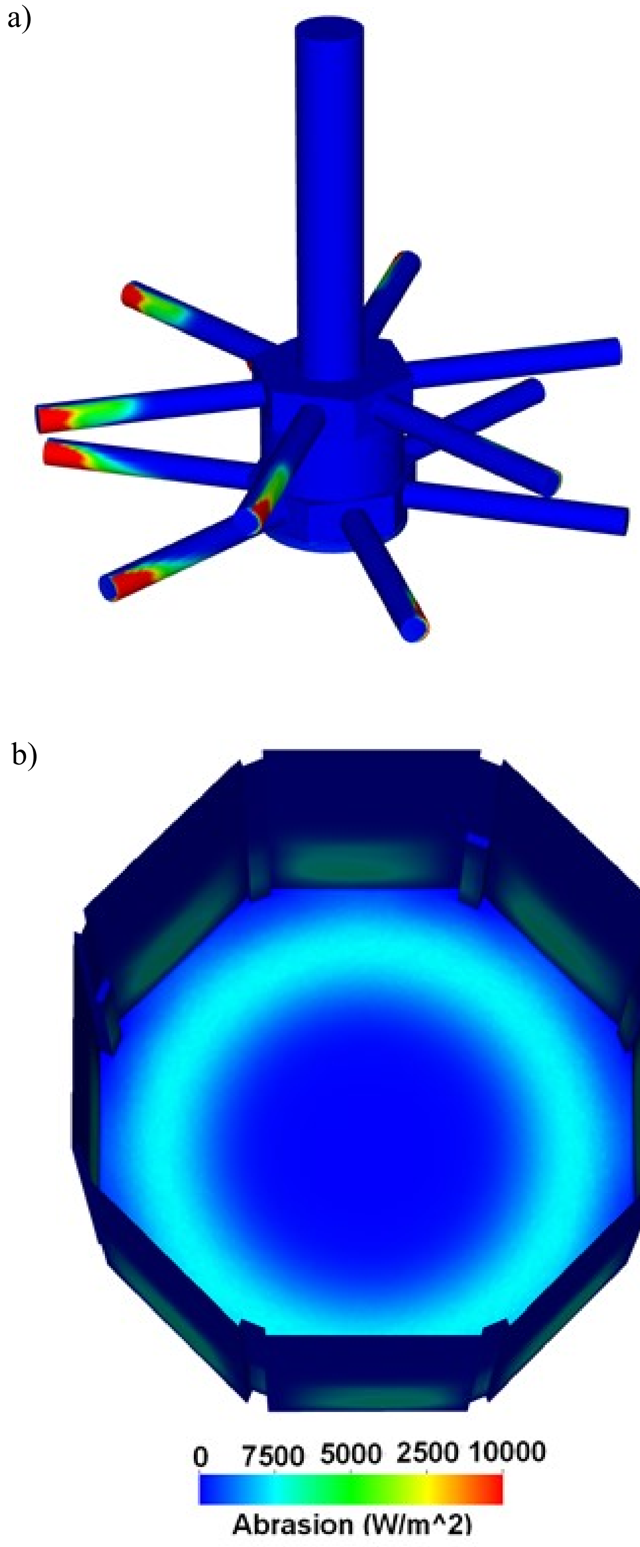

Figure 55: Abrasion wear on the surfaces plotted as rate of shear energy absorption per square metre of a) the impeller and b) the mill shell viewed obliquely from the top down. Highest wear (red) on the impeller occurs at the tip of the arms. Dark blue shows areas where there is little wear.

6 Effect of impeller design on mill performance

In this section the three impeller configurations alluded to in section 3.7 are compared to the commercially available one which is hereafter named the base case. The aspects of mill performance to be studied are the charge structure and flow patterns produced by each configuration, the power drawn by each configuration, energy utilisation and mixing of each configuration.

6.1 Averaged media distribution for different configurations

In this section, an assessment of how the different impeller variants affect charge structure in the SMD, particularly media distribution is presented. As was done for the base case, the transient motions (which are mostly restricted to the free surface regions of the charge) are separated from the underlying steady charge structure and flow. The motion of both the DEM and SPH particles is, therefore, averaged on a cylindrical grid that is co-rotating with the impeller. The resulting average media distribution as indicated by the solid/volume fraction for variants 1, 2 and 3. Variant 1 has two sets of arms, with the upper set having four arms and the lower set having 6 arms. The vertical separation along the shaft, of the two sets of impeller arms is 400 mm as shown in Figure 24. Variant 2 has two sets of four arms on the impeller. The vertical separation of the arm layers is 400 mm. Variant 3 This impeller has two sets of arms. The upper set has six arms while the lower set has four arms. The sets have a vertical separation of 400 mm along the shaft.

These are shown in Figure 56. The volume fraction is collapsed and averaged onto a single vertical plain. The magenta lines show the heights at which the volume fraction is graphically represented in this section. The general vortex shape is like the base case for all variants. Variants 1 and 2 have a slightly different charge shape above the top set of impeller arms. The slope of the charge above the top set of arms is steeper for variant 3 than it is for variants 1 and 2. Gravity and the forces acting on the charge due to the rotational action of the impeller govern the motion of the charge in the SMD. A variant with more arms in the top will push more of the charge towards the mill wall and upwards, resulting in a steep slope of the cone shaped charged above the arms.

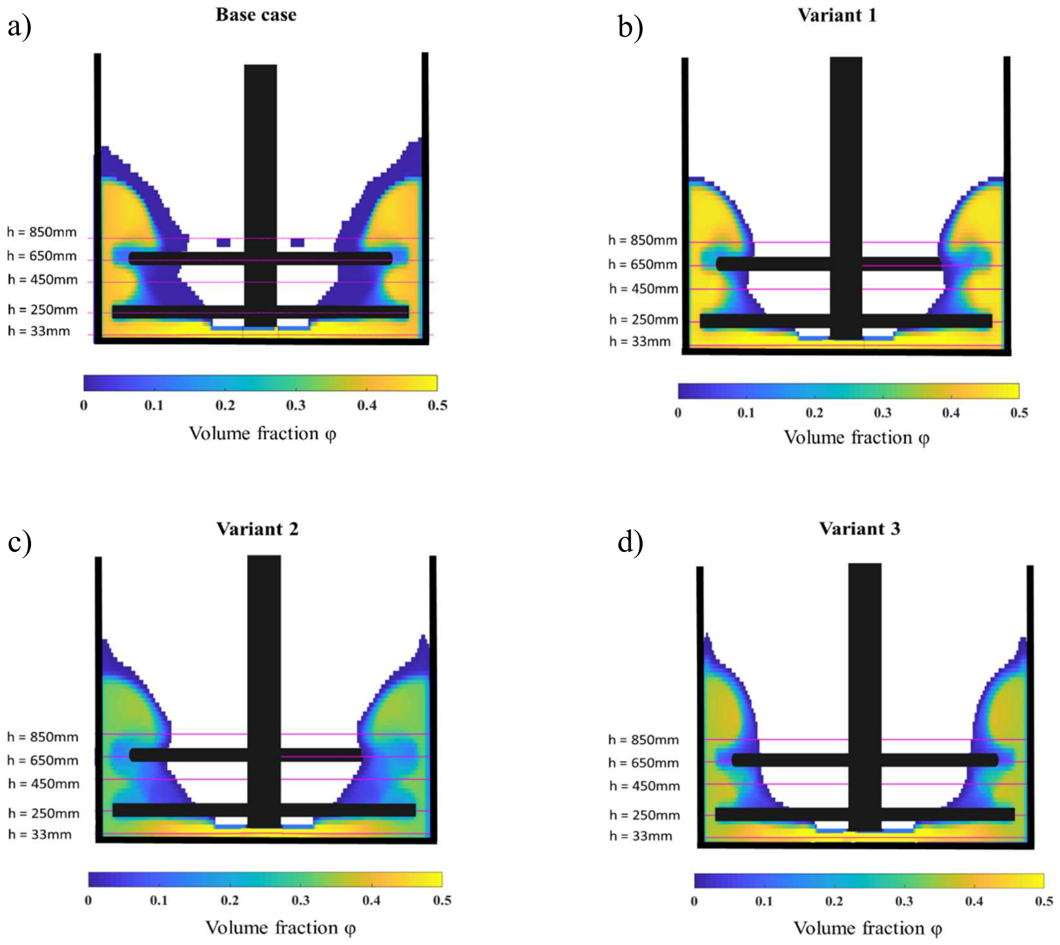

Figure 56: A vertical section through the SMD for a) base case, b) variant 1, c) variant 2 and d) variant 3, showing steady state distribution of average solid fraction.

The media volume fraction plays a key role in the performance of the SMD. The volume fraction profiles for the impeller variants used in this study were extracted at five carefully selected height levels shown by magenta lines in Figure 56. The volume fraction is plotted against the mill radius at the selected heights and is shown in Figure 57. The selected heights in the mill are 33 mm, 20 mm, 450 mm, 650 mm and finally 850 mm. Taking the volume fraction measurements at these locations ensures that the general dimensions of the vortex are captured and that the cavities in the charge produced by the arms do not affect the characterisation.

The onset of the boundary between the vortex and the solid/fluid phase (vortex radius) is in the same region for all variants, except for variant 3 at a height of 850 mm, and variant 2 at a height of 450 mm. The vortex radius for Variant 3 occurs at 720 mm at a height of 850 mm in the mill. This is largest at this height because Variant 3 has more arms in the top row compared to Variants 1 and 2, and fewer arms in the bottom row. The charge in the SMD experiences forces that drive the charge in 4 directions which are:

- Tangentially in the direction of rotation of the shaft
- Upwards against the force of gravity
- Downwards toward the bottom of the mill
- Radially towards the mill wall.

Unlike the base case, variant 3 has less arms in the bottom row. A low number of arms at the bottom row results in less of the charge overcoming gravity and rising high enough to be able to cross the boundary formed by the arms in the top row. The 6 arms in the top row drive the charge that crosses the vertical level of the top row of arms upwards and radially towards the mill wall. This results in a steep slope of the charge shown above the top set of arms and a larger vortex radius compared to the other variants as shown in Figure 57. Below the top set of arms (h= 450 mm) variant 2 has the lowest vortex radius of 600 mm with the base case having the largest radius. This again is due to the number of arms in the top and bottom row for variant 2 is less compared to variant 3 and the base case. The number of arms in the top row and their spacing affect the upward/axial transport of the charge. A variant with 4 arms in the top row will have gravity become more dominant keeping some of the charge from crossing the boundary formed by the top row of arms.

This results in a smaller vortex radius between the two rows of arms for Variant 2 at h= 450 mm. Variant 1 has the same number of arms in the top row as Variant 2, yet it has a slightly bigger vortex radius. Despite having less arms at the top row for variant 1, the force generated by the six arms in the bottom row, is sufficient to lift most of the charge above the top row of arms.

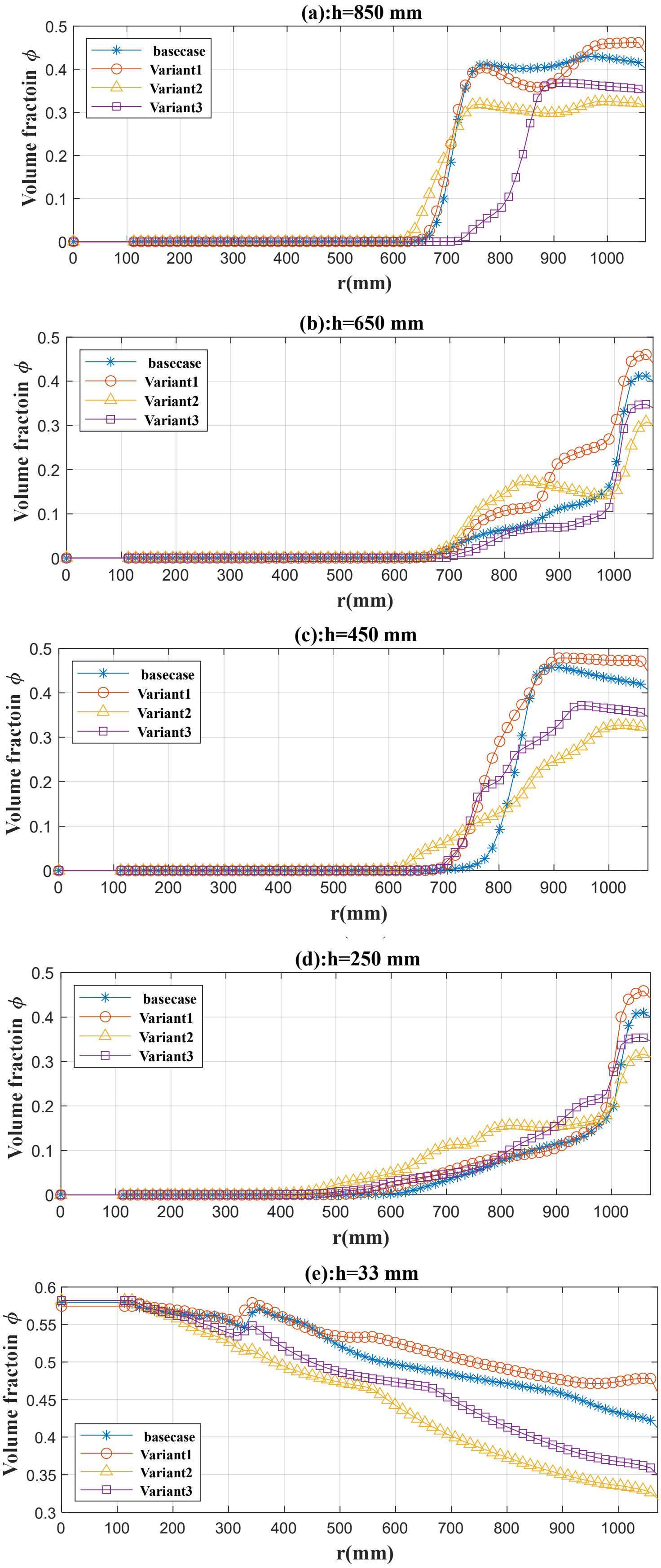

(a):h=850 mm

(b):h=650 mm

(c):h=450 mm

(d):h=250 mm

(e):h=33 mm

Figure 57: Media volume fraction against mill radius at sampled heights for all variants.

Below the bottom row of arms, there is no vortex. For all variants the media volume fraction is highest at the centre of the mill and decreases with increasing radius. Variant 1 and the base case generally have higher media volume fractions than variants 3 and 2. The number of arms in the bottom row affects the media packing in this region. The arms on the bottom row push some of the charge upwards, and some downwards.

The higher the number (surface area) of arms, the higher the volume fraction because they pack the media more tightly. Generally, the media volume fraction in the SMD is highest close to the wall and below the bottom row of arms. Increasing media volume fraction should result in better comminution. This is because the probability of ore particles being trapped between media particles increases with increasing media volume fraction.

To examine the charge structure produced by each impeller configuration around the arms, a top-down view of a horizontal slice of the mill, just above each set of arms is shown in Figure 58. The steady state media volume fraction is shown with the mill wall made transparent at an instance in time for ease of visualising the charge around the impeller arms. Generally, for the base case, the amount of charge pushed by each arm is evenly distributed at each row. For variants 1, 2 and 3, the charge is not evenly distributed between all the arms for both the top and bottom row. As shown in Figure 58, for variants 1 and 2 there are some arms that are not contributing at all to the transfer of energy to the charge.

As has been stated earlier, for the base case each arm essentially pushes the same amount of material. As the shaft rotates, an arm in the bottom row pushes the charge it is in contact with upwards. The arm that follows in the top row pushes some of the upward travelling charge downwards. This downward travelling charge then meets the next arm in the bottom row as illustrated in Figure 59. The orange arrows show the general direction of the charge as it encounters the arms. For the base case, the angular spacing of the arms in each row is the same. The angular spacing between an arm in the bottom row and the one preceding it in the top row is also the same. This results in uniform distribution of the load on each arm as shown in Figure 58.

For variant one starting with the bottom set of arms, there is a pair of arms which is not pushing a load while the other three pairs of arms are (Figure 58). This configurations arm arrangement is similar at the bottom row with the base case. At the top row, there is one pair that is loaded with less of the charge, and another pair with a long train of charge preceding it.

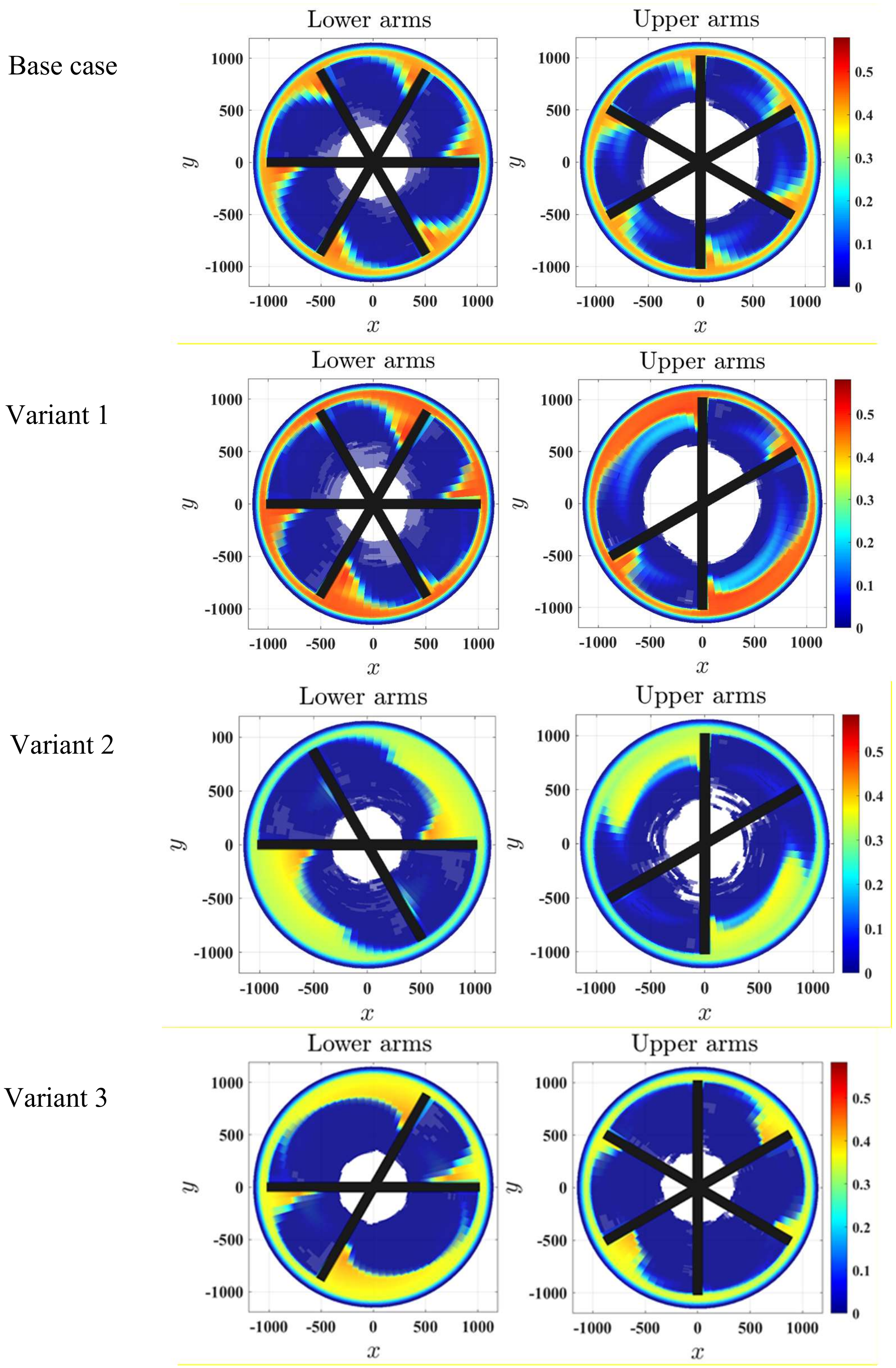

Figure 58: Media distribution around the bottom impeller arms (lower arms) and the top impeller arms (upper arms) for a) the base case, b) variant 1, c) Variant 2 and d) Variant 3. The mill is made transparent and media close to the shell corners is not shown.

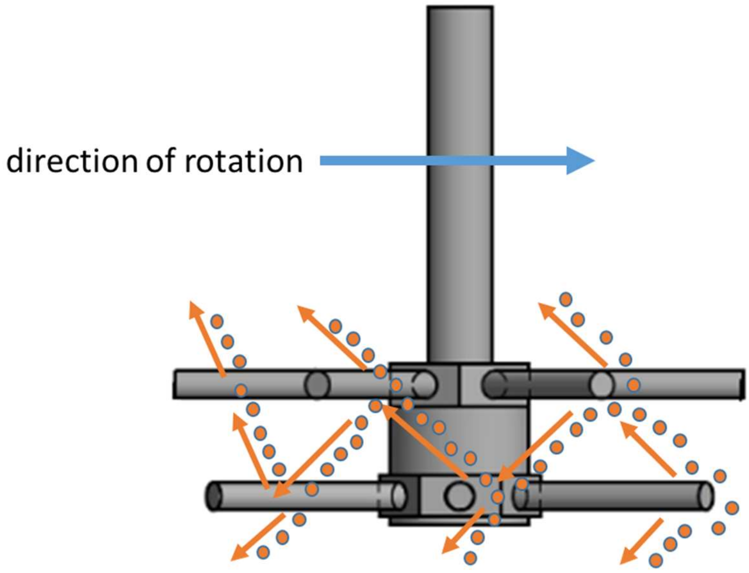

Figure 59: Illustration of the direction of the charge when interacting with the arms for the base case. The orange arrows show the trajectory of the charge.

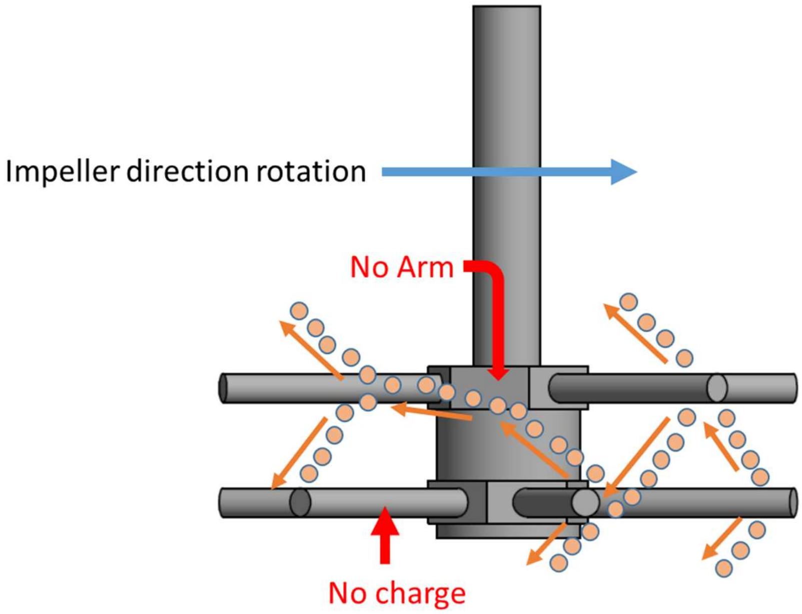

Figure 60: Illustration of the direction of the charge when interacting with the arms for variant 1. The orange arrows show the trajectory of the charge.

The reason for this charge structure at the impeller arms is because of a large angular distance between some of the arms in the top row. In this case the largest angular spacing is 120 degrees. This affects the angular spacing between an arm in the bottom row and the one preceding it in the top row. This angular offset affects how the charge is distributed between the arms. Figure 60 illustrates how the arms in this variant 1 interact with the charge. The absence of an arm in the top row as shown in Figure 60 (large angular spacing between the arms) results in very little to no charge being forced downwards toward the trailing arm in the bottom row. This causes the arms with a bigger angular spacing to have a long train of the charge preceding these arms as shown in Figure 60 and Figure 58. This variant does not utilise the available surface area on the arms below to transfer energy to the charge.

For variant 2, Both the top and the bottom row have arms with an angular spacing of 120 degrees. As the shaft rotates a pair of arms in each row does not have much interaction with the charge. The reason for this uneven distribution of the charges is again the offset position of the arms in the top row relative to the bottom row as illustrated in Figure 61. The region with no arm does not force the charge to travel downwards. The force of gravity is insufficient to force a significant amount of the charge which results in some arms in the bottom having no charge to push.

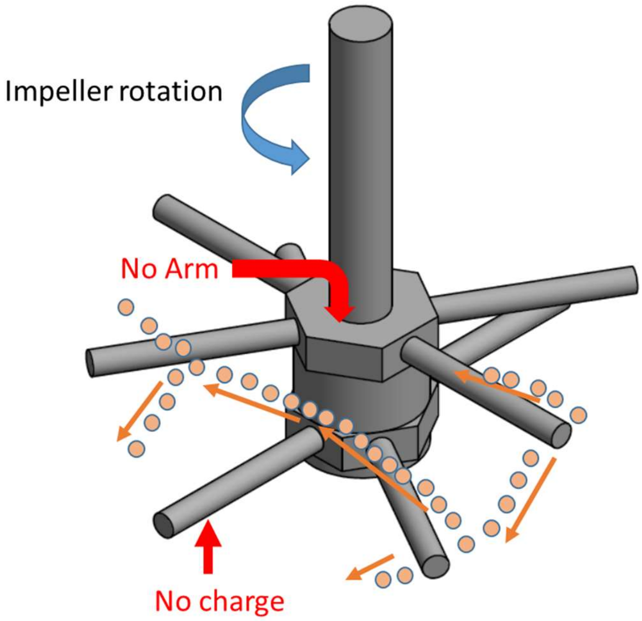

Figure 61: Illustration of the trajectory of the charge when interacting with the arms of variant 2. The red orange arrows show the trajectory of the charge.

Figure 58 also shows Variant 3, which has 4 arms in the bottom row and 6 arms in the top row. This arrangement also has the arms spaced at angular distances of 60 and 120 degrees in the bottom row, while in the top row they are all spaced at 60 degrees. In the bottom row, there are two arms that are pushing most of the charge with the other two pushing comparatively less. The angular spacing (offset) of an arm in the top row and the one directly preceding it in the bottom row (the arm that pushes the charge upward from the bottom of the mill) is crucial, not only for axial transport but for the way the charge is distributed to each arm. If this distance is uniform for all the arms as it is for the base case the charge will be symmetric and the load will be shared amongst all the arms. If the angular spacing is not the same, this causes symmetry in charge distribution to be lost resulting in some arms pushing very little of the charge. Loss of symmetry may also have mechanical implications on the shaft since the load is not shared near equally by the arms.

6.2 Variation in power draw and energy utilisation with impeller design

The different configurations are compared by making use of key mill performance indicators such as power draw and energy spectra. A suitable metric must be used to distinguish between the variants. The total engagement area of the arms with the charge is used. This is done on the basis that power drawn by the mill is a function of the drag forces $F_{d,}$ due to the media and the slurry on the impeller arms. The drag force is also a function of the area of the arms in contact with the charge.

$$F_d = AC_D \, \frac{\rho V^2}{2}, \tag{37}$$

Where A and C_D are the engagement area and the drag coefficient, ρ and V are the density and velocity of the material.The data of the particles motion and position are stored on a cylindrical grid co-rotating with the impeller. To determine the engagement area, the position of the impellers with reference to the grid is identified. Figure 62 Shows the base case impeller configuration with the media volume fraction data at the level of each row of arms. For each row of arms, three levels/heights on the Z axis of the grid contain the volume fraction information in contact with the leading surface of each impeller arm.

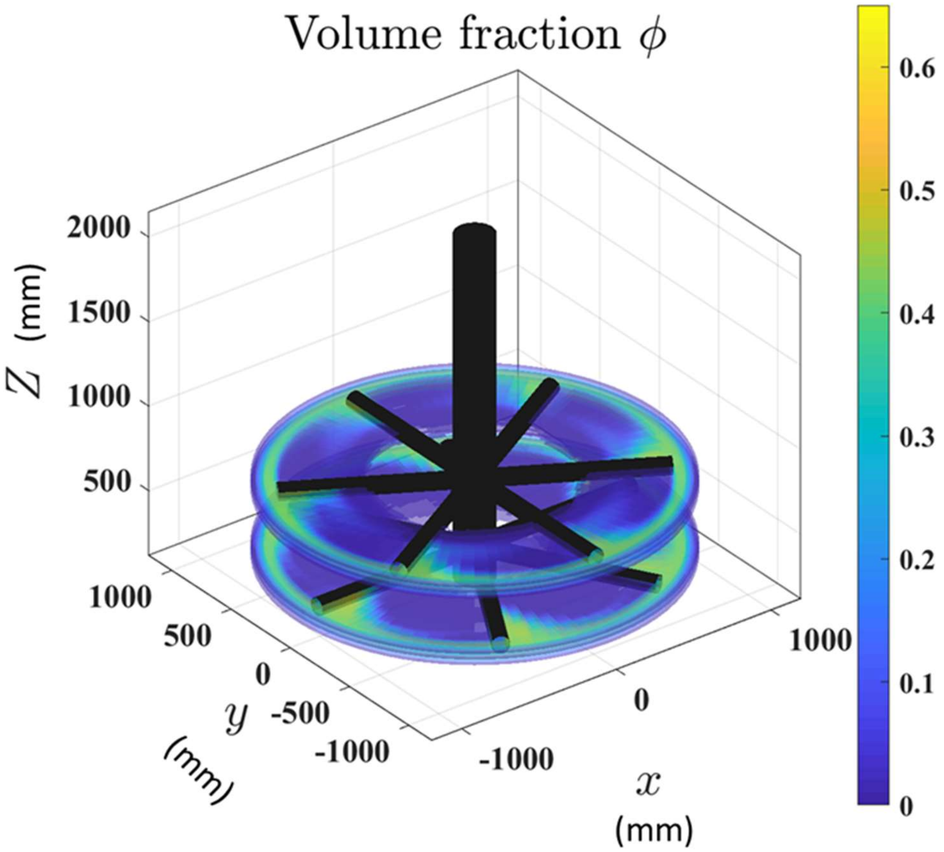

Figure 62: Locating the volume fraction data that will assist in determining the engagement area of each arm. Three levels of the cylindrical grid are sufficient for determining the fraction of each arm covered by the charge. Only the volume fraction of the media for the base case is shown here.

The volume fraction can then be plotted along the length of the arm with a threshhold of 0.05 marking the boundary between the solid or fluid phase and the vortex. Figure 63 shows the volume fraction information at the three grid levels for the top row of arms of the base case. The volume fraction is sampled at three angular locations, two of which are shown by the magenta lines on the images in the first column, while the third location is in between. The volume fraction plots for each arm at each level/height are shown as a plot of the volume fraction against the arm length r which is represented as a fraction of the mill radius R.

The vertical lime green line marks the 0.05 volume fraction threshold, which identifies the boundary between the vortex and the charge on each plot. Once the average engagement length of the arm was determined, the average engagement area for each arm was computed. The sum of these gives the total engagement area of the configuration. A summary of the total engagement area for each variant including the base case is given in Table 15. The arm configuration is represented as a 1 x 2 matrix with the digits in the first and second columns representing the number of arms in the lower and upper sets respectively.

Table 15: Total engagement area for each variant

Variant	Total engagement area (m^2)	Arm configuration	No. of arms on shaft
Base case	4.80	[6 6]	12
1	4.22	[6 4]	10
2	2.76	[4 4]	8
3	3.56	[4 6]	10

Engagement area increases with increasing total number of arms on the shaft. In the case of variant 1 and 3 which have the same number of arms, the one with more arms in the bottom set has the larger engagement area. This is because of the funnel like structure of the vortex in the SMD with the diameter decreasing with depth in the mill. This means that arms in the lowest set will have a higher engagement area than those in higher sets.

A plot of the total power draw and power dissipated in media collisions against the total engagement area is shown in Figure 64. Increasing the engagement area resulted in higher power draw. There is a linear relationship between the engagement area and the total power drawn and Power dissipated in media collisions. The difference between total power draw and the media dissipation for each variant gives the amount of power dissipated in viscous stresses in the slurry. Variant 2 with the lowest number of arms (hence lowest engagement area) dissipates 58 kW in viscous stresses, and has the lowest energy dissipated in media collisions (172 kW). The base case has the highest dissipation in viscous stresses and media collisions which is 102 kW and 286 kW respectively. Generally, the variants with the highest energy dissipated in media collisions mean more energy available for comminution. Whether or not the energy dissipated in viscous stresses contributes to comminution is dependent on the competence of the ore.

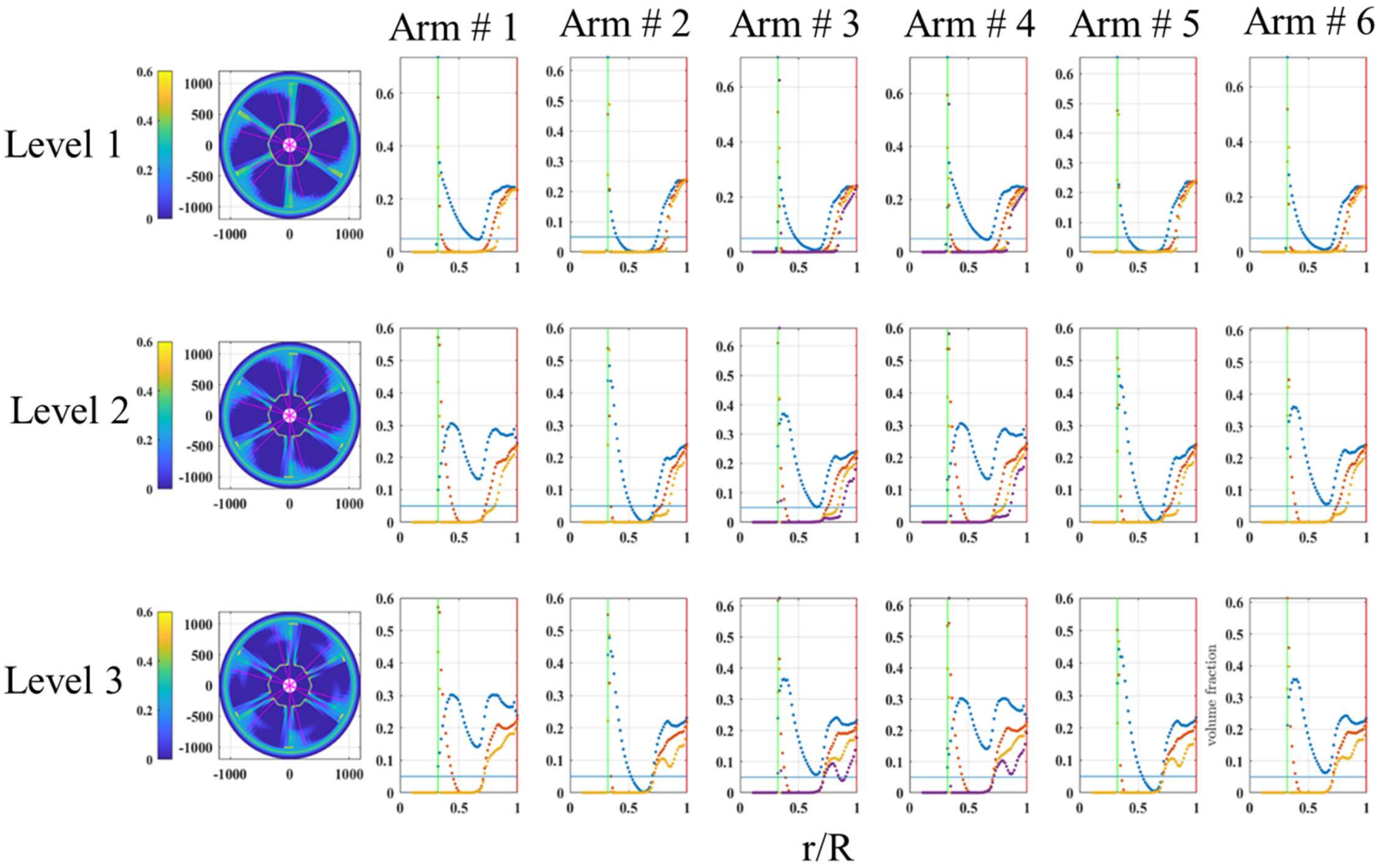

Figure 63: Media volume fraction plots for three heights in the mill. Each row shows data for one of the three layers from solid fraction data is read. The first column is a horizontal slice at just above the top set of arms.

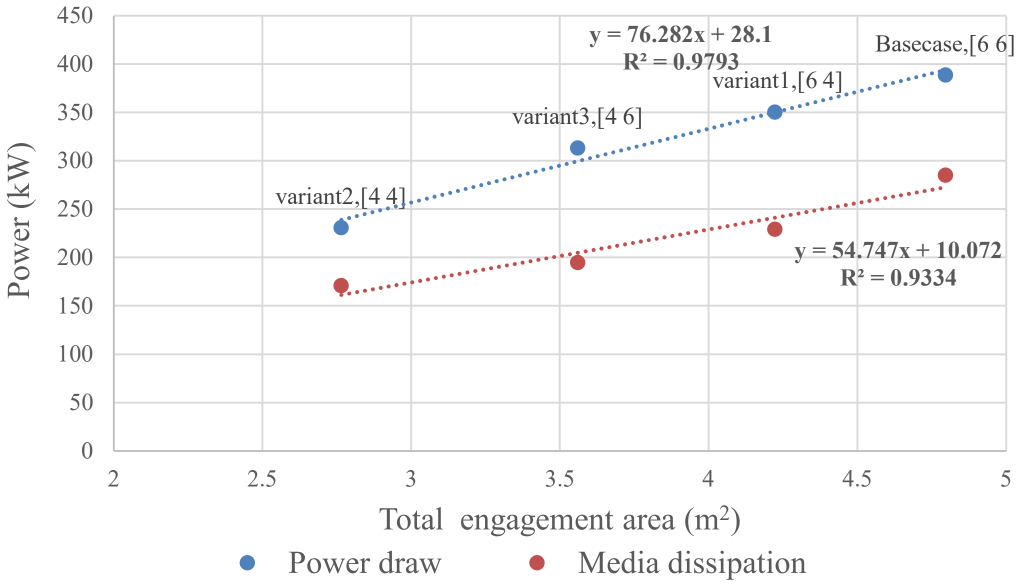

Figure 64: Power draw against engagement area for all variants.

To examine how the grinding collision environment changes with different variants, changes in the collision energy spectra with configuration are investigated. The peak location of the collision energy distributions, together with the associated dissipation rate is used to characterize the spectra, and for comparing the variants. Only the shear component of the spectra was compared because it is more dominant than the normal component. Figure 65 shows a plot of modal peak and its associated dissipation rate for the media-to-media collision energy spectra against total engagement area. As engagement area increases, the modal peaks shift to the lower energies while the associated dissipation rate increases. This is because the media in the charge becomes more compact as the engagement area (number of arms) increases, resulting in a decrease in high energy collisions. This means that the breakage rates due to shear should increase. This can be tested experimentally by grinding the same ore using the two different configurations and comparing the breakage rates.

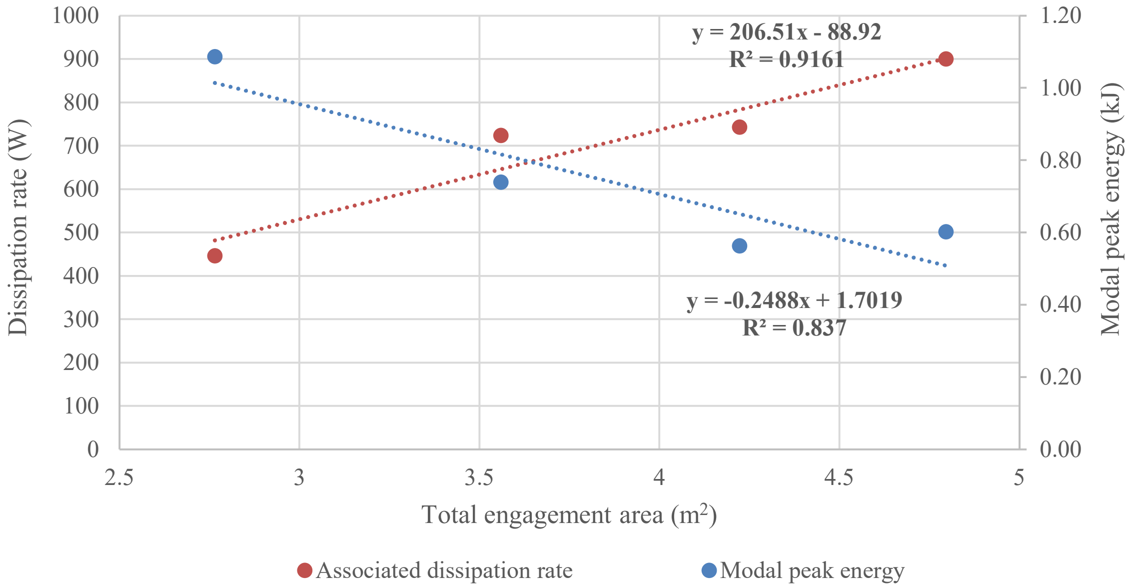

Figure 65: Shear media-to-media collision peak energy and associated dissipation rate against total engagement area.

For the media-to-liner collisions, the peak shear energies and their associated dissipation rates are plotted against total engagement area in Figure 66. The peak energies generally increase with increasing engagement area, while there is no general trend for the associated dissipation rates. Generally, more energy is dissipated in media-to-media collisions than the media-to-liner ones. The modal peak energy for the media-to-media collisions occurs at lower energies than for media-to-liner collisions for all variants. This is important for a grinding device as this is where most of the grinding takes place.

The shear media-to-shell collisions in Figure 67 show an increase for both the modal peak and the associated dissipation rate as the engagement area increases. For the media-to-impeller collisions (Figure 68), the modal peaks decrease while the associated dissipation rates increase with increasing engagement area. This indicates that as the engagement area increases, the media becomes more compact around the arms. Compact media means the path between the media particles and the arms is small; therefore, collisions will shift to lower energies at high frequency. When the media is compactly packed around the arms, more of the force exerted by the arms translates to higher shear media-to-impeller energy dissipation. Since the results presented so far show that high engagement areas result in high media-to-media and Media-to-impeller energy dissipation rates, this suggests there is a trade-off between grinding and wear.

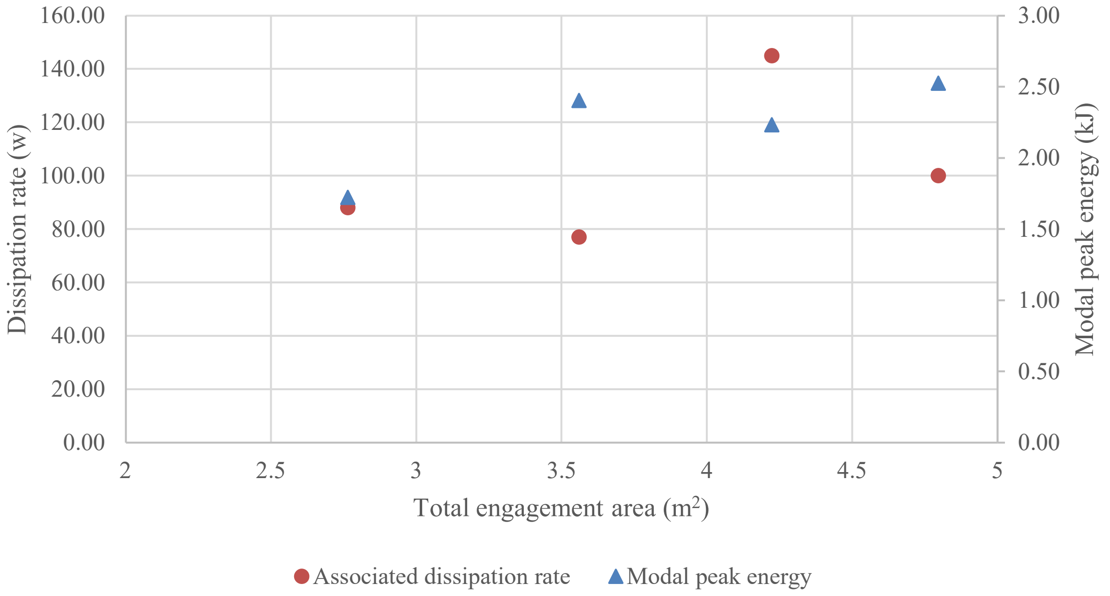

Figure 66: Shear media-to-liner (both shell and impeller) collision peak energy and associated dissipation rate against total engagement area.

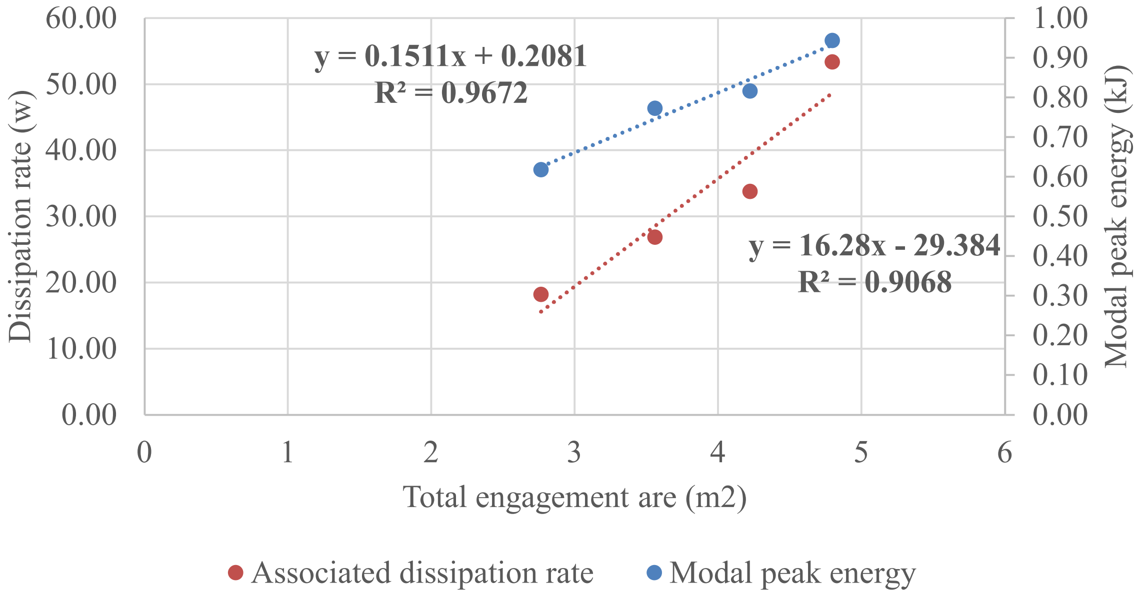

Figure 67: Shear media-to-shell collision peak energy and associated dissipation rate against total engagement area.

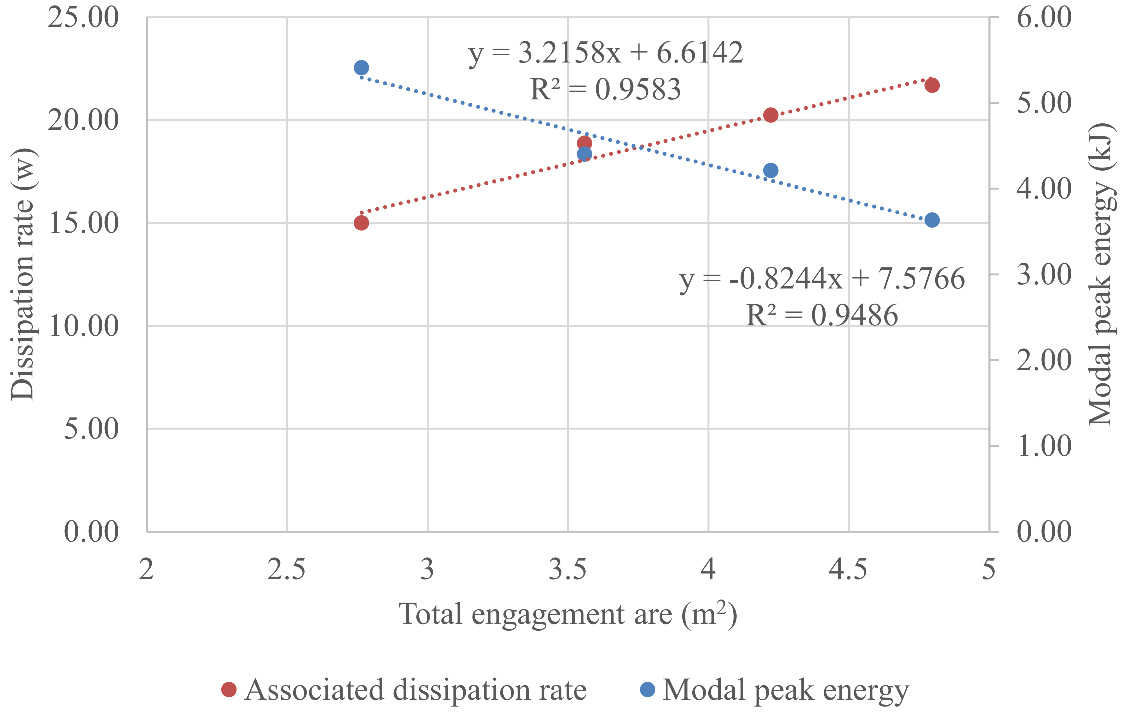

Figure 68: Shear media-to-impeller collision peak energy and associated dissipation rate against total engagement area.

6.3 Transport and mixing variation with impeller design

The metric used to identify the different impeller variants studied for the evaluation of mixing is the average normalised fall height, τ, rather than engagement area. The average normalised fall height is defined as the vertical distance that a media particle falls, in the time it takes an impeller arm to travel the angular distance to the position of the preceding arm. The fall height is calculated for all particles at the top impeller row and not the bottom row (since the media is densely packed below and there is no fall component to the flow). The fall height is then expressed as a fraction of the diameter of the impeller arm. It is expected that the average normalised fall height will affect the axial motion of the media particles in the mill. To quantify mixing, a cubic cell grid is superimposed over the media bed and local averages of the colours are calculated, using all particles in the region with the centre at each grid point. The averages are then used to determine a mixing state by normalisation relative to the maximal range between fully segregated and fully mixed states. The mixing measure used here is the Average % mixed per revolution. This is calculated by determining average mixing rate at 80% mixing divided by the number of revolutions to a mixing state of 80%.

Most of the mixing is due to axial movement of the charge. The calculated values of the average fall height, τ, are shown in Table 16. Table 16 shows that there is a small change in the average normalised fall height with engagement area or configuration.

Figure 69 shows a plot of the average percent mixed per revolution of the shaft, against the average normalised fall height τ. The plots show that the relationship between the mixing metric and τ is linear and that there is a small difference (~3%) in average % mixed per revolution between the largest and the smallest τ.

Table 16: Average normalised fall height of the variants.

Variant	**τ**	Total engagement area (m^2)	Arm configuration	No. of arms on shaft
Base case	1.59	4.80	[6 6]	12
1	2.39	4.22	[6 4]	10
2	2.61	2.76	[4 4]	8
3	1.79	3.56	[4 6]	10

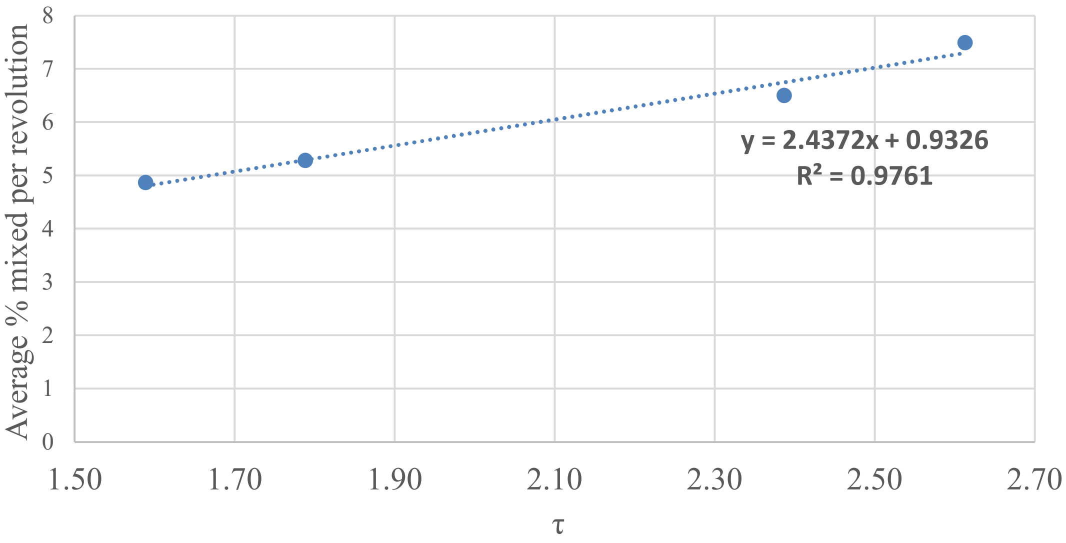

Figure 69: Average fall height against average % mixed per revolution.

The lower fall heights are caused by short azimuthal spacing of the arms. The axial flow of material between these arms is reduced resulting in low mixing. Figure 70 shows the average percent mixed per revolution against the engagement area. The Figure shows a general decrease in mixing per revolution with increasing engagement area. This suggests that there is a trade-off between mixing and grinding. Variant 1 has a higher engagement area (and therefore higher power draw) than variant 3, yet the latter has a lower average percent mixing per revolution than the former (Figure 70). This is because variant 1 has more arms in the bottom row than variant 3. More arms in the bottom row results in more of the charge in that region being pushed upward. Variant 1 also has a higher fall height than variant 3 due to the lower number of arms in the top row. This results in variant 1 having a higher average percent mixed per revolution than variant 3.

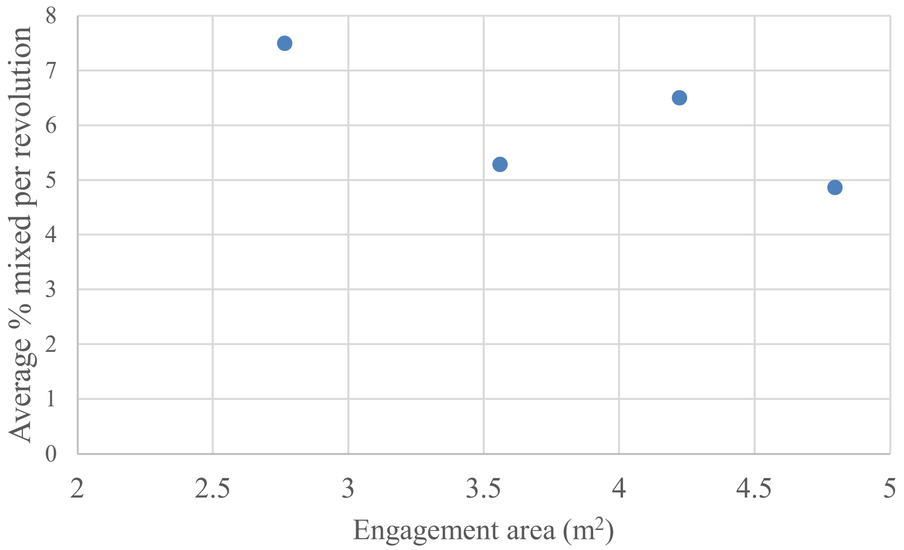

Figure 70: Total engagement area against average % mixed per revolution

The charge height, defined as the distinct height to which most of the solids are lifted in the vessel along with the fluid, for each variant including the base case is shown in Table 17. For mills with the discharge mechanism located at the top of each side, the impellers need to lift the charge to a height that would allow for discharge of material form the mill. The difference in charge height between the base case, variants 1 and 2 is very small, with variant 3 having the highest charge height. The reason for a slightly higher charge height for variant 3 is the arrangement of the arms as discussed in section 6.1. The charge above the top set of arms for variant 3 has a steep slope compared to the other variants. This gives Variant 3 a larger vortex radius resulting in a higher charge hight.

Table 17: Charge height of the variants

Variant	Charge Height (mm)	τ	Total engagement area (m^2)	Arm configuration
Base case	1290	1.59	4.80	[6 6]
1	1256	2.39	4.22	[6 4]
2	1262	2.61	2.76	[4 4]
3	1422	1.79	3.56	[4 6]

To illustrate the charge height of the configurations, a plot of the volume fraction threshold (the boundary of the vortex and the solid/fluid phase) in a horizontal slice of the mill, collapsed onto a 2d plane, is shown in Figure 71. Since the charge is symmetric, only half the mill is shown. The magenta lines show the centre of the arms in the top and bottom rows. The figure shows that the difference is almost unnoticeable. For all the variants considered here, the impeller lifts the charge to a height sufficient to have contact with discharge screens that are situated at the top of each of the eight sides of the SMD.

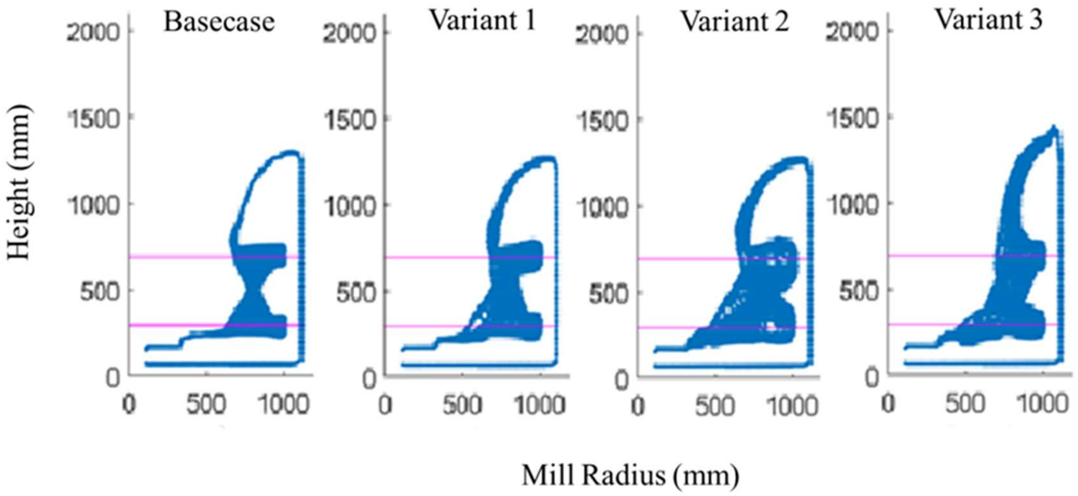

Figure 71: A horizontal section through the mill for all configurations showing the charge.

7 Main observations, conclusions, and recommendations

In this chapter, Key observations from the work are summarised, and conclusions drawn from the results of this work are presented. The novel contribution of this thesis is summarised as well as recommendations for future work.

7.1 Main observations

In addressing the hypotheses, several observations were made for the systems that were modelled. The main observations are presented first to build a case to show how the hypotheses were tested. The observations are listed under different subheadings for ease of reference.

SMD 1100-E and SMD 355-E Media and Slurry flow

- For all the scales of the SMD presented here, the model shows that the action of the impeller creates a centrifugal force that pushes the charge towards the mill walls. This action results in a vortex centred on the shaft, except for the bottom of the mill where the effect of the impeller does not reach.
- The media is fluidised by the rotational action of the impeller and is densely packed with solid fraction around 0.55 and about 0.45 for the SMD 1100-E and the SMD 355-E respectively, at the conditions considered here. Most of the voids between the media are filled by the slurry with any excess being located at or above the free surface of the vortex and at the bottom of the mill just above the base of the impeller.
- The dilation of the media is constrained by the incompressibility of the slurry and controls the degree of separation of the media particles in the bulk of the charge. This is because the average solid fraction in the densely packed areas of the charge (>0.5) is higher for DEM only simulations (0.58), compared to that of the coupled simulation (0.55).
- The results also show that for the SMD at all scales, the rotational action of the impeller arms creates deep depressions in the charge that divide the charge into three vertical regions: one above, one between, and one below the two rows of impeller arms. In addition to energy transfer, the rotational action of the arms produces a pumping like effect which forces nearby charge at all radial distances upwards. This has implications

on transport in the mill, as axial mobility controls the transport of feed materials to regions of high energy dissipation and of ground product out of the mill.

SMD 1100-E and SMD 355-E velocity distribution

- The axial velocity distribution of the media for both scales is like that of the slurry, with the difference being that the slurry is more active than the media at the free surface of the vortex above the impeller arms.

- For the SMD1100-E, radial motion of the charge is restricted to a thin active surface layer of the vortex for both the media and the slurry. Little radial movement of both media and slurry is observed in the bulk of the charge. On the SMD355-E, radial velocity increases with increasing distance from the mill centre and is low at the mill wall. For both mills near the surface layers (which are less densely packed) the slurry displays larger radial mobility than does the media.

- For the SMD1100-E, Tangential velocity is zero at the mill wall and increases with distance from the mill wall to a velocity of 1.5 m/s at the free surface. For the SMD355-E, the tangential (swirl) velocity of the charge (media and slurry) is low at the mill wall and increases radially inwards with the highest swirl speeds occurring at the tip of the impeller arms.

- The tangential component of velocity (swirl) is the largest component in all scales of the SMD, this is because that is the rotational direction of the impeller.

SMD 1100-E and SMD 355-E Power draw and energy utlisation

- For the SMD1100-E 66.0% of the predicted power draw is dissipated through media collisions and 34% through viscous stresses in the slurry phase. This is because the rotational action of the impeller pushes the media towards the mill wall. This results in the media being tightly packed, consequently increasing the likelihood of media contacts.

- The shear and normal media-to-media collisions dissipate 54.0% and 12.0% of the power drawn respectively. The media-to-liner energy dissipation accounts for only 4.0% of the power draw; liner wear is dominated by abrasion. This is due to the fact that most of the motion in the SMD is swirl (tangential), and the media is tightly packed. Therefore, the shear media-to-media and media-to-liner collisions are dominant

- For the SMD355-E, 74% of the power drawn is dissipated in media collisions (both media-to-media and media-to-mill collisions). Dissipation through viscous stresses in the slurry phase accounts for the remaining 26%. Media-to-media and media-to-liner collisions dissipate 68% and 6% of the net power drawn respectively. Like the SMD 100-E, the media is tightly packed by the impeller, increasing the likelihood of media contacts.

- The shear component of the media-to-media collisions is 3.5 times higher than the normal; consequently, energy dissipation (and therefore grinding) is strongly dominated by the shear component of the flow. For the media-to-liner collisions, the shear interactions dissipate 5% compared to the 1% of the normal component. This indicates that the wear on the mill surfaces is also dominated by the shear interactions. The dominance of the shear interactions is because tangential velocity is the dominant component of velocity, coupled with the tight packing of the media leaves little room for normal media contacts.

- The ratio of shear to normal dissipation is higher for media-to-liner collisions than media-to-media ones because the motion of the charge is predominantly swirl, resulting in little normal media-to-liner collisions.

- Spatial distribution of the areas of high energy dissipation are mapped. These are the areas where most of the grinding occurs and are known as the grinding zone. This is the region directly in front of and below the impeller arms, stretching radially inwards towards the vortex and vertically slightly above the top set of arms. These are the regions experiencing high velocities.

Wear pattern in the SMD 355-E

- The abrasion power absorption distribution for the impeller and mill shell are used to study areas of the mill internals likely to experience the most abrasion wear. The mill shell experiences high abrasive wear on the floor, the lower half of the walls and the baffles. On the mill floor, peak wear forms a circular pattern with a radius of 1.0 m, which is the radial location of the tip of the arms.

- The wear decreases radially inwards and outwards. This is due to the decrease in swirl speed of the charge with distance radially, from the tip of the arms toward both the wall and the vortex. There is no abrasion wear below the shaft because the charge is not mobile in this region.

- The wear pattern on all the eight walls is broadly ellipsoidal in shape. The lower parts of the baffles at each corner experience stronger abrasion as these surfaces protrude into the mill and play a role in the charge changing direction at each of the octagonal wall transitions.

SMD mixing and transport

- To study mixing in the SMD, the probability distribution of local averages of an attribute of the particles is used. The attribute used in this work is colour, which is assigned according to initial vertical position. This allowed the progress of mixing to be predicted. Vertical direction of mixing is studied because it is the slowest in the SMD and therefore presents a key limit in grinding performance.

- The charge is 90% mixed after 25 revolutions. This suggests that material can move relatively easily in and out of the grinding zone of the mill. This is because the rotational action of the impeller and the arms produces a pumping like effect that drives the charge (media and slurry) up from the bottom of the mill chamber.

- Only material that is beneath the shaft where there is very little vertical transport will not move relatively easy. This is because of the vertical location of the shaft, a critical design aspect that controls the mobility of the charge at the bottom of the mill.

Impeller variation

- Distribution of the charge along each impeller arm is investigated for all impeller variations. The symmetry of the charge is lost when the spacing of arms in a level/row is not the same. This means that the amount of charge pushed by each arm will be different with some arms having little to no engagement with the charge.

- The general vortex shape is similar for all variants studied to the base case which has two rows of six arms. The variant with 4 arms in the top row and 6 arms in the bottom, and the one with 4 arms in each row have a slightly different charge shape above the top set of impeller arms. The slope of the charge above the top set of arms is steeper for the variant with 6 and 4 arms in the top and bottom row than it is for the variant with the opposite arrangement of arms and one with 4 arms in each row. A variant with more arms in the top will push more of the charge towards the mill wall and upwards resulting in a steep slope of the cone shaped charged above the arms. This means that the diameter of the vortex will be wider for such a variant.

- The total engagement area of the arms, which is defined as the area in contact with the charge is used as a metric to distinguish between the impeller configurations. It was found that engagement area increases with increasing total number of arms on the shaft. Total power draw and the power dissipated in media collisions increases with increasing total engagement area.

- The peak location of the collision energy distributions, together with the associated dissipation rate is used to characterize the spectra, and study how each configuration affects the collision environment. For media-to-media collisions, increasing engagement area shifts the modal peaks to the lower energies while the associated dissipation rate increases. This is because the media in the charge becomes more compact as the engagement area (number of arms) increases, resulting in a decrease in high energy collisions.

- For the shear media-to-liner collisions, both the peak energies and their dissipation rates increase with increasing engagement area. Generally, more energy is dissipated in media-to-media collisions than the media-to-liner ones. The modal peaks for the media-to-media collision spectra generally occur at lower energies than for media-to-liner collisions for all variants.

- The metric used to identify the influence of impeller configuration for the evaluation of mixing is the average normalised fall height, τ. This is defined as the vertical distance that a media particle falls, in the time it takes an impeller arm to travel the angular distance to the position of the preceding arm. The configuration with the greatest number of arms in the top row generally has the lowest fall height. A small difference (~3%) in average percent (%) mixed per revolution between the largest and the smallest τ was observed. The lower fall heights are caused by short azimuthal spacing of the arms.

- There is no significant difference in the charge height generated by the configurations studied here. All the configurations studied lift the charge to heights sufficient to reach the discharge screens that are normally situated on top of each of the eight sides of the grinding chamber.

7.2 Conclusions

The work in this thesis was carried out to test three hypotheses to address the energy environment and flow behaviour in the Stirred Media Detritor (SMD), using the Discrete Element Method coupled with Smoothed Particle Hydrodynamics. The three hypotheses are:

1. Two-way coupled DEM-SPH can simulate the flow of media and fluid in a vertical stirred mill, giving the energy spectra which characterises the grinding environment.
2. Two-way coupled DEM-SPH simulation outputs can be used to understand energy utilisation in the SMD and identify areas of high energy dissipation in the mill known as the grinding zone and determine how efficiently the feed is transported into and out of this area.
3. Outputs from the two-way coupled DE-SPH model can be used to assess the effect different arm configurations have on Charge structure, power draw, mixing and energy utilisation in the SMD.

From the work performed to address the hypotheses regarding flow in the mill and energy dissipated by the media contacts, it was shown that the two-way coupled DEM-SPH can model the motion and interactions of both media and slurry in industrial scale SMDs. The steady state charge structure produced by the DEM-SPH model is similar to what was observed from the experimental work which showed the vortex structure around the shaft. From this the main conclusions that can be drawn are:

- Using a two-way coupled DEM-SPH model, the flow and interaction of media and slurry in an SMD at all scales can be modelled to give the flow structure that is similar to what was obtained in physical experiments. The DEM-SPH simulations indicated that the presence of the slurry resulted in dilation of the charge, which was not the case for DEM only simulated cases which had no slurry.

- The DEM-SPH model provides the probability distribution of different collision energies, which is called the energy spectra that cannot be determined experimentally. The spectra of the SMD plotted as dissipation rate against collision energy is a skewed log normal distribution, which showed that for the SMD 355-E, peak dissipation rates of the order of 1000 W at energies of 0.68 mJ were obtained for the media-to-media collisions. For the SMD 1100-E dissipation rates of the order of 3000 W at energies of 4.2×10^{-4} J were obtained.

- Outputs of the DEM-SPH model provide the energy dissipated by the media collisions which can be used to quantify energy dissipated in viscous stresses. Modelling a system operated wet with only DEM will overestimate the energy dissipated in media collisions by about 46.3% and the energy dissipated in viscous stresses will not be realised.
- The energy spectra characterise the grinding environment and can be used to ascertain energy dissipated in media collisions and viscous stresses. Media collisions dissipate between 66% and 74% of the power drawn for the SMD 1100-E and the SMD355-E respectively. Energy dissipated in viscous stresses is 26% to 34% for the SMD 355-E and the SMD 1100-E respectively. This implies that the contribution of viscous stresses is scale dependant.

From the work performed to address the hypotheses regarding energy utilisation in the SMD, identifying the grinding zone of the mill, and determine transport into and out of this area. The following conclusions were drawn that support the hypothesis.

- The DEM-SPH model provides information on energy dissipated in media-to-media and media-to-liner collisions and for the SMD 355-E simulations performed 68% of the power drawn is dissipated in media-to-media collisions and 6% in media-to-liner collisions while for the SMD 1100-E 54% of the power drawn is dissipated in media-to-media collision and 4% in media to liner collisions.

- The DEM-SPH model showed that over 50% of the power drawn is dissipated in shear media-to-media collisions compared to 3-15% dissipated in normal collisions as observed in both SMD 355-E and SMD 1100-E simulations.

- The outputs of the DEM-SPH model allow the spatial distribution of high energy dissipation in the mill, also known as the grinding zone, to be mapped. The grinding zone is in the regions in advance (azimuthally) and below the tip of the arms extending just above the top set of arms.

- The DEM-SPH model can be used to study the progress of mixing and transport of media caused by the configuration impeller arms in the system and the results from the SMD 355-E indicated that material can be transported quickly into, and out of the grinding zone because the charge is 90% mixed after 25 revolutions.

From the work performed to address the hypotheses regarding assessing the effect different arm configurations have on process outputs, it was shown that the outputs of the two-way coupled DEM-SPH can assist in determining how impeller configuration affects charge structure, energy utilisation and mixing. The main conclusions drawn that are in support of this hypothesis are:

- The DEM-SPH model is used to model the structure of the charge in the SMD caused by different impeller configurations. For the configurations studied, one with uniform angular spacing of arms in each row, and uniform angular spacing between an arm in the bottom row and the one preceding it in the top row, has each arm essentially pushing the same amount of charge hence all the arms participate in transferring energy to the charge. Absence of this uniformity results in some arms pushing little to no charge, meaning that those arms do not contribute to energy transfer to the charge. Therefore, Arm configuration affects the amount of charge around the impeller arms.

- Power drawn by each impeller configuration can be assessed using the DEM-SPH model outputs. The configuration with 6 arms in each row has the highest engagement area of 4.8 m^2, draws 388.6 kW of power and dissipates 285.2 kW in media collisions. The configuration with 4 arms in each row has the lowest engagement area of 2.8 m^3, drawing 230.7 kW of power and dissipating 171.8 kW in media collisions. A configuration that maximises engagement of the arms with the charge will have a higher power draw and high media-to-media energy dissipation than one that has a lower engagement area.

- Low azimuthal distances between arms in a row restricts the transport of material past the arm level, reducing the extent of mixing in the SMD. This is because a row of impeller arms represents a substantial dynamic obstacle restricting axial flow through the level of the arms. For a configuration with 6 arms in the top row, the particles have a shorter travel time, fall a shorter distance and are less likely to pass through the level of the arms.

7.3 Research novelty

The following are the original contributions made in this work towards understanding the operational behaviour of a Stirred Media Detritor.

A two-way coupled transient DEM-SPH model is used to study the flow of grinding media and slurry in two industrial scale SMDs with 1100 kW and 355 kW of installed power respectively. The DEM component is used to model the grinding media charge while the SPH component is used to represent the slurry containing the fines. The outputs of the model give the energy spectra of the SMD which cannot be determined experimentally.

The two-way coupling was used to give a detailed analysis of the flow behaviour of the charge (both solid and fluid phase), particularly the interactions of the media and the slurry. The influence of the fluid on the power draw of the SMD is decoupled from that of the media, which cannot be studied experimentally. The model provides important information on the critical aspects of the flow in an SMD.

The grinding zone of the SMD is determined using the two-way coupled DE-SPH model together with the details of how material moves in and out of the grinding zone.

A methodology has been developed that can be used to design impellers by assessing key metrics that link to performance. A metric for identifying the different configurations is introduced and linked to key performance indicators such as:

- The collision environment
- Mixing and transport
- Wear on mill internals

This provides important information that will assist in impeller design and selection.

7.4 Recommendations

The following recommendations are made based on the outcomes of this thesis.

- The slurry solids concentration is a factor that is important and can affect charge structure, mill power draw and energy utilisation. It is recommended that studies varying the solids concentration and hence, the viscosity of the slurry must be carried out.

- Further studies on scale up methodology for these devices using outputs from DEM-SPH modelling must be carried out. The DEM-SPH outputs can be used to describe the collision environment which can be used for the scale up process.

- Media size is known to affect mill performance indicators studied in this work, A study to look at the effect of the media size is recommended.

- Wear on the mill internals, particularly the impeller arms is a very important aspect which will influence the performance indicators. Studies that model mill performance at different stages of the life of the arms is recommended.

8 References

Abouzeid, N.M., 2016. Eulerian and Lagrangian smoothed particle hydrodynamics as models for the interaction of fluids and flexible structures in biomedical flows. PhD thesis, Univeristy of Manchester.

Agrawala, S., Rajamani, R. K., Songfack, P., & Mishra, B. K. (1997). Mechanics of media motion in tumbling mills with 3d discrete element method. Min. Eng. 10(2), 215-227.

Allen, J., 2011. Stirred milling all you need to know. Metso minerals industries inc. York PA17402 USA.

Allen, J., 2013. Stirred milling machine development and application extension. http://www.ceecthefuture.org/wp-content/uploads/2014/03/Allen.pdf.

Alkac., D., 2005. Modeling flow in the pulp lifter assembly using computational fluid Dynamics. Ph.D. Thesis , University ofUtah.

Altun, O., Benzer, H. and Enderle, U., 2013. Effects of operating parameters on the efficiency of dry stirred milling. Miner. Eng. 43–44, 58–66

Aubram, D., Rackwitz, F., Savidis, S.A., 2010. An ALE finite element method for cohesionless soil at large strains: computational aspects and applications. In: Proceedings: 7th European Conference on Numerical Methods in Geotechnical Engineering.

Austin, L.G., 1990. Ball Mills, Semi-Autogenous Mills and High-Pressure grinding Rolls. The Pennsylvania State University.

Austin, L.G., Shah, I., 1983. A method for inter convension of microtrac and sieve size distributions.

Bailey, S., Hadler, K., Rescorl, T., Wilshaw, N., Lepoint, F. and Clermont, B., 2016. The effect of media loading conditions on vortex stability and grinding performance in SMD milling. In Comminution 16, Cape Town, South Africa.

Banini, G.A., 2000. An integrated description of rock breakage in comminution machines. PhD Thesis, JKMRC, University of Queensland, Australia.

Barreiro, A., Dominguez, J.M., Crespo, A.J.C., Garcia-Feal, O., Gomez Gesteira, M., 2015. Smoothed particle hydrodynamics for free-surface flows. Selec. Topics. Of Comp. Fluid Dyn. 119-136.

Bernhardt, C., Reinsch, E., Husemann, K., 1999. The influence of suspension properties on ultra-fine grinding in stirred ball mills. Powder Tech. 105, 357–361.

Blecher L, Kwade A, Schwedes J., 1996. Motion and stress intensity of grinding beads in a stirred media mill .1. Energy density distribution and motion of single grinding beads. Powder Tech. 86, 59-68.

Bao, J., McElroy, L., Jayasundra, C.T., Yang, R.Y., Yu, S.B., 2012. A soft-sensor approach to impact intensity prediction in stirred mills guided by DEM models. Min. Eng. 219, 151-157.

Barrios, G.K.P., de Carvalho, R.M., Tavares, L.M., 2011. Extending breakage characterisation to fine sizes by impact on particle beds. Miner. Proc. & Extrac. Met. 120:1, 37-44.

Bbosa, L.S., 2013. Probability based models for the power draw and energy spectra of a tumbling mills. PhD thesis, University of Cape Town.

Bond, F.C., 1952. The third theory of comminution. *Trans. AIME*. 193, 484–494.

Beinert, S., Schilde, C., Fragniere, G., Kwade, A., 2015. Analysis and modelling of bead contacts in wet-operating stirred media and planetary ball mills with CFD–DEM simulations. Miner. Eng. 134, 648-662.

Beinert, S., Fragniere, G., Schilde, C., Kwade, A., 2018. Mutiscale simulation of fine grinding and dispersin processes: Stressing probability, stressing energy and resultant breakage rate. Advanced powder tech. 29, 573-583.

Boemer, M., 2015. Discrete element method modelling of ball mills – liner wear evolution. Phd thesis university of Liege

Carvalho, R.M., Tavares, L.M., 2011. Leaping forward in SAG and AG Mill simulation using a mechanistic model framework. In: SAG2011 Conference, Vancouver.

Campbell, C.S., 1990. Rapid granular flows. Annual Rev. Fluid Mech. 22, 57–92.

Chandramohan, R., Powell, M., 2005. Measurement of particle interaction properties for incorporation in the discrete element method simulation. Miner. Eng. 18, 1142-1151.

Chaponda, M., 2011. Effect of operating variables on IsaMill performance using platinum bearing ores. University of Cape Town, MSc thesis.

Cheng, H., Greengard, L., Rokhlin, V., 1999. A fast adaptive multipole algorithm in three dimensions. J. of computational phys. 155 (2), 468-498.

Cleary, P.W., 1996. New implementation of viscosity: tests with Couette flows. SPH Technical Note 8, CSIRO DMS, Technical Report DMS – C 96/32.

Cleary, P.W., 1998a. Predicting charge motion, power draw, segregation, wear and particle breakage in ball mills using discrete element methods. Min. Eng. 11, 1061–1080.

Cleary, P.W., 1998b. Modelling confined multi-material heat and mass flows using SPH. Appl. Math. Modell. 22, 981–993.

Cleary, P.W., Hoyer, D., 2000. Centrifugal mills charge motion: comparison of DEM predictions with experiment. Int. J. Min. Proc. 59, 131–148.

Cleary, P.W., 2001a. Charge behaviour and power consumption in ball mills: sensitivity to mill operating conditions, liner geometry and charge composition. Int. J. Min. Process. 63, 79–114.

Cleary, P.W., 2001b. Recent advances in DEM modelling of tumbling mills. Min. Eng. 14, 1295–1319.

Cleary, P.W., 2001c. Modelling comminution devices using DEM. Int. J. Numer. Anal. Meth. Geomechan. 25, 83–105.

Cleary, P. W., Morrison, R. D., Morell, S., 2003. Comparison of DEM and experiment for a scale model SAG mill. Int. J. Min. Proc. 68, 129-165.

Cleary, P.W., 2004. Large scale industrial DEM modelling. Eng. Comput. 21, 169– 204.

Cleary, P.W., Sinnott, M.D., Morrison, R.D., 2006. Prediction of slurry transport in SAG mills using SPH fluid flow in a dynamic DEM based porous media. Min. Eng. 19, 1517–1527.

Cleary, P. W., Prakash, M., Ha, J., Stokes, N., and Scott, C., 2007. Smooth Particle Hydrodynamics: Status and future potential. Prog. Comp. Fluid Dynamics. 7, 70-90.

Cleary, P. W., 2009a. Industrial particle flow modelling using discrete element method. Eng. Comp. 26(6), 698-743.

Cleary, P. W., 2009b. Ball motion, axial segregation and power consumption in a full scale two chamber cement mill, Min. Eng. 22, 809-820.

Cleary, P.W., Sinnott, M.D., Morrison, R.D., 2008. DEM prediction of particle flows in grinding processes. Int. J. Numer. Methods Fluids 58, 319–353.

Cleary, P.W., Morrison, R.D., 2008. Editorial. Min. Eng. 21, 743.

Cleary, P.W., Morrison, R.D., 2011. Understanding fine ore breakage in a laboratory scale ball mill using DEM. Min. Eng. 24, 352-366.

Cleary, P.W., Morrison, R.D., 2012. Predicting patterns of slurry flow within and discharge from a 3D pilot SAG mill, Min. Eng. 39, 184-195.

Cleary, P. W., Sinnott, M. D., and Pereira, G. G., 2015a, Computational prediction of performance for a full scale Isamill: Part 1 – media motion and energy utilisation in a dry mill, Min. Eng. 79, 220-238.

Cleary, P.W., Sinnott, M.D., Pereira, G.G., 2015b. Computational prediction of performance for a full scale Isamill: Part 2 – wet models of charge and slurry transport. Min. Eng. 79, 239-260.

Cleary, P.W., 2015. Prediction of coupled particle and fluid flows using DEM and SPH. Min. Eng. 73, 85-99.

Cleary, P.W., Owen, P.J., 2016. Using DEM to understand scale-up for a HICOM mill. Min. Eng. 92, 86-109.

Cleary, P.W., Morrison, R., 2016. Comminution mechanisms, particle shape evolution and collision energy partitioning in tumbling mills. Min. Eng. 86, 75-95.

Cleary, P.W., Hilton, J.E., Sinnott, M.D., 2017. Modelling of industrial particle and multiphase flows. Powder Tech. 314, 232-252.

Cleary, P.W., Sinnott, M.D., Morrison, R.D., 2018. Prediction of slurry grinding due to media and coarse rock interactions in a 3D pilot SAG mill using a coupled DEM-SPH model, submitted to: Min. Eng. In press.

Cleary, P.W., Owen, P.J., 2019. Effect of particle shape on structure of the charge and nature of energy utilisation in a SAG mill. Min. Eng. 132, 48-68.

Cundall, P.A., Strack, O.D.L., 1979. A discrete numerical model for granular assemblies. Géotechnique. 29, 47–65.

Daraio, D., Villoria, J., Ingram, A., Alexiadis, A., Stitt, E.H., Marigo, M., 2019. Validation of a discrete element method (DEM) model of the grinding media dynamics within an attritor mill using positron emission particle tracking (PEPT) measurements. Appl. Sci. 9, 22.

Datta, A., Rajamani, R.K., 2001. A direct approach of modelling batch grinding mills using population balance principles and impact energy distribution. Int. J. of Miner. Proc. 64, 181-200.

Derksen, J.J., 2003. Numerical simulation of solids suspension in a stirred tank. Aiche Journal. 49, 2700-2714.

De Carvalho, R.M., Tavares, L.M., 2013. Predicting the effect of operating and design variables on breakage rates using the mechanistic ball mill model. Min. Eng. 43-44, 91 - 101.

De Klerk, D.N., Govender, I., Mainza, A.N., 2019. Geometric features of tumbling mill flow: a positron emission particle tracking investigation. Miner. Eng. 206, 41-49.

Djordjevic, N., 2003. Discrete element modelling of the influence of lifters on power draw of tumbling mills. Min. Eng. 16, 331–336.

Djordjevic, N., 2005. Influence of charge size distribution on net-power draw of tumbling mill based on DEM modelling. Min. Eng. 18, 375–378.

Di Felice, R., 1994. The voidage function for fluid-particle interaction systems. Int. J. Multiph. Flow. 20, 153–159.

Di Renzo, A., Di Maio, F.P., 2004. Comparison of contact-force models for the simulation of collisions in DEM-based granular flow codes. Chem. Eng. Sci. 59, 525–541.

Delaney, G.W., Cleary, P.W., Morrison, R.D., Cummins, S., Loveday, B., 2013. Predicting breakage and the evolution of rock size and shape distributions in AG and SAG mills using DEM. Min. Eng. 50-51, 132-139.

Ding, Z., Yin, Z., Liu, L., Chen, Q., 2007. Effect of grinding parameters on the rheology of pyrite–heptane slurry in a laboratory stirred media mill. Miner. Eng. 20, 701–709.

Duffy, S.M. 1994. Investigation into the performance characteristics of tower mills. Master's thesis, University of Queensland, JKMRC.

Epstein, B., 1948. Logarithmico-normal distribution in breakage of solids Ind. Eng. Chem. 40, 2289-2291.

Fadhel, H. B., Frances, C., 2001. Wet batch grinding of alumina hydrate in a stirred bead mill. Powder Tech. 119, 257 - 268.

Fayed, M. and Otten, L., 1997. Handbook of powder science and technology. Chapman and Hall, New York, NY.

Fernandez, J.W., Cleary, P.W., Sinnott, M.D., Morrison, R.D., 2011. Using SPH one way coupled to DEM to Model Wet Industrial Banana Screens. Min. Eng. 24, 741– 753.

Franke, J., Cleary, P.W., Sinnott, M., 2014. How to account for operating condition variability when predicting liner operating life with DEM - a case study. In Comminution14, Cape Town, South Africa.

Fuerstenau, D. W., Abouzeid, A.Z.M., 2002. The energy efficiency of ball milling in comminution. Int. J. Min. Proc. 67(1-4), 161-185.

Gao, M.W., Weller, K.R., 1993. Fine grinding in mineral processing using stirred ball mills. In 5th mill operator's conference. AUSIMM, 61-67.

Gao, M., Forssberg, E., 1994. Prediction of product size distributions for a stirred ball mill. Powder Tech. 84 (2), 101–106.

Gao, M.W., Forssberg, K.S.E., Weller, K.R., 1996. Power predictions for a pilot scale stirred ball mill. Int'l J. Miner. Proc. 44-45, 641-652.

Gao, M., Holmes, R., Pease, J., 2007. Plenary lecture: The latest developments in fine grinding and ultrafine grinding technologies.

Garg, D., Longo, A., Papale, P., 2018. Modelling free surface flows using stabilized finite element method. Math. Prob. Eng. 2018.

Greengard, L., Rokhlin, V., 1987. A fast algorithm for particle simulation. J. of Computational Phys. 73, 325-348.

Greengard, L., Kropinski, M. C., 1998. An Integral Equation Approach to the Incompressible Navier-Stokes Equations in Two Dimensions. SIAM J. Sci. Comput. 20, 318-336.

Govender, I., McBride, A. T., Powell, M. (2004). Improved Experimental Tracking Techniques for Validating Discrete Element Method Simulations of Tumbling Mills. J. of Experimental Mech. 44(5), 593-607.

Govender, I., Cleary, P.W., Mainza. A., 2013. Comparisons of PEPT derived charge features in wet milling environments with a friction-adjusted DEM model. Chem. Eng. Sci. 97, 162-175.

Gudin, D., Turczyn, R., Mio, H., Kano, J., Saito, F., 2006. Simulation of the movement of beads by the DEM with respect to the wet grinding process. AICHE. 52, 3421-3426.

Gudin, D., Kano, J., Saito, F., 2007. Effect of the friction coefficient in the discrete element method simulation on media motion in a wet bead mill. Advanced Powder tech. 18, 555-567.

He, M., Wang, Y., Forssberg. E., 2006. Parameter effects on wet ultrafine grinding of Limestone through slurry rheology in a stirred media mill. Powder Tech. 161, 10-21.

He, M., Forssberg, E., 2007. Influence of slurry rheology on stirred media milling of quartzite. Int. J. of Miner. Proc. 84, 240 - 251.

Herbst, J.A., Nordell, L., 2001. Optimization of the design of sag mill internals using high fidelity simulation. In: Barratt, Allan, Mular (Eds.), Proc. of the SAG Conference. 4, 150–164.

Herbst, J.A., Sepulveda, J.L., 1978. Fundamentals of fine and ultra-fine grinding in a stirred ball mill, Int'l Powder and Bulk Solids Handling Conference. Chicago, IL. 452-470.

Hennart, S. L. A., Wildeboer, W., van Hee, P. and Meesters, G., 2009. Identification of the grinding mechanisms and their origin in a stirred ball mill using population balances. Chem. Eng. Sci. 64, 4123 - 4130.

Hertz, H., 1882. Uber die Berhrung fester elastischer Korper (On the contact of elastic solids). *Journal fur die Reine und Angewandte Mathematik, 92*(156-171).

Hilton, J. E., Mason, L., and Cleary, P. W., 2010. Dynamics of gas–solid fluidized beds with non-spherical particle geometry. Chem. Eng. Science. 65, 1584—1596.

Hogg, R., 1999. Breakage mechanism and mill performance in ultrafine grinding. Powder Tech. 105, 135-140.

Hou, Y., 2011. DEM simulation and analysis of operating parameters on grinding performance of a vertical stirred mill. MSc thesis, University of British Colmbia, Canada.

Hölzer, A., Sommerfeld, M., 2008. New simple correlation formula for the drag coefficient of non-spherical particles, Powder Tech. 184, 361-365.

Hosain, Md.L., Fdhila, R.B., 2015. Literature review of accelerated CFD simulation methods towards online application in: The 7th International conference of applied energy. 75, 3307-3314.

Hukki, R.T., 1962. Proposal for a solomonic settlement between the theories of von Rittinger, Kick, and Bond. *Trans. AIME*. 223, 403–408.

Hirt, C. W., Nichols, B.D., 1981. Volume of fluid (VOF) method for the dynamics of free boundaries. Journal of Comp. Phys. 39, 201–255.

Inoue, T., Okaya, K., 1996. Grinding mechanism of centrifugal mills – a simulation study based on the discrete element method. Int. J. Min. Process. 44–45, 425–435.

Jankovic, A. 1998. Mathematical modeling of stirred mills, PhD thesis, University of Queensland, JKMRC.

Jankovic, A., 2003. Variables affecting the fine grinding of minerals using stirred mills. Min. Eng. 16, 337–345.

Jankovic, A., 2008. A Review of Regrinding and Fine Grinding Technology - the Facts and Myths. Asia-Pacific, Metso minerals.

Jayasundara, C.T., Yang, R.Y., Yu, A.B., Curry, D., 2008. Discrete particle simulation of particle flow in IsaMill — effect of grinding medium properties. Chem. Eng. J. 135, 103–112.

Jayasundara, C.T., Yang, R.Y., Guo, B.Y., Yu, A.B., Rubenstein, J., 2009. Effect of slurry properties on particle motion in IsaMills. Min. Eng. 22 886-892.

Jayasundara, C.T., Yang, R.Y., Yu, A.B., Rubenstein, J., 2010. Effect of disc rotation speed and media loading on particle flow and grinding performance in a horizontal stirred mill. Miner. Eng. 96, 27-35.

Jayasundara, C.T., Yang, R.Y., Guo, B.Y., Yu, A.B., Govender, I., Mainza A.N., van der Westhuizen, A., Rubenstein, J., 2011. CFD-DEM modelling of particle flow in Isamills – Caomparison between simulations and PEPT measurements. Miner. Eng. 24, 181-187.

Jayasundara, C.T., Yang, R.Y., Yu, A.B., 2012. Effect of slurry properties on particle motion in IsaMills. Min. Eng. 33 66-71.

Jenczewski, T.J., 1972. The grinding of organic dyestuffs, Canadian J. Chem. Eng. 50.

Jonsén, P., Pålsson, B.I., Stener, J., Häggblad, H., Tano, K., Berggren, A., 2014. Development of physically based tumbling mill models. In: IMPC 2014, 20-24 October, Santiago, Chile.

Johnson, K. L., 1985. Contact Mechanics, second ed. Cambridge University Press, New York.

Kapur, P. C., Pande, D., Fuerstenau, D. W., 1997. Analysis of single-particle breakage by impact grinding. Int. J. of Miner. Proc. 49, 223 - 236.

Kafui, D.K., Thornton, C., Adams, M.J., 2002. Discrete particle-continuum fluid modelling of gas–solid fluidised beds. Chem. Eng. Sci. 57, 2395–2410.

Kalala, J.T., Bwalya, M.M., Moys, M.H., 2005. Discrete element method (DEM) modelling of evolving mill liner profiles due to wear. Part I: DEM validation. Miner. Eng. 8, 1392-1397.

Keikkala, V., Paz, A., Komminaho, T., Lehto, H., Loucas, J., 2018. Energy efficient rotor design for Higmills. Miner. Eng. 128, 266-274.

Kharaz, A. H., Gorham, D. A., Salman, A. D., 2001. An experimental study of the elastic rebound of spheres. Powder Tech. 120(3), 281-291.

Kalala, J.T., Breetzke, M., Moys, M.H., 2008. Study of the influence of liner wear on the load behaviour of an industrial dry tumbling mill using the discrete element method (DEM). Int. J. Miner. Process. 86 (1), 33–39.

Kalra, R., 1999. Overview on alternative methods for fine and ultra- fine grinding. In: IIR Conference, Crushing & Grinding ‘99, Perth.

Khanal, M., Morrison, R. D., 2009. Discrete Element Method Simulation of the Effect of Tumbling Time and Particle Size in a 300-mm Diameter Mill. Chem. Eng. Tech. 32(10), 1630-1634.

Kick, F., 1885. Das Gesetz der proportionalen Widerstande und seine anwendung felix. Leipzig, Germany.

Kim, S., Choi, W.S., 2008. Analysis of ball movement for research of grinding mechanism of a stirred ball mill with 3D discrete element method. Korean. J. Chem. Eng. 25, 585-592.

Kim, S., Choi, W.S., Chung, H., 2009. Analysis of grinding rate constant on a stirred ball mill using discrete element method simulation. J. Am. Ceram. Soc. 92, 531-534.

King, R.P., 2001. Modeling and simulation of mineral processing systems. Oxford: Butterworth-Heinemann.

Knorr, B.R., Allen, J., 2010. Selection criteria of stirred milling technologies. In Comminution10, Cape Town, South Africa.

Kulya, C., 2008. Using discrete element modelling (DEM) and breakage experiments to model the comminution action in a tumbling mill. MSc thesis, University of Cape Town South Africa.

Kwade, A., 1999a. Wet comminution in stirred media mills - research and its practical application. Power Tech. 105, 14 - 20

Kwade, A., 1999b. Determination of the most important grinding mechanism in stirred media mills by calculating stress intensity and stress number. Powder Tech. 105, 382 - 388.

Kwade, A. and Schwedes, J., 2002. Breaking characteristics of different materials and their effect on stress intensity and stress number in stirred media mills. Powder Tech. 122, 109 - 121.

Langston, P.A., Tuzun, U., Heyes, D.M., 1994. Continuous potential discrete particle simulations of stress and velocity-fields in hoppers—transition from fluid to granular flow. Chem. Eng. Sci. 49, 1259–1275.

Langston, P.A., Tuzun, U., Heyes, D.M., 1995. Discrete element simulation of granular flow in 2D and 3D hoppers—dependence of discharge rate and wall stress on particle interactions. Chem. Eng. Sci. 50, 967–987.

Lee, H., Cho, H., Kwon, J., 2010. Using the discrete element method to analyse the breakage rate in a centrifugal/vibration mill. Powder Tech. 198, 364–372.

Lisso, M., 2013. Evaluating the effect of operating variables on energy consumption in stirred mills. University of Cape Town, MSc thesis.

Malek-Moghaddam, M., Yahyaesi, M., Banisi, S., 2013. A method to predict shape and trajectory of charge in industrial mills. Miner. Eng, 46-47, 157-166.

Mankosa, M. J., Adel, G. T., Yoon, R. H., 1986. Effect of Media Size in Stirred Ball Mill Grinding of Coal. Powder Tech. 49, 75 - 82.

Martins, S., Radziszewski, P., 2015. Generalizing a shear-volume power model for stirred mill power prediction. Miner. Eng. 77, 150-158.

Mayank. K., Narasimha, M., Govender I., 2015. Two way coupled CFD-DEM model to predict tumbling mill dynamics. In SAG, Vancouver Canada.

Mayfield, N., 2018. Personal communication.

Mainza, A.N., 2006. Contribution to the understanding of the three-product cyclone on the classification of a dual density platinum ore. University of Cape Town, PhD thesis.

Malahe M., 2011. One way coupled DEM-CFD model to simulate the free surface profile of slurry in a tumbling mill M.Sc. Thesis University of Cape town.

Mayank, k., Malahe, M., Govender, I., Mangadoddy, N., 2015. Coupled DEM-CFD model to predict the tumbling mill dynamics. In: IUTAM Symposium on Multiphase flows with phase change: challenges and opportunities, Hyderabad, India.

Mazzinghy, D.B., Alves, V.K., Schneider, C.L., Galery, R., Patricia, M.C., Faria P.M., Alvarenga, T., 2012. Predicting the size distribution in the product and power requirements of a pilot scale Vertimill. Procemin2012. Chile.

McBride, A. T., Powell, M. S., 2006. A structured approach to modelling sag mill liner wear - numerical modelling of liner evolution. SAG 2006, University of British Columbia.

McElroy, L., Bao., J., Jayasundra, C.T., Yang, R.Y., Yu, A.B., 2012. A soft sensor approach to impact intensity prediction in stirred mills guided by DEM models. Powder tech. 219, 151-157.

Mindlin, R. D., Deresiewicz, H., 1953. Elastic spheres in contact under varying oblique forces. J of App. Mech. 20, 327-344.

Mishra, B.K., Rajamani, R.J., 1992. The discrete element method for the simulation of ball mills. App. Math. Model. 16, 598–604.

Mishra, B.K., Rajamani, R.K., 1994. Simulation of charge motion in ball mills. Part 1: experimental verifications. Int. J. Min. Process. 40, 171–186.

Misra, A., & Cheung, J. (1999). Particle motion and energy distribution in tumbling ball mills. Powder Tech. 105, 222-227.

Monaghan, J.J., 1992. Smoothed particle hydrodynamics. Annu. Rev. Astron. Astrophys. 30, 543-74.

Monaghan, J. J., 1994. Simulating free surface flows with SPH. J. Comput. Phys. 110, 399-406.

Moore, A., Gallimore, M., Knorr, B., Radisszewski, P., 2016. Pursuit of best practices with the Stirred Media Detritor. In: Proceedings of Comminution 16, Cape Town, South Africa.

Morrel, S., 2007. A method for predicting the specific energy requirement of comminution circuits and assessing their energy-utilisation efficiency. Miner. Engi. 21, 224-233

Morrison, R., Cleary, P.W., 2004. Using DEM to model ore breakage within a pilot scale SAG mill. Min. Eng. 17, 1117–1124.

Morrison, R.D., Cleary, P.W., 2008. Towards a virtual comminution machine. Min. Eng. 21, 770–781.

Morrison, R.D., Cleary, P.W., Sinnott, M.D., 2009. Using DEM to compare the energy efficiency of pilot scale ball and tower mills. Min. Eng. 22 665-672.

Moukalled, F., Mangani, L., Darwish, M., 2016. The finite volume method in computational fluid dynamics. Springer international publishing, 113.

Molls, H.H., Hornle, R., 1972. DECHEMA—Monography 69 Tl 2. pp. 631–661

Mueller, S., Liewellin, E.W., Mader, H.M., 2010. The rheology of suspensions of solid particles. Proc. R. Soc. A. 466, 1201-1228.

Mulenga, F.K., Moys, M.H., 2014. Effects of slurry filling and mill speed on the net power draw of a tumbling ball mill. Miner. Eng. 56, 45-56.

Napier-Munn, T.J., Morrell,S., Robert, D., Kojovic, T., 1996. Mineral Comminution Circuits: Their Operation and Optimisation, Queensland: Julius Kruttschnitt Mineral Research Centre, 1996.

Ndimande, C.B., Cleary, P.W., Mainza, A.N., Sinnott, M.D., 2019. Using two-way coupled DEM-SPH to model an industrial scale Stirred Media Detritor. Miner. Eng. 137, 259 -276.

Nichols, B.D., Hirt, C.W., 1975. Methods for calculating multidimensional transient free surface flows past bodies. In Proceedings of the 1st Ineternational conference on Num. Ship Hydrodynamics, Gaithersburg, ML.

Norejko, T., van de Wielen, K., Hadler, K., Wilshaw, N., 2018. Linking stirred media detritor vortex stability to operational variables. In Comminution 18, 16-19 April, Cape Town, South Africa.

Novosad, J., 1964. Studies on granular materials I. Collection of Czechslovak Chemical Comm. 29, 2681-2696.

Nesset, J.E., Radziszewski, P., Hardie, C., Leroux, D., 2006. Assessing the Performance and Efficiency of Fine Grinding Technologies. 38th Meeting of the Canadian Mineral Processors, pp. 283-309.

Ntsele, C., and Allen, J. 2012. Technology Selection of Stirred Mills for Energy Efficiency in Primary and Regrinding Applications For The Platinum Industry. South African Institute of Mining and Metallurgy, 781–808.

Palaniandy, S., 2017. Extending the application of JKFBC for gravity induced stirred mills feed ore characterisation. Miner. Eng. 101, 1-9.

Powell, M., Nurick, G.N., 1996. A study of charge motion in rotary mills part 2 – experimental work. Miner. Eng. 9, 343-350.

Powell, M., Govender, I., McBride, A. T., 2008. Applying DEM outputs to the unified comminution model. Min. Eng. 21, 744-750.

Powell, M.S., Weerasekara, N.S., Cole, S., LaRoche, R.D., Favier, J., 2011. DEM modelling of liner evolution and its influence on grinding rate in ball mills. Min. Eng. 24, 341–351.

Radziszewski, P., 2013. Assessing the stirred mill design space, Min. Eng. 41, 9-16.

Radziszewski, P., Allen, J., 2014. Towards a better understanding of stirred technologies - estimating power consumption and energy use. In 46th Annual Canadian Mineral Processors Operators Conference. Ottawa, Ontario.

Rajamani, R.K., Mishra, B.K., 1996. Dynamics of ball and rock charge in SAG mills. In: Proceedings of the SAG Conference, Vancouver, Canada, 700-712.

Rajamani R.K., Alkac D., Delgadillo J.A., Kumar P., Page D., Fillion M., and Pelletier S. 2011. Pulp-Lifter Flow Modeling Study in Pilot Scale Mills and Application to Plant Scale Mills.

In Proceedings of the International Autogenous Grinding, Semiautogenous Grinding and High-Pressure Roll Technology, Vancouver, B.C. Canada.

Rittinger, R.P., 1867. Lehrbuch der Aufbereitungskunde. Ernst and Korn, Berlin, Germany.

Rule, C. M., Knopjes., C.M., Atkinson, R.J., 2008. Ultra-fine grinding of intermediate flotation concentrates. In: 3rd International Platinum Conference 'Platinum in transformation', The South African Institute of Mining and Metallurgy.

Rule, C.M., 2011. Stirred milling – new comminution technology in the PGM industry. The Journal of The South African Institute of Mining and Metallurgy. 111, 101–107.

Santham, P.R., Dreizin, E.L., 2012. Predicting conditions for scaled-up manufacturing of materials prepared by ball milling. Powder tech. 221, 403-411.

Santhanam, P.R., Ermoline, A., Dreizin, E., 2013. Discrete element model for an attritor mill with impeller responding to interactions with milling balls. Chem. Eng. Sci. 101, 366-373.

Shibayama, A., Mori, S., 1999. A history of the tower mill pulverizer. J. Res. Proc. Soc. Japan. 46 (1), 24–30

Shi, F., Kojovic, T., 2007. Validation of a model for impact breakage incorporating particle size effect. Int. J. Min. Process. 82(3), 156–163.

Sinnott, M.D., Cleary, P.W., Morrison, R.D., 2006a. Analysis of Stirred Mill performance using DEM simulation: Part 1 – media motion, energy consumption and collisional environment. Min. Eng. 19, 1537–1550.

Sinnott, M.D., Cleary, P.W., Morrison, R.D., 2006b. Analysis of Stirred Mill performance using DEM simulation: Part 2 – coherent flow structures, liner stress and wear, mixing and transport. Min. Eng. 19, 1551–1572

Sinnott, M.D., Cleary, P.W., Morrison, R.D., 2011a. Slurry flow in a tower mill. Min. Eng. 24, 152–159.

Sinnott, M.D., Cleary, P.W., Morrison, R.D., 2011b. Is media shape important for grinding performance in stirred mills?. Min. Eng. 24, 138–151.

Sinnott, M.D., Cleary, P.W., Morrison, R.D., 2015. Simulation of overflow ball mill discharge and trommel flow using combined DEM and SPH modelling. Proc. SAG 2015, Paper 30, Vancouver, September (2015).

Sinnott, M. D., Cleary, P. W., and Morrison, R. M., 2017. Combined DEM and SPH simulation of overflow ball mill discharge and trommel flow, Min. Eng. 108, 93-108.

Sinnott, M.D., Cleary, P.W., 2017. Particulate and water mixing in the feed box for a screen, Min. Eng. 109, 109-125.

Sout-Iglesius, A., Idelsohn, S.R., Marti, J., Zamora-Rodriguez, R., Onate. E., 2008. Modeling of free surface flows with elastic bodies interactions. In: 27th Synposium on naval hydrodynamics. Seol, Korea.

Tavares, L., King, R., 1998. Single-particle fracture under impact loading. Int. J. Min. Process. 54(1), 1–28.

Tamblyn, R.J., 2009. Analysis of energy requirements in stirred media mills. University of Birmingham, PhD thesis.

Teng, H. and Zhao, T. S., (2000). An extension of Darcy's law to non-Stokes flow in porous media, Chemical Engineering Science, 55, 2727-2735.

Theuerkauf J, Schwedes J., 1999. Theoretical and experimental investigation on particle and fluid motion in stirred media mills. Powder Tech. 105, 406-412.

Thornton, C., Cummins, S., Cleary, P.W., 2013. An investigation of the comparative behavior of alternative contact force models during inelastic collisions. Powder Tech. 233, 30–46.

Toraman, O.Y., Katircioglu, D., 2011. A study of the effect of process parameters in stirred ball mill. Miner. Eng. 22, 26-30.

Traneçon, A., de Luca, P., Binetry, C., Kunhert, J., 2006. Finite Pointset Method (FPM): A meshfree approach for incompressible flow situations applied to composite materials. 8th international conference on flow processes in composite materials, Douai, France.

Tuzun, M.A., 1993. A detailed study on comminution in a vertical stirred ball mill, PhD thesis, University of Natal, South Africa.

Varinot, C., Hiltgun, S., Pons, M. N., Dodds, J., 1997. Identification of the fragmentation mechanisms in wet-phase fine grinding in a stirred bead mill. Chem. Eng. Sci. 52 (20), 3605 - 3612.

Van der Westhuizen, A.P., Govender, I., Mainza, A.N., Rubenstein, J., 2011. Tracking the motion of media particles inside an IsaMill™ using PEPT. Miner. Eng. 24, 195–204.

Venugopal, R., Rajamani, R. K., 2001. 3D simulation of charge motion in tumbling mills by the discrete element method. Powder Tech. 115, 157-166.

Venugopal, R., Rajamani, R.K., 2001. 3D simulation of charge motion in tumbling mills by the descrete element method. Powder Tech. 115 (2), 157-166.

Van Nierop, M. A., Glover, G., Hinde, A. L., & Moys, M. H. (2001). A discrete element method investigation of the charge motion and power draw of an experimental two-dimensional mill. Int. J. of Min. Proc. 61, 77-92.

Walton, O. R., Braun, R. L., 1986. Viscosity, granular-temperature, and stress calculations for shearing assemblies of inelastic, frictional disks. J. of Rheol. 30, 949-980.

Walton, O.R., 1993. Numerical simulation of inclined chute flows of monodisperse inelastic, frictional spheres. Mechanics of Mater. 16, 239–247.

Wang, Y., Forssberg, E., 2000. Product size distribution in stirred media mills. Miner. Eng. 13(4), 459 – 46.

Wang, M.H., Yang, R.Y., Yu, A.B., 2012. DEM investigation of energy distribution and particle breakage in tumbling ball mills. Powder Tech. 223, 83-91.

Weit, H., & Schwedes, J. 1987. Scale-up of power consumption in agitated ball mills. Chem. Eng. & Technol. 10 (1), 398-404.

Weerasekara, N.S., Powell, M.S., Cole, S., Favier, J., 2010. Modelling breakages environ- ment in tumbling mills using DEM and analyzing the outputs. The Fifth Interna- tional Conference on Discrete Element Methods, Queen Mary, University of London, London, London, UK.

Weller, K., Gao, M., 1999. Ultra-fine grinding. AJM Crushing and Grinding Conference, Kalgoorlie.

Wills, B.A., 1992. Mineral processing technology. Pergamon press.

Wills, B.A., Napier-Munn, 2006. Mineral-processing Technology. 7th ed. Elsevier Science and Technology Books

Xu, B.H., Yu, A.B., 1997. Numerical simulation of the gas-solid flow in a fluidized bed by combining discrete particle method with computational fluid dynamics. Chem. Eng. Sci. 52, 2785–2809.

Yang, R. Y., Yu, A. B., McElroy, L., & Bao, J. (2008). Numerical simulation of particle dynamics in different flow regimes in a rotating drum. *Powder Technology, 188*, 170-177.

Yang, R. Y., Zou, R. P., & Yu, A. B., 2003. Microdynamic analysis of particle flow in a horizontal rotating drum. Powder Tech. 130, 138-146.

Yamamoto Y., Soda, R., Kano, J., Saito, F., 2014. Application of DEM modified with enlarged particle model to simulation of bead motion in a bead mill. Particuo. 14. 103-108.

Yang, R.Y., Jayasundara, C.T., Yu, A.B., Curry, D., 2006. DEM simulation of the flow of grinding media in IsaMill. Min. Eng. 19 (10), 984–994.

Yue, J., Klein, B., 2004. Particle breakage kinetics in horizontal stirred mills. Miner. Eng. 18, 325-331.

Zheng, J., Harris, C. C., Somasundaran, P., 1996. A study on grinding and energy input in stirred media mills. Power Tech. 86, 171 - 178.

Zhou, Y.C., Wright, B.D., Yang, R.Y., Xu, B.H., Yu, A.B., 1999. Rolling friction in the dynamic simulation of sandpile formation. Physica A. 269, 536–553.

Zhu, H.P., Yu, A.B., 2002. Averaging method of granular materials. Physical Review E 66, 021302.

9 Appendix

9.1 Mill speed selection

Since the impeller speed for the two industrial scales is not public, the speed of the SMD 18.5-E Which is known (200 rpm), is used as the base case to determine the speed of the industrial scale mills. The mills are charged with 8mm media balls to 26% of the grinding volume as stated in section 3.4. DEM only simulations were at all speeds specified in section 3.5 until steady state is reached. To compare the charge structures, a horizontal slice through the centre of the mill is taken for all scales. The horizontal sections are taken at four phases of the impeller for the base case which is the SMD 18.5-E. The media is coloured by velocity and the axial component of velocity as shown in Figure 72. The maximum velocity and axial velocity chosen for the SMD 18.5-E is 5 m/s and ±2 m/s respectively. The charge structure of the industrial scale mills at all the speeds tested is compared to that of the SMD 18.5-E at similar impeller phases. To select the velocities at the industrial scale to compare with the SMD 18.5-E, a scale factor V_{scale} is used which is determined by the following formula

$$V_{scale} = \frac{RPM_{industrial\,scale} D_{Industrial\,scale}}{RPM_{pilot\,scale} D_{pilot\,scale}}, \qquad (38)$$

Where $D_{industrial\ scale}$ is the mill diameter of the industrial scale SMD and $D_{pilot\ scale}$ is the mill diameter of the SMD 18.5-E.

The power data for the different speeds used is shown below.

	Case	scale ratio of velocity	Fixed power (KW)	RPM	Diam of Impeller (m)	Tip speed	power draw (kW)
SMD18.5	1	1	18.5	220	0.694	7.994	16
	2	1	18.5	200	0.694	7.268	14
	3	1	18.5	180	0.694	6.541	12
SMD355	1	2.07	355	135	2.044	14.448	400
	2	1.97	355	129	2.044	13.806	349
	3	1.84	355	120	2.044	12.843	300
	4	1.76	355	115	2.044	12.308	270
	5	1.68	355	110	2.044	11.773	250
	6	1.53	355	100	2.044	10.702	200
SMD1100	1	2.06	1100	83.75	3.204	14.050	988
	2	1.92	1100	78	3.204	13.085	972
	3	1.84	1100	75	3.204	12.582	835

From the comparison of the charge structure, the speeds selected for the SMD 335-E and the SMD 1100-E are 115 rpm and 78 rpm respectively. These speeds are in no way optimal from a process perspective. They are only used to study the operational behaviour of these devices.

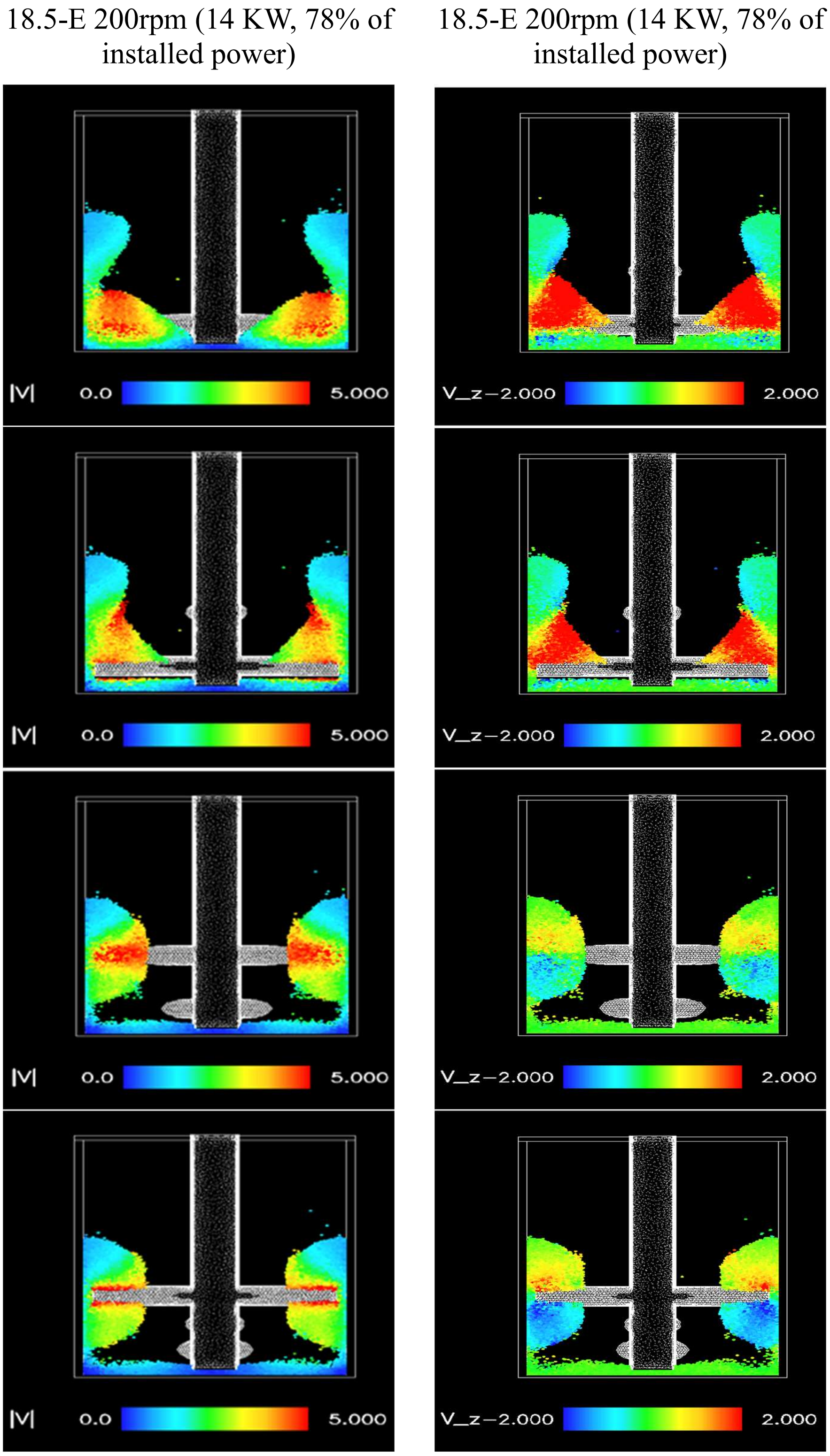

18.5-E 200rpm (14 KW, 78% of installed power)

18.5-E 200rpm (14 KW, 78% of installed power)

Figure 72: Horizontal section through the SMD 18.5-E. Each row shows a different phase of the impeller. Media is coloured by velocity in the first column, and axial velocity in the second column.

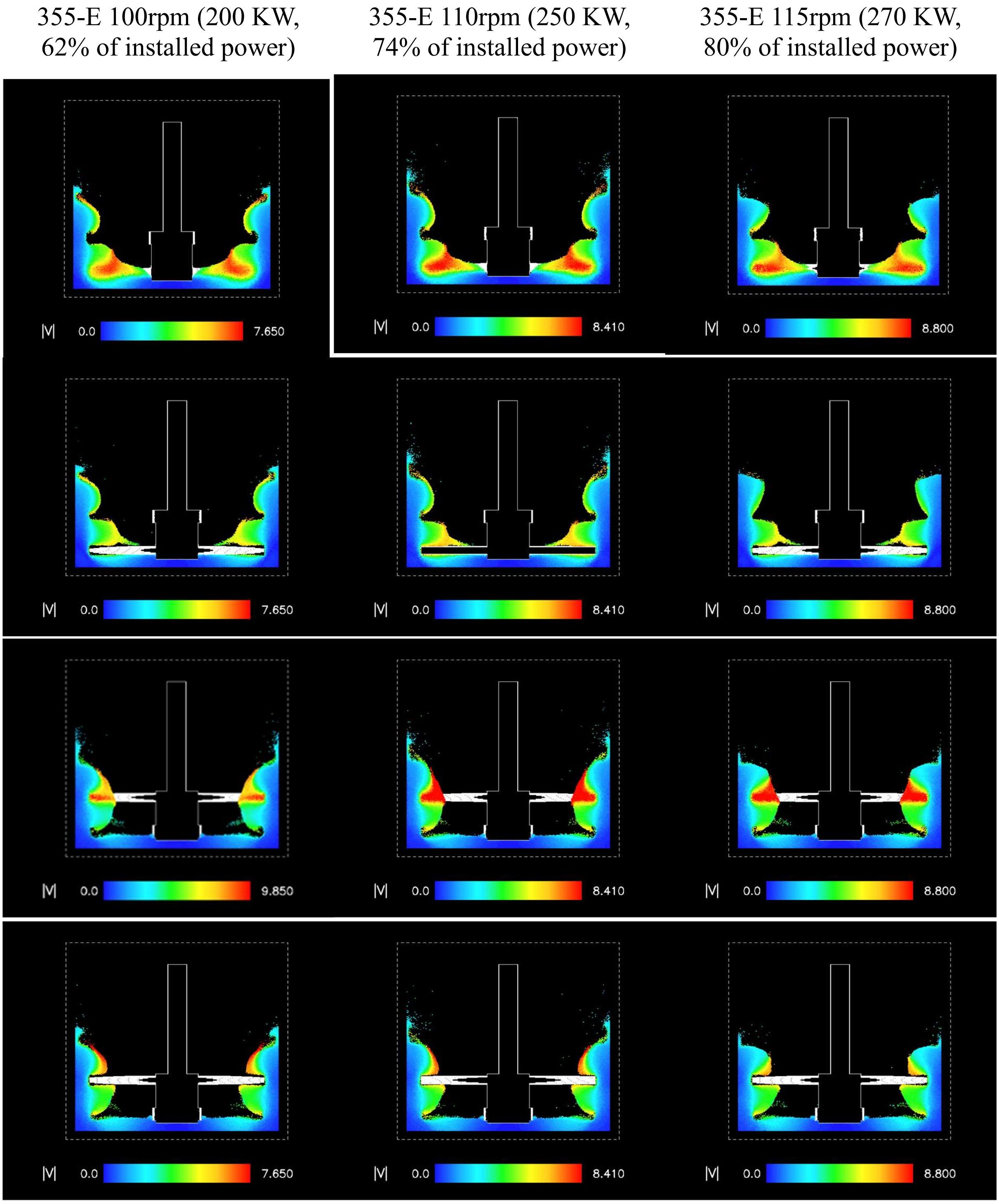

355-E 100rpm (200 KW, 62% of installed power)

355-E 110rpm (250 KW, 74% of installed power)

355-E 115rpm (270 KW, 80% of installed power)

Figure 73: Horizontal section through the SMD 355-E. Each row shows a different phase of the impeller like that of the SMD18.5-E. Media is coloured by velocity.

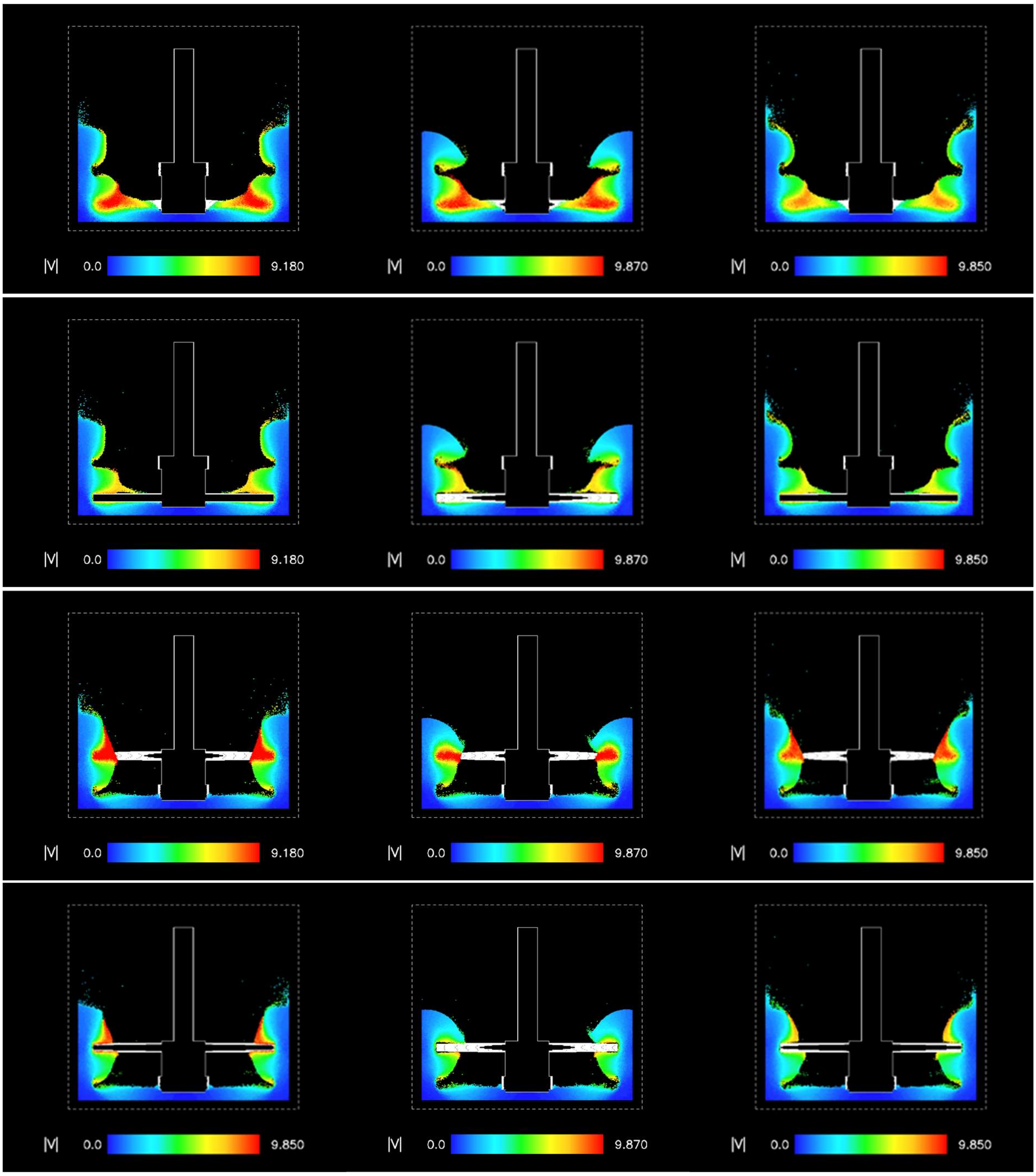

355-E 120rpm (300 KW, 87% of installed power)

355-E 129rpm (356 KW, 99% of installed power)

355-E 135rpm (400 KW, 105.9% of installed power)

Figure 74: Horizontal section through the SMD 355-E. Each row shows a different phase of the impeller like that of the SMD18.5-E. Media is coloured by velocity.

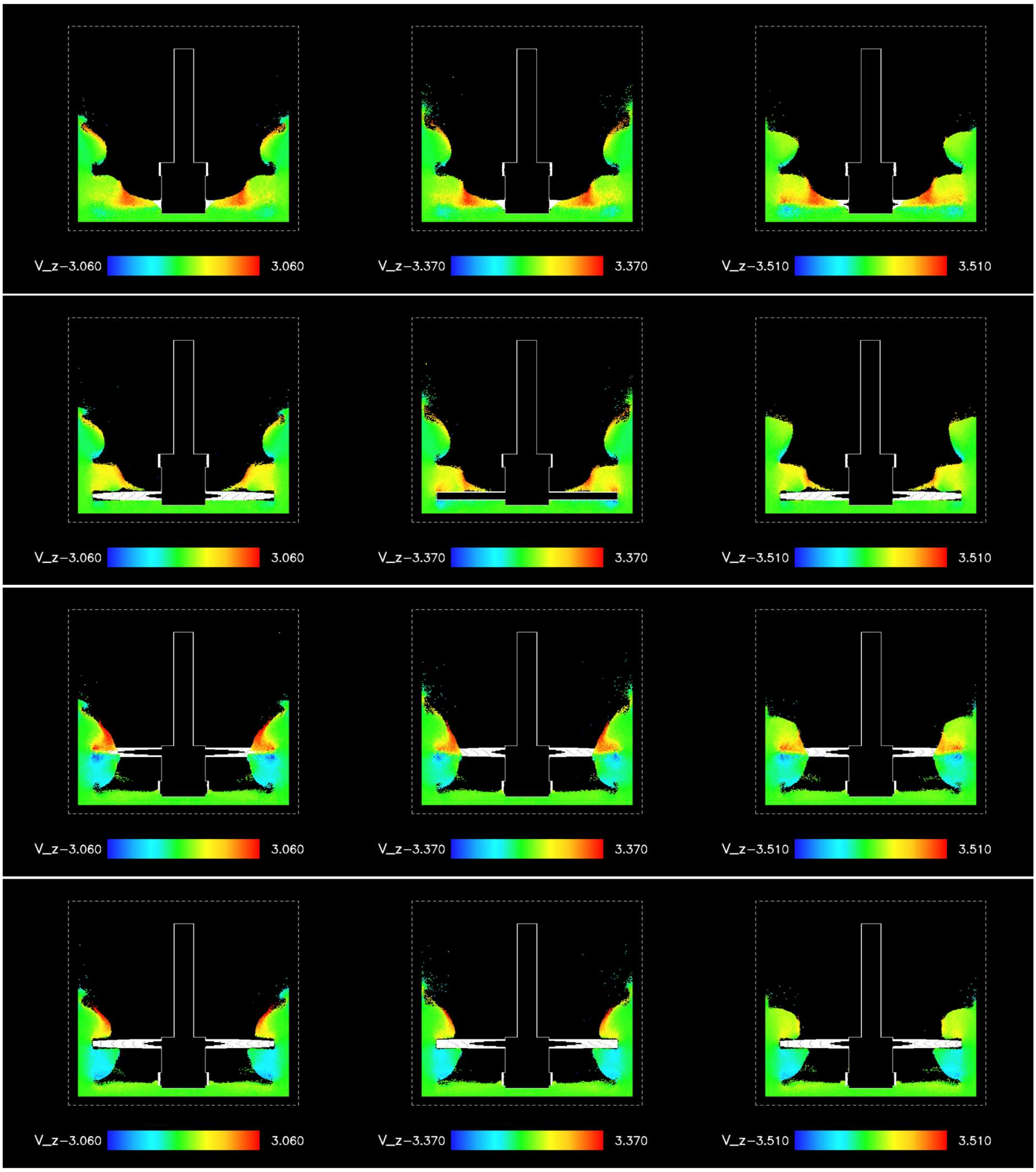

355-E 100rpm (200 KW, 62% of installed power)

355-E 110rpm (250 KW, 74% of installed power)

355-E 115rpm (270 KW, 80% of installed power)

Figure 75: Horizontal section through the SMD 355-E. Each row shows a different phase of the impeller like that of the SMD18.5-E. Media is coloured by velocity.

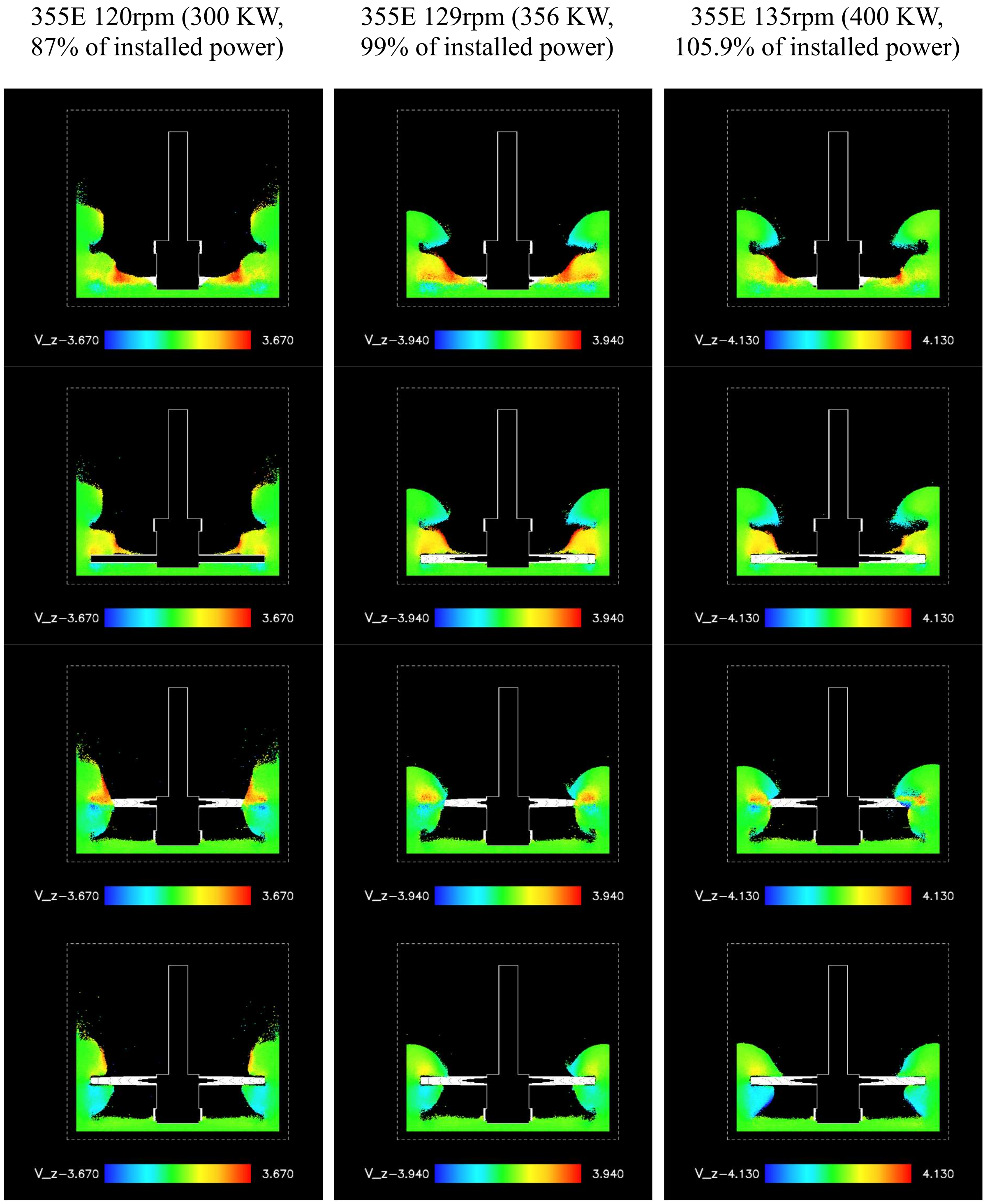
355E 120rpm (300 KW, 87% of installed power)

355E 129rpm (356 KW, 99% of installed power)

355E 135rpm (400 KW, 105.9% of installed power)

Figure 76: Horizontal section through the SMD 355-E. Each row shows a different phase of the impeller like that of the SMD18.5-E. Media is coloured by axial velocity.

1100-E 75rpm (835 KW, 75% of installed power)

1100-E 78rpm (972 KW, 88% of installed power)

1100-E 83.75rpm (1080 KW, 92% of installed power)

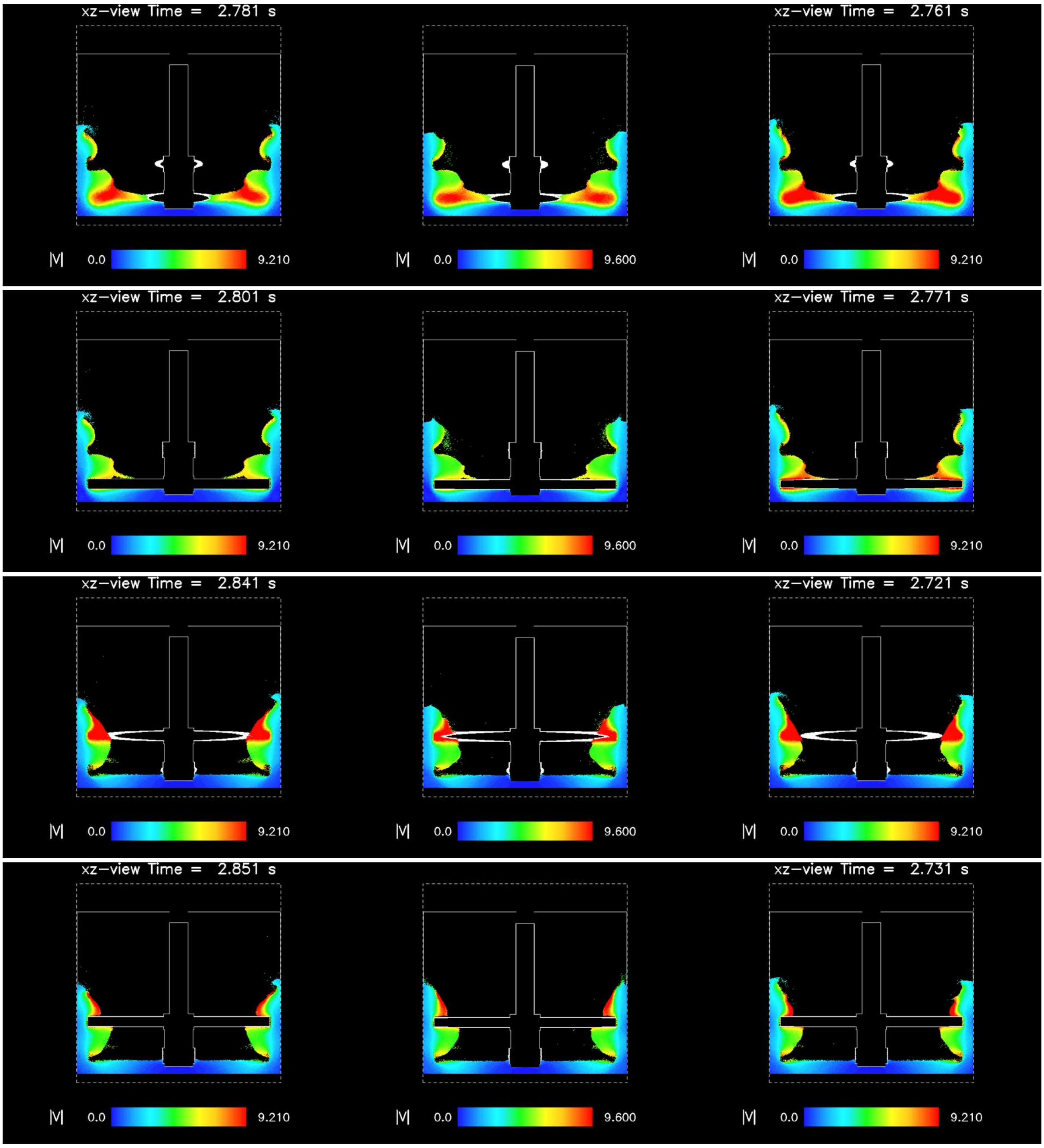

Figure 77 Horizontal section through the SMD 1100-E. Each row shows a different phase of the impeller like that of the SMD18.5-E. Media is coloured by velocity.

1100-E 75rpm (835 KW, 75% of installed power)

1100-E 78rpm (972 KW, 88% of installed power)

1100-E 83.75rpm (1080 KW, 92% of installed power)

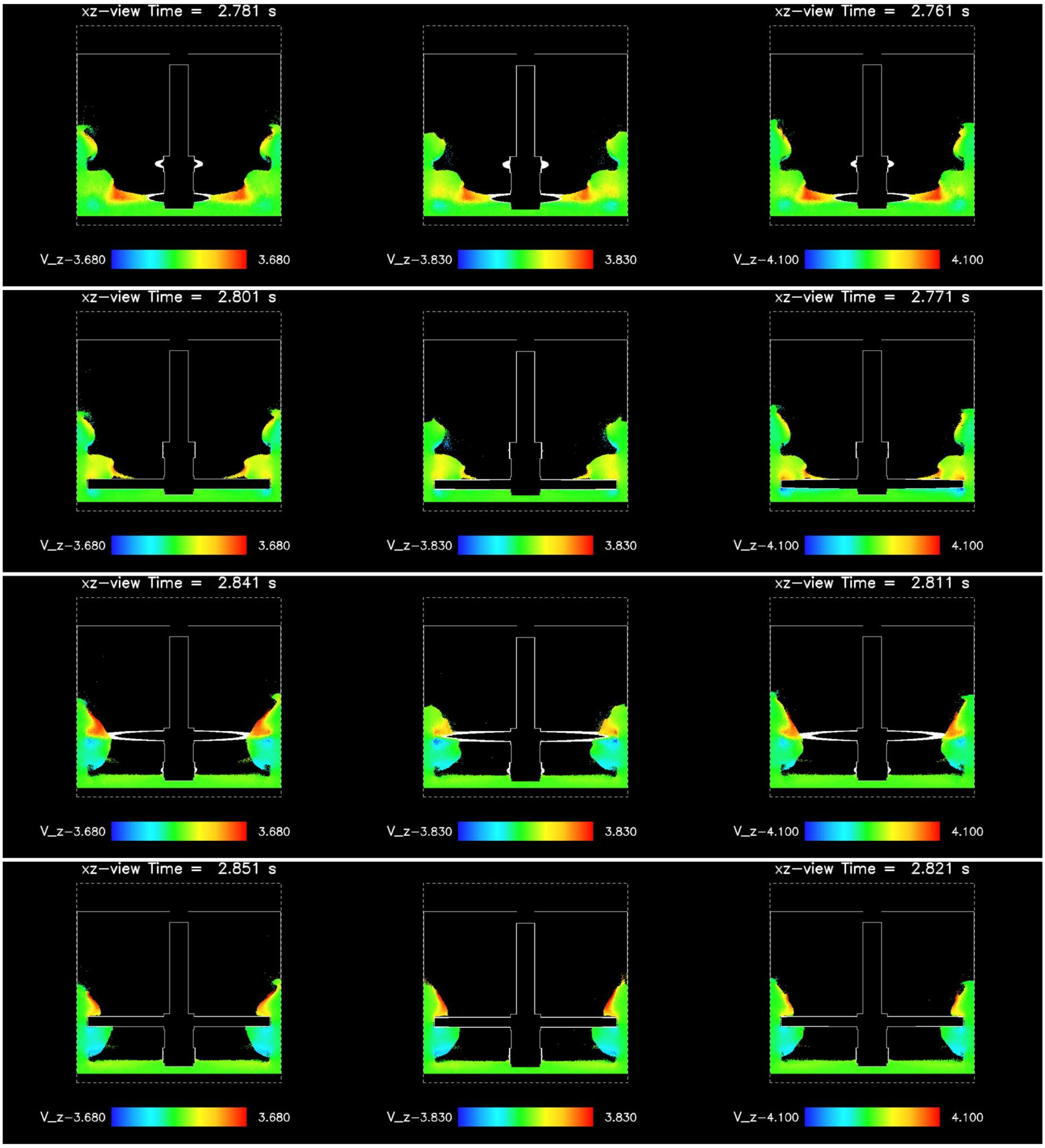

Figure 78: Horizontal section through the SMD 1100-E. Each row shows a different phase of the impeller like that of the SMD18.5-E. Media is coloured by axial velocity.

9.2 Power Data

Power data for the SMD 355-E simulations

Variant	Average Power kW	% of installed power	Media Dissipation (kW)	Slurry Dissipation (kW)	% dissip. in viscous stresses	% of power draw media-media collisions
Base case	388.60	109.46	286.27	102.33	26.33	73.67
1	350.36	98.69	256.48	93.88	26.80	73.20
2	230.71	64.99	171.82	58.89	25.53	74.47
3	313.21	88.23	229.59	83.62	26.70	73.30

9.3 ELS Data

	ELS Modal peaks								
	All collisions			Media-media			Media Liner		
Variant	Normal (mJ)	Shear (mJ)	Total (mJ)	Normal (mJ)	Shear (mJ)	Total (mJ)	Normal (mJ)	Shear (mJ)	Total (mJ)
Base case	0.14	0.68	0.76	0.14	0.60	0.68	1.07	2.52	2.52
1	0.16	0.66	0.73	0.15	0.56	0.66	1.47	2.23	2.39
2	0.78	1.21	1.57	0.72	1.09	1.44	1.80	1.72	2.14
3	**0.21**	**0.82**	**0.90**	**0.20**	0.74	**0.82**	**1.82**	**2.40**	**2.73**

	Dissipation rates for associated peaks								
	All collisions			Media-media			Media Liner		
Variant	Normal (w)	Shear (w)	Total (w)	Normal (w)	Shear (w)	Total (w)	Normal (w)	Shear (w)	Total (w)
Base case	300.00	1200.00	1500.00	200.00	900.00	1000.00	5.00	100.00	190.00
1	186.00	743.00	952.00	186.00	743.00	951.00	12.00	145.00	160.00
2	135.00	513.00	650.00	123.00	446.00	566.00	21.00	88.00	96.00
3	**174.00**	**727.00**	**948.00**	**182.00**	**724.00**	**943.00**	**9.10**	**77.00**	**82.00**

	ELS Modal peaks					
	Mill Shell			Impeller		
Variant	Normal (mJ)	Shear (mJ)	Total (mJ)	Normal (mJ)	Shear (mJ)	Total (mJ)
Base case	0.03	0.94	0.96	0.80	3.63	4.13
1	0.02	0.82	0.80	0.76	4.21	4.12
2	0.00	0.62	0.62	0.80	5.41	5.10
3	**0.02**	**0.77**	**0.76**	**0.92**	**4.40**	**5.01**

	Dissipation rates for associated modal peaks					
	Mill Shell			Impeller		
Variant	Normal (w)	Shear (w)	Total (w)	Normal (w)	Shear (w)	Total (w)
Base case	2.00	53.37	53.37	5.00	21.69	25.53
1	1.24	33.78	33.78	4.94	20.24	23.90
2	-	18.23	19.49	4.27	15.00	22.00
3	**1.10**	**26.88**	**30.00**	**5.00**	**18.87**	**23.00**

	Boundary wear					
Variant	Total boundary energy (kJ)	% of Total Energy	Shell (kJ)	% of Total Energy	Impeller (kJ)	% of Total Energy
Base case	5.68	4.00	3.86	2.70	1.82	1.30
1	101.40	3.90	62.63	2.40	38.78	1.50
2	61.85	3.70	33.67	2.00	28.18	1.70
6	42.24	3.70	25.53	2.20	16.71	1.50

9.4 Matlab Code for data extraction and analysis

The data files from the DEM-SPH solvers are pfm_g01_f00059.dat file. The following code was written to read that format and convert it to a matlab M file and for the data do be ordered and labelled for analysis

```
%%
function [pcf, pmot, pmots] = f_binRead(fileName, varargin)

    warning off;

    if ~isempty(varargin)
        fnSw = varargin{1};
    else
        fnSw = struct();
    end
    if ~isfield(fnSw, 'offset')
        fnSw.offset = 0;
    end

    %% import data file
    [~, C] = importPFM(fileName);
    C = C{1};
    header = C{1};
    C = C(2:end);

    %% inline functions
    isint = @(x)round(x)==x;
    isint_cell = @(x)round(x(1))==x(1) & x(1)~=0;

    %%
    if ~isfield(fnSw, 'sampleFraction')
        fnSw.sampleFraction = 0.1;
    end
    Ntotal = numel(C);

    %% stage 1
    Nsample = round(fnSw.sampleFraction * Ntotal);
    if ~isempty(fnSw.offset)
        fnSw.offset = 0;
    elseif fnSw.offset > Ntotal-Nsample
        fnSw.offset = Ntotal-Nsample-1;
    end
    sampleRange_ii = (1:Nsample) + fnSw.offset;

    fprintf('Sample fraction of data file = %3.2e\n',
fnSw.sampleFraction);
    fprintf('Size of data sampled from file = %d / %d\n',
Nsample, Ntotal);
    %
    lineCell = cell(Nsample, 1);
```

```
    wh1 = waitbar(0, ['Sorting Stage 1: ', fileName,' ...']);
    tic

    for cii = sampleRange_ii
        waitbar(cii/Nsample, wh1);
        tmp = textscan(C(cii), '%f32');
        lineCell{cii} = tmp{1}';
    end

    t1 = toc;
    fprintf('Stage 1 duration = %4.3f seconds.\n', t1);
    close(wh1)

    %% stage 2
    %-% find the lines containing integers
    intLines = cellfun(isint_cell, lineCell);
    sii = find(intLines);
    numInst = numel(sii);

    %-% sort data into groups of lines
    %-% separated by the integer bearing lines (grid numbers
supposedly)
    lineConc = cell(numInst, 1);
    wh2 = waitbar(0, ['Sorting Stage 2: ', fileName,' ...']);
    tic
    for ii = 1:numInst
        waitbar(ii/numInst, wh2);
        s0 = sii(ii);
        if ii<numInst
            s1 = sii(ii+1) - 1;
        else
            s1 = numel(lineCell);
        end
    %     [s0, s1]
        lineConc{ii} = [lineCell{s0:s1}];
    end
    t2 = toc;
    fprintf('Stage 2 duration = %4.3f seconds.\n', t2);
    close(wh2)

    %% Pattern of a repeating series of groups containing 20,
18, 19 and 13 values
    % turns each set of groups with same number of columns in
to a cell with
    % each column in a different cell.
    % next would be to label each cell with a field name and
store in a struct
    lc20 = formatBinData( lineConc, 20 ); % pcf(1:18)
collisional force data
    lc18 = formatBinData( lineConc, 18 ); % pmot(1:15) GF
MOTIONS data
```

```
    lc19 = formatBinData( lineConc, 19 ); % pmots(1:15) SPH
MOTIONS data
    lc13 = formatBinData( lineConc, 13 ); % blank

    %%
    fieldnames20 = {'xg', 'yg', 'zg', ...
        'Fx', 'Fy', 'Fz', 'Fmag', 'Fn', 'Ft', ...
        'Pnorm', 'Pshear', 'Ptot', ...
        'Cxx', 'Cxy', 'Cyy', 'Czz', 'Cyz', ...
        'KEimp', 'KEimp_i', 'Pslide'};
    pcf = generateStructFromCell(lc20, fieldnames20);

    %%
    fieldnames18 = {'xg', 'yg', 'zg', ...
        'Vr', 'Vt', 'Vz', ...
        'Re_xx', 'Re_xy', 'Re_yy', 'Re_xz', 'Re_zz', 'Re_yz',
'Spin', 'Re_ww', ...
        'granularTemp', 'volumeFrac', 'bulkDensity', 'Tavg'};
    pmot = generateStructFromCell(lc18, fieldnames18);

    %%
    fieldnames19 = {'xg', 'yg', 'zg', ...
        'Vr', 'Vt', 'Vz', ...
        'Re_xx', 'Re_xy', 'Re_yy', 'Re_xz', 'Re_zz', 'Re_yz',
...
        'KE_turb', 'p', 'T', ...
        'Shear', 'volumeFrac', 'bulkDensity', 'unknown'};
    pmots = generateStructFromCell(lc19, fieldnames19);

    save(strrep(fileName, '.dat', '.mat'), 'pcf', 'pmot',
'pmots');
end
```

The following code was used to read the data in the m files created by the code shown above.

```
close all;
clear all;
clc;

%%
driveLetter = 'S';

%%
if ~exist('pcf', 'var')
    filePath = {'C:\Users\uqcndima\OneDrive - The University
of Queensland\My_personal\Aubrey_feedback\Variantsmatfiles\',
...
        [driveLetter, ':\SMD\'], ...
```

```
        'F:\SMD\', ...
        'P:\Work\Data\SMD\', ...
        'W:\SMD\', ...
        'B:\Data\SMD\'};

    filePath = dirCheck(filePath);
    [fileName, Fii] = dirFish(filePath, '*.mat');
end

rho_m = 2700; % density of media, kg/m^3
rho_f = 1379.31; % density of fluid, kg/m^3
rpm = 115;
omega = rpm * 2*pi/60; % rotational speed of impeller, rad/s
g = 9.8;

if iscell(fileName)
    nfiles = numel(fileName);
else
    nfiles = 1;
end

%%
geomVariantMap = containers.Map;
geomVariantMap([filePath, 'pfm_g02_f00059.mat']) =
@getSMDGeom_Var0;
geomVariantMap([filePath, 'pfm_g02_f00045.mat']) =
@getSMDGeom_Var1;
geomVariantMap([filePath, 'pfm_g02_f00103.mat']) =
@getSMDGeom_Var2;
geomVariantMap([filePath, 'pfm_g02_f00053.mat']) =
@getSMDGeom_Var3;
geomVariantMap([filePath, 'pfm_g02_f00083.mat']) =
@getSMDGeom_Var4;
geomVariantMap([filePath, 'pfm_g02_f00090.mat']) =
@getSMDGeom_Var5;
geomVariantMap([filePath, 'pfm_g02_config_6_f00083.mat']) =
@getSMDGeom_Var6;


variants = cellfun(@func2str, geomVariantMap.values,
'UniformOutput', false);
variants = cellfun(@(s)s(end), variants, 'UniformOutput',
false)';

P_calc_map = containers.Map; %kW?
P_calc_map([filePath, 'pfm_g02_f00059.mat']) = 388.6;
P_calc_map([filePath, 'pfm_g02_f00045.mat']) = 350.36;
P_calc_map([filePath, 'pfm_g02_f00103.mat']) = 230.71;
P_calc_map([filePath, 'pfm_g02_f00053.mat']) = 351.98;
P_calc_map([filePath, 'pfm_g02_f00083.mat']) = 261.02;
P_calc_map([filePath, 'pfm_g02_f00090.mat']) = 269.35;
```

```
P_calc_map([filePath, 'pfm_g02_config_6_f00083.mat']) =
313.21;
P_calc_map([filePath, 'pfm_g03_f00071.mat']) = 968;

Power_dissipation = [286.27, 102.33; ...
    171.82 58.89; ...
    203.56 148.42; ...
    182.93 78.08; ...
    177.09 92.26; ...
    229.59, 83.62; ...
    296.03, 119.56];
Power_dissipation = Power_dissipation(cellfun(@str2num,
variants)+1, :);

chargeHeight_conrad = [1.27785, 1.24509 1.27785 1.31082
1.77009, 1.37634 1.44207];
chargeHeight_conrad = chargeHeight_conrad(cellfun(@str2num,
variants)+1);

%% loop initialisations
% nfiles
P_impeller_drag_fluid   = zeros(nfiles, 1);
P_impeller_drag_grains  = zeros(nfiles, 1);
P_impeller_lift         = zeros(nfiles, 1);
P_DEM                   = zeros(nfiles, 1);

engage_m_mean           = zeros(nfiles, 2);
engage_f_mean           = zeros(nfiles, 2);
totalEngagement_m       = zeros(nfiles, 1);
totalEngagement_m_err   = zeros(nfiles, 1);
totalEngagement_f       = zeros(nfiles, 1);
totalEngagement_f_err   = zeros(nfiles, 1);

geom                = cell(nfiles, 1);
geomConfig          = cell(nfiles, 1);
impellerLevels_zii  = cell(nfiles, 1);
daxStruct_f         = cell(nfiles, 1);
daxStruct_m         = cell(nfiles, 1);
dthStruct_m         = cell(nfiles, 1);
dthStruct_f         = cell(nfiles, 1);
engagementData_m    = cell(nfiles, 1);
engagementData_f    = cell(nfiles, 1);
dP_drag_m_i         = cell(nfiles, 1);
dP_lift_m_i         = cell(nfiles, 1);
dP_drag_f_i         = cell(nfiles, 1);
dP_lift_f_i         = cell(nfiles, 1);
l2d_ratio           = cell(nfiles, 1);
chargeHeight        = cell(nfiles, 1);
fluidHeight         = cell(nfiles, 1);

for fii = 1:nfiles
```

```
    if iscell(fileName)
        filename = fileName{fii};
    else
        filename = fileName;
    end
    [pmot, pmots, pcf, grids, gridDims, geom{fii}] ...
        = loadPFMdata(filename, geomVariantMap(filename));

    gridR = grids{1}; gridTheta = grids{2};
    gridZ{fii} = grids{3};%-min(grids{3}); %gridZ = grids{3};

    %% restructure linear arrays in to nz layers of nx x ny
matrices
    %-% axial structure
    daxStruct_m{fii} = processStructCellArray(pmot, 'zg',
grids, gridDims);

    daxStruct_f{fii} = processStructCellArray(pmots, 'zg',
grids, gridDims);

    %-% angular structure
    dthStruct_m{fii} = processStructCellArray(pmot, 'yg',
grids, gridDims);

    dthStruct_f{fii} = processStructCellArray(pmots, 'yg',
grids, gridDims);

    %% finding relevant z bins for impeller arms
    za = arrayfun(@(z)[z-geom{fii}.r_arm, z+geom{fii}.r_arm],
...
        geom{fii}.z_arm, 'UniformOutput', false);
    impellerLevels_zii{fii} = ...
        cellfun(@(z)find((z(1)<=gridZ{fii} &
gridZ{fii}<=z(2))), za, ...
        'UniformOutput', false);

    %% calculate impeller arm engagement zone
    dth = deg2rad(15); % angular interval for sample
    volFrac_thresh = 0.05; % volume fraction threshold for
engagement

    [Engagement_m_mean, Engagement_m_std,
engagementData_m{fii}] = ...
            computeImpellerArmEngagement(daxStruct_m{fii},
geom{fii}, ...
            impellerLevels_zii{fii}, volFrac_thresh, dth);

    [Engagement_f_mean, Engagement_f_std,
engagementData_f{fii}] = ...
```

```
            computeImpellerArmEngagement(daxStruct_f{fii},
geom{fii}, ...
            impellerLevels_zii{fii}, volFrac_thresh, dth);


end

%% summarize impeller power total due to drag (lift) from
solids and liquids
[P_drag_grains, dP_drag_grains] = ...
    sumImpellerPower(dP_drag_m_i, geomConfig);
[P_lift_grains, dP_lift_grains] = ...
    sumImpellerPower(dP_lift_m_i, geomConfig);
[P_drag_fluid, dP_drag_fluid] = ...
    sumImpellerPower(dP_drag_f_i, geomConfig);

P_drag_impeller = P_drag_const * ...
    (rho_m * P_drag_grains + rho_f * P_drag_fluid);
dP_drag_impeller = P_drag_const *
sqrt(rho_m^2*dP_drag_grains.^2 + ...
    rho_f^2*dP_drag_fluid.^2);

P_lift_impeller = P_lift_const * rho_m * P_lift_grains;

[P_drag_impeller, P_lift_impeller]

P_impeller = P_drag_impeller + P_lift_impeller;
dP_impeller = sqrt(P_drag_const^2 * rho_m^2 *
dP_drag_grains.^2 + ...
    P_drag_const^2 * rho_f^2 * dP_drag_fluid.^2 + ...
    P_lift_const^2 * rho_m^2 * dP_lift_grains.^2);

[P_impeller, dP_impeller]

%%
cellfun(@(g)range(g.z_arm), geom)

%%
fii = 1;
% geomConfig{fii}
lii = 2;
aii = 1:geomConfig{fii}(lii);
sph = armEngagementChecker(daxStruct_f{fii}, geom{fii},
volFrac_thresh, ...
    engagementData_f{fii}, lii, aii);

sii=1; sph(sii).Position = [sph(sii).Position(1:2),
1.1*sph(sii+1).Position(3:4)];
sii=8; sph(sii).Position = [sph(sii).Position(1:2),
1.1*sph(sii+1).Position(3:4)];
```

```
sii=15; sph(sii).Position = [sph(sii).Position(1:2),
1.1*sph(sii+1).Position(3:4)];

%%
% fluidGrainPowerRatio = ...
%     (rho_f * cell2mat(dP_drag_fluid))./(rho_m *
cell2mat(dP_drag_grains))

%%
% engage_sum = max([totalEngagement_m, totalEngagement_f], [],
2);
% engage_sum = mean([totalEngagement_m, totalEngagement_f],
2);
engage_sum = totalEngagement_m; engage_err =
totalEngagement_m_err;
% engage_sum = totalEngagement_f; engage_err =
totalEngagement_f_err;
% engage_sum = [totalEngagement_m; totalEngagement_f];
% engage_err = norm([totalEngagement_m_err,
totalEngagement_f_err]);
% engage_err = [totalEngagement_m_err; totalEngagement_f_err];

figure; hold on;
impellerArmArea = pi * (geom{fii}.r_arm/1000) *
(geom{fii}.R_arm/1000);

engagementArea_total = impellerArmArea * engage_sum;
engagementArea_err = impellerArmArea * engage_err;
weights = 1./engagementArea_err;

y = P_DEM; ylabel('$P_{DEM}$');
% y = cellfun(@(c)c(1), chargeHeight); ylabel('charge
height');
x = engagementArea_total; xlabel('solids engagement area
(m$^2$)');

p = plot(x, y, 'o', ...
    'MarkerSize', 10, ...
    'MarkerFaceColor', 'auto');

ax = gca;
% %[ft, gof] = fitLinear(x, y);
% text(1.25*ax.XLim(1), ax.YLim(2), sprintf('$R^2$ = %5.3f',
gof.rsquare))
%
% ffSw.do_tight = 0;
% formatFigure(gcf, ffSw);
%
 txtStr = cellfun(@(v, s)sprintf('%s: %s', v, s), ...
     variants(str2num(Fii)), cellfun(@num2str, geomConfig, ...
     'UniformOutput', false), 'UniformOutput', false);
```

```
 text(0.997*x, y, txtStr, 'FontSize', 8);
%
% xii = linspace(0.9*min(x), ...
%     1.1*max(x), 1000);
% plot(xii, ft(xii), 'r--');
%
% %%
% figure;
% x = engage_m_mean(:,1);
% ex = engage_m_mean(:,2);
% y = P_DEM;
% p = errorbar(x, y, zeros(size(y)), zeros(size(y)), -.5*ex,
.5*ex, 'o', ...
%     'MarkerSize', 10, ...
%     'MarkerFaceColor', 'auto');
% % p = plot(P_DEM, engage(:,2), 'o', ...
% %     'MarkerSize', 10, ...
% %     'MarkerFaceColor', 'auto');
% ylabel('$P_{DEM}$');
% xlabel('mean engagement ratio');
% ffSw.do_tight = 0;
% formatFigure(gcf, ffSw);
%
% text(x, y, txtStr, 'FontSize', 8);
%
% %%
% figure; hold on;
% % p = errorbar(P_DEM, engage(:,1), engage(:,2), 'o', ...
% %     'MarkerSize', 10, ...
% %     'MarkerFaceColor', 'auto');
% p = plot(engage_m_mean(:,2), P_DEM, 'o', ...
%     'MarkerSize', 10, ...
%     'MarkerFaceColor', 'auto');
% ylabel('$P_{DEM}$');
% xlabel('deviation of engagement ratio');
% ffSw.do_tight = 0;
% formatFigure(gcf, ffSw);
%
% text(engage_m_mean(:,2), P_DEM, txtStr, 'FontSize', 8);

%%

cl = 20;

sii = [1:7];
% cd =
% P_impeller = cd * P_impeller_drag + cl * P_impeller_lift;
% mu_lift = ;
% P_impeller_lift_friction = mu_lift * P_impeller_lift;
% P_model = P_impeller_drag_grains + P_impeller_drag_fluid;% +
P_impeller_lift_friction;
```

```
P_model = P_drag_impeller; dev = dP_drag_impeller;
% P_model = P_impeller; dev = dP_impeller;

% y = P_model(sii);
% x = P_DEM(sii);
% e = dev(sii);
% w = 1./e;
%
% figure; hold on;
% p = plot(x, y, 'o', ...
%     'MarkerSize', 10, ...
%     'MarkerFaceColor', [1 1 1]*0.8);
% errorbar(x, y, e, 'b.');
% ylabel('$\frac{1}{c_d}P_{\mbox{drag}}$ (kW)');
% xlabel('$P_{DEM}$ (kW)');
%
% [ft, gof] = fitLinear(x, y)
% ax = gca;
% text(1.25*ax.XLim(1), 0.9*ax.YLim(2), ...
%     sprintf('$R^2$ = %5.3f\n$p_1$ = %5.3f', gof.rsquare,
ft.p1));
%
% formatFigure(gcf);
%
% text(0.9975*x, y, txtStr(sii), 'FontSize', 8);
%
% xii = linspace(0.9*min(x), 1.1*max(x), 1000);
% plot(xii, ft(xii), 'r-');

%%
figure; hold on;
% x = engagementArea_total;
x =  P_drag_const * rho_m * P_drag_grains;
y = P_lift_const * rho_m * P_lift_grains;
plot(x, y, 'o', ...
    'MarkerSize', 10, ...
    'MarkerFaceColor', 'auto');
xlabel('Power to overcome drag due to solids (kW)');
ylabel('Power to overcome lift friction due to solids (kW)');

ax = gca;
[ft, gof] = fitLinear(x, y);
text(1.5*ax.XLim(1), 0.9*ax.YLim(2), sprintf('$R^2$ =
%5.3f\nratio = %5.3f', gof.rsquare, ft.p1))

formatFigure(gcf);

% text(0.9975*x, y, txtStr, 'FontSize', 8);
%
% xii = linspace(0.9*min(x), 1.1*max(x), 1000);
% plot(xii, ft(xii), 'r-');
```

```
%% radial-axial charge profile
%-%
%-%

vShape = cellfun(@(d)calculateVortexShape(d, 0.1),
dthStruct_m, ...
    'UniformOutput', false);

%-%
figure;
sn = 3; sm = 3;
for vii = 1:numel(vShape)

    vvShape = cell2mat(vShape{vii});

    subplot(sn, sm, vii); hold on;
    plot(vvShape(:,1), vvShape(:,2), '.');
    ax = gca;
    ax.YLim = [0 geom{1}.Lax];


    cellfun(@(ii)line(ax.XLim, [1 1]*gridZ{vii}(mean(ii)),
'Color', 'm'), ...
        impellerLevels_zii{vii});

    xlabel(txtStr{vii});
    axis equal
    ax.XLim = [0 max(gridR)];
end

%%
[x, y, stats] = Bin1D_custom(vvShape(:,2), vvShape(:,1), 30);

figure; hold on;
% plot(vvShape(:,2), vvShape(:,1), '.')
% plot1D(x', y, stats);
plot(y, x', '.:');

%%
fii = 1; % data set index
lii = 1; % impeller level index
aii = 1; % impeller arm index
thii = find(engagementData_m{fii}.thii{lii}{1});
Vt = dthStruct_m{fii}{thii(aii)}.Vt(:,
impellerLevels_zii{fii}{lii});

% roii = ~isoutlier(Vt);
% Vt(~roii) = NaN;

figure; hold on;
plot(gridR, Vt/omega, '.')
```

```
xlabel('$R$')
ylabel('$V_t$');

ax = gca;
line([1 1]*geom{fii}.R_arm, ax.YLim)
line([1 1]*geom{fii}.R, ax.YLim)

formatFigure(gcf);

%%
isoStruct = pmots;
isoStruct.R = arrayfun(@(ii)grids{1}(ii), isoStruct.xg);
isoStruct.Theta = arrayfun(@(ii)grids{2}(ii), isoStruct.yg);
isoStruct.Z = arrayfun(@(ii)grids{3}(ii), isoStruct.zg);
[isoStruct.X, isoStruct.Y] = pol2cart(isoStruct.Theta,
isoStruct.R);

%%
figure;
fii = 1;
lii = 1; %level of impeller
aii = 4; % impeller number
fileName{fii};

thii = find(engagementData_m{fii}.thii{lii}{aii});
dtmp = dthStruct_m{fii}(thii);
dtmp = collapseStructures_mean(dtmp);

Vrz = sqrt(dtmp.Vr.^2+dtmp.Vz.^2);
V = sqrt(dtmp.Vr.^2+ dtmp.Vt.^2 + dtmp.Vz.^2);

rii = dtmp.R <= geom{fii}.R;

% quiver(dtmp.R(rii), dtmp.Z(rii), dtmp.Vr(rii), dtmp.Vz(rii),
1.5);
patchie(dtmp.R(rii), dtmp.Z(rii), ...
    dtmp.Vr(rii)./Vrz(rii), dtmp.Vz(rii)./Vrz(rii), 15,
Vrz(rii));

% quiver(dtmp.R(rii), dtmp.Z(rii), dtmp.Vr(rii),
dtmp.Vz(rii));
% patchie(dtmp.R(rii), dtmp.Z(rii), dtmp.Vr(rii),
dtmp.Vz(rii), 5, Vrz(rii));

ax = gca;
line([1 1]*geom{fii}.R, [0, geom{fii}.Lax], ...
    'Color', 'k', 'LineWidth', 3);
line([0 geom{fii}.R], [0, 0], ...
    'Color', 'k', 'LineWidth', 3);
```

```
arrayfun(@(zii)line([0 geom{fii}.R_arm], [1
1]*gridZ{fii}(zii), ...
    'Color', 'm', 'LineWidth', 3), ...
    impellerLevels_zii{fii}{2});

arrayfun(@(zii)line([0 geom{fii}.R_arm], [1
1]*gridZ{fii}(zii), ...
    'Color', 'c', 'LineWidth', 3), ...
    impellerLevels_zii{fii}{1});

title(['Radial-axial flow field at impeller ', num2str(aii),
...
    ' on level ',num2str(lii),'.']);
xlabel('$r (mm)$');
ylabel('$Z (mm)$');

formatFigure(gcf);

% This section is the Quiver plot for plotting
% quiver3(isoStruct.X, isoStruct.Y, isoStruct.Z, ...
%     isoStruct.Vr, isoStruct.Vt, isoStruct.Vz);

% plotImpeller3D(geom{fii});

%%
% close all; clc;
fii = 1;
lii = 1;
aii = [2 5];
% ax = velocityFieldSampler(dthStruct_f{fii},
daxStruct_f{fii}, geom{fii}, ...
%     engagementData_f{fii}, lii, aii);
ax = velocityFieldSampler(dthStruct_m{fii}, daxStruct_m{fii},
geom{fii}, ...
    engagementData_m{fii}, lii, aii);
```